Effects of large earthquakes on a KBS-3 repository

Evaluation of modelling results and their implications for layout and design

Billy Fälth, Harald Hökmark

Clay Technology AB

Raymond Munier, Svensk Kärnbränslehantering AB

June 2010

SKB

Effects of large earthquakes on a KBS-3 repository

Evaluation of modelling results and their implications for layout and design

Billy Fälth, Harald Hökmark

Clay Technology AB

Raymond Munier, Svensk Kärnbränslehantering AB

June 2010

Summary

This report addresses the risk that seismic events could impair the integrity of the buffer-canister system in a KBS-3 repository for spent nuclear fuel. Sweden is presently considered an area of low seismicity, with earthquakes rarely exceeding magnitude four. In particular the south-eastern portion of Sweden, where SKB's candidate sites Forsmark and Laxemar are located, is relatively inactive. However, the possibility that future glacial cycles in Sweden will influence regional seismicity cannot be ruled out. The last major deglaciation (~ 10,000 years ago) in northern Sweden was accompanied by widespread reverse faulting. Therefore, we assume that the type of future post-glacial earthquakes that could potentially have an impact on the safety of the final repository are those of a dip-slip nature (reverse faulting).

The seismic risk relevant to the repository is fracture shear displacements across deposition holes induced by the effects of a nearby earthquake. If a shear displacement is large, the shear velocity not too low and the intersection geometry unfortunate, the forces transferred from the moving rock walls across the bentonite buffer could theoretically cause plastic deformations in the canister extensive enough to damage it. For the SR-Site safety assessment a 0.05 m fracture displacement across a deposition hole counts as canister damage, regardless of the actual shear velocity and the actual intersection geometry.

A large set of results from dynamic earthquake simulations are generated using *3DEC*, a three-dimensional distinct-element code for discontinuous media modelling. The earthquakes are of reverse type, i.e. as with existing mapped post-glacial faults in northern Sweden. The modelling does not attempt to reproduce an expected typical post-glacial Forsmark or Laxemar event. Instead, input data that control potentially important seismic parameters such as event magnitude, amount of stress drop, fault dip and slip velocity, are varied systematically in schematic and generic simulations to cover event ranges that are potentially relevant to the safety assessment. The fault rupture is initiated at a predefined hypocentre and pro-grammed to propagate outward along the fault plane with a specified rupture velocity until it is arrested at a prescribed rupture area boundary. The *3DEC* models include large numbers of explicitly modelled host rock fractures with varying orientations at different distances from the earthquake fault. The coseismic response of these "target fractures", i.e. the induced target fracture slip, is the main output from the simulations.

It is well known that fracture slip scales with fracture size. Therefore, for convenience all target fractures have the same reference size (150 m equivalent radius), such that all results can easily be converted to apply for arbitrarily-sized fractures. The results are presented as time histories for the most affected target fractures and as cumulative plots of the peak slip for all target fractures in each specific model or in each category of models, as shown in the examples in Figure S-1.

As expected, fractures located close to the slipping fault move more than more distant fractures. The sensitivity to distance is found to be significant in all models, but is most significant for earthquakes of the smallest magnitudes analysed here; magnitude 5.5. For the smallest distance between the slipping fault and target fractures considered in the models (200 m), the induced fracture slip was found to vary between 0 and 0.112 m, depending on the earthquake parameters (moment magnitude, stress drop, slip velocity etc.) and on the target fracture orientation and position relative to the hypocentre. The modelling results indicate that the fault slip velocity is the most important parameter, whereas the earthquake magnitude is, relatively seen, less important. The goal of the modelling is to find out under what reason-ably realistic conditions target fractures would slip in excess of the 0.05 m canister damage threshold. As such, a reality check is made on the simulations to filter out results obtained from simulations that appear to represent earthquakes with unrealistic fault slip velocities. Based on findings in the literature, 4.5 m/s is considered an upper velocity bound for large and realistic events.

Results from simulations judged to be reasonably realistic are compiled to establish critical radii as functions of the perpendicular distance between fault and fracture centre. The critical radius represents the size of a fracture that could slip by 0.05 m but not more for a given seismic load. Critical radii are defined for two categories of earthquakes: those that could occur on faults with trace lengths between 3 and 5 km and those occurring on faults longer than 5 km.
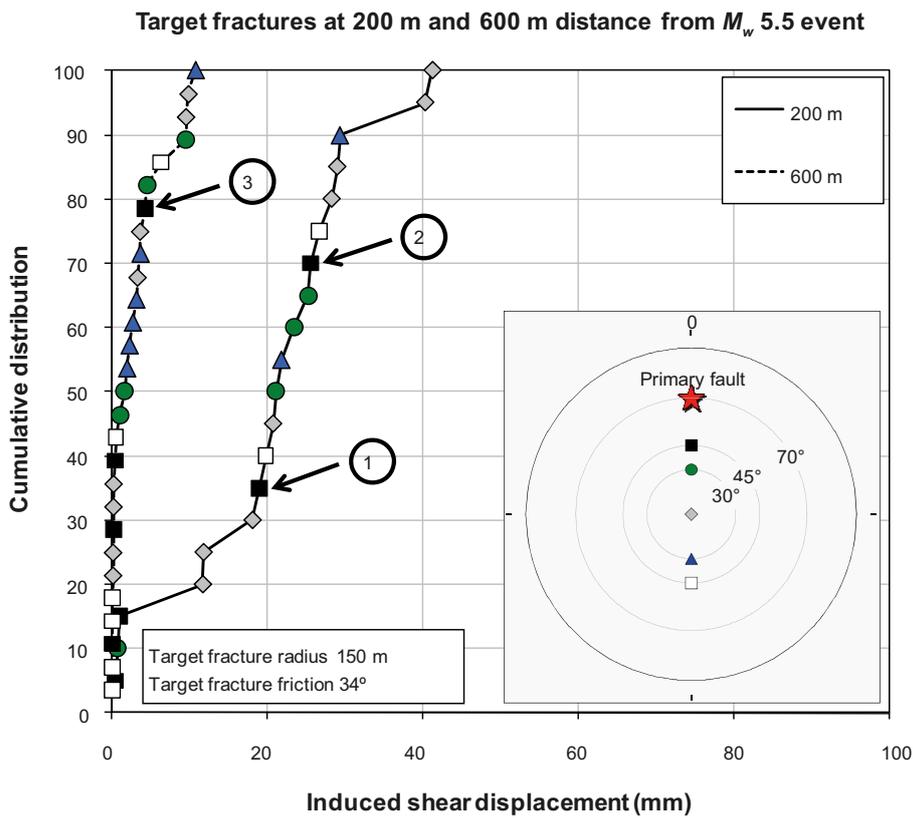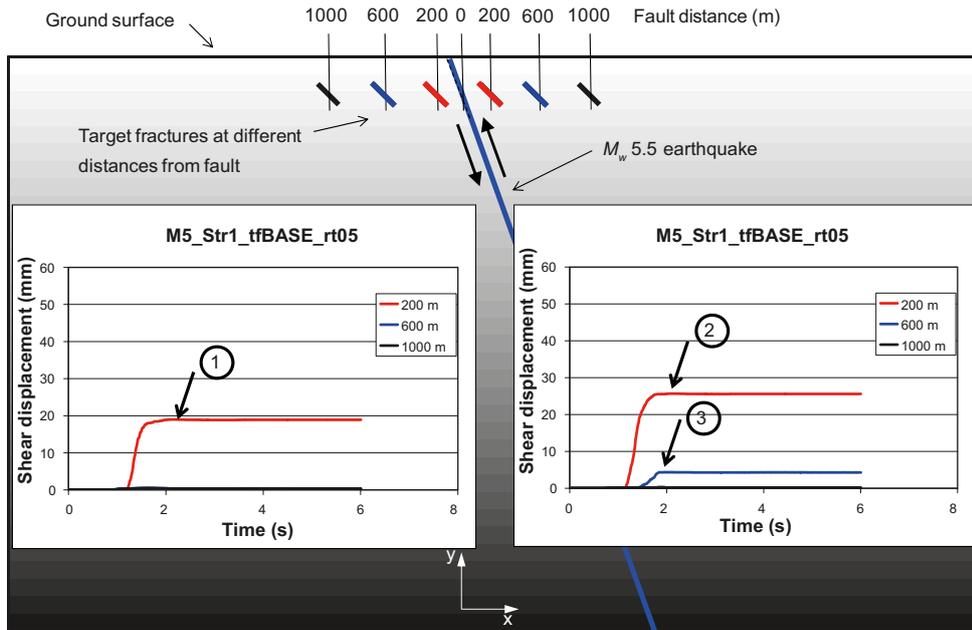
Figure S-1. *Upper: Examples of slip time histories for fractures dipping 45 degrees and striking parallel with the earthquake fault in one particular model. The two graphs show the different response in the footwall and hanging wall of the fault generating the seismic event. Lower: Cumulative plot showing the peak slip for all fractures at 200 and 600 m distance in that type of model. The inset shows the fracture orientation code. The numbered arrows identify results shown in the history plots.*

Schematic layout rules, based on the calculated critical radii, are suggested. Regardless of the calculation results, no canisters should be deposited within a 100 m respect distance from deformation zones with trace lengths larger than 3 km. As far as the 100 m respect distance is concerned, these rules are consistent with the layout upon which the SR-Site safety assessment is based (Layout D2). Values of critical radii are important to the implementation of that layout, since they contribute to determine which canister positions that must be rejected and, consequently, the projected loss of deposition holes.

The schematic layout rules are based on the assumption that every deformation zone, regardless of its orientation, is a potential seismogenic fault that could rupture at its maximum seismic moment, which is a direct function of the size of the deformation zone. This is obviously an overly conservative assumption; whether a zone is or will be seismically active is a function of multiple geological parameters including *in situ* stresses, rock mechanical properties, and deformation zone orientations relative to principal stress directions. One part of the report concerns the stability of differently oriented deformation zones under post-glacial stress conditions. Glacially induced stresses, obtained from ice-crust-mantle analyses performed at the Geophysical Institute of Uppsala University /Lund et al. 2009/ for the Forsmark site, are added to three different *in situ* stress fields. The three stress fields correspond to different views of how stresses and stress ratios may vary with depth much below the well characterized site model rock volume. The resulting stress fields are used to assess the stability of deformation zones at the Forsmark site during a glacial cycle. Given the assumption that future glacial cycles will be similar to the last one, it can be concluded that only a few deformation zones need to be considered as potentially unstable and require respect distances. It will, consequently, be possible to specify layout versions following Layout step D2 in a way that makes more efficient use of the target rock volume. Figure S-2 shows Forsmark deformation zones that have respect distances in Layout D2. Based on the results of the stability analysis it is recommended that only zones denoted "unstable" should have respect distances in following layout versions.
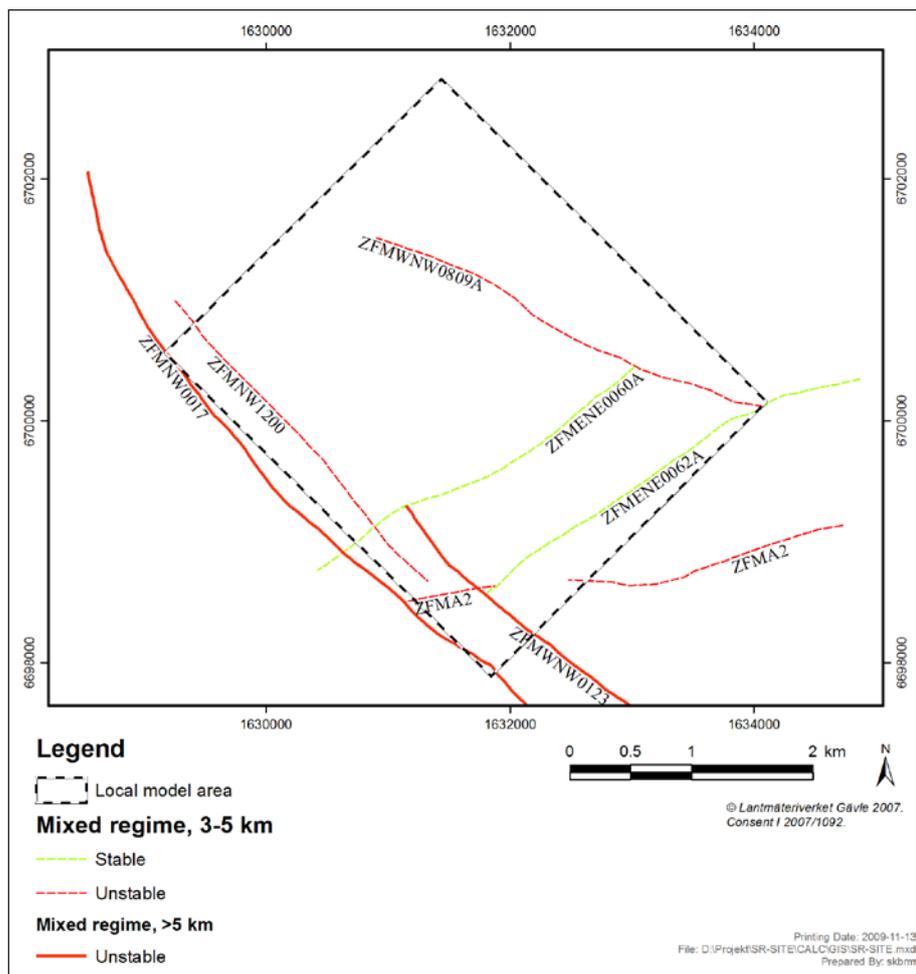
Figure S-2. Forsmark deformation zones with trace lengths larger than 3 km. Stable zones are marked green whereas potentially unstable zones are marked red.

Contents

1 Introduction and background

1.1 General

The concept for storing spent nuclear fuel applied by SKB is the KBS-3 system in which the spent fuel will be encapsulated in canisters consisting of a cast iron insert surrounded by a copper shell. The canisters will be emplaced in vertical deposition holes in crystalline rock at a depth of approximately 500 m below ground surface. The canisters will be surrounded by a barrier of bentonite clay for isolation and mechanical protection. Since the fuel will be hazardous for very long times the time perspective utilized in the safety assessment work is hundreds of thousands of years. This report addresses the potential risk to the repository that earthquakes occurring within that time frame could impair the integrity of the buffer-canister system.

Current seismicity in Sweden is quite low, with most earthquakes occurring in the south-western portion of the country, along the northeast coast of the Gulf of Bothnia and in Norrbotten /Slunga 1991, Bödvarsson 2002–2010/. The south-eastern portion of Sweden, where both of SKB's candidate repository sites (Forsmark and Laxemar) are located, is relatively inactive, cf. Figure 1-1, left. Although large earthquakes (magnitude about 8) have occurred in Sweden, it is generally agreed that these events were connected to the late stages of deglaciation at the end of the previous ice-age /Lagerbäck 1988, Arvidsson 1996, Bödvarsson et al. 2006, Lagerbäck and Sundh 2008/. While the unambiguous evidence for large post-glacial earthquakes are concentrated in northern Fennoscandia, it cannot be
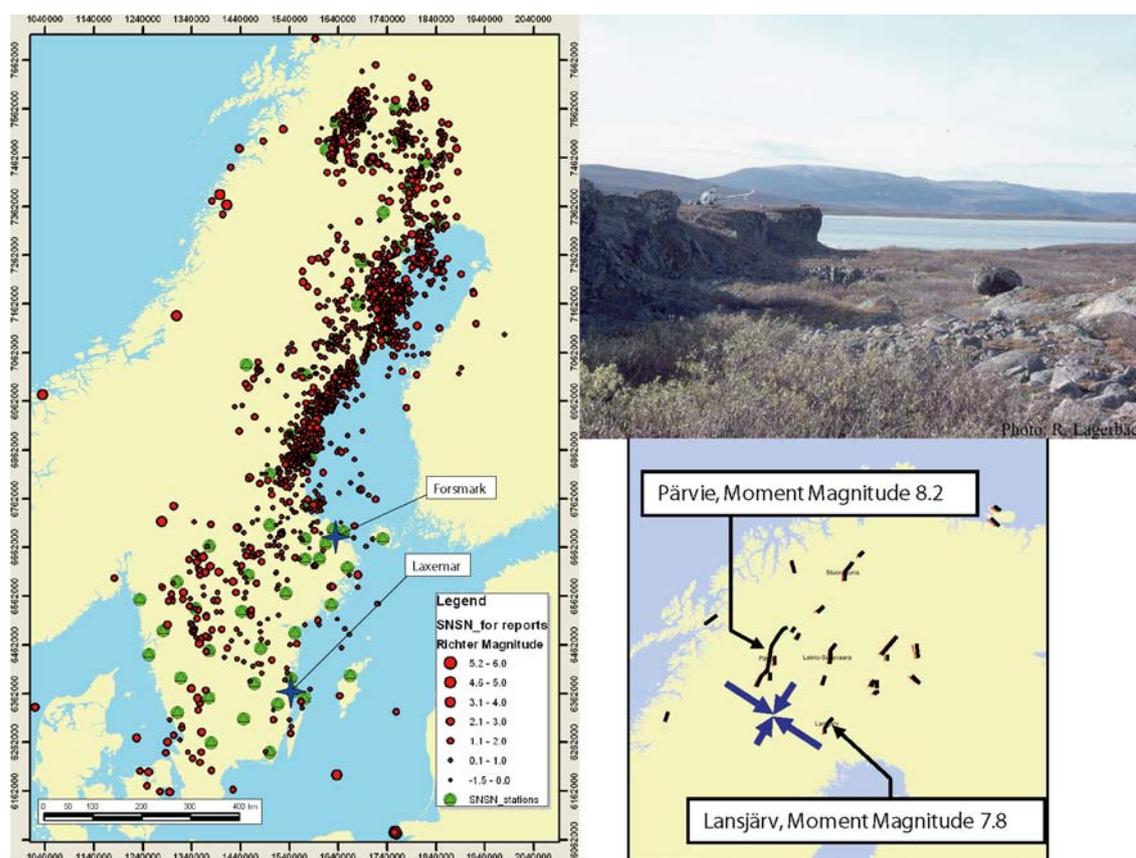
Figure 1-1. Left: present day seismic activity. Swedish National Seismic Network (SNSN) data compiled from /Bödvarsson 2002–2010/. Upper right: Pärvie Fault. The fault displacement is the height of the visible rock to the left in the picture. Picture /from Lagerbäck and Sundh 2008/. Lower right: traces of a number of documented PGF's. Pärvie and Lansjärv magnitudes are from /Muir Wood 1993/ and /Arvidsson 1996/ The stress tensor symbol indicates the approximate orientation of the horizontal stresses at the time of the last deglaciation as derived from /Lund et al. 2009/.

excluded that some large events could have occurred also in central and southern Sweden /Munier and Hökmark 2004/ (In the present report, the term "post-glacial" is used to describe events that are induced by a glacial load and take place either as a direct response to the ice retreat or during subsequent times). /Lagerbäck and Sundh 2008/ argue that post-glacial earthquakes of magnitudes larger than 7 are very unlikely to have occurred in the southern parts of Sweden; however, the possibility of moderately-sized events cannot be discounted. /Lagerbäck and Sundh 2008/ also conclude that post-glacial seismicity comparable with the northern Fennoscandia seismicity at the end of the latest glaciation did not take place in response to previous glacial cycles. At present there is no clear-cut answer to the question of why only the latest glaciation appears to have produced large and numerous earthquakes, and why they occurred only in northern Fennoscandia. The consequence of this uncertainty is that the repository safety assessment cannot completely disregard the possibility of future large post-glacial earthquakes.

1.1.1 Causes of post-glacial seismicity

There are three possible causes of potential instability at the time of deglaciation.

1. Increase of horizontal stresses due to the accumulation of tectonic strain energy under the stabilizing ice cover. Without the stabilizing ice cover, the strain energy continuously produced by large-scale tectonic compression can be assumed to be released incrementally, i.e. as aseismic shear movements along suitably-oriented deformation zones, such that the crust is constantly in a state of stress equilibrium determined by the frictional properties of the deformation zones /Leijon 1993, Zoback and Townend 2001, Scholz 2002/. The weight of the ice cover stabilizes the deformation zones, inhibiting the release of stored strain energy and causing horizontal stresses to increase. When the ice cap (with its associated vertical load) disappears, the excess strain energy caused by the induced horizontal stresses remains. The end result is that some deformation zones, particular those that dip in the direction of the resulting major horizontal stress, may become unstable.

2. Increase of horizontal stresses due to crustal bending. The weight of the ice will cause the crust to bend at a rate that is dependent on the mechanical properties of the crust as well as on the rheological properties of the viscous mantle beneath the crust, cf. e.g. /Muir Wood 1993, Lund 2006, Lund et al. 2009/. The compressive flexural stresses generated in the upper parts of the crust will add to the existing horizontal stresses. When the ice cover and its associated vertical stress loads disappear, the coupling between the lower crust and the viscous mantle will delay the isostatic rebound of deformed crust. Again, the end result is that components of the glacially-induced horizontal stresses will remain, which can potentially destabilize favourably-oriented deformation zones.

3. Residual pore overpressures. There is a possibility that fluid pressures at the ice/bedrock interface will generate increased pore pressures in the rock beneath the ice. The evolution of the excess pore pressure will vary with vertical depth and depend on the time history of the interface pressure and the hydraulic diffusivity of the rock mass. When the ice disappears it will take some time for the pore pressure to return back to undisturbed conditions. Elevated residual pore pressures reduce the effective stresses along deformation zones, and can potentially augment other destabilizing effects.

Figure 1-2 illustrates how the bedrock stress field varies during a glacial cycle. The potential instability at the end of a glacial cycle is due to high horizontal stresses induced by ice loading and potentially augmented by elevated residual pore pressures. The magnitude of the excess stresses depends on the duration and thickness of the ice cover, the mechanical properties of the crust and the rheology of the mantle, the tectonic strain rate and on the speed of the ice retreat /Lund et al. 2009/. The pore overpressure will depend also on the hydraulic diffusivity and on climate conditions, e.g. on whether and in what way impermeable permafrost layers may contribute to subglacial hydrogeologic conditions.

All three of the mechanisms listed above may potentially contribute to instability at the time of deglaciation. /Lagerbäck and Sundh 2008/ suggest that the triggering effects of residual fluid overpressures, developed under a permafrost layer that persisted to the very end of deglaciation, could explain why post-glacial faulting may only have occurred in northern Fennoscandia. In that environment, the ice cover likely accumulated over a deeply-frozen permafrost landscape, resulting in continuously frozen conditions at the ice cap bed. It is uncertain, however, whether the tectonic strain effect is important relative to the effects of crustal flexure and fluid overpressures. Tectonic strain rates on the order of 10^{-11}/year, as suggested by /Muir Wood 1995/, would correspond to a stress increase of approximately 0.1 MPa over a period of 100,000 years, provided that the weight of the ice cover is sufficient to inhibit
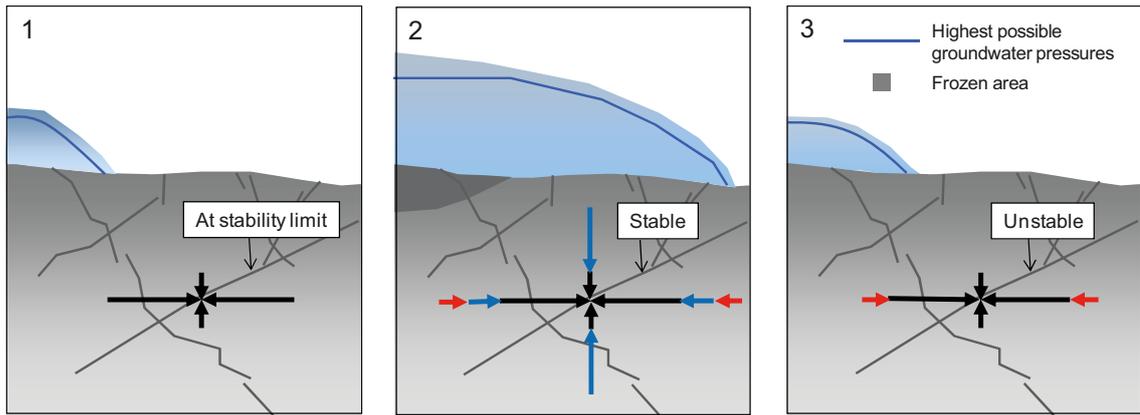
Figure 1-2. *Schematics of stress evolution during a glacial cycle. 1: present-day anisotropic stress field. 2: Stress field under stabilizing ice cover with vertical stress increased by the weight of the ice and horizontal stresses increased because of direct elastic response to the vertical load (blue), tectonic strain and crustal flexure (red). 3: Stress field in region below and outside margin of retreating ice. Stresses induced by tectonic strain and crust flexure remain, giving increased stress anisotropy and, possibly shear failure along fractures and fracture zones dipping in the direction of the major horizontal stress.*

strain energy release completely. Figure 1-3 shows the height of the ice at the time of glacial maximum during the last (Weichselian) glacial stage, as well as the expected height and duration of the ice at the Forsmark and Laxemar sites during a future glacial cycle (assuming the next glaciation to develop as the last one). The stabilizing ice load for a glaciation lasting for 20,000 years would result in less than 3 MPa of horizontal stress increase, even assuming a tectonic strain rate of $1.5 \cdot 10^{-9}$/year /Slunga 1991/, i.e. about two orders of magnitude higher than the 10^{-11}/year rate suggested by /Muir Wood 1995/. /Wu 2009/ considers the tectonic stresses to be time in-variant on a 20,000 year time scale, meaning that tectonic strain rates are sufficiently low that strain accumulation is not important to the stress evolution during a glacial cycle.

As stated above there is evidence that intensive seismic activity associated with glacially-induced faulting took place in northern Fennoscandia (Lapland) in direct conjunction with the melting of the most recent ice cap (the Lansjärv Fault, the Pärvie Fault, etc cf. Figure 1-1, right) /Arvidsson 1996/.
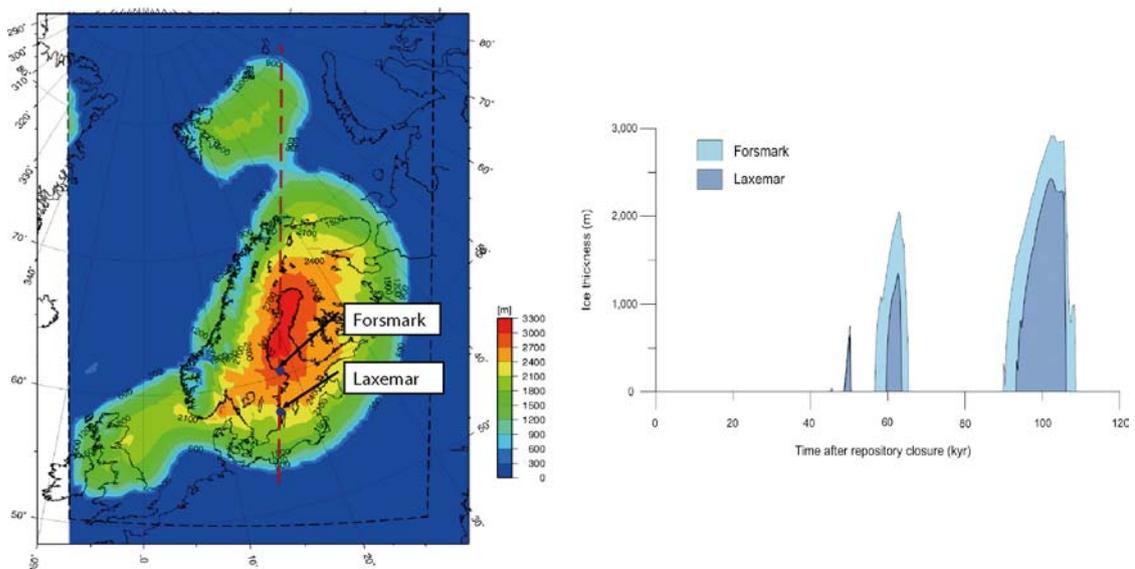
Figure 1-3. *Left: Height of the ice sheet at 18.4 ka BP when the latest ice had its largest extent, modified from /Lund et al. 2009/. Right: Projected evolution of the ice sheet thickness at Forsmark and Laxemar, redrawn from /SKB 2006b/. Projected evolution is based on history of the last glaciation.*

The amount of seismic activity in the area might at some period of time have been comparable to that in tectonically active areas such as plate boundaries. Given that the major compressive stress in the region is horizontal and oriented approximately perpendicular to the fault scarps observed in the region (Figure 1-1, lower right hand diagram), post-glacial seismic activity was most likely associated with reverse faulting. Whether the increased horizontal stresses were due to downwarping alone or if tectonic strain accumulation contributed is uncertain. It is also likely that pore pressure variations had an impact on the stability of the faults at the time of the earthquakes. Considering that the *in situ* stresses at seismogenic depths (say below 2 km) are much larger than the glacially-induced stresses regardless of source mechanism (cf. /Lund et al. 2009/), the large Lapland earthquakes are likely to have been triggered by, rather than powered by, glacial disturbances. Possibly the long unbroken ice cover duration estimated for northern Fennoscandia /Lund et al. 2009, SKB 2006b/ may have contributed to the localisation of post-glacial faulting to that region.

1.1.2 Present-day seismicity

Present-day seismicity is not only low in frequency and modest in magnitude (Figure 1-1, left); for the largest documented historical events the focal depths appear to have been many kilometres, i.e. much below the repository depth projected at the Forsmark and Laxemar sites. The foci of the 1986 magnitude 4.5 Skövde earthquake and its aftershocks, for instance, were located at depths between 20 and 35 km /Arvidsson et al. 1992/. The most recent one, the 2008 magnitude 4.3 Skåne County earthquake, occurred at about 10 km depth /USGS 2008/. Earthquakes of magnitude 5 and smaller have rupture areas of just a few square kilometres, cf. following sections. This means that there would be several kilometres between the repository and the nearest parts of the fault plane for typical present-day earthquakes such as, for instance, the 2008 Skåne County earthquake and the 1986 Skövde earthquake, even if the repository were sited at the epicentre.

Gutenberg-Richter frequency-magnitude relationships established by /Bödvarsson et al. 2006/ for the Forsmark site give a 0.9% probability of an earthquake of magnitude 5 or larger within the next 1,000 years within a 10 km radius of the proposed Forsmark repository site. Projecting these source terms to a 5 km radius gives a probability of 0.2%. Assuming that the next glaciation will occur in approximately 50,000 years (cf. Figure 1-3), this gives about 12% probability of an earthquake of magnitude 5 or larger within a horizontal 5 km range from the repository under present-day stress conditions. The majority of these events will occur at depths too large to be of any consequences to the repository; the net result is that the effective probability of a damaging earthquake is less. In the unlikely case that a rupture event reaches the repository horizon or the ground surface close to the repository, the mechanical consequences for the repository are not judged to be sufficiently different from the consequences of a post-glacial earthquake to require a specific analysis, even though the type of fault motion may be different (strike-slip rather than reverse dip-slip). At the Forsmark site there is a pronounced reverse-type stress field in the upper kilometre of the crust meaning that the response of the repository host rock is not likely to be very different from that of an earthquake along a reverse-slip fault even if the rupture is initiated at depth in a strike-slip environment. It is therefore suggested that simulation results obtained for post-glacial earthquakes should be regarded as reasonably representative of the types of events that could occur under present-day stress conditions.

1.1.3 Summary

Given the available seismic record, the tectonic environment and *in situ* stress states observed in the vicinity of the Forsmark and Laxemar sites, the most-likely type of earthquakes that potentially could impact the safety and long-term performance of a spent-fuel repository are assumed to be post-glacial reverse type faulting events, similar to those pictured in Figure 1-1. However, there are several key uncertainties, including:

- the relative importance of tectonic strain accumulation and crustal bending for increasing the horizontal stresses,
- the importance of pore overpressures and pressure variations,
- the *in situ* stress field at large depths,

that preclude an understanding of why evidence of post-glacial faulting have been observed in northern Fennoscandia, but not in southern Sweden, e.g. around the Forsmark and Laxemar sites. Therefore, in the present report the potential effects of post-glacial faulting on the repository are analysed without any attempts to establish whether a future glacial cycle actually would generate the type of instability that resulted in the northern Baltic Shield post-glacial earthquakes some 10,000 years ago.

1.2 Seismic risk

1.2.1 General

This report does not attempt to forecast the scope and extent of post-glacial seismicity in the Forsmark and Laxemar regions after a future glacial cycle; however, the occurrence of such events is recognized as a real possibility. The consequences for a spent-fuel repository of seismogenic slip along nearby reverse faults similar to those seen in the stratigraphic record in northern Fennoscandia at the end of the last glacial cycle are examined because, at least at present, the uncertainties are too large to allow for the possibility to be disregarded.

The first step in the process of evaluating the issue of future post-glacial seismicity is to establish in what ways earthquakes could impact the safety and long-term performance of a spent repository; i.e. the identification of specific risks.

Liquefaction

The risk of liquefaction (i.e. a soil-water system behaves as a liquid because of shaking, stress increases or liquid pressure increases) of buffer and backfill in response to seismic events has been assessed in the past (cf. /SKB 2006a/). Liquefaction of the buffer was ruled out because of the high bentonite density. Liquefaction of the tunnel backfill was found to be very unlikely and, should it occur, of no consequences for performance and safety. These conclusions are established to be valid also in the SR-Site assessment /SKB 2010a/.

Shaking

Earthquake damage is usually associated with the effects of ground motion (shaking). Earthquake engineering efforts are therefore almost exclusively focussed on mitigating the effects of shaking on buildings and other surface structures. For buried objects such as oil & gas pipelines and other critical infrastructure, most records attribute earthquake-related damage to rupture of the surrounding medium, soil-structure interactions, soil-rock interactions or soil liquefaction at shallow depths (cf. e.g. /Falcão and Bento 2004, Yoshizaki and Sakanoue 2004/). There are few records of damage caused solely by oscillations induced by ground motion. There are some reports, however, of shaking damage to concrete pipes composed of cylinders jointed together to form pipelines. In these structures, damage was concentrated at the pipe joints, which were pulled apart by transient ground deformations /O'Rourke et al. 2004/. There are also records of damage of shaking on underground structures with free rock surfaces such as mines, road tunnels and railway tunnels /La Pointe et al. 1997, Bäckblom and Munier 2002, Aydan et al. 2010/. The buffer-canister system utilized in the KBS-3 repository do not have any free surfaces or weak joints and is, additionally, of very small dimensions (metre scale) compared with typical seismic wavelengths (kilometre scale). This means that the canister, the bentonite buffer that isolates it and the rock volume nearest the deposition hole will move together, i.e. in phase.

Given these constraints, and also noting that the repository will be located deeper below ground surface (where wave amplitudes are smaller) than all of the underground structures considered in the previous case studies of /Bäckblom and Munier 2002/ and /Munier and Hökmark 2004/, it can be concluded that shaking will not have any impact on the integrity of the buffer-canister system.

Rock failure

Stress waves will influence the effective background stress field such that tangential stresses around deposition holes will increase at the time of stress peaks. This may, possibly, result in brittle failure (spalling) in the walls of the holes. This type of stress-induced failure is expected to occur during the period of high thermal stresses a few tens of years after deposition of the heat-generating spent fuel /Hökmark et al. 2010/. The spalling process is, however, known to be sensitive to confining pressures such that support pressures not larger than a few tens of kPa will suppress or even inhibit the failure /Glamheden et al. 2010/. During the period of high thermal stresses the support pressure may be low in deposition holes in which the bentonite buffer has not taken up any water and, consequently, not established any swelling pressure. At the time of post-glacial earthquakes, however, the buffer will have developed a full swelling pressure since long. The full pressure is 1 MPa at minimum /SKB 2010a/. In comparison to the projected disturbance of the near-field permeability caused by failures in the walls of unsupported, or poorly supported, deposition holes during the early stages of the repository evolution, the additional disturbance caused by tangential stress peaks at later times, when the support pressure is much higher, can be disregarded.

It has been proposed that there could be a risk that the repository will act as a plane of weakness, which promotes large-scale fracturing of the rock mass as it is subjected to mechanical loads /SKB 2003/. Normal and shear stress variations on horizontal planes at repository depth caused by nearby large earthquakes are output from the dynamic numerical models presented in this report. These results are used as input to another study /Lönnqvist et al. 2010/ where the risk that the repository may act as a plane of weakness is assessed. According to /Lönnqvist et al. 2010/ the system of tunnels in the repository will have only marginal impact on the rock mass stability provided that the tunnel spacing is not less than about 20 m.

Changes in hydraulic conditions

The shaking and the stress redistribution generated by an earthquake will propagate, shear, close and dilate fractures in the host rock. The extent of these deformations will depend upon the size, location and orientation of the individual fractures in relation to each other and to the earthquake generating fault. It will also depend on the fracture properties, on the *in situ* stress situation and on the character of the earthquake. Some of these deformations will be permanent and result in increased or reduced transmissivities, depending on whether the fracture closed or opened in response to the earthquake, and on whether shear displacements took place under low or high normal stresses /Hökmark et al. 2010/.

One effect of the most-likely type of post-glacial seismic event (i.e. a reverse type event) is to relax horizontal stresses (cf. Figure 1-2). According to the simulation results presented later in this report (Figure 5-9), the horizontal stress relaxation may be of the order of 7 MPa within a distance range of about 1 km from the fault. As noted by /Muir Wood and King 1993/ this would have some impact on the hydraulic conditions. Applying the stress-transmissivity relation suggested by /Hökmark et al. 2010/, the stress relaxation gives an estimated transmissivity increase of up to 100% in steeply dipping, optimally trending fractures and fracture zones. For arbitrarily oriented fractures it is not possible to quantify the effects on transmissivity: There may be increased compression of some fractures with accompanying transmissivity reductions as a result. Fracture slip may occur under high or low normal stresses with very different transmissivity effects .Thus, a post-glacial earthquake may produce both a systematic but modest transmissivity increase in some steeply dipping fractures (and fracture zones) and a less systematic reorganization of the overall flow pattern. The estimated systematic transmissivity increase is of the same magnitude as those estimated to take place due to e.g. thermal loading during the early temperate phase or by glacial loads /Hökmark et al. 2010/.

The seismic impact on the transport properties in general does not appear to be an issue for the safety assessment. If, however, a canister is mechanically damaged as a result of an earthquake, the fractures connecting that particular deposition hole with the biosphere are assumed to short-circuit the hydraulic system without any attempts to quantify the actual mechanical and hydromechanical disturbances imposed upon the fracture system /SKB 2010b/.

Shear displacements across deposition holes

As concluded above, shaking and rock failure in the walls of deposition holes will not damage any canisters. The only seismic risk relevant to the repository is that of fracture shear displacements across deposition holes, cf. Figure 1-4, right. If the fracture shear displacement is large, the shear velocity not too low and the intersection geometry unfortunate, the forces transferred from the moving rock walls across the buffer to the canister may theoretically cause plastic deformations in the copper shell or in the steel insert extensive enough that the canister must count as damaged, with a harmful release of nuclides as a potential consequence. The damage definition is a question of interpreting results of numerical stress-deformation analyses of the buffer-canister system, cf. /Börgesson and Hernelind 2006/.

In the most recent safety analysis, SR-Can, damage criteria of 0.1 m of fracture shear displacement across a deposition hole were used, regardless of the shear velocity and the intersection geometry. This criterion was based on results given in /Börgesson and Hernelind 2006/, but has since been subject to revision based on the results and conclusions of more recent stress-deformation analyses of the buffer-canister system. The buffer-canister analyses were performed assuming high shear velocities (1 m/s). The damage threshold established for the SR-Site safety assessment is 0.05 m /SKB 2009a/. The fracture shear velocity has importance for the potential of canister damage since the shear stiffness of the bentonite buffer is rate-dependent. At present there is no agreed view on the damage thresholds that should apply for lower, or much lower, shear velocities.

Shear displacements across deposition holes as pictured in Figure 1-4, right can potentially occur because the deposition hole is intersected by (cf. Figure 1-5):

1. a slipping earthquake fault (cf. Section 1.2.2),

2. a fracture that is mechanically connected to a slipping earthquake fault (cf. Section 1.2.3),

3. a fracture that is remotely reactivated by the effects of a slipping earthquake fault (cf. Section 1.2.4).
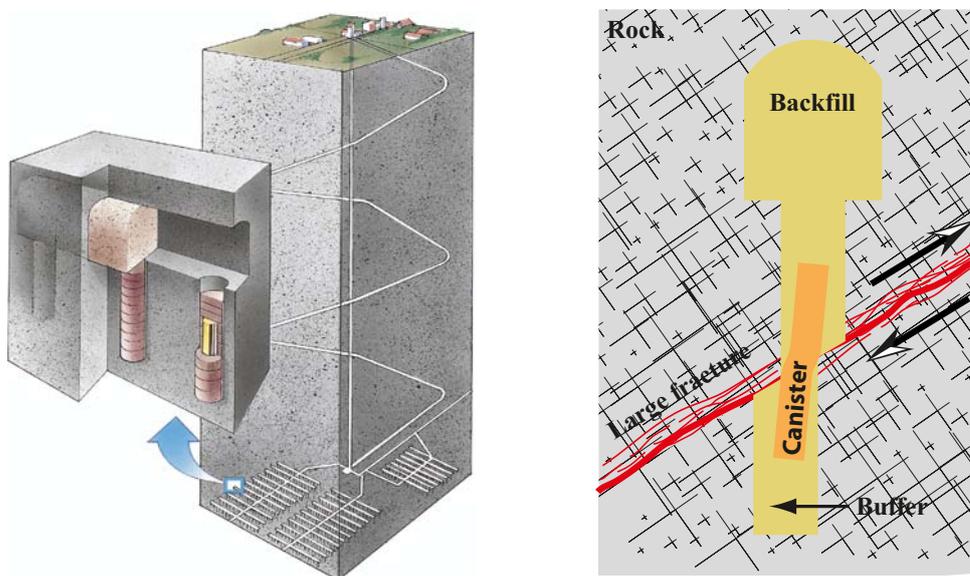
Figure 1-4. *Left: Schematic of KBS-3 repository with ramp, system of horizontal tunnels and vertical deposition holes. Right: Shear displacement across deposition hole.*
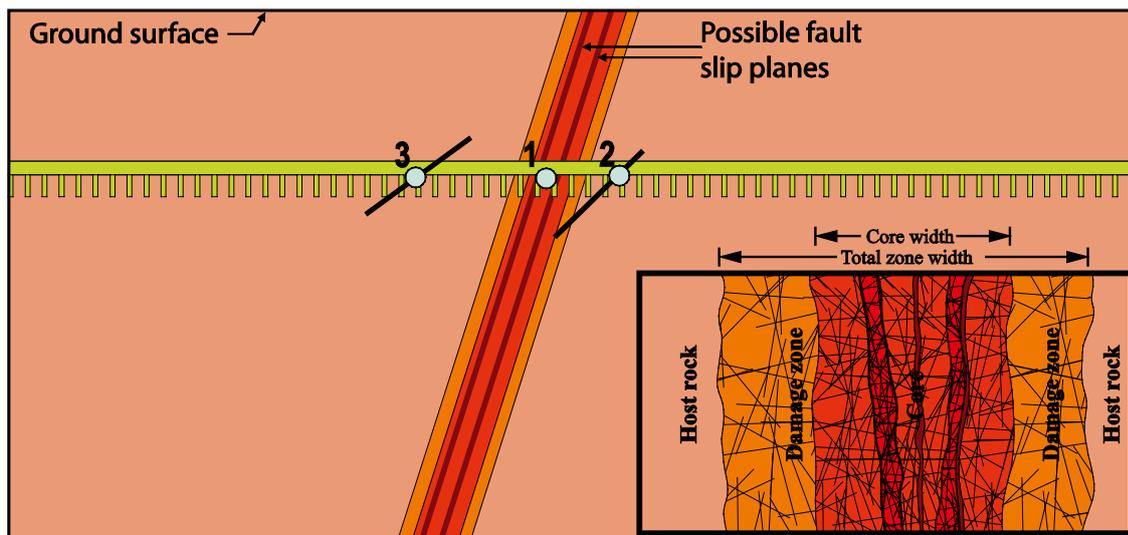
Figure 1-5. *Shear displacements across a deposition hole can potentially occur because the deposition hole intersects 1) a slipping earthquake fault, 2) a fracture that is mechanically connected to a slipping earthquake fault, 3) a fracture that is remotely reactivated by a slipping earthquake fault. Inset shows deformation zone components, cf. /Munier and Hökmark 2004/.*

1.2.2 Earthquake fault displacements

This section relates to direct shear displacement along a seismogenic fault (cf. Figure 1-5, Case 1). Figure 1-6 shows regression correlations between moment magnitude (M_w), maximum displacement, surface rupture length and rupture area derived by /Wells and Coppersmith 1994/ from a database of 224 well-documented crustal earthquakes. According to the relationships presented by Wells and Coppersmith, fault displacement of 0.05 m appears to require an earthquake of M_w 5.7 or larger or, considering the spread around the regression, at least not smaller than M_w 4.5 (Figure 1-6a). Figure 1-6 (b) shows that a M_w 4.5 earthquake corresponds to a rupture area of between 2 km^2 and 30 km^2. Fractures or deformation zones of this size will be safely detected during repository construction if not during the site investigation, meaning that canisters will not be positioned such that they could be damaged by the direct effects of earthquakes originating on existing fault planes /Munier 2006, Munier 2010/.

The following caveats relating to the relevance of the regressions shown in Figure 1-6 should be understood:

1. The regressions are based mainly on large earthquakes. Extrapolating these relationships to earthquakes of magnitude 4.5 or smaller is a very uncertain process. /La Pointe et al. 1997/ suggested that because the effective stiffness decreases with fracture size, the regressions are likely to overestimate displacements on small faults (a, c, d).

2. The regressions regard surface displacements (a, c, d). Subsurface displacements may be significantly larger. /Slunga 1991/, for instance, reported that the 1986 magnitude 4.5 Skövde earthquake with a focal depth of about 26 km had a peak displacement of about 0.3 m. /Bödvarsson et al. 2006/ suggested that a typical magnitude 5 earthquake in Sweden would have a peak displacement of about 0.5 m, a rupture area a little less than 1 km^2, and a depth of about 20 km. Yet, for displacements at shallow depths such as the repository depth, the surface displacements are probably valid approximations for peak displacement.

3. There are no records of reverse-slip earthquakes with surface rupture lengths less than 4 km in the database (c, d). Extrapolating to shorter rupture lengths (and smaller magnitudes) is problematic. In addition, surface rupture length is difficult to measure for earthquakes less than magnitude 6.0 /La Pointe et al. 1997/.

The database used by Wells and Coppersmith does not include any records of post-glacial earthquakes of the type thought to occur in Fennoscandia; therefore, the relationships indicated by these regressions should be interpreted with caution.
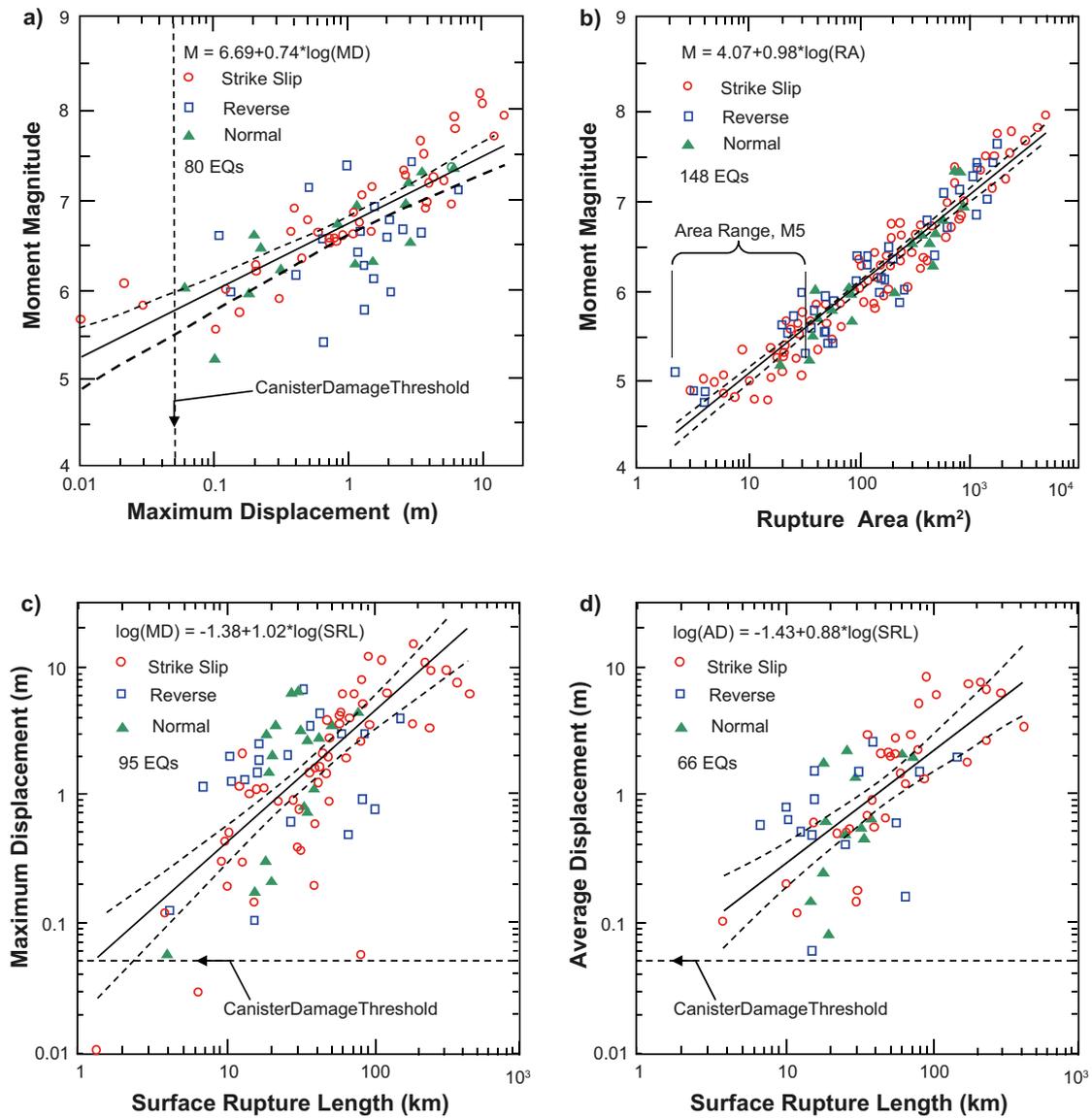
Figure 1-6. *Regression relations. Redrawn from /Wells and Coppersmith 1994/.*

The probability that future earthquakes will occur as ruptures of pristine rock rather than as reactivations of existing deformation zones is estimated to be too small to be considered in the seismic risk assessment. /Larsson and Tullborg 1993/ concluded that the fracture pattern and the heterogeneities of the crust in the Baltic Shield has developed over a sufficiently long time (hundreds of millions of years under several different stress regimes) that a sufficient range of fracture orientations exist in all parts of the shield to ensure that, regardless of the orientation of any future potential principal horizontal stress, future deformation will take place by the reactivation of existing, suitably-oriented and located, fractures and fracture zones. For large post-glacial earthquakes in northern Fennoscandia, it is commonly agreed that brittle deformation (faulting) largely followed pre-existing crustal structures such as ductile shear zones, albeit with some jumps from segment to segment /Stanfors and Ericsson 1993/.

In summary, potential earthquake faults can be concluded to be either too small to produce displacement larger than the damage threshold or too large to elude detection during construction.

1.2.3 Slip on fractures directly connected with earthquake faults

There is no generally valid way of estimating the amount of slip that can occur on connected fractures (cf. Case 2, Figure 1-5) as a result of the main slip on the fault. The conditions that would determine that slip, e.g. the style of the mechanical connection and the structure of the fault, are much too uncertain, spatially- and temporally-varying and complicated to allow for quantitative assessment. However, provided that the intersected position is outside the damage zone (Figure 1-5) the slip on the connected fracture cannot be more than a fraction of the maximum slip on the earthquake fault. To produce a slip of 0.05 m or larger, the maximum slip on the earthquake fault would need to be significantly larger than 0.05 m, say 0.1 m, meaning that the moment magnitude would have to be 5.5 or larger (cf. Figure 1-6a). This requires a rupture area of 20 km^2 or, to be conservative, at least 10 km^2 (Figure 1-6b) For shallow earthquakes a 10–20 km^2 rupture area is estimated to require a surface trace lengths of 3 km or more (Note that the surface trace length is an upper bound estimate of the potential surface rupture length). This means that canisters positioned outside the damage zone of potential earthquake faults with trace lengths less than 3 km will not be damaged. For deformation zones with trace lengths of 3 km (or more), the possibility of a M_w 5.5 earthquake (or larger) cannot be completely excluded. For such large zones it will be necessary to ensure that no deposition holes are intersected by fractures large enough to be connected with possible fault slip planes. In practice this means that positions within a band outside the core of such zones cannot be used. The width of the band must not necessarily be large; deposition holes intersected by very large fractures will not be accepted anyhow.

1.2.4 Secondary displacements

The possibility that fractures or faults at some distance from an earthquake fault may reactivate in direct response to the seismic waves and the stress redistribution following slip on the fault is the major concern (Case 3 in Figure 1-5). Unlike aftershocks, which are products of relaxing stress concentrations produced by the main rupture of the earthquake, such secondary movements would occur without any time delay as soon as the seismic waves arrive, and cannot be trusted to follow size-displacement relations such as those pictured in Figure 1-6. This means that secondary shear displacements on fractures small enough to elude detection during construction, at least theoretically, could exceed the damage threshold if the earthquake is sufficiently large. Contrary to the shear displacements hypothesized in Case 2 (cf. Figure 1-5), which can be handled by avoiding deposition in a narrow band close to the deformation zone, there is no obvious way of handling remotely activated displacements. The case of secondary displacement associated with post-glacial dip-slip seismic events on reverse faults is the one that demands particular consideration in the safety assessment of a KBS-3 repository.

1.3 Mitigating the seismic risk

1.3.1 SR-Can, layout D1

In the most recent safety analysis (SR-Can), the risks associated with shear displacements across deposition holes were controlled by use of respect distances in the repository layout and acceptance criteria for deposition holes. Figure 1-7 illustrates the concept of respect distance as applied in layout D1 for Forsmark and Laxemar /Munier and Hökmark 2004, SKB 2006a/. Following the discussion in Section 1.2.3, events on faults with surface trace lengths shorter than 3 km would not be large enough to generate slip exceeding the threshold directly on connected fractures (Figure 1-5, #2), or remotely on fractures a distance away from the zone (Figure 1-5, #3). Therefore only deformation zones with surface trace lengths of 3 km or more need to have respect distances. For such zones canisters should not be deposited within a 100 m respect zone outside any possible slip plane within these zones. At distances between 100 and 200 m from the nearest possible slip plane canister positions intersected by fractures with radii larger than 75 m are rejected. At 200 m distance and larger, positions intersected by fractures with radii larger than 150 m are rejected. No canisters should be deposited within the damage zone surrounding the core of the zone, irrespective of the width of that zone. These rules were based on results of numerical analyses conducted by /Fälth and Hökmark 2006/. As far as the modelling approach is concerned, the numerical background material supporting the SR-Can layout rules was similar to the one presented in following chapters of this report. However, the range of events was limited to M6 earthquakes.
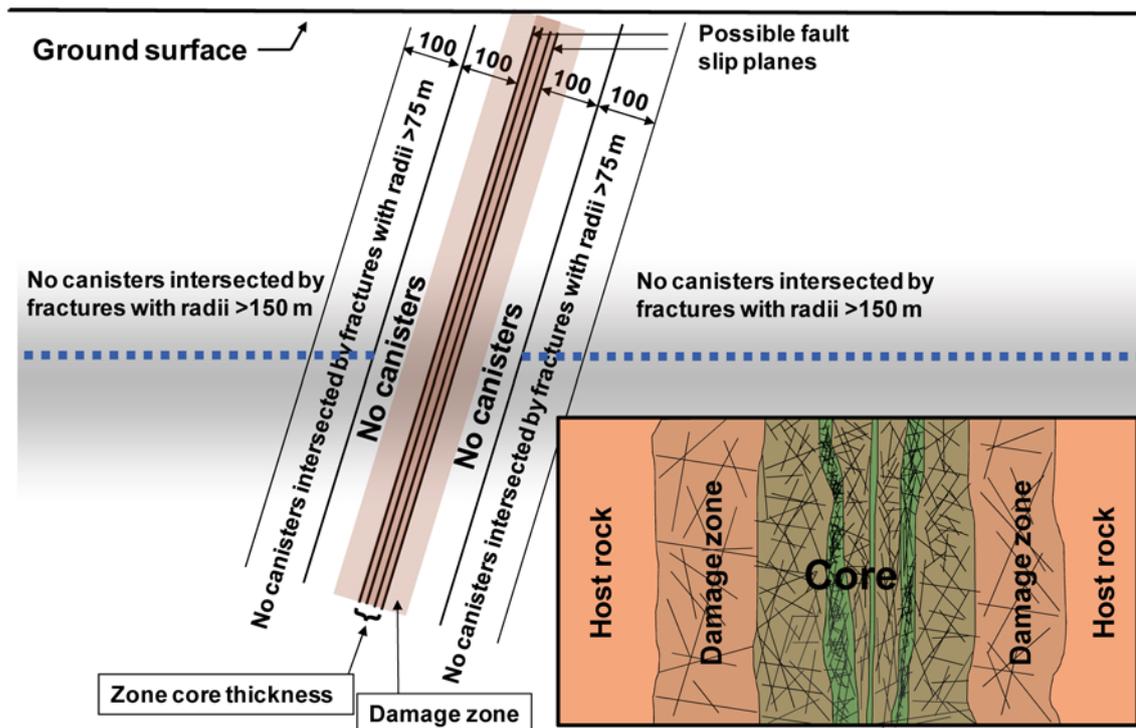
Figure 1-7. Schematic of respect distances applied in layout D1. All planes within the core of the deformation zone are regarded as potential slip planes. Inset shows deformation zone components, cf. /Munier and Hökmark 2004/. The total thickness of deformation zones (core + damage zone) at the Forsmark site is estimated to be in the range 10–100 m /Stephens et al. 2007/.

1.3.2 SR-Site, layout D2

The SR-Site safety analysis will be based on layout version D2 /SKB 2009b/. As far as respect distances are concerned the layout rules applied in layout version D2 are similar to those of layout D1, i.e. all fracture zones with surface trace lengths larger than 3 km have respect distances. There are the following differences:

• In SR-Site fault planes located within the damage zone count as potential slip planes. As such, deposition is not permitted within 100 m from the outer boundary of the damage zone (cf. Figure 1-8). This is more conservative than the rules applied during SR-Can.

• For the SR-Site assessment the canister damage threshold will be 0.05 m rather than 0.1 m.

• The critical fracture radii (the size of the fractures that determine whether intersected canister positions should be accepted or rejected) will vary with distance from the closest potential slip plane.

Recommendations of critical radii as function of distance from potential earthquake faults are given at the end of this report.

1.3.3 Future layout revisions

The layout rules applied for layouts D1 and D2 may turn out to be unnecessarily conservative. It is not obvious that all fracture zones, regardless of their orientations, should be considered to be potentially seismogenic in the post-glacial stress regime. In future layout versions it may be possible to exclude some of the zones, depending on the outcome of further evaluations of the stability analyses such as the one reported by /Lund et al. 2009/ combined with further evaluations of the results presented in this report. This possibility is discussed in Section 8.5.1.
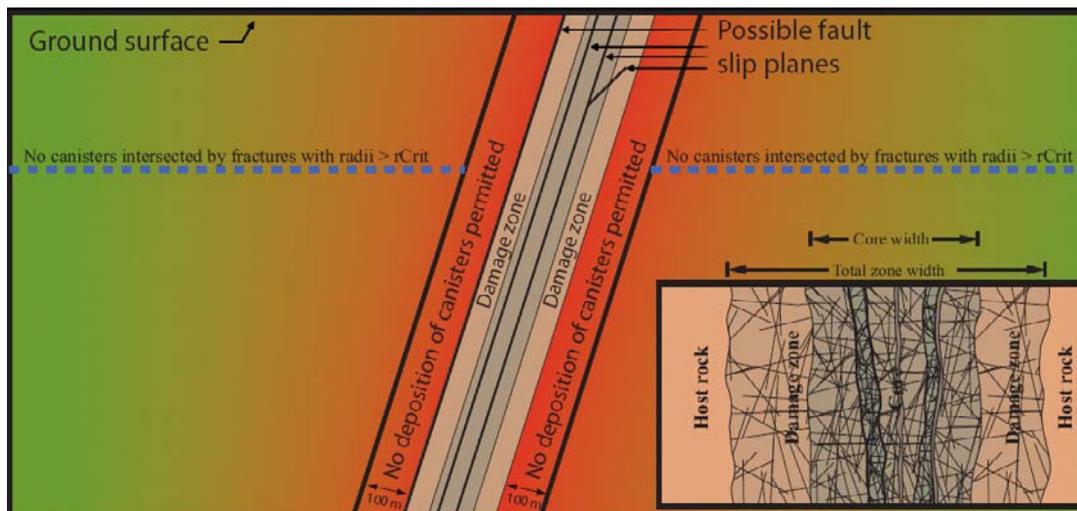
Figure 1-8. *Respect distance rules, layout D2. The critical fracture radii, r_{Crit}, (the size of the fractures that determine whether intersected canister positions should be accepted or rejected) will vary with distance from the closest potential slip plane.*

1.4 Seismic risk assessment

1.4.1 SR-Can

The results of numerical modelling performed in the past /Fälth and Hökmark 2006/ were used not only to establish design rules, but also to estimate the number of canisters that would be damaged given that the design rules cannot be fully complied with. In the SR-Can safety analysis it was assumed that a small fraction of the canister positions were intersected by undetected fractures with radii larger than 75 m (in the 100 m–200 m range, cf. Figure 1-7) and 150 m (outside the 200 m range, Figure 1-7). In the risk assessment all these fracture were taken to slip by 0.1 m or more in response to a post-glacial earthquake, irrespective of the distance to the earthquake or the orientation of the fracture. As inferred from Table 1-1, this is a very conservative handling of the numerical background material in /Fälth and Hökmark 2006/.

1.4.2 SR-Site

For SR-Site, the canister damage threshold is 0.05 m of slip across deposition holes rather than 0.1 m as for SR-Can /SKB 2009a/. All recommendations listed at the end of this report will be based on the 0.05 m threshold.

The SR-Site risk assessment will be based on a less schematic and less conservative way of accounting for modelling results than the SR-Can approach shown in Table 1-1. The numerical background material, which is presented in this report, is expanded compared to the SR-Can material to include simulations of both larger and smaller earthquakes.

The SR-Site assessment will be based on results from simulations of events that appear to be conservatively selected and represented, rather than over-conservatively as in SR-Can. The selection of relevant simulation cases is based on comparison between simulated and real earthquakes. Results from simulations that turn out to give unrealistic values of parameters (such as fault slip velocity) when compared with corresponding values for real earthquakes are not used in the final evaluation (for determining critical radii, cf. Figure 1-8).

In the SR-Site assessment, some deformation zones with trace lengths > 3 km may not have to be considered seismogenic faults. Deformation zones with orientations that are unfavourable to re-activation in a post-glacial stress field may potentially be excluded. Figure 1-9 shows deformation zones at the Forsmark site with different trace lengths at the –470 m level. Figure 1-10 shows the deformation zones in a lower hemisphere pole plot. The map and the pole plot will be revisited in connection with stability analyses and layout discussions in Chapter 7 and 8.

TR-08-11

Table 1-1. SR-Can handling of risk.

Numerical model-ling results, M_w 6.2 earthquake /Fälth and Hökmark 2006/	200 m distance from earthquake fault with 8 km surface trace length	600 m distance from earthquake fault with 8 km surface trace length	1,000 m–1,500 m distance from earthquake fault with 8 km surface trace length
	Fractures with 150 m radius: No fractures (out of 22) slipped more than 58 mm. Median slip: about 28 mm	Fractures with 150 m radius: No fractures (out of 26) slipped more than 25 mm. Median slip: about 7 mm	Fracture with 150 m radius: No fractures (out of 48) slipped more than 10 mm. Median slip: < 2 mm
SR-Can risk assessment assumption	100–200 m distance from any fault with surface trace length > 3 km		200 m distance and larger from any fault with surface trace length > 3 km.
	All fractures with radius 75 m and larger slip by 100 mm or more		All fractures with radius 150 m and larger slip by 100 mm or more
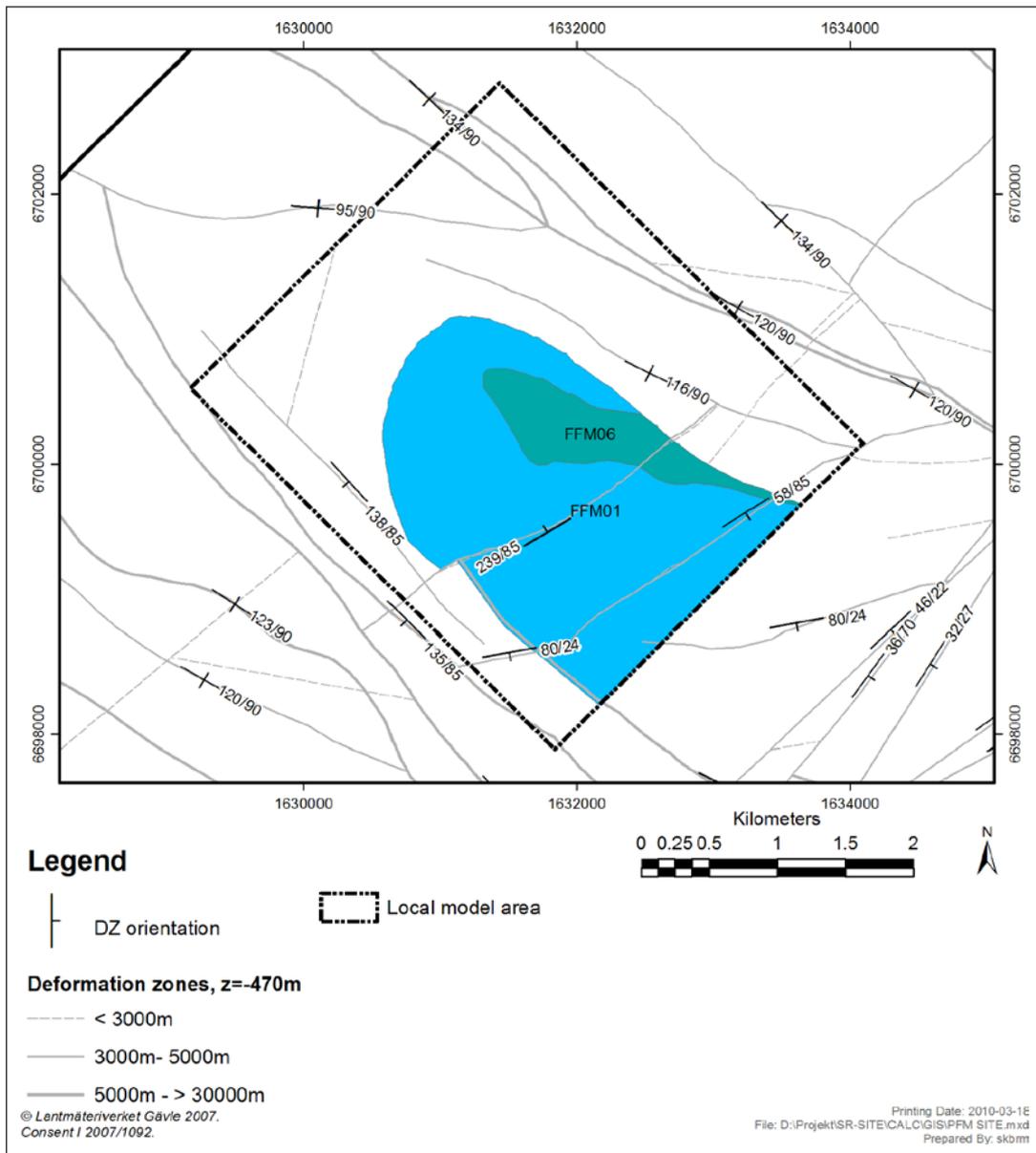
Figure 1-9. *Map showing deformation zones at repository depth within the Forsmark local model area.[1] The numbers indicate strike/dip. /Stephens et al. 2008/.*

---

[1] Modelldatabasen, 2007b. Model: DZ_PFM_REG_v22.rvs. Version 0.3. Approved 2007-08-31. Modified 2007-11-29. Modeller: A. Simeonov. Simon ID: GEO_IZTKKYIL. https://service.projectplace.com/pp/pp.cgi/r180716254.
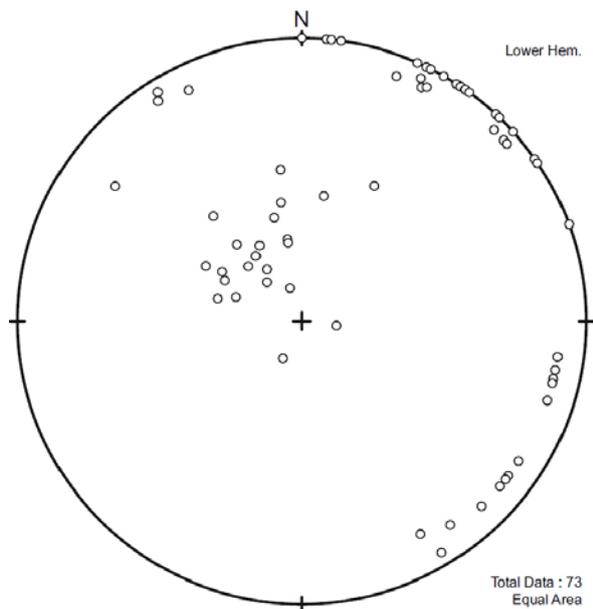
Figure 1-10. *Pole plot showing the orientations of all Forsmark deformation zones[2] /Stephens et al. 2008/.*

1.5 Objectives and scope

1.5.1 Objectives

The modelling methodology and simulations described in this report are designed to fulfil the following objectives.

- Explore the consequences (in terms of secondary shear displacements on existing fractures) of earthquakes occurring on pre-existing faults in a way similar to that used for the SR-Can assessment /Fälth and Hökmark 2006/. Because of the many uncertainties associated with the geological conditions (*in situ* stress at large depths, glacially-induced stresses, pore overpressures, etc.) required to generate slip along post-glacial faults, the simulations should not attempt to reproduce what is thought as a 'typical' post-glacial earthquake at Forsmark or Laxemar. Rather, the simulations should be generic and cover magnitude and stress drop ranges that are potentially relevant for the safety assessment.

- Generate a larger set of results from dynamic earthquake simulations than were used for the SR-Can assessment. The expanded numerical background material should include larger as well as smaller earthquakes compared to the SR-Can simulations.

- Demonstrate and increase the confidence in the simulation technique used to generate the background material further.

- Evaluate the results of the simulations with respect to relevance and conservativeness to determine the type of results that should be used for the risk assessment in SR-Site (e.g. compare output parameters with records from real earthquakes).

- Provide recommendations for the handling of the earthquake risk scenario (risk assessment in SR Site, layout revisions in detailed layout version following layout D2).

[2] Modelldatabasen, 2007b. Model: DZ_PFM_REG_v22.rvs. Version 0.3. Approved 2007-08-31. Modified 2007-11-29. Modeller: A. Simeonov. Simon ID: GEO_IZTKKYIL. https://service.projectplace.com/pp/pp.cgi/r180716254.

1.5.2   Scope – this report

Chapter 2 gives a brief summary of different static and dynamic modelling approaches used to address the earthquake problem in previous studies.

Chapter 3 contains a description of the reference seismic events used to assess the relevance and conservativeness of the numerical models.

Chapter 4 describes the dynamic modelling approach: the numerical tools, the cases selected for analysis, the geometry of fractures and fault planes in the different models, the way host rock fractures and earthquake faults are represented, the boundary conditions and the initial conditions, and the way the rupture is initiated and controlled in the models.

Chapter 5 presents the results of the modelling efforts described in Chapter 4. The result presentation has both the purpose of illustrating the modelling technique and to present the main results, i.e. the amount of fracture shear displacement that may be induced at different distances from the source fault in differently-oriented fractures. The sensitivity of the calculated target fracture slip to variations of different parameters, such as fault slip velocity, fault and fracture orientation, pore pressure, and fracture strength, are studied, along with the variability of earthquake magnitude. In order to illustrate the modelling technique, the fault slip development and its sensitivity to variations of input parameter is presented.

Chapter 6 presents direct comparisons of model output parameters with relevant data from the scientific literature, as well as with results from earlier modelling work. This chapter also discusses the relevance and validity of certain aspects of the models.

Chapter 7 provides recommendations on how the modelling results should be interpreted and used in the safety assessment work and in future layout revisions. The chapter comprises two main parts.

*   Schematic layout rules: Results from simulations judged to be reasonably realistic are compiled to establish critical fracture radii as functions of the perpendicular distance between fault and fracture centre. The critical radius represents the size of a fracture that could slip by 0.05 m but not more for a given seismic load. Schematic layout rules based on the calculated critical fracture radii are suggested.

*   Deformation zone stability: This part concerns the stability of differently-oriented deformation zones under post-glacial stress conditions. Glacially-induced stresses obtained from ice-crust/mantle analyses performed at the Geophysical Institute of Uppsala University /Lund et al. 2009/ are added to three different *in situ* stress fields. The resulting stress fields are used to assess the stability of deformation zones at the Forsmark site during a glacial cycle. Recommendations are given about which zones that should be considered as potentially unstable under post-glacial stress conditions.

In Chapter 8, the findings presented in the report are concluded and discussed.

There are four appendices:

Appendix A: Static large-scale model used to calibrate stress-field.
Appendix B: Definition of target fractures.
Appendix C: Recurrence.
Appendix D: Deformation zone stability at the Laxemar site.

2 Previous work

The issue of the effects of post-glacial seismic activity on a geological spent-fuel repository has been addressed in previous studies. This section presents a brief summary of the different approaches that have been used in past studies.

2.1 Static approach

The earthquake scenario described in the risk analysis of the SR-97 safety report /SKB 1999/ was based on estimates made by /La Pointe et al. 1997/ of fracture shear movements induced by earthquakes. The code used in that work is a 3-dimensional displacement discontinuity code called Poly3D /Thomas 1993/. The modelling was based on the assumption that the static stress redistribution resulting from an earthquake provides the dominating contribution to the fracture movements, i.e. oscillatory components can be ignored. A M_w 6 earthquake occurring at a distance of 2 km from the edge of the repository was simulated through static analysis (Figure 2-1a). A number of frictionless circular fractures with different sizes and orientations were distributed throughout the modelling medium according to a statistical Discrete Fracture Network (DFN) model.

The results from the study were presented in terms of the maximum shear displacement of the fractures versus their size (Figure 2-1b). However, the interpretation of the results was not straightforward since the fractures had varying sizes and orientations. /Munier and Hökmark 2004/ estimated the maximum displacement on 100 m radius fractures by using the worst-case size-displacement ratio from the modelling results. The calculation by /Munier and Hökmark 2004/ suggested that the maximum induced shear displacement of a 100 m radius friction-free fracture at 2 km distance from the fault would be 12–13 mm.

In the study by /La Pointe et al. 1997/, the amount of induced fracture displacement was estimated for numerous fractures with varying orientations and sizes. However, the study had a number of conceptual limitations:

- there is no dynamic logic in Poly3D,
- fractures were friction-free,
- the medium was stress free initially.

It has been considered necessary to account also for dynamic effects in order to make the simulations more realistic. Additionally, the effects of *in situ* stresses and the mechanical properties of the fractures are potentially important to the scope and extent of seismically-induced fracture reactivation. In the following modelling efforts, the problem of induced fracture displacements was addressed by use of dynamic models.
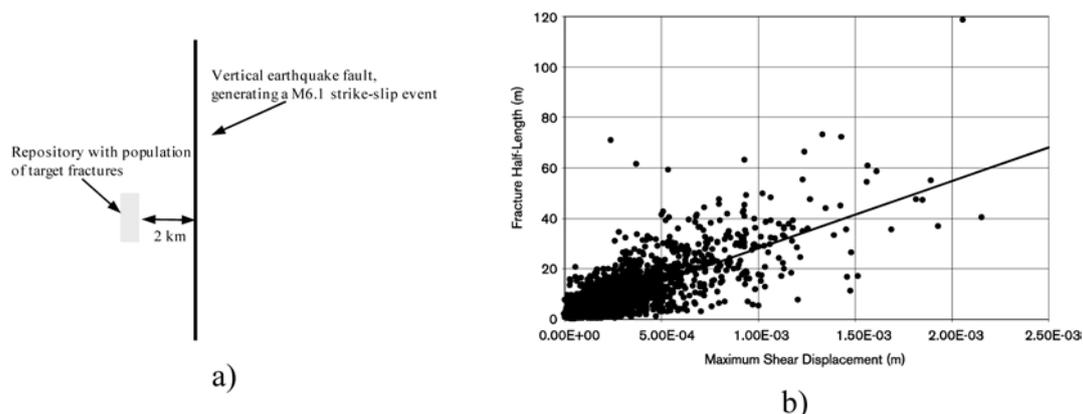
Figure 2-1. *a) Schematic plan view of repository volume and earthquake fault. b) Relation between induced displacement and fracture size for frictionless fractures. From /Munier and Hökmark 2004, Figures 3-3 and 3-4/ based on /La Pointe et al. 1997/.*

2.2 Dynamic approaches

2.2.1 WAVE/FLAC3D

/Munier and Hökmark 2004/ reported results from modelling work that was conducted using the codes *WAVE* and *FLAC3D*. Several different modelling approaches were applied during this work, and are described in the following three subsections. The sections denoted *FLAC3D*(I) and *FLAC3D*(II) describe two different modelling approaches where the code *FLAC3D* was used.

FLAC3D(I)

FLAC3D was used to analyse models that only included one rock fracture. Dynamic boundary conditions were applied as stress histories at the bottom of the models. The dynamic boundary conditions were derived from results obtained from a *WAVE* model. The dynamic load represented a M_w 6 earthquake at 2 km, 6 km and 10 km, respectively, from the fracture. The load was applied such that all base points moved together, i.e. the load simulated a plane wave.

Numerous cases with different assumptions for fracture shear strength and *in situ* stress state were studied. The largest induced fracture displacement in a 200 m x 200 m fracture with a friction angle of 30° located at a 2 km distance was approximately 1.5 mm. The modelling technique applied in these models has some limitations, though. Using only pure dynamic loads means that the modelling approach only considers dynamic earthquake effects, i.e. no stress redistribution effects, on the fractures are accounted for. Another limitation is that the plane wave assumption made in this approach is valid only for cases where the distance between the source of seismic energy and the target fracture is large.

WAVE

In addition to providing boundary conditions to *FLAC3D* models, the *WAVE* code was used to analyse models that included both the seismogenic fault and the fracture subjected to the effects of the slipping earthquake fault. The fault plane was positioned with its upper tip 1 km below the ground surface. The earthquake was simulated by forcing the fault to move in a way as to obtain a predefined rupture propagation velocity and a predefined slip distribution. The resulting seismic moment corresponded to a M_w 6 earthquake. The approach means that both dynamic and static effects were taken into account. Effects on friction-free as well as non-zero friction fractures were studied. Due to code limitations the fractures and the fault had to be aligned to the same Cartesian coordinate system. Thus, the orientation of the fractures could not be chosen arbitrarily and the fault had to be either horizontal or vertical.

FLAC3D(II)

FLAC3D was also used to analyse models where both the seismogenic fault and the studied fractures were included. In contrast to the *WAVE* approach described above, this second round of *FLAC3D* modelling did not simulate an earthquake by the prescription of fault displacements. Instead, an initial stress state was prescribed so as to cause potential instability along the seismogenic fault. The fault slip was then generated by a controlled reduction of the fault strength. This approach was considered to be more realistic since the fault moved in response to instability and resulted in model stress drops (similar to natural earthquakes) rather than an increase in model stresses. The amount of the resulting fault slip corresponded to a M_w 6 earthquake. The approach made it possible to study fracture shear displacements induced by both dynamic and static effects. Fractures (200 m x 200 m) at both 1 km and 2 km distance from the fault were studied. The maximum induced displacement in a fracture with a 15° friction angle at a distance of 1 km was 0.3 mm.

The analyses in this third simulation were preliminary, with only a limited number of results. In order to obtain results for fractures with more realistic strength properties, with varying orientations and at smaller distances from the source fault, more elaborate models were developed. These are presented in Section 2.2.2.

2.2.2 3DEC

3DEC analyses simulating M_w 6 earthquakes were conducted by /Fälth and Hökmark 2006/. The approach was similar to that of the *FLAC3D(II)* analyses described in Section 2.2.1. The models included both the earthquake fault and fractures. Initial stresses were applied to cause potential instability along the seismogenic fault, with slip generated through a controlled reduction of the fault strength. As in the *FLAC3D(II)* study, the *3DEC* modelling technique made it possible to study fracture shear displacements induced by both dynamic and static effects. Two models corresponding to the fault geometries shown in Figure 2-2 were analysed. In the model denoted Case A, the upper tip of the fault was located 1 km below the ground surface. In the model denoted Case B, the fault breached the ground surface. In contrast to the *FLAC3D(II)* modelling approach, numerous fractures with different orientations were included at 500 m depth in both models. The fractures were located at four different distances (200 m, 600 m, 1,000 m and 1,500 m) from the fault. The fractures had shear strengths that correspond to lab scale data obtained from SKB´s candidate sites /SKB 2005a, b, SKB 2006c/.

The largest induced fracture shear displacements were found in the Case B model. At 200 m distance from the fault the displacement was about 60 mm and at 600 m distance it was 25 mm. The larger amount of induced shear displacement in the Case B model can be explained by the higher fault slip velocities, which were the result of the ground breaching fault geometry.

2.3   Summary of previous work

Table 2-1 is a summary of the modelling work presented in this chapter. As can be seen, a considerable effort has been made in order to address the problem of earthquake-induced secondary fracture shear displacements. The work spans more than ten years, with several different conceptual modelling approaches applied to four different software packages. The *3DEC* study by /Fälth and Hökmark 2006/ is the most recent and most elaborated work and is the point of departure for the present study. This new study expands on the study by /Fälth and Hökmark 2006/ through the inclusion of results valid for earthquakes both larger and smaller than M_w 6. As indicated in Table 2-1, the results from /Fälth and Hökmark 2006/ are unnecessarily conservative if applied to smaller events (e.g. M_w 5 or less). In addition, further assessment of the relevance and conservativeness of the modelling technique was required.

In the present study there are no faults with geometries as in Case A in Figure 2-2. Buried ruptures turned out to give less induced shear displacements than corresponding ground breaching ruptures (because of the much lower fault slip velocities and the larger fault-fracture distances). Additionally, all documented post-glacial events are characterised by visible fault scarps. This is in agreement with stability observations made later in this report: Glacially-induced disturbances are more important at shallows depths than at deeper levels.
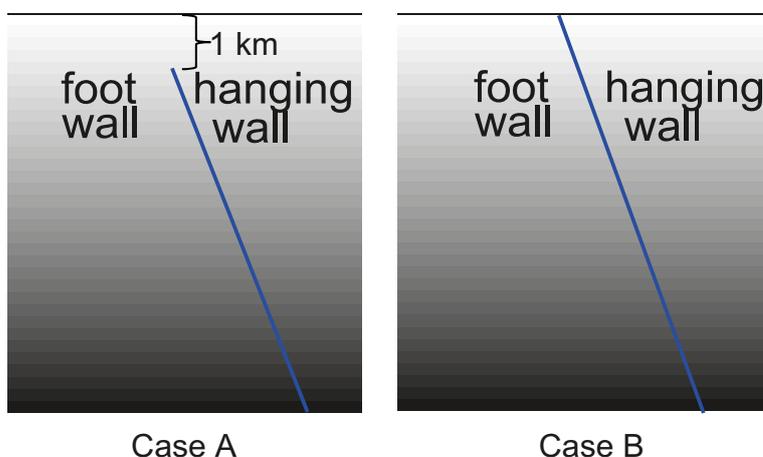
Figure 2-2. *Conceptual geometries of the cases analysed in previous study by /Fälth and Hökmark 2006/. Case A: Fault with its upper edge 1 km below ground surface. Case B: Fault that breaches the ground surface.*

Table 2-1. Summary of previous modelling work.

Code/Study	Event	Target fractures	Main limitations of code/study	Reference
Poly3D	All types of events.	All sizes and all orientations.	Dynamic effects not considered. Statistical approach makes direct derivation of respect distances difficult. No account for initial stress field.	/La Pointe et al. 1997, Munier and Hökmark 2004/.
FLAC3D(I)	M_w 6 dip-slip on vertical fault.	100 m radius frictionless friction 15° friction 30°.	Static effects not considered. Oscillations approximated by plane wave. No relevant account of initial stress field.	/Munier and Hökmark 2004/.
WAVE	M_w 6 dip-slip on vertical fault.	100 m radius frictionless friction 15° friction 30°.	Faults must be either vertical or horizontal. Target fractures must be either vertical or horizontal. No relevant account of initial stress field.	/Munier and Hökmark 2004/.
FLAC3D(II)	M_w 6 dip-slip on 70° dipping fault.	100 m radius frictionless friction 15°.	Preliminary study with few results.	/Munier and Hökmark 2004/.
3DEC	M_w 6 dip-slip on 70° dipping fault.	150 m radius friction 34°.	Only one earthquake magnitude tested.	/Fälth and Hökmark 2006/.
	Two different fault geometries tested.	Several orientations and locations.	Results over conservative for the application to smaller events.	

3 Reference seismic events

In this study, the amount of induced fracture shear displacement that can potentially occur along a fracture due to a nearby earthquake is estimated through the use of numerical dynamic models. The models are generic in nature, i.e. the model geometries and *in situ* stresses have no couplings to any specific site or earthquake. The rupture mechanism is simulated in a schematic way, using a typical value of the rupture propagation velocity and assuming uniform fault strength properties across the fault plane (cf. Chapter 4). A number of model parameters are varied, including fault rupture area (seismic moment, corresponding to earthquake magnitude), fault slip velocity, and *in situ* stress state.

An important objective of this study is to evaluate the results of the simulations with respect to relevance and conservativeness to find the type of results that should be used for the risk assessment in SR-Site. This is done through the comparison of results from the models with data from real seismic events found in the literature (cf. Chapter 6).

This chapter provides brief descriptions of faulting observed in nature that are used as references in the evaluation of the relevance and conservativeness of the numerical models. Section 3.1 describes the large post-glacial faults that are found in northern Fennoscandia. Since the presence of these faults is the reason that studies of post-glacial seismic risk are necessary, they serve as particularly relevant references. The ratio between the amount of fault slip and the fault size in the numerical models is compared with estimates of the corresponding parameters for these faults.

The observations made of the post-glacial fault scarps indicate that the post-glacial earthquakes were very powerful. However, there are no ground acceleration- or velocity records available for any post-glacial seismic events. In order to evaluate the relevance and conservativeness of the models with respect to such parameters, the model data have to be compared with recordings from a more recent event where such data are available. Thus, velocity data from the numerical models are compared with velocity data recorded during the 1999 Chi-Chi (Taiwan) earthquake. This particular earthquake is used as a reference seismic event not only because it was very powerful and exhibited high velocities, but also because it was well-documented, thanks to a dense seismic network close to the source fault. The Chi-Chi earthquake is described in Section 3.2.

3.1 The Lapland post-glacial faults

Faults of the Lapland post-glacial fault province are found in a diamond-shaped region about 300 km E-W and 500 km N-S, in northern Sweden, northern Finland and in the county of Finnmark in Norway. The province is comprised of a series of reverse fault scarps, including the Pärvie, Lansjärv and Stuoragurra faults, which have surface offsets of up to tens of metres in some places. The longest of these scarps is the Pärvie Fault, which stretches almost unbroken for 165 km /Muir Wood 1993/ (Figure 3-1).

Trenching across fault scarps has made it possible to study the stratigraphy of glacial (till) and post-glacial sediments close to fault traces and thereby estimate the date and the type of faulting /Lagerbäck 1988/. These faults have been confirmed to be of post-glacial origin, see. e.g. /Lagerbäck 1979, Lagerbäck 1988, Olesen 1988/. It is widely accepted that these faults were formed as the result of large earthquakes in conjunction with the latest deglaciation some 10,000 years ago /Johnston 1989, Muir Wood 1989, Muir Wood 1993, Arvidsson 1996, Lagerbäck and Sundh 2008/. The moment magnitude (M_w) of the earthquake responsible for the Pärvie Fault scarp has been estimated to be about 8 /Muir Wood 1993, Arvidsson 1996/, with a surface displacement of up to 10 m in some places (Figure 3-2). There is also general consensus that the fault movements took place as reactivation of existing fracture zones, rather than the creation of new faults /Stanfors and Ericsson 1993, Munier and Fenton 2004/. Hypotheses as to why the large-scale faulting occurred only in northern Fennoscandia include higher tectonic strain accumulation due to longer ice coverage and reduced fault stability due to high pore pressures that developed beneath the permafrost (cf. Section 1.1.1).
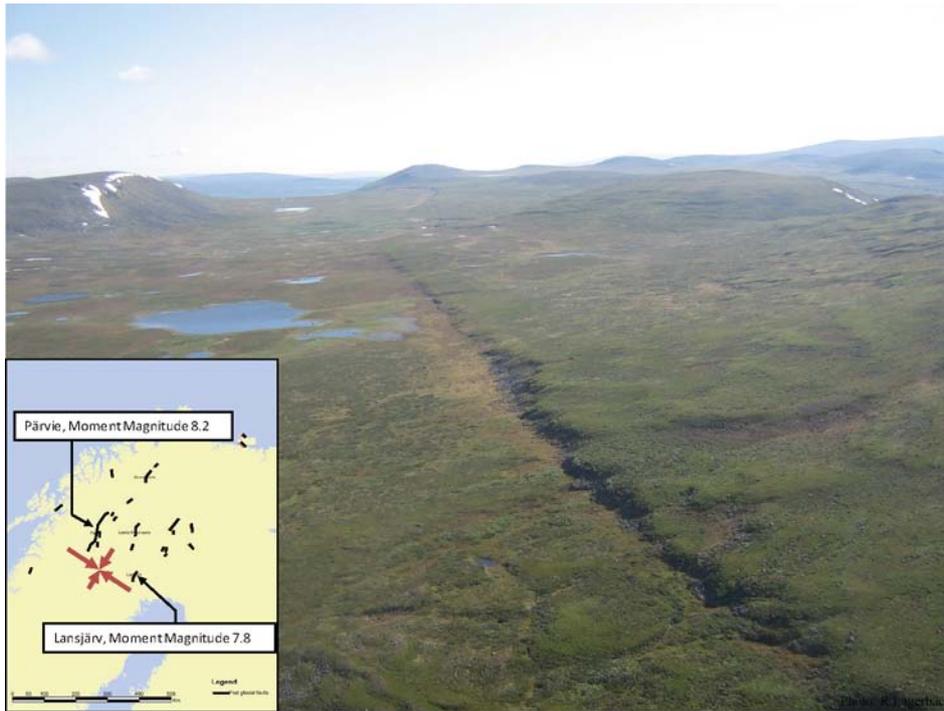
Figure 3-1. *The picture shows the Pärvie Fault. The insert shows the locations of the most prominent glacio-isostatic faults. Photo by R Lagerbäck 2008. (Robert Lagerbäck, Geological Survey of Sweden, personal communication 2008).*
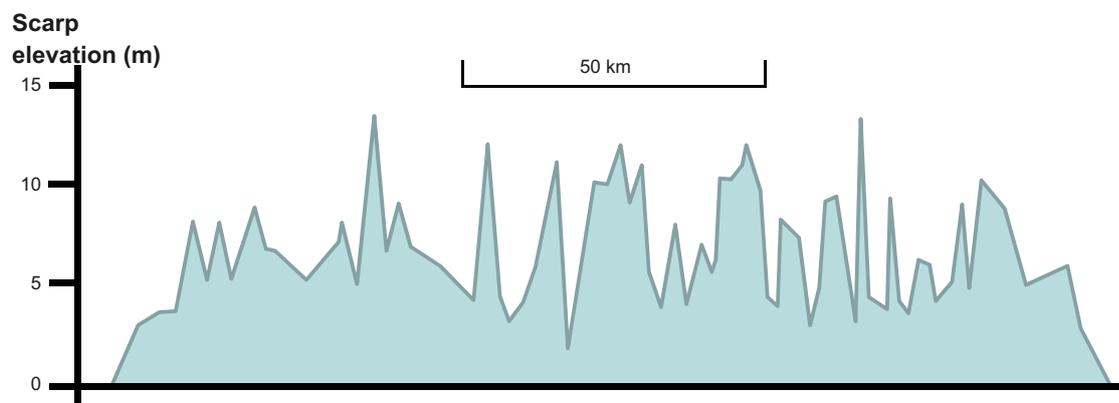
Figure 3-2. *Surface displacement along the Pärvie Fault. Redrawn from /Muir Wood 1993/.*

3.2   The 1999 Chi-Chi, Taiwan, earthquake

The 21 September 1999, Chi-Chi, Taiwan earthquake (M_w 7.6) was the largest earthquake to strike Taiwan in the 20th century. The hypocentre depth was about 7.5 km and the epicentre was close to the town of Chi-Chi, which is located approximately 12 km west of the Sun Moon Lake (Figure 3-3). The earthquake caused serious damage to energy facilities, agriculture, engineering structures and critical lifeline structures. 9,909 buildings were destroyed and 7,575 buildings partially damaged by the earth tremor. Approximately 2,400 people were killed and about 10,000 injured /Bäckblom and Munier 2002/. The ground shaking during the earthquake was extremely strong. Two stations for free-field strong motions instruments experienced horizontal peak ground accelerations (PGA) of more than 1g, while at several other locations PGA's of more than 0.8 g were registered /Bäckblom and Munier 2002/.
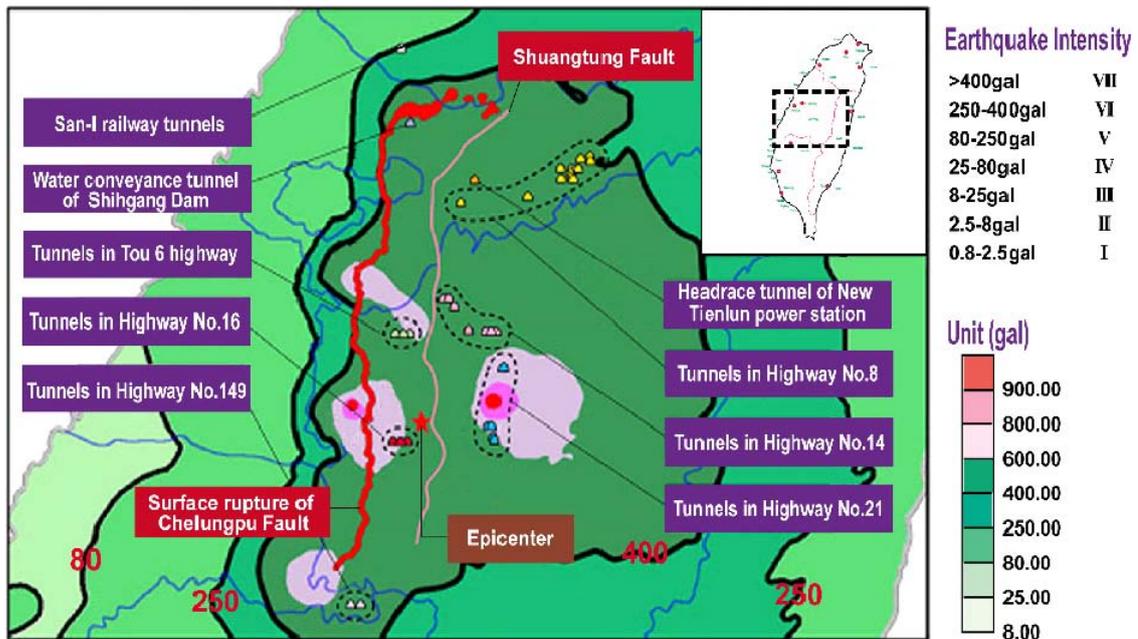
Figure 3-3. *Intensity (Chinese Intensity Scale) and peak ground acceleration in gal (1 Galileo is 1 cm/s²,*
1000 gal is 10 m/s² ~ 1.02 g) due to the Chi-Chi earthquake (T T Wang 2001, Personal communication).

The earthquake had a moment magnitude, M_w, of 7.6, ruptured about 85 km of the Chelungpu Fault, and produced a complicated pattern of surface faulting. The earthquake slip consisted mainly of thrust movement on a shallow fault plane dipping 20–30° to the east /Ma et al. 2001/. The stations near the largest observed surface offset recorded the largest ground displacements (up to 12 m) and ground velocities (up to 4.5 m/s) ever measured by seismic monitoring instruments. Using data recorded during the earthquake, fault slip velocities close to the ground surface have been estimated to be in the range of 3.0–4.5 m/s /Ma et al. 2003/. The strong motion data that was recorded during the 1999 Chi-Chi earthquake is freely accessible via internet at the home page of the Central Weather Bureau of Taiwan /CWB 2009/.

Even though the tectonic setting of Taiwan differs from that of Sweden, and the local conditions around the Chelungpu Fault may differ from those at the Forsmark site, the Chi-Chi earthquake data serve as an example of strong motions that may result from large thrust movement seismic events, such as typical end-glacial earthquakes. Additionally, the modelling results obtained for large thrust movement events in this study indicate that the fault slip velocity is important to the amount of induced, secondary slip on nearby fractures. Therefore, synthetic earthquakes producing slip velocities higher than the maximum Chi-Chi slip velocity are considered physically not relevant and are not used in the final results evaluation. Results from simulations giving slip velocities much lower than the Chi-Chi max velocity are not regarded as sufficiently conservative. Therefore, slip velocities obtained in the numerical models are systematically compared with the maximum Chi-Chi velocity to get perspectives on the realism and the degree of conservatism.

4 Modelling approach

4.1 General

There are little data available of the predominant stress conditions in northern Fennoscandia when the large post-glacial earthquakes took place some 10,000 years ago. There are no strong motion data from any of the post-glacial faults in this region, since they have not ruptured significantly during the time when recording instrumentation was available. However, studies of the fault scarps (cf. Chapter 3) have provided sufficient information to determine the type of faulting that occurred and to make estimates of the moment magnitudes of the events.

In order to make estimates of the possible impact on rock fractures from a nearby post-glacial seismic event, earthquakes are simulated through the use of generic numerical models. The approach, which is similar to that applied by /Fälth and Hökmark 2006/ (cf. Section 2.2.2), is to analyse models where both the earthquake fault and the studied fractures are included. *In situ* stresses that result in the intended seismic moment are applied. The stresses have no couplings to any specific site or earthquake. The earthquake is then generated in a schematic way. The rupture mechanism is simulated through a pro-grammed reduction of the fault shear strength, which results in fault slip with a corresponding release of strain energy. A typical value of the rupture propagation velocity is used, while fault strength properties are assumed to be uniform over the fault plane. After the rupture has finished, the fault strength has reached zero (or a low residual strength), which gives an average net stress drop equal (or close) to the average initial shear stress along the fault. This modelling approach makes it possible to study target fracture displacements due to both static stress redistributions and dynamic oscillation effects.

The models are analysed dynamically using the distinct element code *3DEC* (**3** Dimensional **D**istinct **E**lement **C**ode), version 3.0 /Itasca 2003/. M_w 6.2 models, similar to those analysed by /Fälth and Hökmark 2006/, M_w 5.5 models and M_w 7.5 models are analysed. In order to analyse the M_w 7.5 models, so-called truncated models are developed. The concept of truncated models is described in Section 4.10.

In Section 4.5 through 4.8, the features that are common to all models are described. After that, the features that are specific to the M_w 5.5 and M_w 6.2 models are described in Section 4.9. The features specific to the M_w 7.5 models are described in Section 4.10.

4.2 Problem statement

There are a number of questions that are to be addressed by the numerical modelling.

- What are the static and dynamic impacts of an earthquake upon nearby fractures in terms of induced shear displacement?
- How does the induced shear displacement correlate to the distance from the source?
- How does the induced shear displacement correlate to the moment magnitude of the earthquake?
- What is the importance of the fracture geometry and the fracture orientation?

We address these questions through the analysis of generic numerical models which utilize the following setup:

- A seismic dip slip event takes place in a pre-existing fault. The fault is a reverse fault, as was proposed for glacially-induced faults observed in northern Fennoscandia. See e.g. /Lagerbäck 1988, Muir Wood 1993, Munier and Fenton 2004/.
- The earthquake is of magnitude five or larger and the fault breaches the ground surface.
- At 500 m depth, fractures are located at different distances from the fault.

4.3 Description of the numerical tool

3DEC is a three-dimensional numerical program based on the distinct element method for discontinuum modelling. *3DEC* simulates the response of discontinuous media (such as jointed rock masses) subjected to either static or dynamic loading. The code employs an explicit time-stepping solution scheme. The discontinuous medium is represented by an assemblage of discrete blocks. The discontinuities are treated as boundary conditions between the blocks; large displacements along discontinuities and rotations of blocks are allowed. Individual blocks behave either as rigid or deformable material. Deformable blocks are subdivided into a mesh of finite-difference elements, and each element responds according to a prescribed linear or non-linear stress-strain law. The relative motion of the discontinuities is also governed by linear or non-linear force-displacement relations for movement both in the normal and shear directions. *3DEC* is based on a "Lagrangian" calculation scheme that is well-suited to model the large movements and deformations of a blocky system /Itasca 2003/. See also e.g. /Jing and Stephansson 2007/. The code documentation contains several examples that verify the performance of the dynamic logic.

3DEC also contains a built-in programming language called *FISH*, which makes it possible to extend *3DEC*'s usefulness by the definition of custom functions and variables /Itasca 2003/. *FISH* is used in the modelling work to define circular rock fractures and to initiate and propagate the rupture along the earthquake fault.

4.4 Concepts and definitions

A number of parameters and concepts used in the model descriptions and in the results discussions are listed and explained below.

4.4.1 Primary fault

The primary fault is here used as notation for the geological formation along which the rupture process is taking place during the earthquake (i.e. the 'seismogenic' fault). In the models described in this report, the primary fault is represented by one discrete planar feature. Using a discrete plane to represent a zone with finite thickness that may be non-planar and which may consist of several slipping planes is of course a simplification. However, since the studied fractures are located at some distance from the primary fault, the details of the fault representation are not regarded as critical for the purpose of this study.

4.4.2 Target fracture

A target fracture is a rock fracture located in the vicinity of the primary fault which can potentially be reactivated by the seismic event. The amount of slip on such fractures is the main concern in this study. The target fractures are represented in the numerical models as circular perfectly planar discs. Real fractures may be irregular, non-planar or have other imperfections that restrain shear movements. Hence, the planar representation used here contributes to an overestimation of the induced fracture shear displacement. The methodology used for defining target fractures is described in Section 4.6 and in Appendix B.

4.4.3 Strength reduction time, *rt*

The strength reduction time, *rt*, is an input parameter to the rupture propagation algorithm in the models analysed here. It is defined as the time over which the shear strength is ramped down to zero (or to a residual strength) at any point on the primary fault. A variation of *rt* effectively results in a variation of the fault slip velocity.

4.4.4 Moment magnitude and seismic moment

Magnitude is a dimensionless parameter used to quantify the size of an earthquake. The earliest magnitude scale was the local magnitude, M_L, introduced by Charles Richter in 1935 for earthquakes in southern California /Richter 1935/. It is often referred to as the "Richter scale" and is based on the resulting amplitude of waves that are recorded on a seismogram and on functions that are calibrated to

account for regional conditions. Other magnitude scales have also been developed. One scale which has become the common measure of large earthquakes is the moment magnitude, M_w, cf. /Kanamori 1977, Hanks and Kanamori 1979/. This scale is based on the seismic moment, M_0. The moment magnitude is used in this report, and is defined as:

$$M_w = \frac{2}{3}\log_{10} M_0 - 6.07 \qquad \text{Equation (4-1)}$$

The seismic moment M_0 is calculated as

$$M_0 = G\bar{u}A \qquad \text{Equation (4-2)}$$

where G is the shear modulus of the rock mass and $\bar{u}$ is the average slip along the rupture area A.

4.5   Geometric outlines of models

In order to facilitate the understanding of the modelling principles, this section presents a broad description of the conceptual model outlines. Different model geometries are used when simulating earthquakes of different magnitudes. Figure 4-1 illustrates the geometries of the M_w 5.5 and M_w 6.2 models whereas the geometry of the M_w 7.5 models is shown in Figure 4-2. All of the models simulate a large rock mass where the upper boundary represents the ground surface. A large plane representing a pre-existing discontinuity (the primary fault) is created. This plane breaches the upper boundary (the ground surface) of the model. The fault length and fault width are here denoted L_f and W, respectively.

The geometry shown in Figure 4-1 is used in the M_w 5.5 and M_w 6.2 models and includes a fault with a finite length, L_f, i.e. the model width, L_z, is large enough that the entire primary fault can be accommodated within the model volume ($L_f < L_z$). Since the vertical boundary at $z = 0$ is a symmetry plane the actual simulated fault length is $2L_f$. A more detailed description of these models is presented in Section 4.9.

	M_w 6.2	M_w 5.5(dip70)	M_w 5.5(dip30)
L_x	30 km	30 km	30 km
L_y	15 km	15 km	15 km
L_z	10 km	10 km	10 km
L_f	4.0 km	1.5 km	1.5 km
W	5.6 km	4.0 km	4.0 km
h	3.2 km	2.0 km	1.0 km
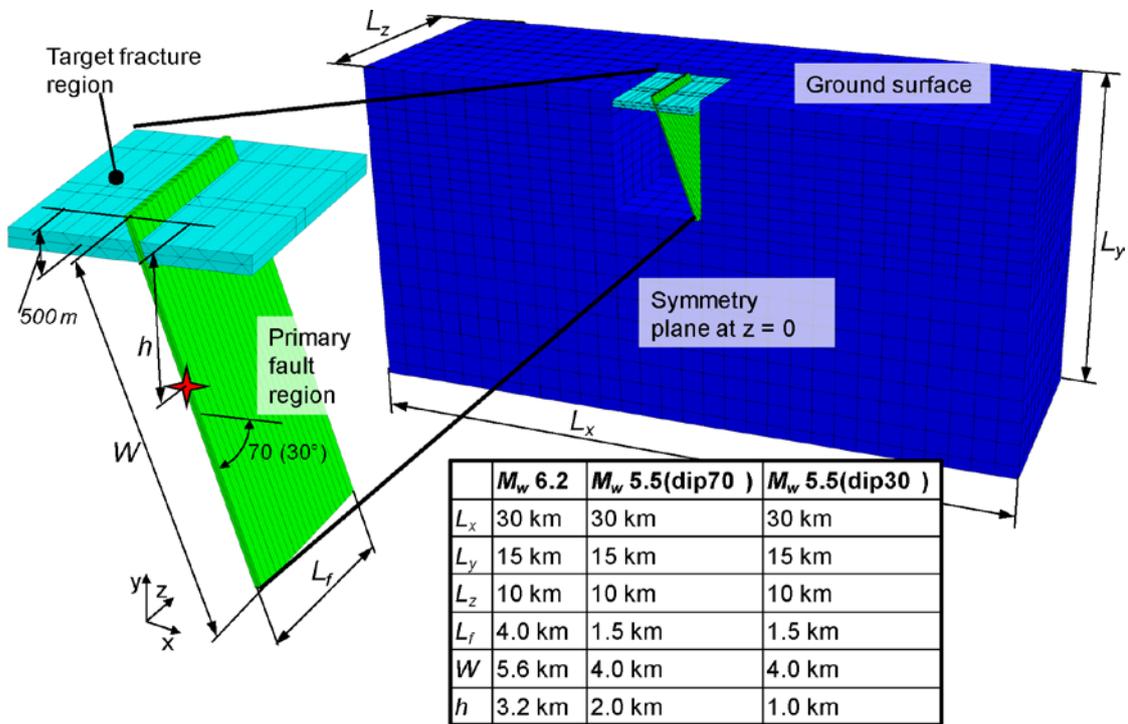
Figure 4-1. *Geometric outlines of M_w 5.5 and M_w 6.5 models. Parts of the model geometry are hidden in the figure in order to show the primary fault and the target fracture region. The system of orthogonal planes is a set of construction planes used to define the geometry and to facilitate the discretisation of the continuum.*
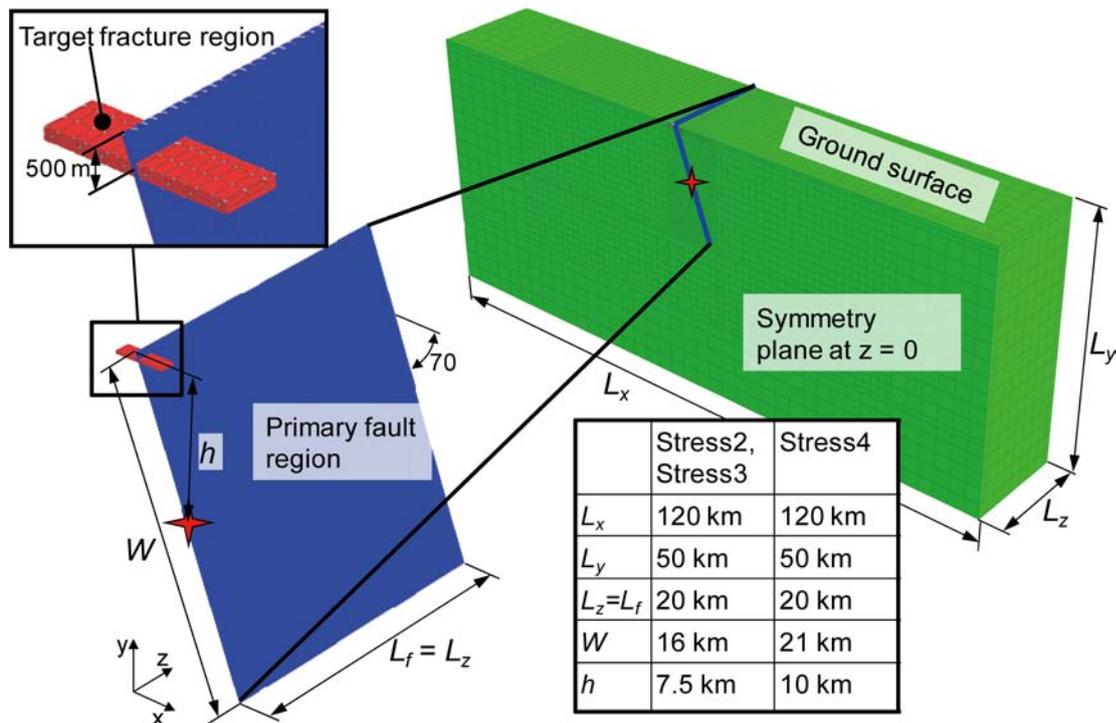
Figure 4-2. *Geometric outlines of M_w 7.5 models. Parts of the model geometry are hidden in the figure in order to show the primary fault and the target fracture region. The system of orthogonal planes is a set of construction planes used to define the geometry and to facilitate the discretisation of the continuum. Note that the fault length, L_f, is equal to the model width, L_z.*

Due to memory allocation limitations in the code, another type of model geometry is used when larger (M_w 7.5) events are simulated (Figure 4-2). In this type of model the fault plane intersects the entire model width, i.e. the fault length, L_f, is equal to the model width, L_z. A more detailed description of these models is given in Section 4.10.

A volume denoted the target fracture region is defined close to the primary fault at a depth of 500 m. The depth is in accordance with the planned depths of a real repository /SKB 2010c/. In the target fracture region, a number of cut planes are created at different distances from the fault. Circular target fractures, all with a radius of 150 m are then defined. All target fractures are located with their centres at a depth of 500 m. More detailed descriptions of the principles of target fracture definition are given in Section 4.6 and in Appendix B. The target fracture locations and orientations in the different models are described in Section 4.9 and Section 4.10.

4.6   Target fractures

Inside the target fracture region (cf. Figure 4-1 and Figure 4-2) a number of target fractures are created. In order to study the importance of the distance from the source earthquake and of the fracture orientation (cf. Section 4.2), numerous fractures at different locations and with different orientations are included in each model. *3DEC* cannot handle full discrete fracture network models (DFN); instead, the influence of fracture orientation is studied by use of a few arbitrarily-chosen orientations (Figure 4-3a). The circular fractures are created from *3DEC* cut planes (Figure 4-3b).The fractures are perfectly planar and circular with a radius of 150 m. All fractures are located with their centres at a depth of 500 m. The methodology used when the circular fractures are created from *3DEC* cut planes is described in Appendix B.
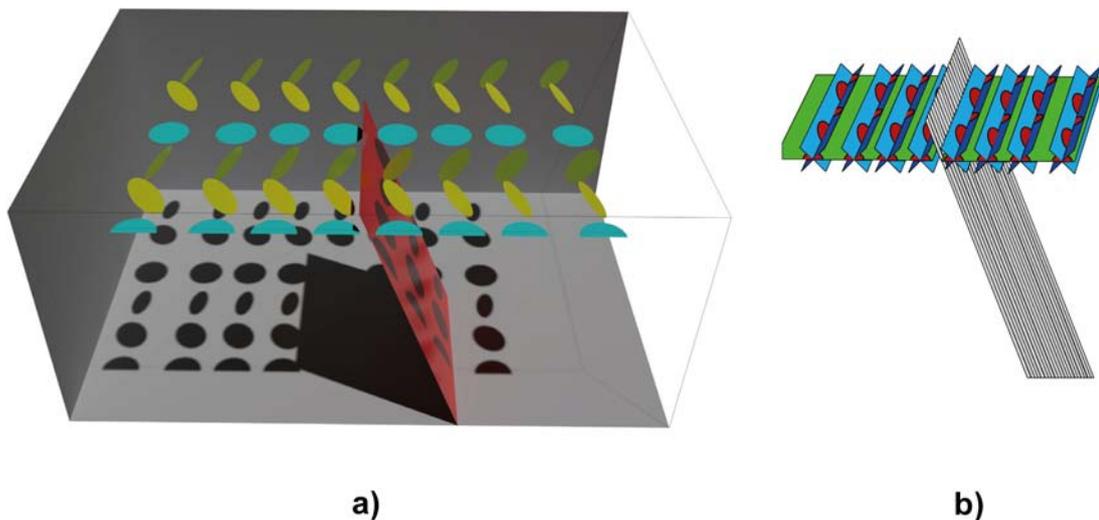
Figure 4-3. *a) Sketch of the principle showing the circular target fractures located at different locations relative to the primary fault. b) The circular fractures are created from 3DEC cut planes.*

4.7 Material properties

4.7.1 Rock mass

The rock mass between the target fractures and outside the repository region is assumed to be linearly elastic, isotropic, homogenous and continuous. As such, no fractures other than the target fractures defined along *3DEC* cut planes are explicitly modelled. Applying a linear elastic material model for the majority of the rock mass is judged to be relevant. According to the rock mechanics site description model /Glamheden et al. 2007/ there are no significant differences between intact rock behaviour and large scale rock mass behaviour at relevant confining stress levels. The fracture frequency is sufficiently low and the compression sufficiently high that the response of the rock mass can be approximated with that of an elastic continuum. The linear elastic assumption is supported also by other authors, see e.g. /Scholz 2002, Stein and Wysession 2003/.

Since the rock mass is assumed to behave purely elastically, attenuation is not accounted for explicitly in the models (except for the small effects of target fracture slip) whereas seismic waves attenuate in real rock masses because of inelastic deformations. For the short distances and the competent rock mass considered for the present purpose, attenuation effects are judged to be small. Ignoring this effect is nevertheless conservative.

The material property parameter values are presented in Table 4-1. The parameter values of the rock mass are the same as those used in the study by /Fälth and Hökmark 2006/. The values of Young's modulus and Poisson's ratio are generic, but are in good agreement with data from SKB's candidate sites /Glamheden et al. 2007, Hakami et al. 2008/.

4.7.2 Target fractures

The target fractures are assumed to respond to loads according to an idealised elasto-plastic material model with linear joint stiffness, zero tensile strength and shear failure according to a Coulomb criterion. The values of friction angle and cohesion are in agreement with data obtained from the Forsmark candidate site /Glamheden et al. 2007/. Sensitivity analyses with respect to friction angle and dilation angle were carried out, the results of which are presented in Section 5.4.9.

The values of normal stiffness and shear stiffness are generic. The normal stiffness is considerably lower than what is reported for fractures at Forsmark /Glamheden et al. 2007/. The fracture normal stiffness is normal stress-dependent /see e.g. Jacobsson and Flansbjer 2005, 2006/ and the values reported for Forsmark are determined from lab test data as secant stiffness evaluated between the unloaded state and full loading. This gives high stiffness values, which corresponds to relatively high

Table 4-1. Material property parameter values.

Component	Parameter	Value	Unit
Rock mass	Density, ρ	2,700	kg/m^3
	Young's modulus, E	75	GPa
	Poisson's ratio, v	0.25	–
Primary fault	Friction angle	0 or 6[*]	deg
	Cohesion[**]	0	MPa
	Tensile strength	0	MPa
	Normal stiffness	10	GPa/m
	Shear stiffness	10	GPa/m
Target fractures	Friction angle	34	deg
	Dilation angle	0	deg
	Cohesion	0.5	MPa
	Tensile strength	0	MPa
	Normal stiffness	10	GPa/m
	Shear stiffness	10	GPa/m

[*] Applied in some M_w 5.5 models.
[**] Final, after completed rupture.

normal stresses. In the dynamic models analysed here, however, fracture slip may be triggered by temporary reduction or loss of normal stress. Thus, a relatively low normal stiffness value, which corresponds to low normal stresses, is here considered to be relevant. The shear stiffness is in good agreement with the values for fractures at the Forsmark site /Glamheden et al. 2007/.

4.7.3 Primary fault

The values of friction angle and cohesion for the primary fault are fictitious, with no coupling to real site data. The aim is a generic simulation of earthquake effects, rather than a source-specific model. This aim is accomplished by using a schematic and idealised algorithm for the rupture propagation (Section 4.8). The parameter values in Table 4-1 are used in that algorithm. The base case assumption is a zero fault residual friction angle. It turns out that zero fault residual strength results in large, possibly irrelevant fault oscillations following the completed rupture, cf. Section 5.1. In order to limit fault oscillations without reducing stress drop and moment magnitude more than marginally, a trial low, non-zero, fault residual strength was applied in some models. The 6 degree friction angle value is arbitrarily chosen and corresponds to a friction coefficient of about 0.1. The value is in agreement with the value used in a previous study by /Andrews 2006/. Note that, although moment magnitudes are almost unaffected by this small residual fault strength, the fault slip velocity may change quite significantly, meaning that results, i.e. the target fracture response, cannot be trusted to be sufficiently conservative (cf. Section 3.2).

4.8 Calculation sequence

There are two main components of the simulation workflow: The static phase (Subsection 4.8.1) and the dynamic phase (Subsection 4.8.2).

4.8.1 Static phase

Each model analysis starts with the static phase. *In situ* stresses are applied and the model is allowed to achieve complete static equilibrium under gravity. A high cohesive strength is assigned to the primary fault in order to prevent it from slipping during this phase. The conditions at the end of this calculation phase are characterised by large shear stresses acting along the fault plane (Figure 4-4a). The shear stresses result from high horizontal stresses perpendicular to the fault strike. This represents the conditions preceding a large post-glacial seismic event along a pre-existing fault as indicated in Figure 1-1, lower right.
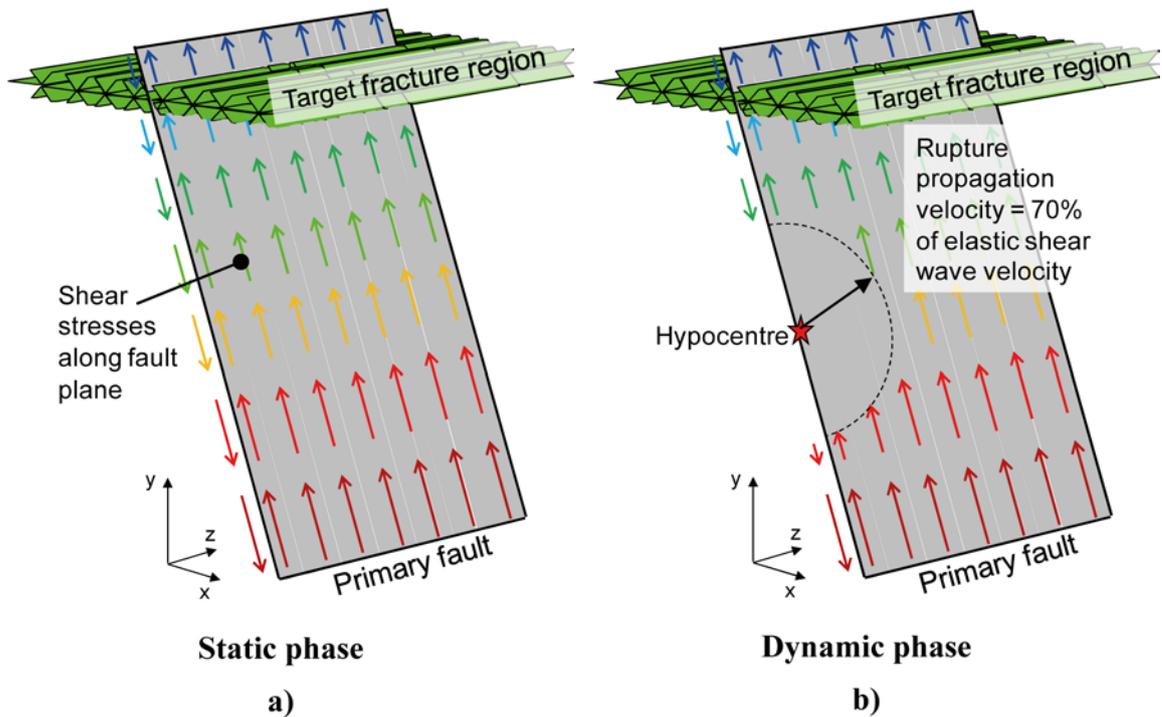
Figure 4-4. *Schematic cartoons illustrating a) the conditions at the end of the static phase, which are characterised by large shear stresses acting along the fault plane, and b) how the rupture is initiated at the hypocentre and is programmed to propagate radially along the fault plane. The rupture is allowed to reach the edges of the primary fault area.*

4.8.2 Dynamic phase

This second calculation phase simulates the seismic event. The rupture is initiated and programmed to propagate along the primary fault according to a specified scheme. The rupture is initiated at hypocentre depth and the rupture front is programmed to move outwardly in the radial direction at a speed of 70% of the rock mass shear wave velocity (Figure 4-4b). At every time step, the shear stress state of each sub-contact in the fault is checked and assigned a cohesive strength equal to the shear stress acting at that particular location. Upon rupture front arrival, the cohesive strength is ramped down to zero (or to a specified residual strength). The basic assumption is to have zero residual strength, though a friction angle of 6° is used in some models (cf. Table 4-1). The strength reduction is done over a specified period of time (here denoted "reduction time, *rt*", cf. Section 4.4.3). The meaning of reduction time, *rt*, is illustrated in Figure 4-5, which shows fault shear stress reductions at four points located at different distances from the hypocentre. In the diagram it can also be observed how the shear stress is locally increased as the rupture front approaches each location. Note that the modelling routine only controls the strength of the fault and how it is ramped down at each location; displacements are uncontrolled.

The rupture is allowed to propagate to the edges of the primary fault area. This means that the entire fault rupture patch has zero (or low) strength at the end of the analysis. Applying zero residual shear strength results in an average static stress drop equal to the initial average fault shear stress.

The routine that is used to control rupture initiation and propagation is developed in the built-in programming language *FISH* and is the same as used by /Fälth and Hökmark 2006/.
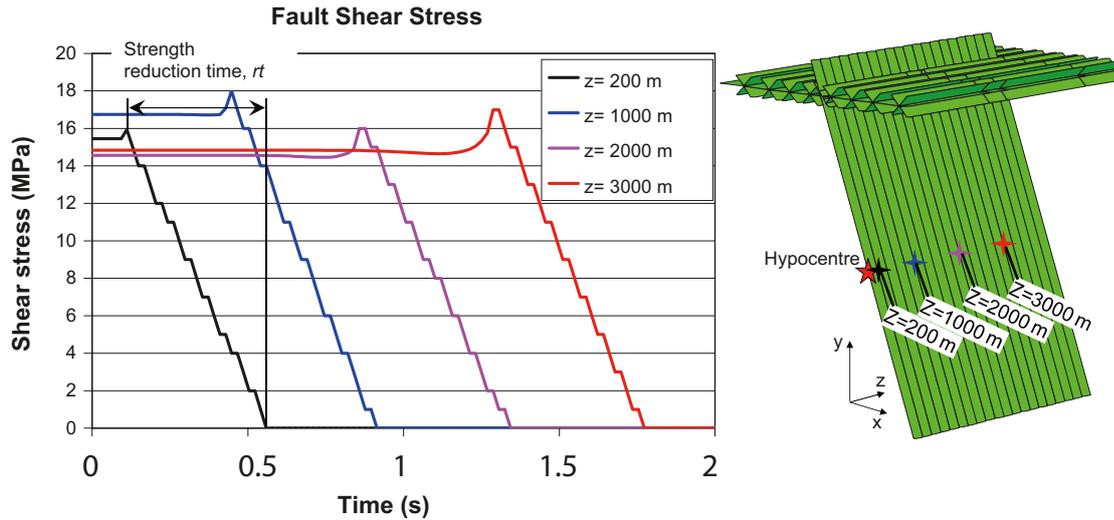
Figure 4-5. *The diagram shows reductions of the fault shear stress at four locations with different z-coordinates (horizontal distances to the hypocentre). The meaning of strength reduction time, rt, is illustrated. Note how the shear stress is locally increased as the rupture front approaches each location.*

4.9 Model dimensions, initial conditions and boundary conditions in the M_w 5.5 and M_w 6.2 models

This section describes the features that are specific for the M_w 6.2 models and the M_w 5.5 models. The following subsections describe the models dimensions, the finite-difference mesh, target fracture locations and orientations, initial stresses and boundary conditions.

4.9.1 Model outlines and dimensions

Figure 4-6 shows the outlines and dimensions of the M_w 5.5 and M_w 6.2 models. The models include both the primary fault and the target fracture region. The basic assumption is that the seismogenic fault dips at 70° with respect to the horizontal plane. In some M_w 5.5 models, a 30° dip angle is used. Since the boundary at $z = 0$ is a symmetry plane, the actual simulated fault length is $2L_f$, i.e. 3 km in the M_w 5.5 models and 8 km in the M_w 6.2 models. The hypocentre is located approximately at the centre of the fault plane, meaning that the hypocentre depth, h, differs between the models depending on the fault width and the fault dip.

4.9.2 Finite-difference element mesh

To ensure proper wave transmission through the continuum, the finite-difference zone edge lengths, Δl, must not be larger than one-eighth of the wave length associated with the highest frequency, f, in the spectrum /Itasca 2003/:

$$\Delta l \leq \frac{1}{8}\frac{C_s}{f}$$

Equation (4-3)

$$C_s = \sqrt{\frac{G}{\rho}}, \quad G = \frac{E}{2(1+\upsilon)}$$

Here, C_s is the wave propagation speed, G is the shear modulus, E is the Young's modulus and υ is Poisson's ratio of the continuum. With the mechanical properties assumed in this study (cf. Table 4-1), Equation 4-3 gives a shear wave propagation speed, C_s, of 3,333 m/s.

The outlines of the mesh in the M_w 5.5 and M_w 6.2 models are shown in Figure 4-7. The numbers in the figure indicate the maximum zone edge lengths in the different parts of the model. In the repository volume where the target fractures are located and along the primary fault, the models are specifically
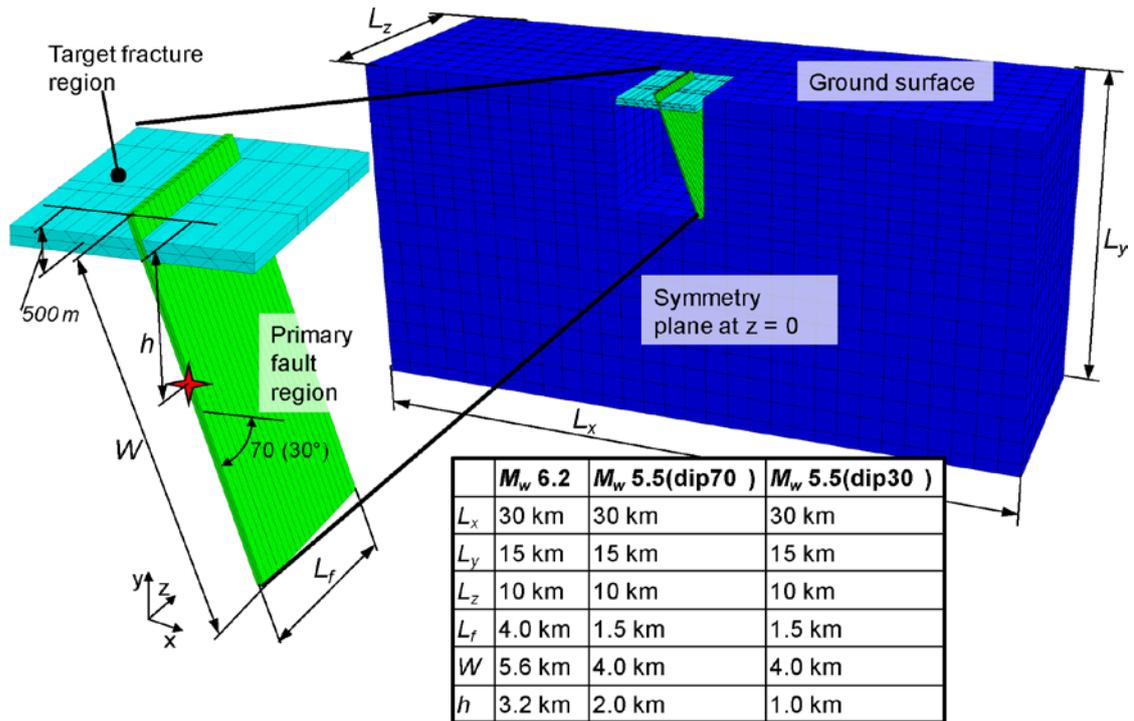
Figure 4-6. *Outlines and dimensions of the M_w 5.5 and M_w 6.2 models. There are two sets of M_w 5.5 models with 70° and 30° primary fault dip angles, respectively. Note that parts of the model geometry have been hidden for illustrative purposes.*

	M_w 6.2	M_w 5.5(dip70)	M_w 5.5(dip30)
L_x	30 km	30 km	30 km
L_y	15 km	15 km	15 km
L_z	10 km	10 km	10 km
L_f	4.0 km	1.5 km	1.5 km
W	5.6 km	4.0 km	4.0 km
h	3.2 km	2.0 km	1.0 km
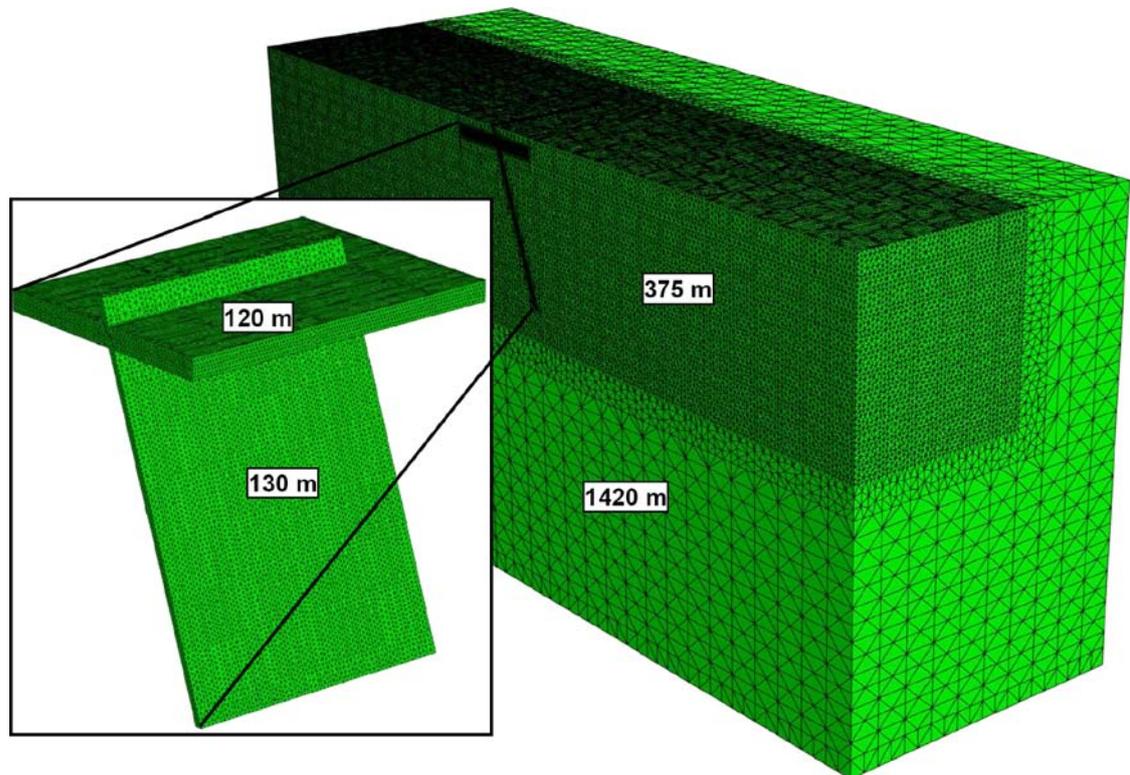
Figure 4-7. *Outline of the finite-difference mesh in the M_w 5.5 and M_w 6.2 models. The numbers indicate the maximum zone edge lengths in the different parts of the models.*

densely meshed as indicated by the inset. The rock volume which surrounds the primary fault and the repository region is discretised with average and maximum edge lengths of about 130 m and 375 m, respectively. According to Equation 4-3, this should ensure proper wave transmission of frequencies up to about 1.1 Hz in this volume.

In the more distant parts of the model, a coarser mesh is used. The maximum edge length in these parts is 1,420 m (Figure 4-7), which ensures proper wave transmission of frequencies up to about 0.3 Hz. However, this only influences the stress wave transmission in parts where the dynamic response has little importance for the main results in the central parts of the models. The outer model regions are incorporated mainly to prevent boundary effects from influencing the static parts of the results. The M_w 5.5 and M_w 6.2 models include about 1,500,000 and 2,800,000 finite-difference zones, respectively.

4.9.3   Target fractures

This section describes the locations and orientations of the target fractures in the M_w 5.5 and M_w 6.2 models. In order to study the importance of the distance from the source earthquake and of the fracture orientation (cf. Section 4.2), numerous fractures at different locations and with different orientations are included in each model. *3DEC* cannot handle full discrete fracture network models (DFN). Instead the influence of fracture orientation is studied by use of a few arbitrarily chosen orientations. The circular fractures are created using the methodology described in Appendix B. All fractures are perfectly planar and circular with 150 m radius.

By different combinations of fractures with different orientations, several fracture configurations can be created. Five fracture configurations are used in the M_w 5.5 and M_w 6.2 models. These are presented in Table 4-2 which shows the number of target fractures for each orientation. There are both horizontal fractures and dipping fractures. Two dip angles (30° and 45°) are tested. For the 30° dipping fractures there are two strike directions and for the 45°-fractures there are six. Note that the fault always has strike 0° but may have varying dip.

A complete set of sketches illustrating the fracture configurations is presented in Appendix B, but as an example, the BASE CASE configuration used in the M_w 5.5 models is shown in Figure 4-8. The right inset is a sketch of the principle of the fracture configuration. The sketch is a top-down vertical view from above of the target fracture region. The intersection between the fault plane and the repository horizon at 500 m depth is indicated by the solid blue line. The numbers indicate the horizontal distances from the fault plane, i.e. the Cartesian distances are slightly smaller. Two target fracture dip directions are used: the same direction as the fault and opposite to that of the fault. The dip directions of the fractures are indicated by arrows inside the circles. All dipping fractures have a dip angle of 45°. The left inset shows the *3DEC* cut planes used to create this fracture configuration.

Table 4-2. Target fracture (TF) configurations and number of fractures for each orientation (dip/strike). The fault always has strike 0° but may have varying dip.

Config	Fault dip	TF dip 0° —	TF dip 30° Strike 0°	TF dip 30° Strike 180°	TF dip 45° Strike 0°	TF dip 45° Strike 45°	TF dip 45° Strike 135°	TF dip 45° Strike 180°	TF dip 45° Strike 225°	TF dip 45° Strike 315°
BASE (M5.5)	70°	16			16			16		
BASE (M6.2)	70°	40			32			24		
ALT1 (M6.2)	70°	8				8	12		8	12
ALT2 (M5.5)	30°	16			16			16		
ALT3 (M5.5)	70°	16	16	16						
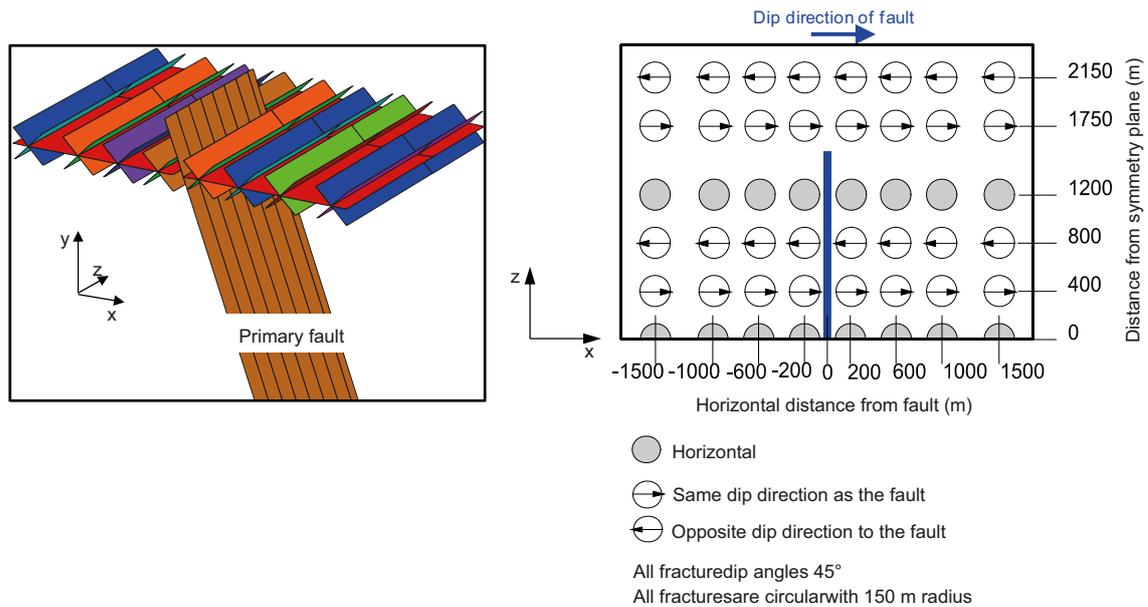
Figure 4-8. The right picture is a sketch of the principle showing the target fracture locations and orientations in the BASE CASE fracture configuration in the M_w 5.5 models. The sketch is a top-down vertical view from above of the target fracture region. The solid blue line indicates the intersection between the fault plane and the repository horizon at 500 m depth. The arrows indicate the dip directions of the dipping fractures which all dip at 45°. The left inset shows the 3DEC cut planes used to create this fracture configuration.

4.9.4   Initial stresses

Figure 4-9 shows the initial model stresses as a function of depth (y) applied in the M_w 5.5 and M_w 6.2 models. The initial stress state is denoted Stress1. The horizontal and vertical stress components are taken to be principal stresses, as shown by the inset. The purpose of the modelling work is to simulate seismic events of reverse type in a generic and schematic way. In order to accomplish this, reverse type stress fields are created by orienting the major (σ_H) and minor (σ_h) horizontal stresses normal and parallel to the fault strike, respectively. Note that the choice of stress orientations is an idealisation. In real faults, which may strike at an angle to the regional principal stress orientation, a reverse fault movement may also have elements of strike-slip (oblique slip).

The major horizontal stress (σ_H) is calibrated so as to give the average fault displacement necessary to obtain the intended seismic moment. For the fault and stress geometries assumed here, the minor horizontal stress, σ_h, is not important for the fault behaviour (whereas it may be for the target fractures). The initial stresses are defined according to Table 4-3. Note that y is zero at the ground surface (upper boundary of model) and negative at depth. The general convention in this report is that compressive stresses are positive. However, certain *3DEC* plots may utilize an alternate convention; in that case, it will be declared explicitly.

The initial model stress state results in shear stresses along the fault plane. Since the fault shear strength in the models is ramped down to zero (or close to zero) as the rupture propagates, the stress drop (fault shear stress reduction) obtained is equal to the initial fault shear stress. The amount of stress drop and its distribution along the fault are important parameters, as they affect the fault slip velocities and slip distribution. Figure 4-10 shows the initial fault shear stresses as function of both down-dip distance and of depth. The meanings of down-dip distance and of depth are illustrated by the insets. As can be seen in the diagrams the shear stresses in a gently-dipping fault (30° dip) are higher than those in a steeper one (70° dip) at the same depth.

The Stress1 initial stress state at 500 m depth is illustrated by the Mohr's circle diagram in Figure 4-11. Fractures dipping 30° and 45° in the $\sigma_H - \sigma_v$ plane (with strikes parallel to that of the primary fault, cf. Appendix B) have stability margins of about 0.1 MPa and 2 MPa, respectively. Horizontal fractures have about 5 MPa stability margin. Fractures oriented in arbitrarily-oriented planes (corresponding to the shaded area) all have larger stability margins than those dipping in the $\sigma_H - \sigma_v$ plane.
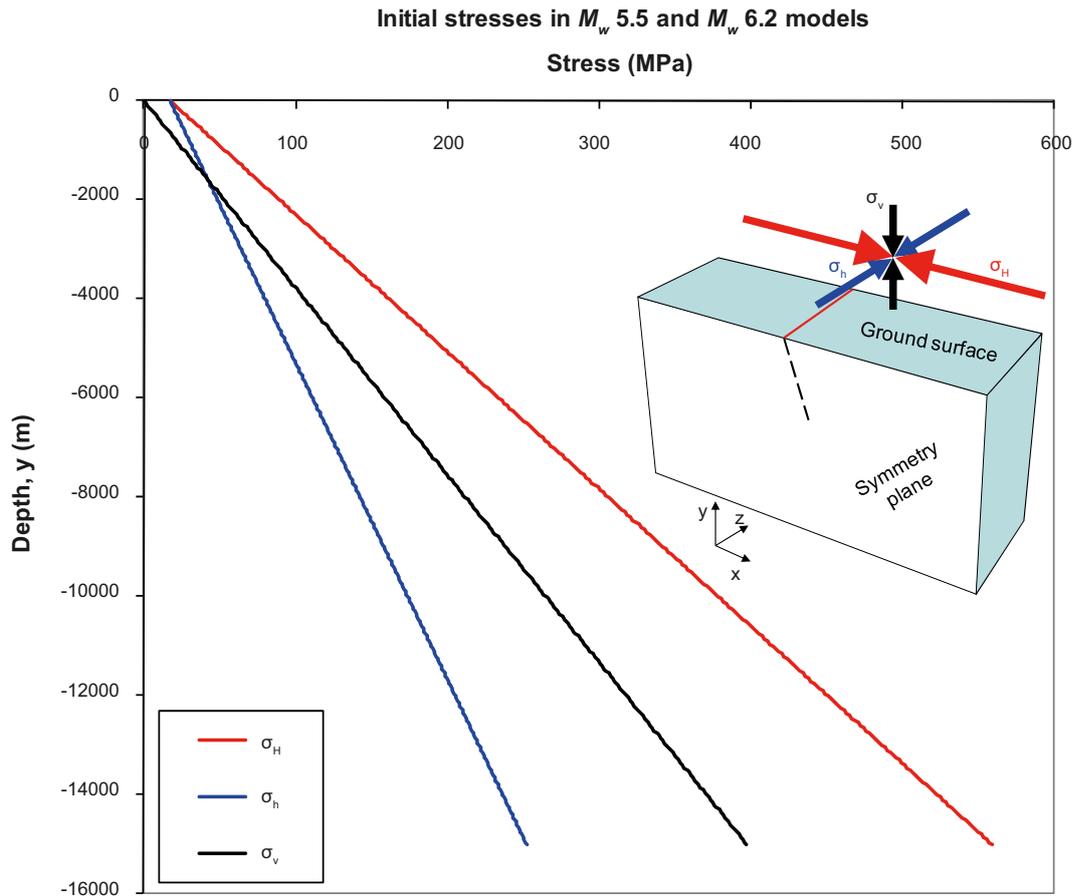
Figure 4-9. *Stress1 initial stress directions and variations with depth, y, in the M_w 5.5 and M_w 6.2 models. Note that y is zero at the ground surface (upper boundary of model) and negative at depth.*

Table 4-3. Stress1 initial stresses as function of depth, *y*, in the M_w 5.5 and M_w 6.2 models. Note that *y* is zero at the ground surface (upper boundary of model) and negative at depth. The right column shows the resulting average initial fault shear stress. The angles indicate the dip of the primary fault.

Model	σ_H (MPa)	σ_h (MPa)	σ_v (MPa)	Average initial fault shear stress (MPa)
M6.2 fault dip 70°				14
M5.5 fault dip 70°	17.25–0.0361y	17.18–0.0156y	–0.0265y	11
M5.5 fault dip 30°				12
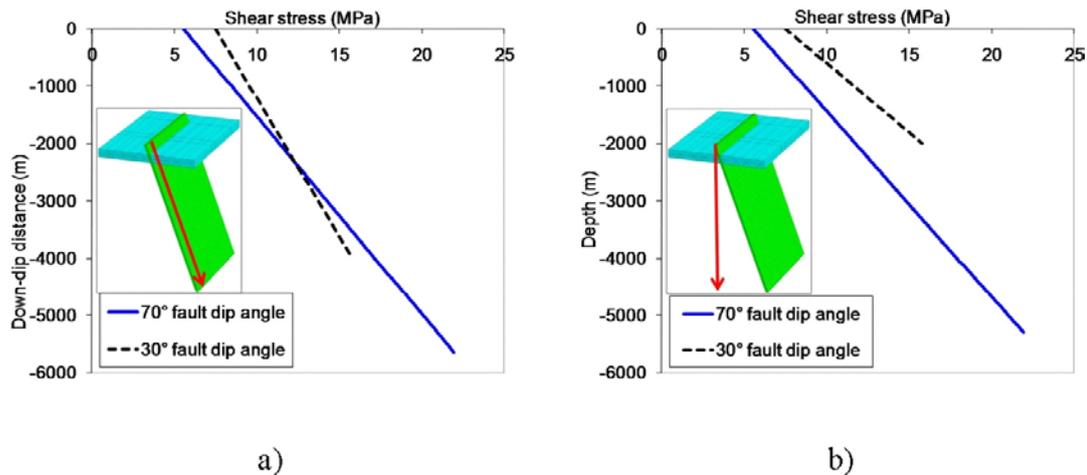
Figure 4-10. *Initial fault shear stresses as function of a) down-dip distance and of b) depth in the M_w 5.5 and M_w 6.2 models. The meanings of down-dip distance and depth are illustrated by the insets.*
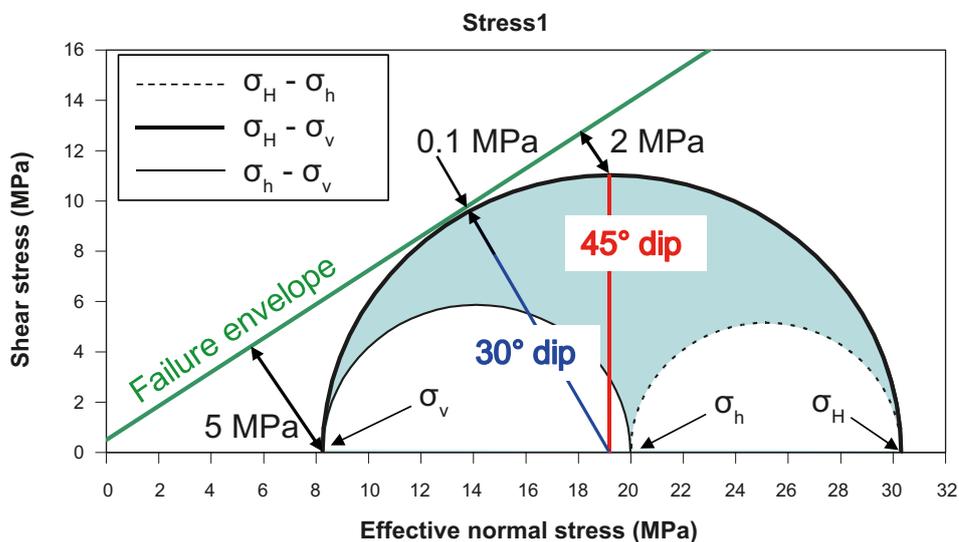
Figure 4-11. *Mohr's circle diagram illustrating the Stress1 initial stresses at 500 m depth. The green line is the failure envelope for the target fractures. The numbers indicate the stability margins for horizontal fractures and for fractures dipping 30° and 45° in the $\sigma_H - \sigma_v$ plane.*

The difference between σ_H and σ_h is about 10 MPa at 500 m depth. This can be compared with the corresponding stress differences reported for the SKB's candidate sites. The $\sigma_H - \sigma_h$ difference at 500 m depth at the Forsmark site is about 18 MPa /Glamheden et al. 2007/ and at the Laxemar site it is about 11 MPa /Hakami et al. 2008/.

During glaciation, increased pore pressures will develop in the bedrock beneath the ice sheet, and possibly remain after ice retreat. The residual pore overpressure at the repository level is a function of the duration of the ice cover and of the bedrock hydraulic properties (cf. Section 1.1.1). At the margin of the retreating ice the residual excess pore pressure might be on the order of 1 MPa at maximum /Chan et al. 2005, Hökmark et al. 2010/.

The pore pressure influences the stability of fractures and deformation zones. As a basic model assumption, the effect of a constant 5 MPa pore pressure is included in all target fractures, i.e. the hydrostatic undisturbed pressure at 500 m depth. The effects of a 1 MPa pore overpressure are investigated in one M_w 5.5 model by applying a 6 MPa total pore pressure in the target fractures. Note that the programmed behaviour of the primary fault is independent of any pore pressure assumptions.

4.9.5   Boundary conditions

Figure 4-12 illustrates the model boundary conditions. The vertical boundary at $z = 0$ is a symmetry plane (cf. Figure 4-6). Thus, this boundary is locked for displacements in the normal direction (roller boundary) for the duration of the entire analysis. At all the other vertical boundaries and at the model bottom, roller boundary conditions are set during the static phase. During the dynamic phase, these boundaries are set to act as non-reflecting (viscous) boundaries. This kind of boundary condition prevents the edges from reflecting waves back into the model. The top boundary is a free surface that does allow for surface reflections. Possible wave reflections from other deformation zones are not accounted for in the models.

The viscous boundary conditions eliminate irrelevant reflections, but there is a risk that they give undesired static contributions to the results. The reaction forces acting at the boundaries at the end of the static phase are maintained by the viscous boundaries during the dynamic phase. This is a consequence of how viscous boundary conditions are formulated in *3DEC*. As the primary fault slips and the stresses in the model are relaxed, the boundaries are automatically moved into the model in order to maintain the stress at the boundary. If the model is too small, this may result in overestimated shear movement on the fault.

4.10   Model dimensions, initial conditions and boundary conditions in the M_w 7.5 models

4.10.1   Model outlines and dimensions

Truncation

In the M_w 5.5 and M_w 6.2 models the entire fault plane can be fully included within the model boundaries (Figure 4-13a). The seismic moment of a M_w 7 earthquake is, however, about 30 times larger than that of a M_w 6 earthquake, meaning that the width and length of the fault plane as well as all other models dimensions would have to be increased accordingly. Due to memory allocation limitations in the *3DEC* version used in this project, it is therefore not possible to use full 3D-models when earthquakes of M_w 7 or larger are simulated.
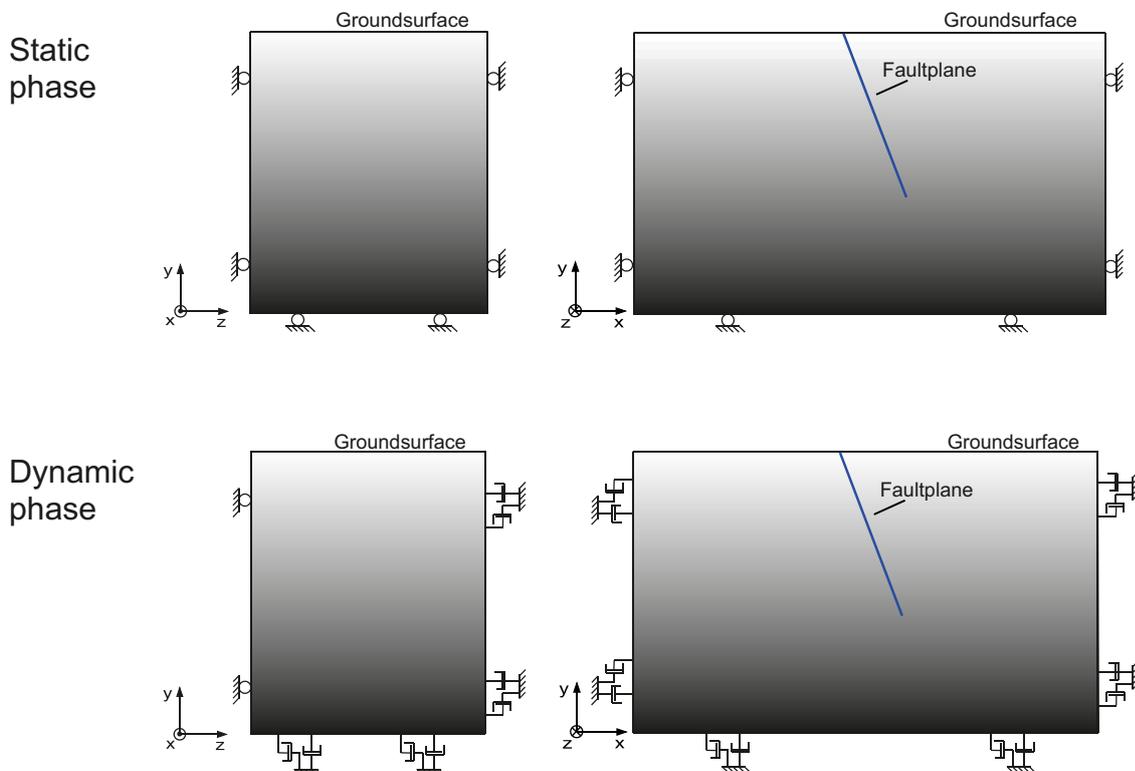
Figure 4-12. *Boundary conditions in M_w 5.5 and M_w 6.2 models. The roller boundary conditions used during the static phase are switched into viscous (non-reflecting) boundaries during the dynamic phase. The roller boundary condition is kept at $z = 0$ (symmetry plane) during the entire analysis.*
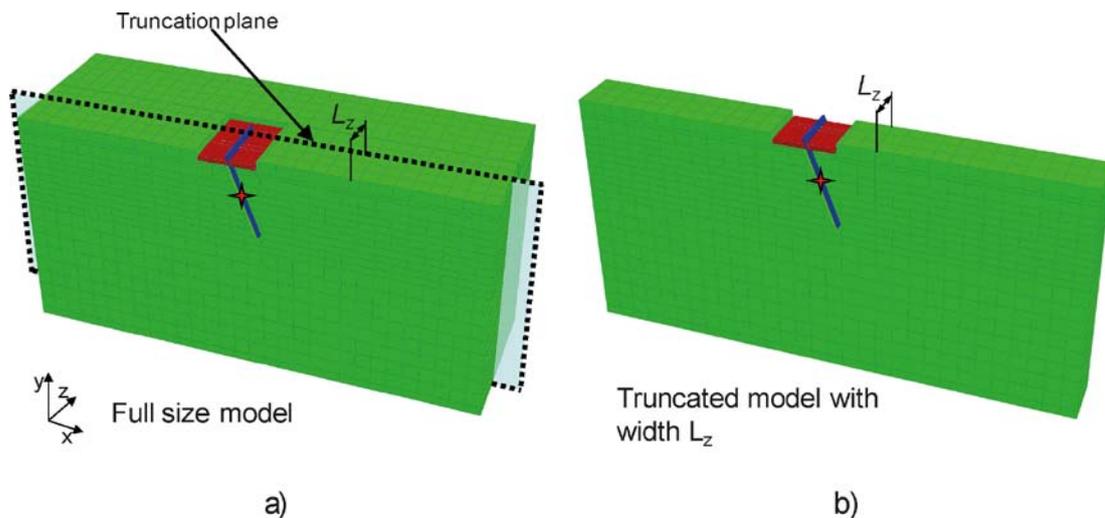
Figure 4-13. *The principle for truncation of model. Left: Full size model that includes the entire fault plane. Used to model M_w 5.5 and M_w 6.2 events. Right: Truncated model in which the fault plane is cut at the truncation plane. Used to model M_w 7.5 events.*

In order to simulate earthquakes of about M_w 7 or larger, truncated models are developed. The principle behind a truncated model is shown in Figure 4-13b. In the truncated models, the fault plane extends all the way through the model. Consequently, the model simulates the behaviour of a limited length-portion of a fault. Since symmetry boundary conditions are used for the truncation plane (i.e. zero displacements in normal direction), this geometry represents a fault of infinite length and with an infinite number of hypocentres as shown in Figure 4-14.
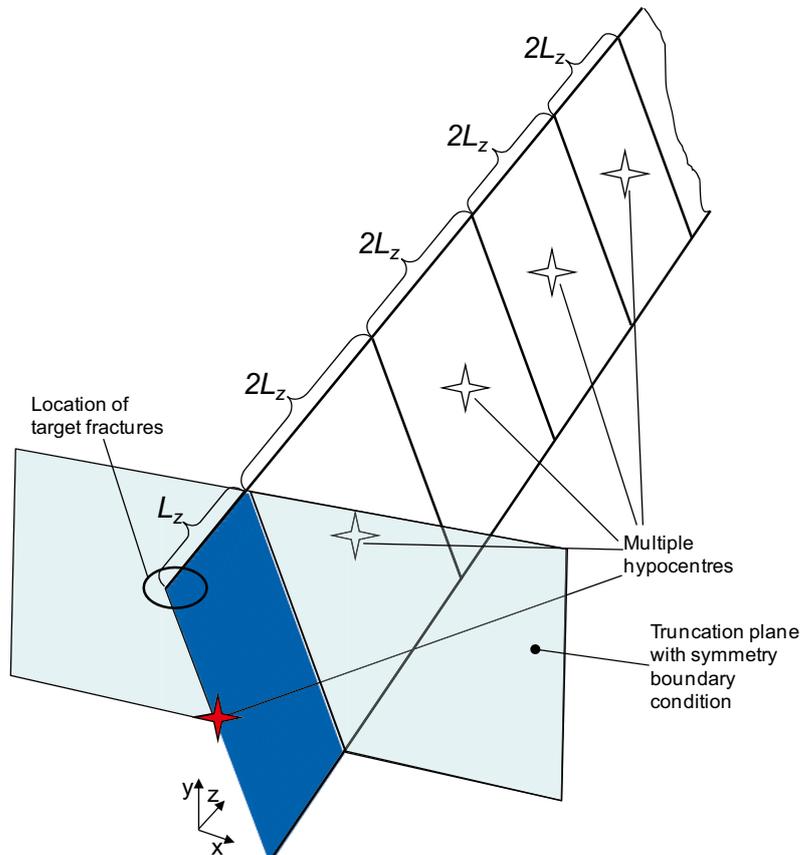
Figure 4-14. *Having symmetry boundary condition at the truncation plane means that the truncated model simulates a fault of infinite length and with an infinite number of hypocentres.*

Truncated model width

If the model width, L_z, is set small compared to other dimensions, the model would tend to resemble a 2D model with a line of densely spaced hypocentres. In order to capture the 3D-aspect of the rupture process, the model width, L_z, has to be large enough for the effects of the truncation boundary (e.g. wave reflections, disturbance of the rupture propagation) not to influence the response of the target fractures.

The truncation technique was tested on a M_w 6.2 model for which full 3D results are available. The 10 km wide full 3D model was truncated at 1 km, which corresponds to about 30% of the hypocentre depth. This gave a target fracture slip increase of about 30% just above the hypocentre and almost 100% at the truncation boundary (Figure 4-15). This shows that the truncation plane should be located at a significantly larger distance from the hypocentre. For the M_w 7.5 model five distances were tried: 0.8 km, 2.8 km, 8 km, 12 km and 16 km. These correspond to 10, 37, 106, 160 and 213% of the hypocentre depth, respectively. For the two smallest distances the induced slip was influenced by the truncation boundary, whereas the distance to the boundary did not appear to be important if it was more than 8 km, at least for fractures located close to the epicentre (Figure 4-15).

The test suggests that truncated M_w 7.5 models are valid approximations (with good margins) provided that the model width is large, say 20 km or more, and that only target fractures within a distance of two km from the epicentre are monitored.

Model dimensions

The model dimensions finally used in the M_w 7.5 models are shown in Figure 4-16. The model width (L_z) is set to 20 km. According to the results shown in Figure 4-15, having L_z = 16 km should be enough, but the use of L_z = 20 km provides a reasonable margin. It gives, for instance, the possibility to increase the fault width, W, and hypocentre depth, h, during the course of the work without jeopardizing the validity of the results. Figure 4-16 indicates two fault geometries. The geometry with W = 16 km is used together with the Stress2 and Stress3 initial stress models. When using this geometry, the hypocentre depth is h = 7.5 km. The fault width W = 21 km and hypocentre depth h = 10 km are used together in the Stress4 initial stress model. The initial stress models are described in Section 4.10.4. All M_w 7.5 models have fault dip angle 70°.

Induced slip at different z-coordinates
Foot wall side, 200 m distance, dip dir 90
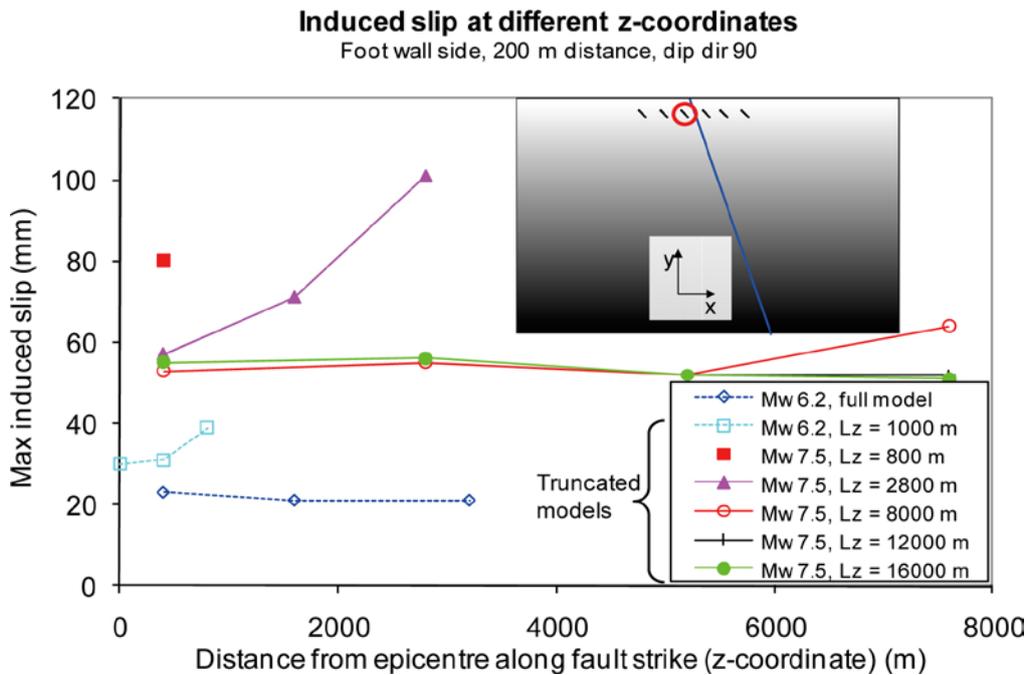
Figure 4-15. Induced target fracture slip in truncated models of different width. Results from a full 3D M_w 6.2 model are included for comparison. Dashed lines represent M_w 6.2 model results while all other results are M_w 7.5 models. Each plot symbol represents the result from one individual target fracture. All fractures are located 200 m from the primary fault and dip as shown in the inset.
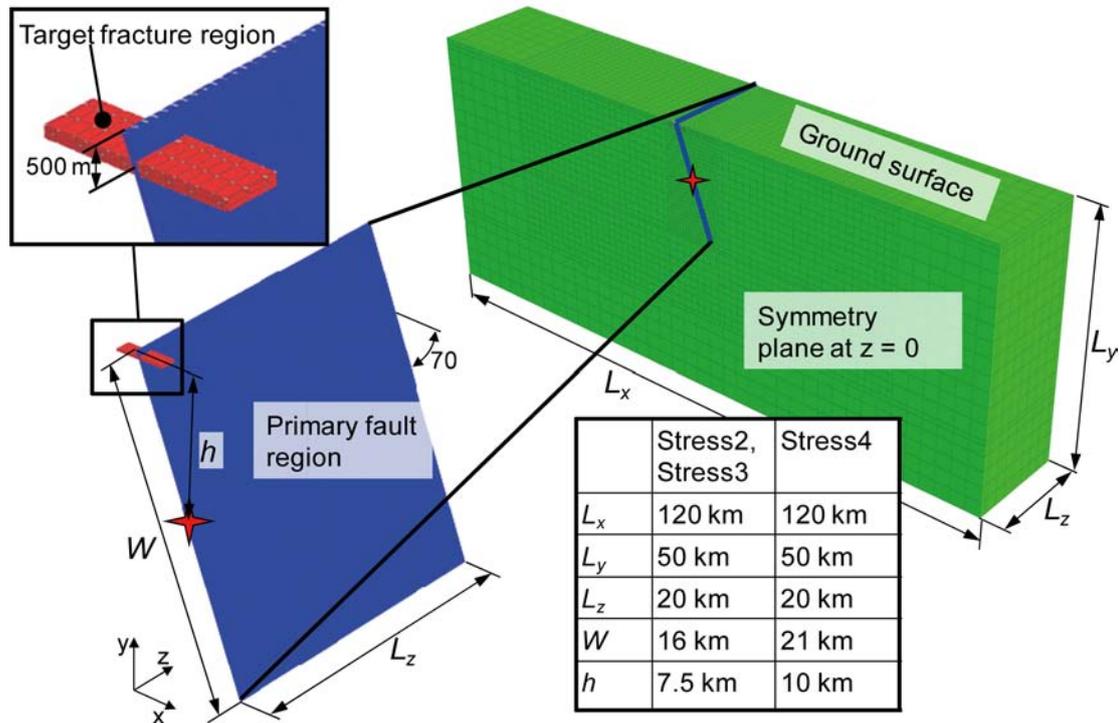
Figure 4-16. *Geometry and dimensions of the M_w 7.5 models.*

4.10.2 Finite-difference mesh

Figure 4-17 shows the finite-difference mesh used in the M_w 7.5 models. The numbers in the figure indicate the maximum zone edge lengths in the different regions. In the target fracture region where the target fractures are located and along the primary fault, the models are specifically densely meshed as indicated by the lower inset. The repository region and the volume surrounding the primary fault are discretised with maximum edge lengths of about 110 m and 210 m, respectively. According to Equation 4-3, this ensures proper wave transmission of frequencies up to about 3.8 Hz and 2.0 Hz in these volumes, respectively. The model has about 3,300,000 finite-difference zones.

4.10.3 Target fractures

This section describes the locations and orientations of the target fractures in the M_w 7.5 models. In order to study the importance of the distance from the source earthquake and of the fracture orientation (cf. Section 4.2), a number of target fractures at different locations and with different orientations are included in each model. *3DEC* cannot handle full discrete fracture network models (DFN); instead the influence of fracture orientation is studied by use of a few arbitrarily chosen orientations. The target fractures are created using the methodology described in Appendix B and are circular in shape with a radius of 150 m.

By different combinations of fractures with different orientations, five fracture configurations are created. These are presented in Table 4-4 which shows the number of target fractures for each orientation. There are both horizontal fractures and dipping fractures. Three dip angles (30°, 45° and 60°) are tested. For the 30° dipping fractures there are two strike directions and for both the 45° and 60° fractures there are four. Note that the fault always has strike 0° and dip angle 70°. The fracture configurations are not used together in the same model, i.e. only one configuration is used at a time. All fracture configurations are illustrated and described in detail in Appendix B.
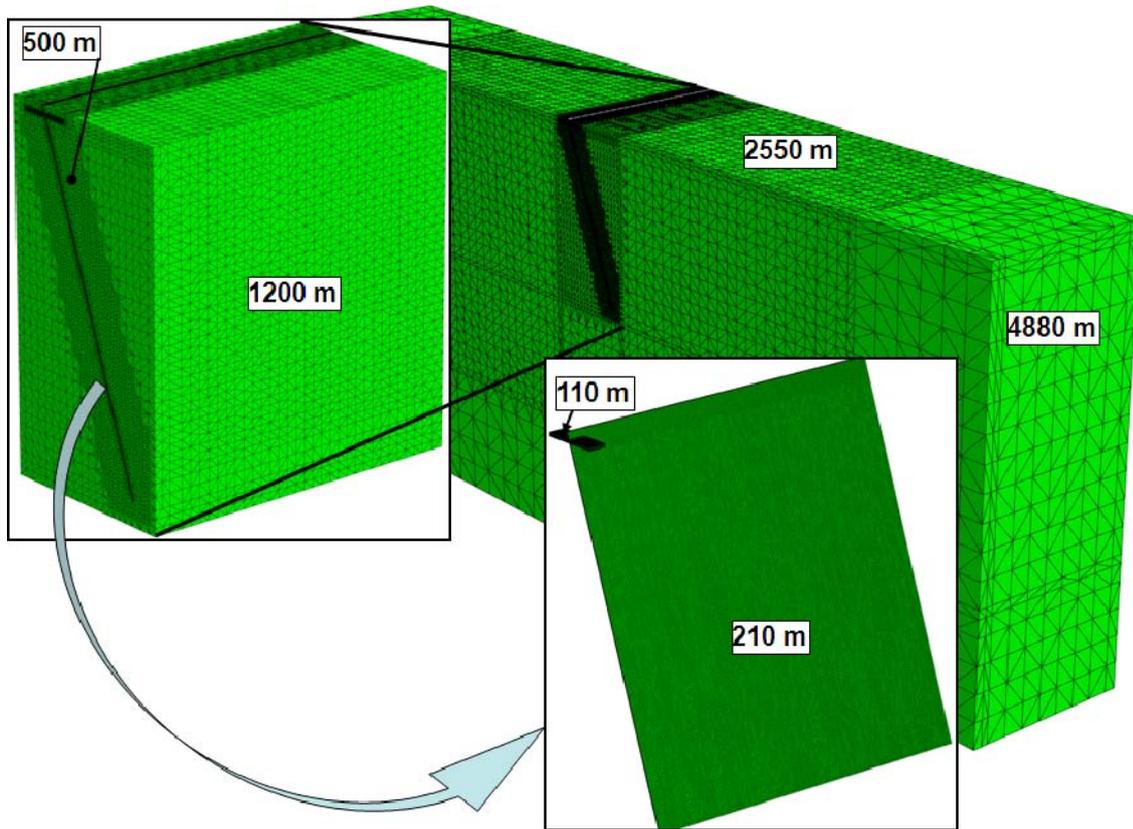
Figure 4-17. *The finite-difference mesh in the M_w 7.5 model. The numbers indicate the maximum zone edge lengths used in the different regions.*

Table 4-4. Target fracture (TF) configurations and number of fractures for each orientation (dip/strike). The fault always has strike 0° and dip angle 70°.

Config	TF dip 0°	TF dip 30°		TF dip 45°				TF dip 60°			
	–	Strike 0°	Strike 180°	Strike 0°	Strike 45°	Strike 180°	Strike 225°	Strike 0°	Strike 45°	Strike 180°	Strike 225°
BASE	8			8		8					
ALT1	8	8	8								
ALT2	8							8		8	
ALT3	8				8		8				
ALT4	8								8		8

4.10.4 Initial stresses

Figure 4-18 shows the initial stresses as function of depth, *y*, applied in the M_w 7.5 models. Three different initial stress states are tested. The stress states were denoted Stress2, Stress3 and Stress4, respectively, and are defined according to Table 4-5. The horizontal and vertical stress components are taken to be principal stresses as shown by the inset.

The major horizontal stress (σ_H) is calibrated to give the average fault displacement needed to obtain the intended seismic moment. For the geometry assumed here, the minor horizontal stress (σ_h) is not important for the fault behaviour (whereas it may be for the target fractures). Note that *y* is zero at the ground surface (upper boundary of model) and negative at depth.
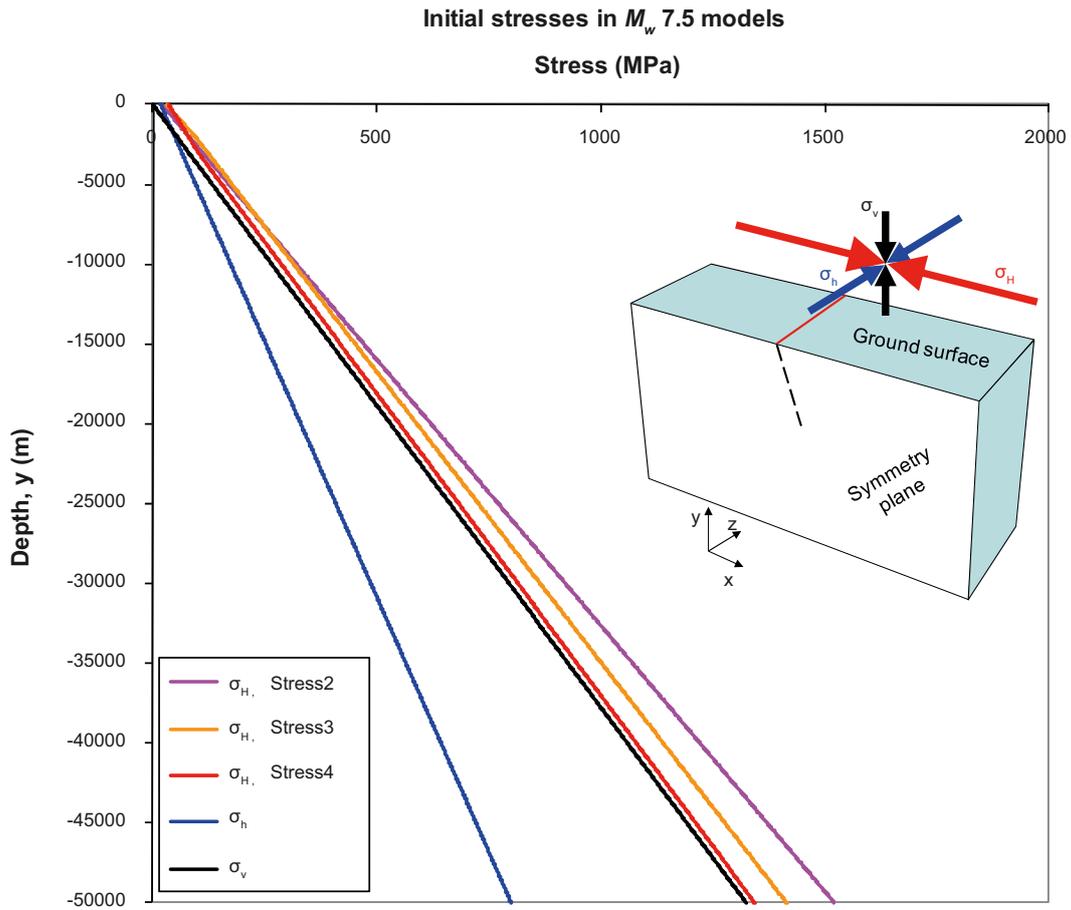
Figure 4-18. *In situ stress directions and variations with depth, y, in the M_w 7.5 models. Note that y is zero at the ground surface (upper boundary of model) and negative at depth.*

Table 4-5. Initial stress states in the M_w 7.5 models as function of depth, *y*. The right column shows the resulting average initial fault shear stresses. Note that *y* is zero at the ground surface (upper boundary of model) and negative at depth.

Stress state	σ_H	σ_h	σ_v	Average initial fault shear stress (MPa)
Stress2	20.25–0.0300*y*			15
Stress3	$\begin{cases} 30.00-0.0320y \ (-2{,}000 \le y \le 0) \\ 39.00-0.0275y \ (y \le -2{,}000) \end{cases}$			15
		17.18–0.0156*y*	–0.0265*y*	
Stress4	$\begin{cases} 35.00-0.0220y \ (-3{,}000 \le y \le 0) \\ 21.72-0.0264y \ (y \le -3{,}000) \end{cases}$			7

The *in situ* stress state results in shear stresses along the fault plane. These are plotted as function of down-dip distance in Figure 4-19. The meaning of down-dip distance is illustrated by the inset. Since the fault shear strength in the models is ramped down to zero as the rupture propagates, the stress drop (fault shear stress reduction) obtained is equal to the initial fault shear stress. The amount of stress drop and its distribution along the fault are important parameters, as they affect the fault slip velocities and slip distribution.

Initial fault shear stress
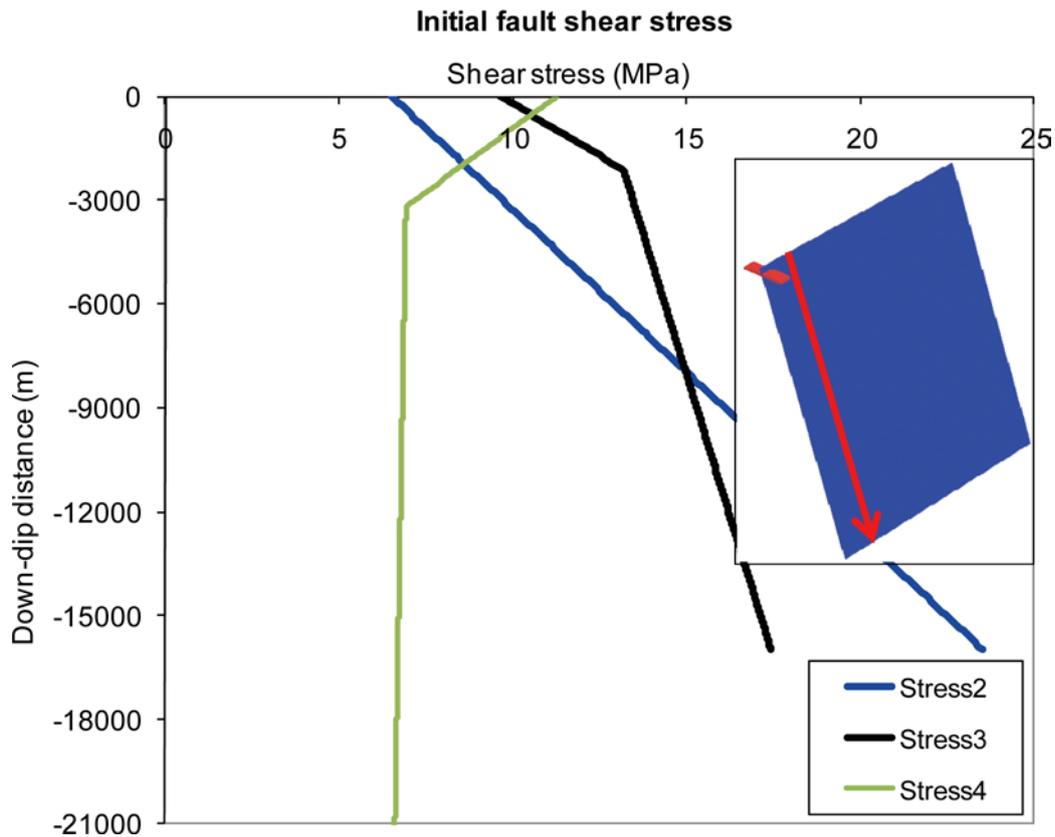
Figure 4-19. Initial fault shear stresses as function of down-dip distance in the M_w 7.5 models. The meaning of down-dip distance is illustrated by the inset.

The major horizontal stress (σ_H) in the Stress2 state is set to create both the same average initial shear stress on the primary fault and the same initial shear stress in the target fractures at 500 m depth as in the M_w 5.5 and M_w 6.2 models (cf. Figure 4-11a). The σ_H-component in the Stress3 state gives the same average initial fault shear stress as the Stress2 state, but with a different distribution along the fault. The shear stresses at shallow depths are higher in the Stress3 state.

The major horizontal stress (σ_H) in the Stress4 state is calibrated using a static model (see Appendix A) to produce a resulting average fault slip to fault width ratio similar to what has been estimated for the Pärvie Fault by /Muir Wood 1993, Arvidsson 1996/. This stress state results in a considerably lower initial average fault shear stress compared to the Stress2 and Stress3 states.

Figure 4-20 shows a Mohr's circle diagram that illustrates the initial stresses at 500 m depth in the Stress4 stress state. The $\sigma_H - \sigma_h$ difference at 500 m depth is important to the stability of target fractures that strike at an angle to the primary fault. The minor horizontal stress (σ_h) is set such that the $\sigma_H - \sigma_h$ difference is about 21 MPa. For the Forsmark and Laxemar candidate sites, the difference between the horizontal stress components at 500 m depth is estimated to be about 18 MPa /Glamheden et al. 2007/ and 11 MPa /Hakami et al. 2008/, respectively. According to /Lund et al. 2009/, the difference between the glacially-induced major and minor horizontal stress addition components at the end of a glacial cycle is about 3 MPa. If it is conservatively assumed that the glacially-induced stress components are aligned with the present day stress field, this would result in differences between the horizontal stress components at the end of a glaciation of about 21 MPa and 14 MPa at the Forsmark and Laxemar sites, respectively. As such, the $\sigma_H - \sigma_h$ difference in the Stress4 state is similar to that estimated here for the Forsmark site at the end of a glaciation (Figure 4-20).
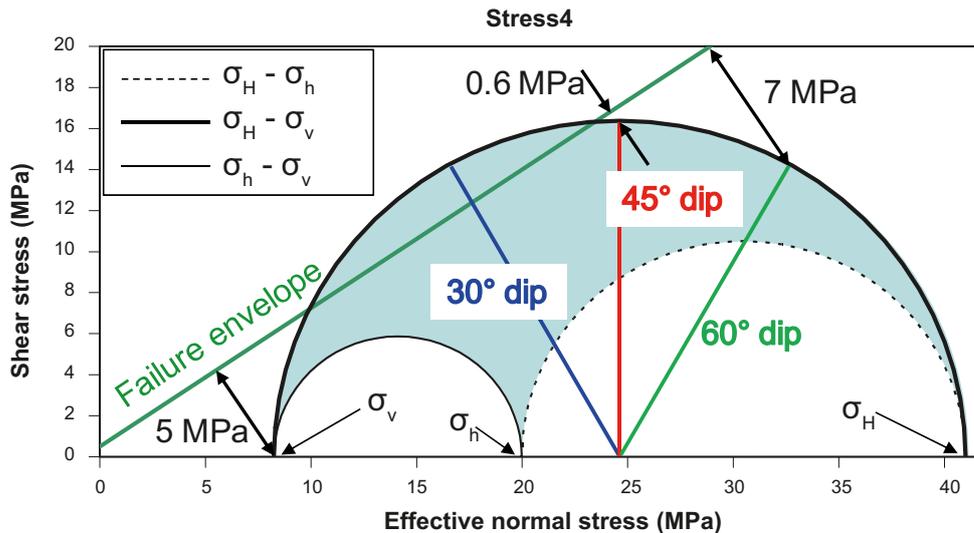
Figure 4-20. *Mohr circle diagram illustrating the initial stresses at 500 m depth for the Stress4 stress state. The green line is the failure envelope for the target fractures. The numbers indicate the stability margins for fractures dipping 45° and 60° in the σ_H – σ_v plane. The 30° dipping fractures are initially in a state of failure.*

The numbers in Figure 4-20 illustrate the stability margins for both horizontal fractures and for fractures dipping 45° and 60° in the σ_H – σ_v plane. Horizontal fractures have, roughly, a 5 MPa stability margin, while fractures dipping 45° and 60° have 0.6 MPa and 7 MPa stability margins, respectively. Fractures dipping at 30° are initially in a state of failure.

The pore pressure influences the stability of fractures and deformation zones. As a basic model assumption, the effect of a constant 5 MPa pore pressure is included in all target fractures, i.e. the hydrostatic undisturbed pressure at 500 m depth. In order to account for the effects of residual pore overpressures that may remain at repository level after ice retreat (cf. Sections 1.1.1 and 4.9.4), the effects of a 1 MPa pore overpressure are investigated in one M_w 7.5 model by applying a 6 MPa total pore pressure in the target fractures. Note that the programmed behaviour of the primary fault is independent of any pore pressure assumptions.

4.10.5 Boundary conditions

The boundary conditions in the static and dynamic analysis phases are illustrated in Figure 4-21. During the static phase the boundary conditions are identical to what was applied in the M_w 5.5 and M_w 6.2 models, i.e. roller boundary conditions (no displacements in normal direction) are applied at all boundaries except for the upper boundary which represents the free ground surface. During the dynamic phase the boundary conditions are also the same as in the M_w 5.5 and M_w 6.2 models, except for the boundary representing the truncation plane, which has rollers and thus acts as a symmetry plane (cf. Section 4.10.1).
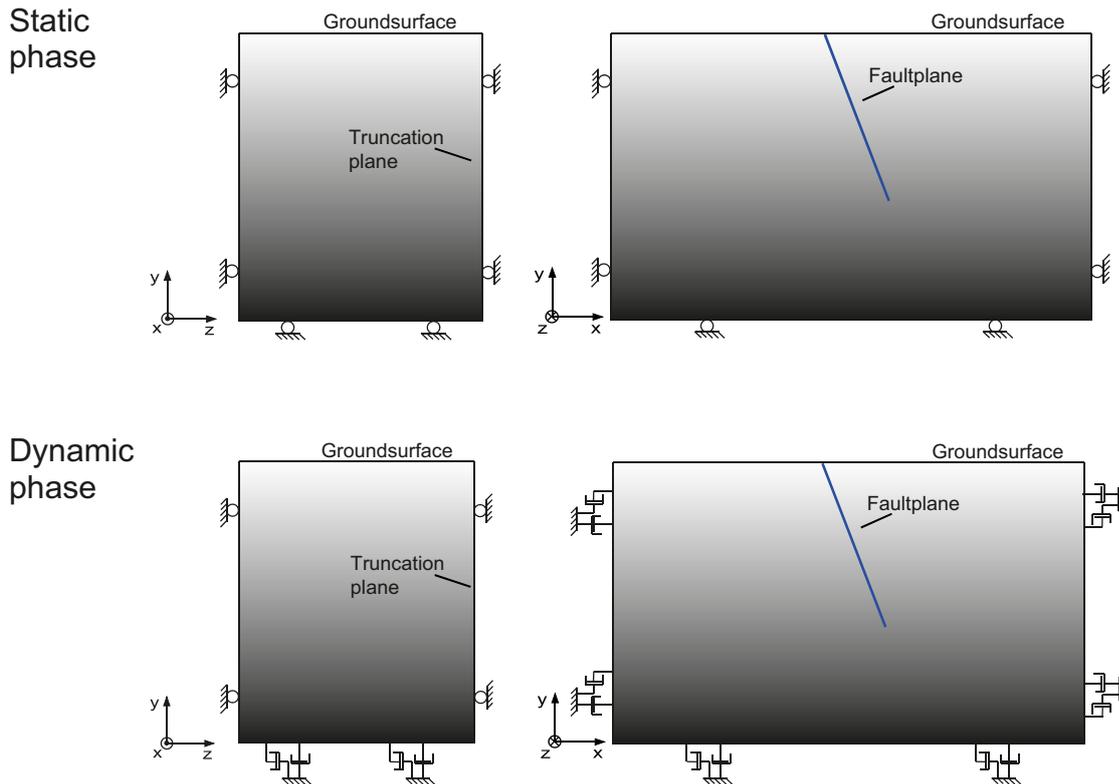
Figure 4-21. *Boundary conditions in M_w 7.5 models. The roller boundary conditions used during the static phase are switched into viscous (non-reflecting) boundaries during the dynamic phase. The roller boundary condition is kept at z = 0 (symmetry plane) and at the truncation plane (see lower left).*

4.11   Model map

Table 4-6 presents a summary of the M_w 5.5 models. Four of the models have the default primary fault dip angle of 70°, while two models have a primary fault dip angle of 30°. Two of the models have a residual fault friction angle of 6°. In one model the effect of an excess pore pressure of 1 MPa is applied (total pore pressure 6 MPa). In one model all dipping target fractures have a dip angle of 30° instead of 45°. In all M_w 5.5 models, the Stress1 initial stress state is used.

Table 4-7 presents the M_w 6.2 models. The first model is similar to the Case B model (cf. Section 2.2.2) analysed by /Fälth and Hökmark 2006/ but with a finer discretisation of the continuum and run in single precision mode. The second model is similar to the first one but with rt = 2 seconds, which gives a lower maximum fault slip velocity. Then there is one model in which the alternative target fracture configuration ALT1 is included, i.e. the target fractures are oriented such that they strike at an angle to the primary fault.

Table 4-8 presents the M_w 7.5 models. Three out of the four models that have fault width 16 km use the Stress2 initial stress state but different reduction times (rt). In one model, the Stress3 initial stress state is used.

Seven M_w 7.5 models have a larger fault width (21 km). In these models, the Stress4 initial stress state is used. This stress state is calibrated to give the same resulting average fault slip to width ratio as has been estimated for the Pärvie Fault by /Muir Wood 1993, Arvidsson 1996/. Three of the models apply the BASE CASE fracture configuration, in which the dipping fractures strike parallel to the primary fault. Four of the models apply fracture configurations other than the BASE CASE. In one model, the effect of having a 1 MPa excess pore pressure (total 6 MPa) in the target fractures is tested.

Table 4-6. Summary of M_w 5.5 models.

Model	Fault width W (km)	Initial stress model	Target fracture config.	Reduction time, rt (s)	Fault residual friction angle (°)	Comment
M5_Str1_tfBASE_rt05	4	Stress1	BASE CASE	0.5	0	
M5_Str1_tfBASE_rt05_pp6						6 MPa pore pressure
M5_Str1_tfBASE_rt05_res					6	
M5_Str1_tfALT2_rt05			ALT2		0	Fault dip angle 30°
M5_Str1_tfALT2_rt05_res			ALT2		6	
M5_Str1_tfALT3_rt05			ALT3		0	Target fracture dip 30°

Table 4-7. Summary of M_w 6.2 models.

Model	Fault width, W (km)	Initial stress model	Target fracture config.	Reduction time, rt (s)	Comment
M6_Str1_tfBASE_rt05	5.6	Stress1	BASE CASE	0.5	Corresponds to Case B model in /Fälth and Hökmark 2006/
M6_Str1_tfBASE_rt2				2.0	
M6_Str1_tfALT1_rt05			ALT1	0.5	

Table 4-8. Summary of M_w 7.5 models.

Model	Fault width, W (km)	Initial stress model	Target fracture config.	Reduction time, rt (s)	Comment
M7_Str2_tfBASE_rt05	16	Stress2	BASE CASE	0.5	
M7_Str2_tfBASE_rt1				1.0	
M7_Str2_tfBASE_rt2				2.0	
M7_Str3_tfBASE_rt05		Stress3		0.5	
M7_Str4_tfBASE_rt05	21	Stress4	BASE CASE	0.5	
M7_Str4_tfBASE_rt1				1.0	
M7_Str4_tfBASE_rt1_pp6				1.0	Pore pressure 6 MPa
M7_Str4_tfALT1_rt1			ALT1	1.0	Target fracture dip 30°
M7_Str4_tfALT2_rt1			ALT2	1.0	Target fracture dip 60°
M7_Str4_tfALT3_rt1			ALT3	1.0	Target fracture dip 45° and alternative dip directions
M7_Str4_tfALT4_rt1			ALT4	1.0	Target fracture dip 60° and alternative dip directions

5 Modelling results

This chapter presents the results of the numerical modelling. Not all results from all models are presented. Complete sets of results are not presented for those types of results that are similar for all models. Instead, examples are shown in order to demonstrate the modelling technique and to show the sensitivity to input parameters. However, the main results, i.e. the amount of induced target fracture shear displacements, are presented for all models.

5.1 Primary fault slip, slip velocities and moment magnitude

Table 5-1 presents values of moment magnitude, seismic moment, maximum primary fault slip and maximum primary fault slip velocity derived from the models. The moment magnitudes are determined after completed simulations by summing the seismic moments (cf. Section 4.4.4) for all sub-contacts in the primary fault plane and then converting them into moment magnitude. The M_w 7.5 models simulate a fault with an infinite length; as such, an assumption regarding the fault length has to be made in order to calculate the seismic moments (which depend on the rupture area) in these models. For purposes of moment-magnitude calculation, the length of the primary fault in these models is assumed to be 60 km, i.e. about three times the fault width in the largest models.

The maximum fault slip results are included in Table 5-1 in order to facilitate a comparison between the models and literature data such as those in Figure 1-6 and Figure 6-8. The modelling results indicate that the fault slip velocity is a parameter that is important for the amount of induced fracture shear displacement. Slip velocities are not a regular output parameter from *3DEC*; they are derived from fault slip histories by calculation of the time derivative of the displacement (Figure 5-1). The following can be observed in Table 5-1:

- The value of strength reduction time, *rt*, (cf. Figure 4-5) influences the fault slip velocity but not the amount of resulting slip (and therefore does not influence the moment magnitude). When the fault has zero residual strength the amount of slip is governed only by the initial stress conditions and the fault geometry.

- A low residual fault shear strength is applied in two models (one with a fault dip angle of 70° and one with a dip of 30°). The residual shear strength has a greater impact on the amount of slip when the fault is steeply-dipping. Given the stress conditions assumed (horizontal stress considerably higher than the vertical stress) in the modelling work, a smaller dip angle results in lower normal stresses on the fault with a corresponding lower sensitivity to the friction properties.

Figure 5-2 shows vector plots of primary fault slip after 1, 5 and 10 seconds in the M6_Str1_tfBASE_rt05 model. The vectors are coloured according to their magnitudes, while the earthquake hypocentre is indicated by a star. The upper boundary represents the ground surface. The plot at 1 second illustrates how the rupture is initiated at the hypocentre and propagates radially along the fault plane (The idealised propagation path is controlled by the algorithm described in Section 4.8.2). After about 2 seconds the rupture front has reached all parts of the fault. It is also shown by the plots that the maximum slip is found at the ground surface at the symmetry plane and that the slip is zero along both the vertical edge and along the bottom edge due to the elastic conditions. Figure 5-3 shows similar plots at 5, 11 and 20 seconds from the M7_Str4_tfBASE_rt05 model. Due to the truncation of the model the resulting slip distribution is identical along the entire fault length.

Figure 5-4 shows the temporal development of primary fault slip at four points at hypocentre depth in the M6_Str1_tfBASE_rt05 model. The points are located at different distances from the hypocentre (right inset). The plot shows how slip is initiated at different times as the rupture front passes the points. After about 2 s, the rupture front has passed over the entire fault area and the fault shear strength has been ramped down to zero across the entire fault surface (i.e. the idealised representation of the stress drop in an earthquake). At subsequent times, there is nothing in the fault that prevents slip along the primary fault plane, and so the oscillations induced by the rupture continue until they are smoothed out by the general numerical damping and the effects of the non-reflecting boundary conditions. The behaviour of a model where the fault has a residual strength is different. This is illustrated in Figure 5-5a.

Table 5-1. Moment magnitudes, seismic moments, maximum primary fault slip and maximum slip velocities.

Model	M_w	Seismic moment (Nm)	Max fault slip (m)	Max fault slip velocity (m/s)	Comment
M5_Str1_tfBASE_rt05	5.5	$2.6 \cdot 10^{17}$	1.1	3.2	
M5_Str1_tfBASE_rt05_res	5.3	$1.2 \cdot 10^{17}$	0.71	1.9	Fault residual strength
M5_Str1_tfBASE_rt05_pp6	5.5	$2.6 \cdot 10^{17}$	1.1	3.2	
M5_Str1_tfALT3_rt05	5.5	$2.6 \cdot 10^{17}$	1.1	3.2	
M5_Str1_tfALT2_rt05	5.6	$2.8 \cdot 10^{17}$	1.4	5.0	Fault dip 30°
M5_Str1_tfALT2_rt05_res	5.6	$2.7 \cdot 10^{17}$	1.4	5.1	Fault dip 30° Fault residual strength
M6_Str1_tfBASE_rt05	6.2	$2.6 \cdot 10^{18}$	2.9	4.6	
M6_Str1_tfBASE_rt2	6.2	$2.6 \cdot 10^{18}$	2.9	2.3	
M6_Str1_tfALT1_rt05	6.2	$2.6 \cdot 10^{18}$	2.9	4.6	
M7_Str2_tfBASE_rt05	7.5[*]	$2.6 \cdot 10^{20}$ [*]	10.2	6.5	
M7_Str2_tfBASE_rt1	7.5[*]	$2.6 \cdot 10^{20}$ [*]	10.2	4.3	
M7_Str2_tfBASE_rt2	7.5[*]	$2.6 \cdot 10^{20}$ [*]	10.2	3.0	
M7_Str3_tfBASE_rt05	7.6[*]	$2.9 \cdot 10^{20}$ [*]	13.2	8.5	
M7_Str4_tfBASE_rt05	7.5[*]	$2.5 \cdot 10^{20}$ [*]	10.0	6.8	
M7_Str4_tfBASE_rt1	7.5[*]	$2.5 \cdot 10^{20}$ [*]	10.0	4.2	
M7_Str4_tfBASE_rt1_pp6	7.5[*]	$2.5 \cdot 10^{20}$ [*]	10.0	4.2	
M7_Str4_tfALT1_rt1	7.5[*]	$2.5 \cdot 10^{20}$ [*]	10.0	4.2	
M7_Str4_tfALT2_rt1	7.5[*]	$2.5 \cdot 10^{20}$ [*]	10.0	4.2	
M7_Str4_tfALT3_rt1	7.5[*]	$2.5 \cdot 10^{20}$ [*]	10.0	4.2	
M7_Str4_tfALT4_rt1	7.5[*]	$2.5 \cdot 10^{20}$ [*]	10.0	4.2	

[*] Assuming a fault length of 60 km.

$$\dot{u}_{t_i} = \frac{\Delta u_i}{\Delta t} \qquad i = 1, 2, ..., n$$
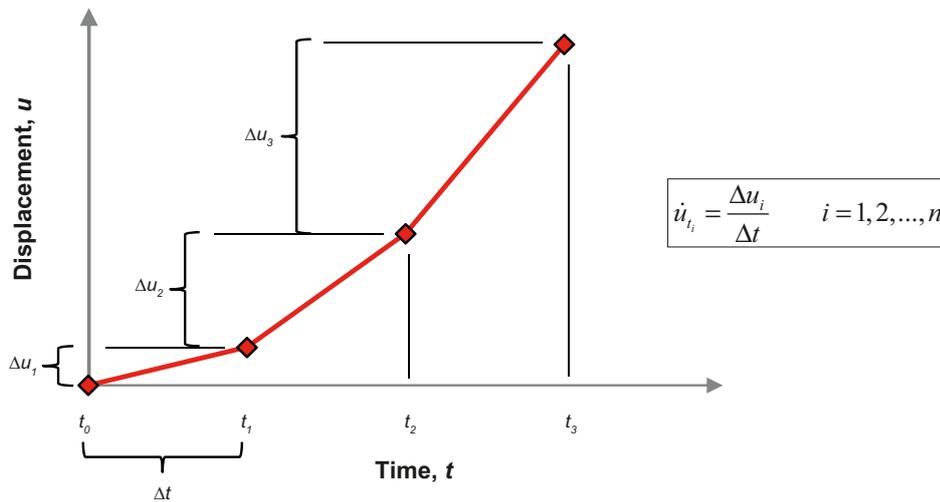
Figure 5-1. *Principle for derivation of slip velocities from displacement records.*
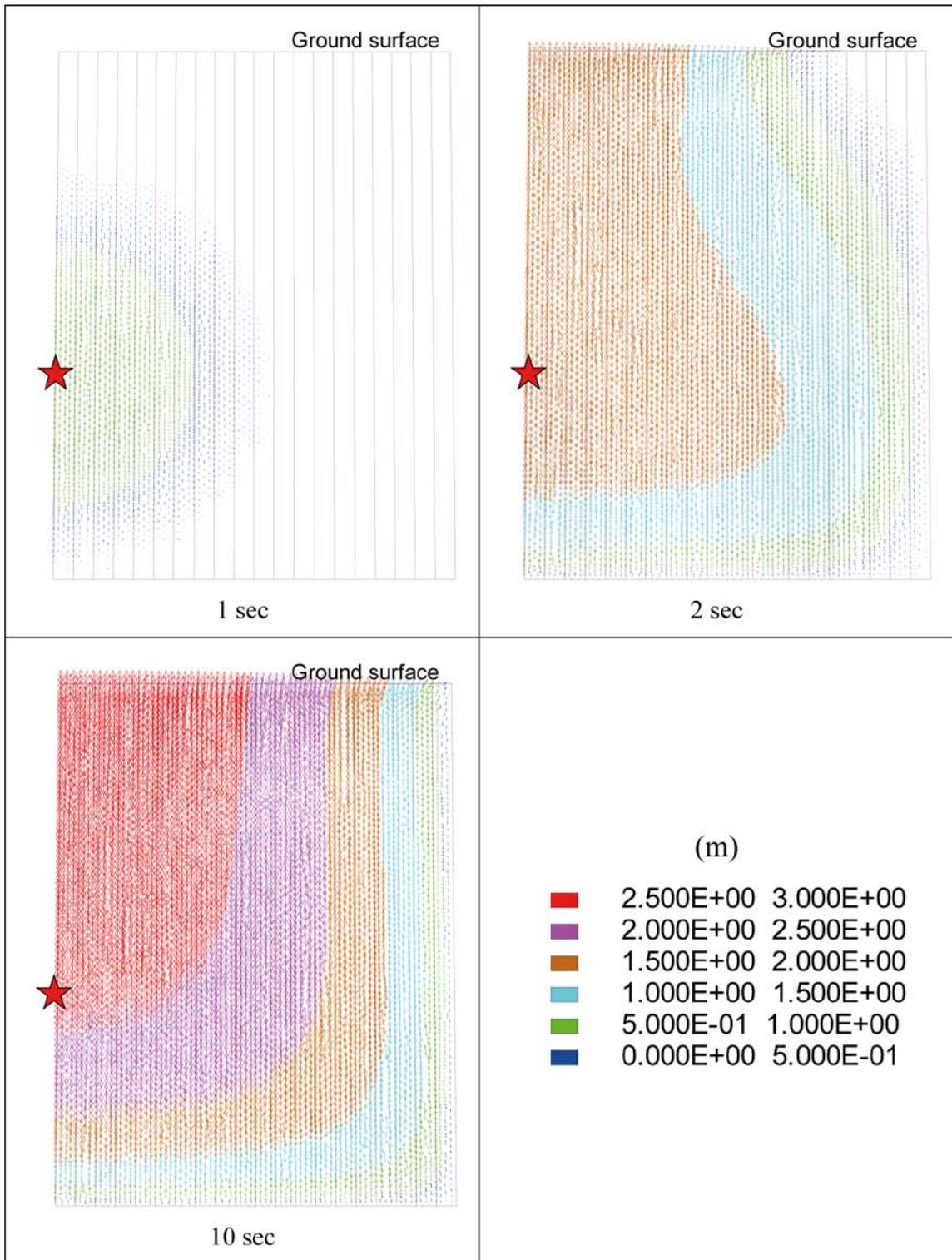
Figure 5-2. *Vector plots showing primary fault slip at three instances of time in the M6_Str1_tfBASE_rt05 model. The vectors are coloured according to their magnitudes. The star indicates the hypocentre.*
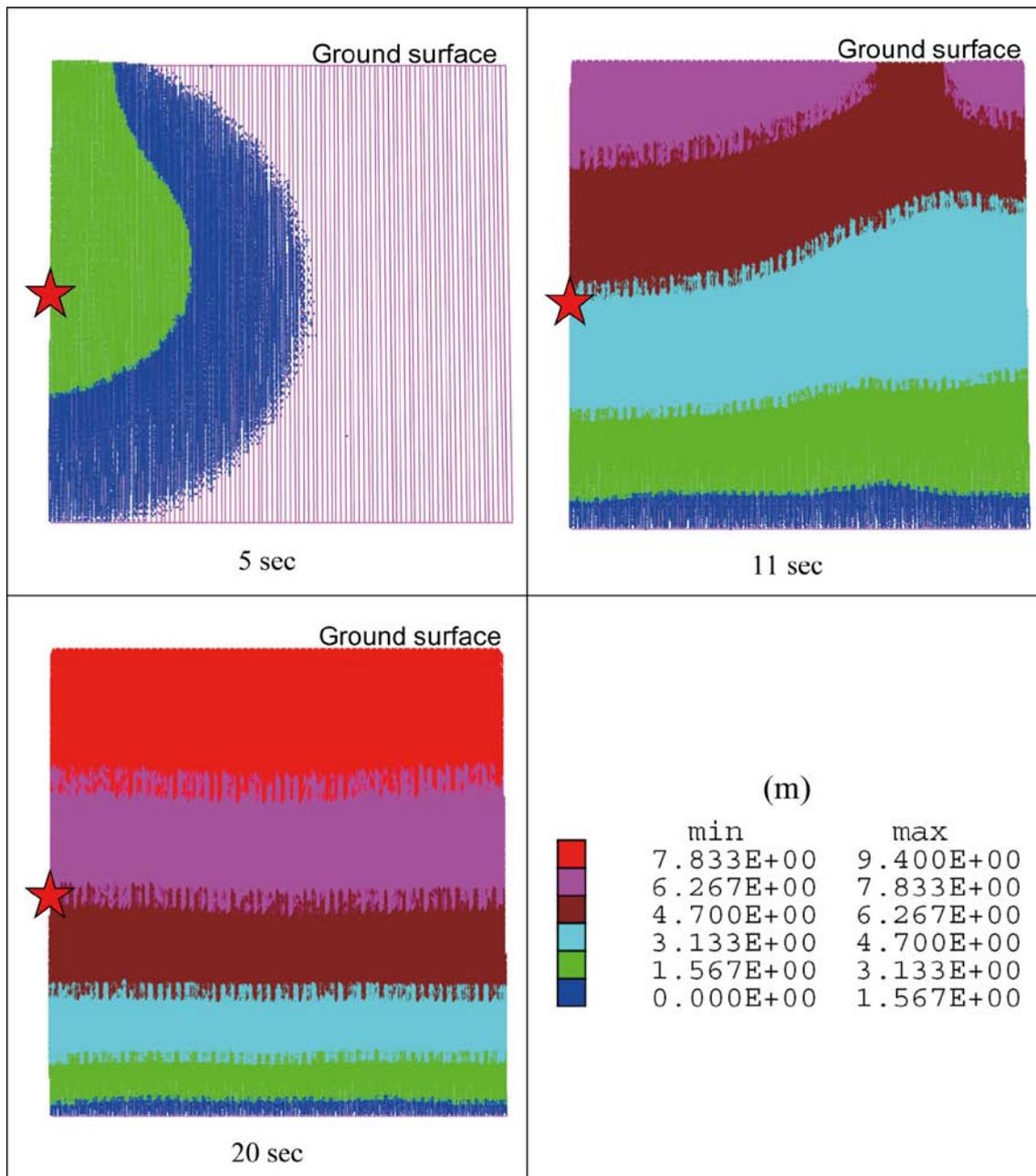
Figure 5-3. *Vector plots showing primary fault slip at three instances of time in the M7_Str4_tfBASE_rt05 model. The vectors are coloured according to their magnitudes. The star indicates the hypocentre.*
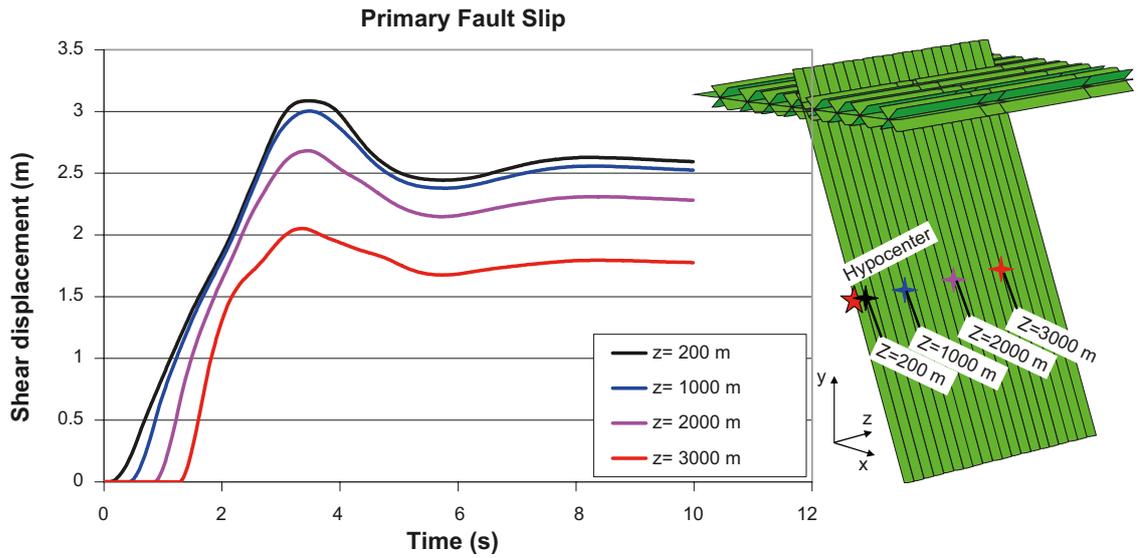
Figure 5-4. *Temporal development of primary fault slip at four points at hypocentre depth in the M6_Str1_tfBASE_rt05 model. The points are located at different distances from the hypocentre.*
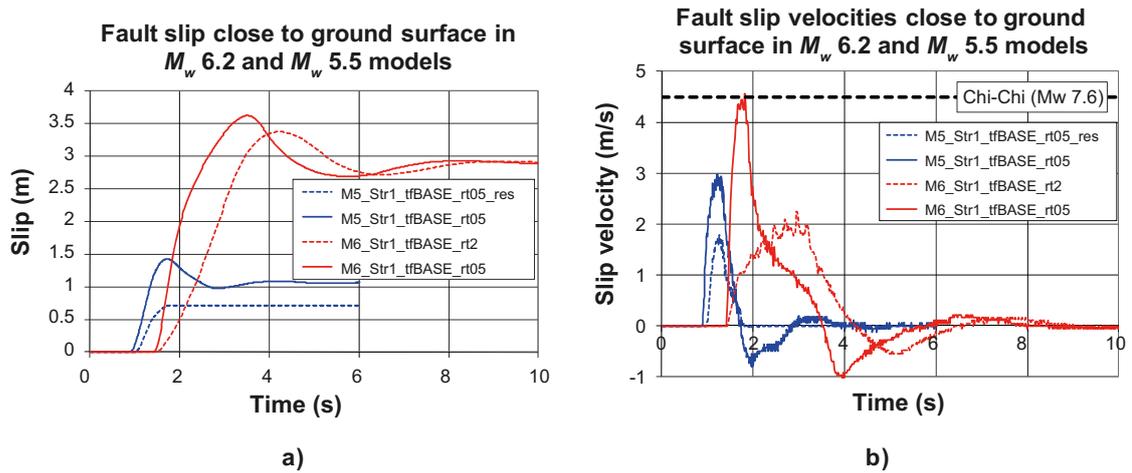
Figure 5-5. *Results from M_w 5.5 and M_w 6.2 models. a) Temporal development of primary fault slip close to the ground surface. b) Primary fault slip velocities close to ground surface. The largest slip velocity reported for the 1999 Chi-Chi earthquake /Ma et al. 2003/ is indicated by the dashed black line.*

Figure 5-5 shows results from two M_w 6.2 models and two M_w 5.5 models (with fault dip angle 70°). The M_w 6.2 models are identical except for the different values of strength reduction time, rt (cf. Section 4.8). The M_w 5.5 models are identical except for the fault residual friction ($\mu = \tan 6°$) applied in one of the models. Figure 5-5a shows the temporal development of primary fault slip close to the ground surface. Figure 5-5b shows the temporal development of fault slip velocities at the same location. The following can be observed:

- *M_w 6.2 models:* The model with $rt = 0.5$ s has a peak slip velocity that is close to what has been estimated for the 1999 Chi-Chi earthquake /Ma et al. 2003/. Thus, the velocity in this model can be regarded as relatively high. Therefore, the corresponding dynamic effects on the surrounding continuum can be regarded as strong. The model with the longer strength reduction time ($rt = 2$ s) has a significantly reduced peak slip velocity and a minor reduction of the peak slip value. Since both models have zero residual strength, the amount of resulting slip is the same.

- *M_w 5.5 models:* The M_w 5.5 models have much lower slip velocities than the M_w 6.2 model (with $rt = 0.5$). The amount of slip is also much smaller. This is an effect of the smaller rupture area in these models. When the M_w 5.5 models are compared it becomes clear that the residual strength applied in one of them is important for the model behaviour. The residual shear strength significantly reduces both slip velocity and the total amount of slip. In addition, oscillations are absent in the model with an assigned residual primary fault shear strength.

Figure 5-6 shows a plot of resulting primary fault slip versus depth along a scanline at z = 0 in eight models. The models represent different fault geometries and initial stress conditions. Two of the models have a residual fault strength corresponding to a friction angle of 6°. The following can be observed:

- The maximum slip is located at the ground surface and range between 0.7 m and 13 m. The amount of slip and its distribution along the fault is governed by the fault geometry, but also by the initial stresses. The M7_Str2_tfBASE_rt05 and M7_Str3_tfBASE_rt05 models, for instance, have the same fault geometry and same average initial shear stress (stress drop). However, since the initial shear stresses are differently distributed over the fault plane (cf. Figure 4-19), there is a significant difference in the maximum slip at the ground surface.

- Fault residual frictional strength appears to have little importance for gently-dipping faults whereas it has large importance for steeply-dipping ones: The slip in the M5_Str1_tfBASE_rt05_res model is reduced significantly compared to what is found in the M5_Str1_tfBASE_rt05 model whereas the slip in the M5_Str1_tfALT2_rt05 and M5_Str1_tfALT2_rt05_res models (with fault dip angle 30°) are effectively equal (cf. Table 5-1). Due to the anisotropic stress conditions assumed here (i.e. with the major horizontal stress larger than the vertical stress), steeply-dipping faults (which are in high compression) are more sensitive to residual fault frictional strength variations than sub-horizontal ones (which are in low compression).

- The majority of the curves have a (nearly) vertical tangent for slip = 0. This is caused by the elastic representation of the continuum. For faults with zero residual strength the propagating rupture is abruptly arrested at the lower edge of the pre-defined rupture area and the slip drops rapidly to zero, whereas the slip may taper off more gently if the fault has residual friction. For the gently-dipping fault the slip-depth relations are almost identical for the two cases (friction 0° and 6°). This is presumably because of the low normal stress (i.e. friction is not as important as for steeply-dipping faults, cf. previous point).
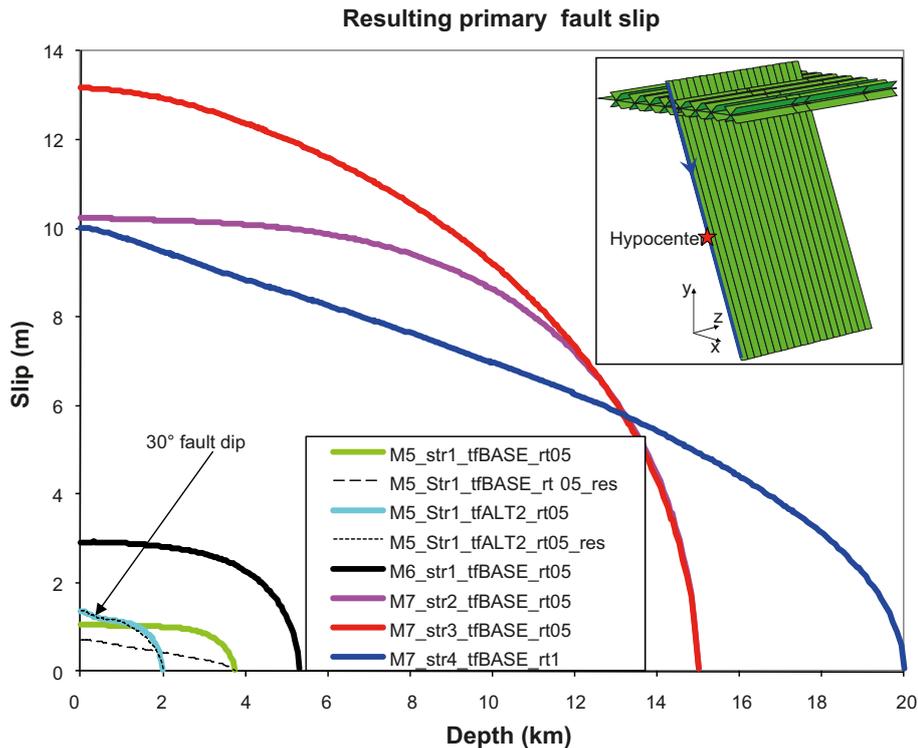
**Figure 5-6.** *Resulting primary fault slip along the scanline indicated by the inset.*

5.2 Rock deformations and stress changes

Figure 5-7 and Figure 5-8 show rock deformation vector plots at different time steps in the M6_Str1_tfBASE_rt05 and M7_Str4_tfBASE_rt05 models. The vector lengths and colours are set according to the vector magnitudes. The larger number of vectors in some regions is due to the presence of denser mesh geometry near areas of interest. The plots are captured in vertical viewing planes close to the hypocentre. As also seen in Figure 5-2 and Figure 5-3, the rupture is initiated at the hypocentre and then propagates along the fault plane. The plots also show that the resulting displacements at the model boundaries are small. The maximum x-displacements at the vertical boundaries are about 0.15 m in M6_str1_tfBASE_rt05 and 0.08 m in M7_str4_tfBASE_rt05. This suggests that the model boundaries are located far enough away to have a negligible influence on the central regions of the models. (Note the model lengths are conditioned to the magnitudes, and to the expected maximum fault slip, meaning that the difference in these boundary displacements is not significant of anything of importance. The point is just to establish that they are small in relation to the model dimensions).

The rock deformations illustrated in Figure 5-7 and Figure 5-8 are accompanied by extensive stress changes in the model. An example of this is shown in Figure 5-9, which shows stress changes caused by the earthquake in a vertical section at repository depth. The section is located 600 m from the symmetry plane in the M6_str1_tfBASE_rt05 model. Positive values indicate compressive stress reduction (stress relaxation). The major stress changes take place in the horizontal direction and amount to 10 MPa on average at this location in the model (middle). In the vertical direction, there are minor stress changes of a few MPa (bottom). The reduction of horizontal stresses means that the stress anisotropy is reduced significantly, which works to increase the target fracture stability. This is further discussed in Section 5.3.
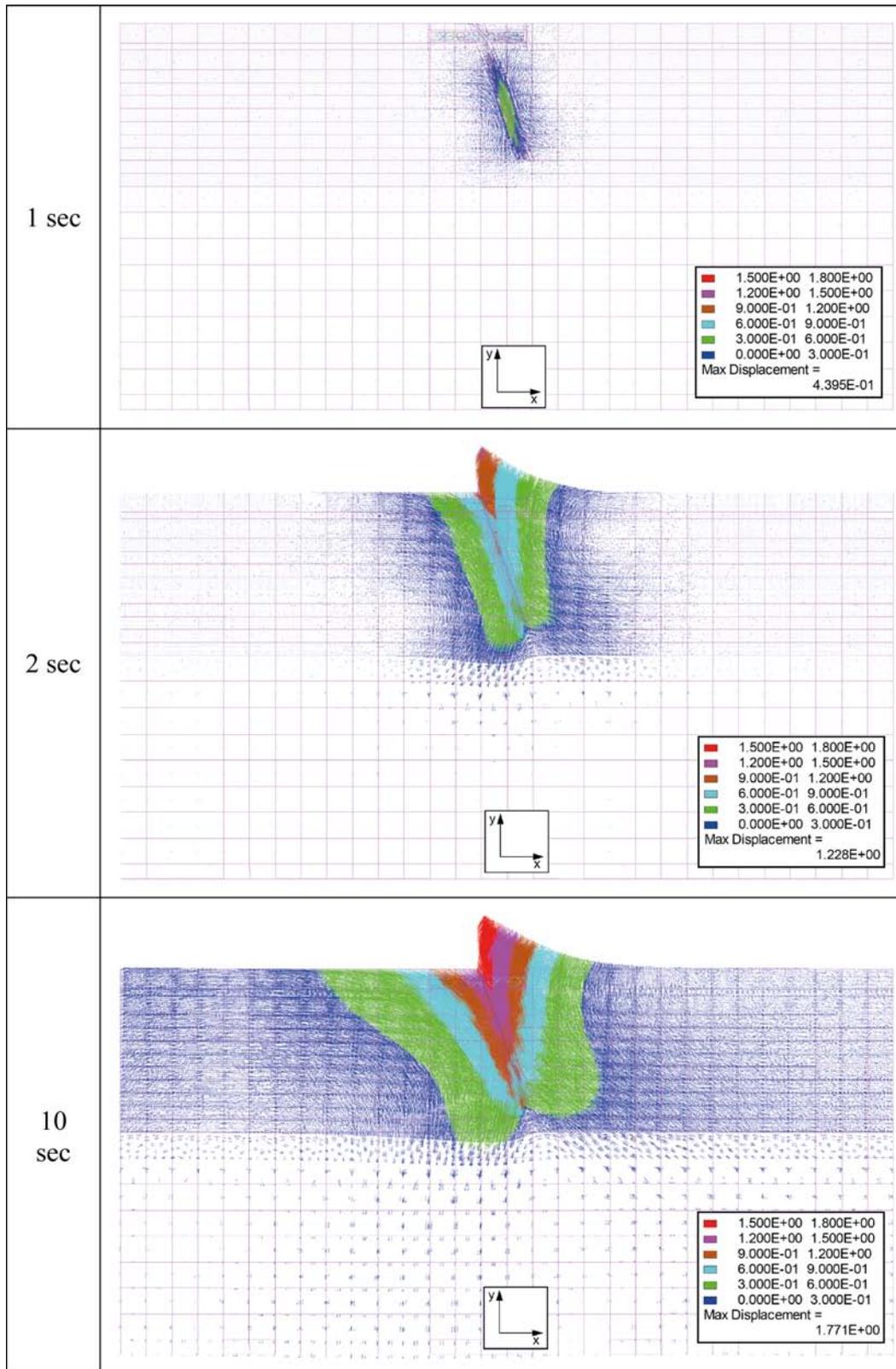
Figure 5-7. *Vector plots showing rock deformations in a vertical section close to the symmetry plane at three instances of time in M6_str1_tfBASE_rt05. The vector lengths and colours are set according to their magnitudes.*
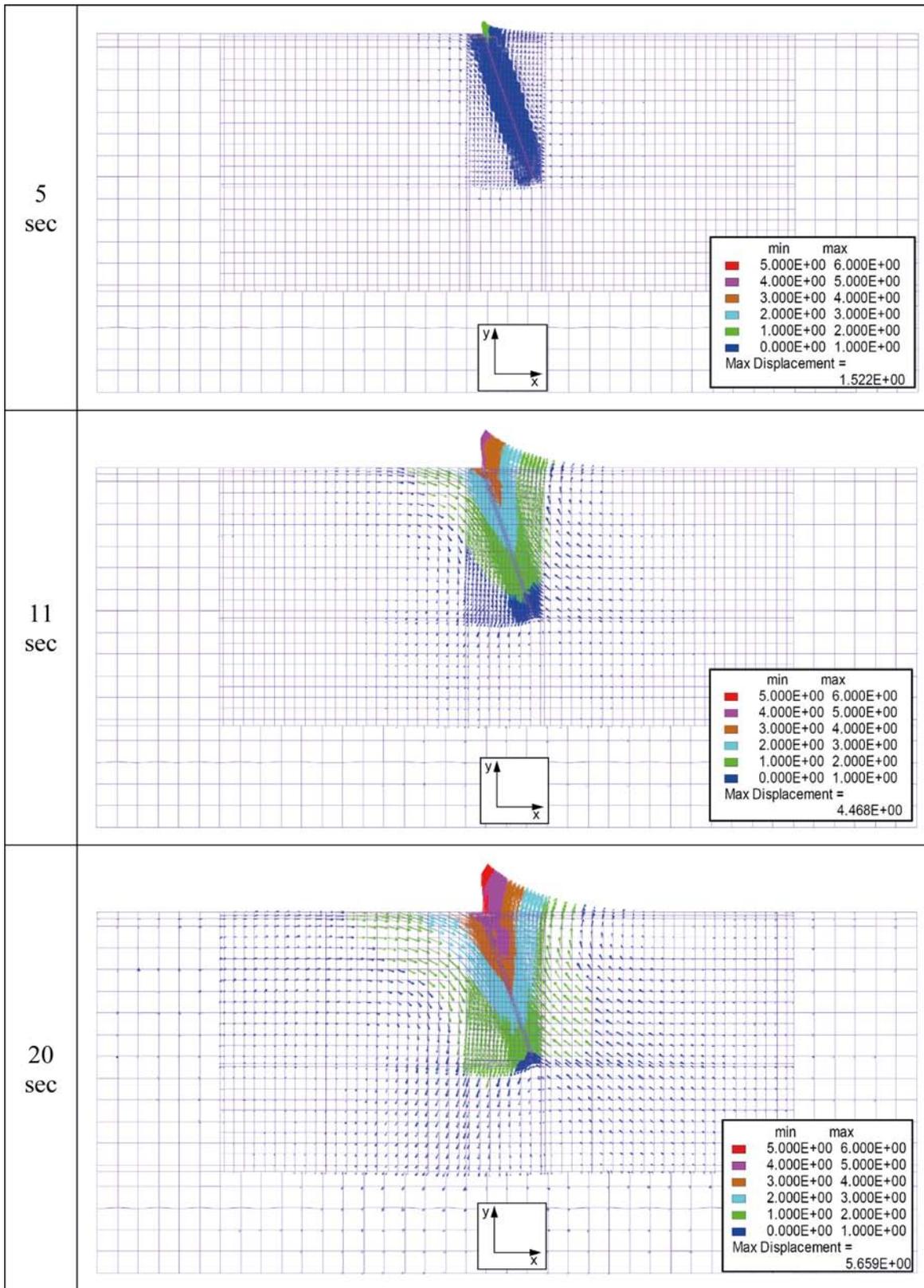
Figure 5-8. *Vector plots showing rock deformations in a vertical section at three instances of time in M7_str4_tfBASE_rt05. The vector lengths and colours are set according to their magnitudes.*

|	
Location of vertical viewing plane	600 m Stress changes calculated as $$\Delta\sigma_{ij} = \sigma_{ij}(t=10) - \sigma_{ij}(t=0)$$
Stress changes plotted as principal stress vectors	
Contours of σ_{xx} changes	
Contours of σ_{yy} changes	
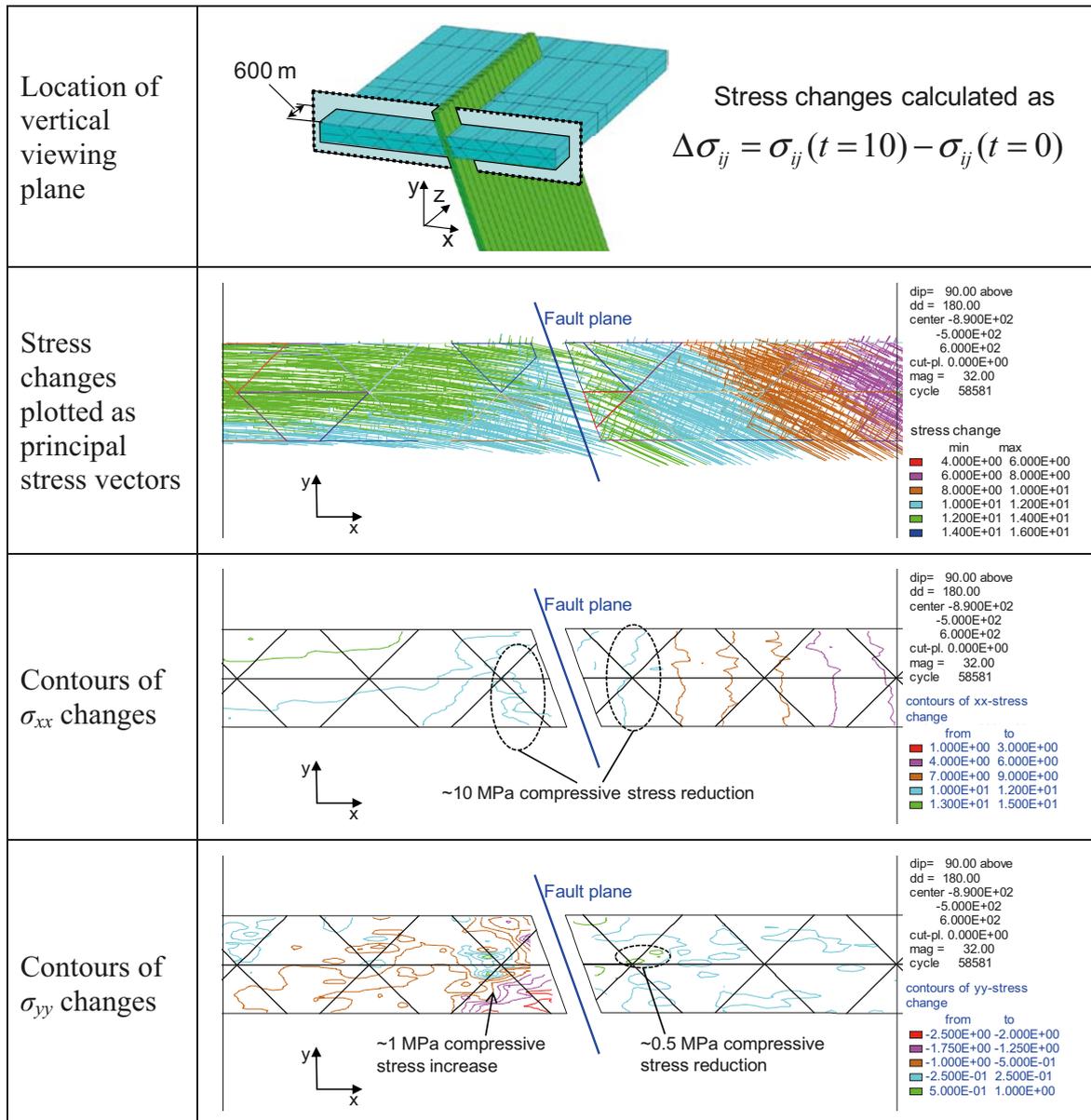
Figure 5-9. *Stress changes at 500 m depth in M6_str1_tfBASE_rt05 calculated as the difference between the stresses at t = 0 s and t = 10 s. The vertical viewing plane is located at z = 600 m, i.e. between target fractures. Positive values indicate compressive stress reduction (stress relaxation) and negative values indicate compressive stress increase.*

5.3 Target fracture stability

As shown in the previous section, a rupture event (earthquake) along the primary fault results in a relaxation of horizontal stresses, which in turn leads to less anisotropic stress conditions in the model and a greater stability of dipping target fractures (located away from the fault's vertical edge).

Figure 5-10 shows a Mohr's circle diagram illustrating the stresses corresponding to the Stress1 and Stress2 initial stress states (black semicircle) at a depth of 500 m. Note that these stress states are equal at 500 m depth but differ at other depths (cf. Sections 4.9.4 and 4.10.4). In the same diagram there are also red semicircles, which illustrate final stress states on both sides of the fault in the M6_str1_tfBASE_rt05 model. The final stresses were picked at 200 m from the primary fault and 600 m from the symmetry plane. The initial stability margin for fractures dipping 45° in the σ_H–σ_v plane is about 2 MPa, and for fractures dipping ~ 30° it is close to zero. After the earthquake, σ_H has been reduced while σ_v is effectively unchanged. This relaxation of the horizontal stress results in a net increase in fracture stability. For fractures dipping at 45° the stability margin now is in the range of 3–4 MPa.

Figure 5-11 is a Mohr's circle diagram illustrating the initial stresses at 500 m depth in the Stress3 and Stress4 initial stress states (black semicircle). These two stress states are equal at 500 m depth but differ at other depths (cf. Section 4.10.4). In these stress states, σ_H is larger than in the Stress1 and Stress2 stress states shown in Figure 5-10. This results in an initial instability for fractures with a 30° dip and a stability margin of approximately 0.6 MPa for fractures with dips of 45°. The instability of gently-dipping fractures means that they will move and stop at the stability limit; as such, they will be in a state of failure and sensitive to changes in the stress field caused by for instance an earthquake. The diagram also shows red semicircles that illustrate the resulting stress states at both sides of the fault in the M7_str4_tfBASE_rt1 model. The relaxation of σ_H gives a net increase of the stability margin. For fractures with a 45° dip, the relaxation of σ_H results in an increase of 3 MPa and 1.5 MPa in the footwall and hanging wall, respectively.
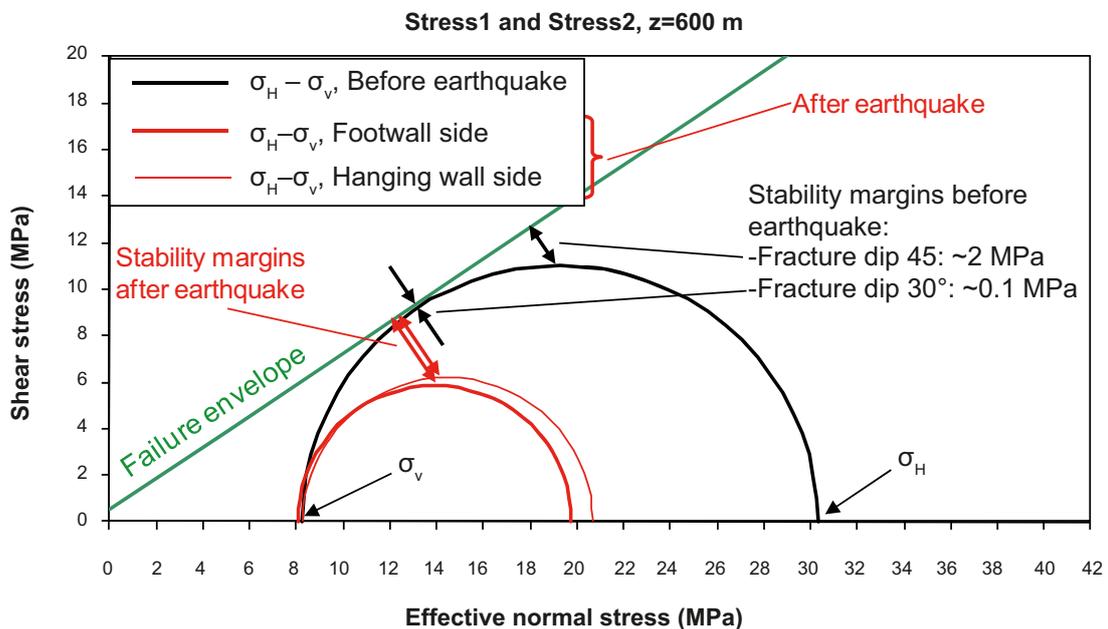
Figure 5-10. *Mohr circle diagram illustrating the initial stresses at 500 m depth for the Stress1 and Stress2 initial stress states along with resulting stress states after earthquake at a point 600 m from the symmetry plane in the M6_str1_tfBASE_rt05 model. The green line is the failure envelope for the target fractures.*

Stress3 and Stress4, z=600 m
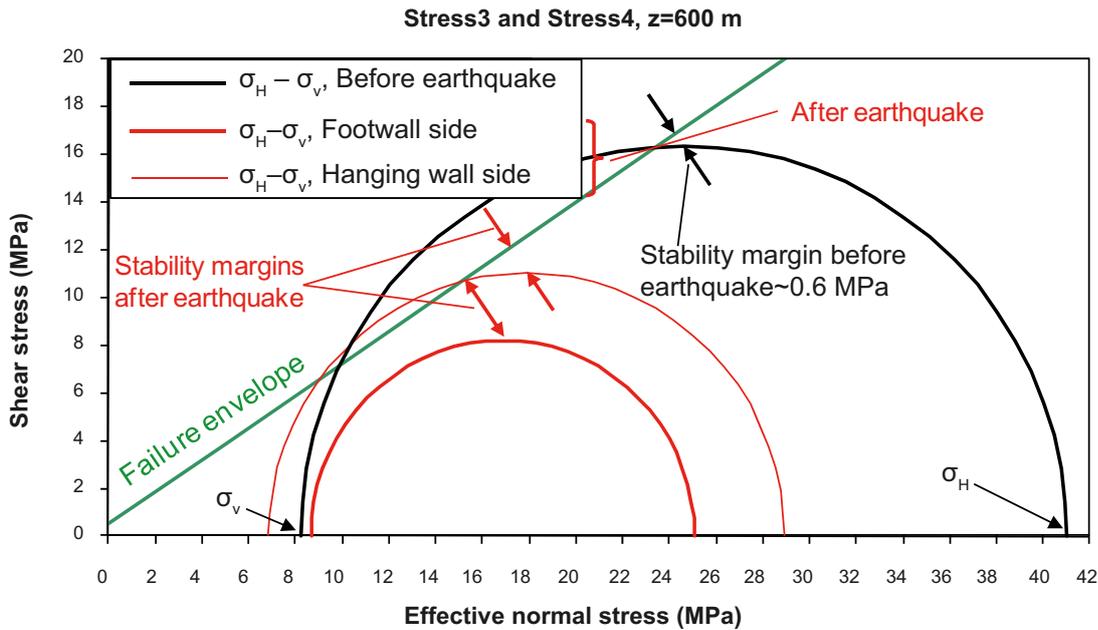
Figure 5-11. *Mohr circle diagram illustrating the initial stresses at 500 m depth for the Stress3 and Stress4 initial stress states along with resulting stress states at a point 600 m from the symmetry plane in the M7_str4_tfBASE_rt1 model. The green line is the failure envelope for the target fractures.*

The discussion above deals with stress changes at positions far from the edge of the fault, where an earthquake produces stress relaxations, with a corresponding increase in target fracture stability. However, close to the edges of the fault, the fault movement may increase deviatoric stresses, which potentially will decrease target fracture stability. This is illustrated by the Mohr's circle diagram in Figure 5-12. The resulting stresses (red semicircles) are picked from the same M_w 6.2 model as in Figure 5-10, but at a location close to the primary fault edge (z = 4,000 m). The circles indicate that the stability limit is exceeded for fractures within a 50° dip range.

The Mohr's circle diagrams shown in Figure 5-10 and Figure 5-11 indicate that target fractures located far away from the primary fault's vertical edge become more stable due to the fault movement, whereas fractures close to the edge become less stable. This means that, if only the quasi static stress redistribution governed the fracture displacements, fractures far from the fault edge should not slip in response to the earthquake. However, it turns out that the seismic waves radiating from the primary (source) fault are important to the stability of differently-oriented fractures. Figure 5-13 shows the temporal development of shear stress, σ_{ss}, and effective normal stress, $\sigma_{n,eff}$, on planes oriented as target fractures. The stresses are recorded at three points located in the continuum between the target fractures at a distance of 200 m from the fault in the M6_str1_tfBASE_rt05 model. No slip is permitted at the recording points. Along with the stress curves the diagrams show the shear strength for a hypothetical fracture at the actual location. The shear strength is a function of the normal effective stress according to

$$c + \sigma_{n,eff}\tan\varphi = 0.5 + \sigma_{n,eff}\tan 34° \qquad\qquad \text{Equation (5-1)}$$
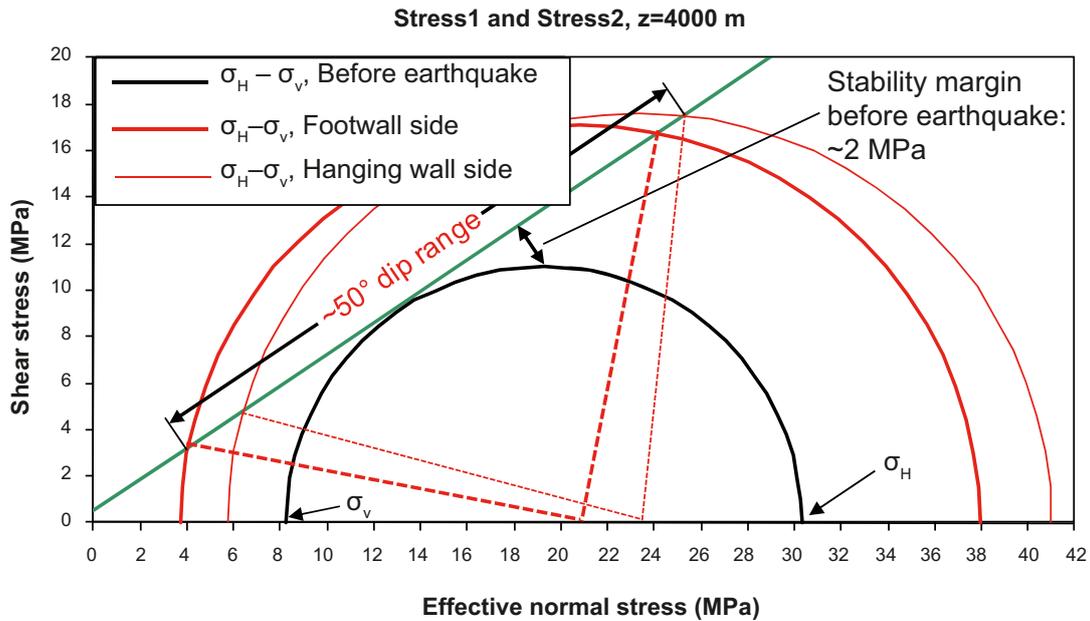
Figure 5-12. *Mohr circle diagram illustrating the Stress1 and Stress2 initial stress states along with resulting stress states at a point 200 m from the primary fault and 4,000 m from the symmetry plane in the M6_str1_tfBASE_rt05 model. The green line is the failure envelope for the target fractures.*

Figure 5-13a and Figure 5-13b show stress histories recorded in two differently-oriented planes close to the fault edge (z = 4,000 m). The other four diagrams (Figure 5-13c-f) show recordings at points far from the edge (z = 600 m) in differently-oriented planes on both sides of the fault. The sketches to the right of each diagram indicate the location and orientation of the plane in which the stresses were recorded. An arrow indicates the dip direction for dipping planes, whereas an "H" indicates a horizontal plane. All dipping planes have a dip angle of 45°. The following can be observed:

- Close to the fault edge the permanent deformations result in permanent instability (Figure 5-13a, Figure 5-13b). This is particularly true for the horizontal plane (Figure 5-13a). The initial stability margin in this plane is about 5 MPa, but after the fault movement the shear stress exceeds the potential fracture strength by about 15 MPa.

- Between about 1.2 s and 1.8 s after rupture initiation, there is an increase in shear stress and a simultaneous decrease in normal stress in three of the cut planes in the primary fault footwall (Figure 5-13c, Figure 5-13d and Figure 5-13e). The normal stress change reduces the shear strength to a level below that of the acting shear stress for about 0.5 s. During that time, a fracture placed at this location would slip. This indicates that dynamic stress oscillations may contribute to induced target fracture slip, i.e. that dynamic effects may trigger slip in fractures that would be stable according to the static stress state. A static analysis would not capture slip occurring as result of such a temporary loss of strength.

- The planes shown in (Figure 5-13e) and (Figure 5-13f) have the same orientation but are located on different sides of the primary fault. This causes their stress histories to differ significantly. In the plane in the footwall (Figure 5-13e) there is a short period of instability, but in the plane in the hanging wall (Figure 5-13f) the shear stress never exceeds the shear strength.
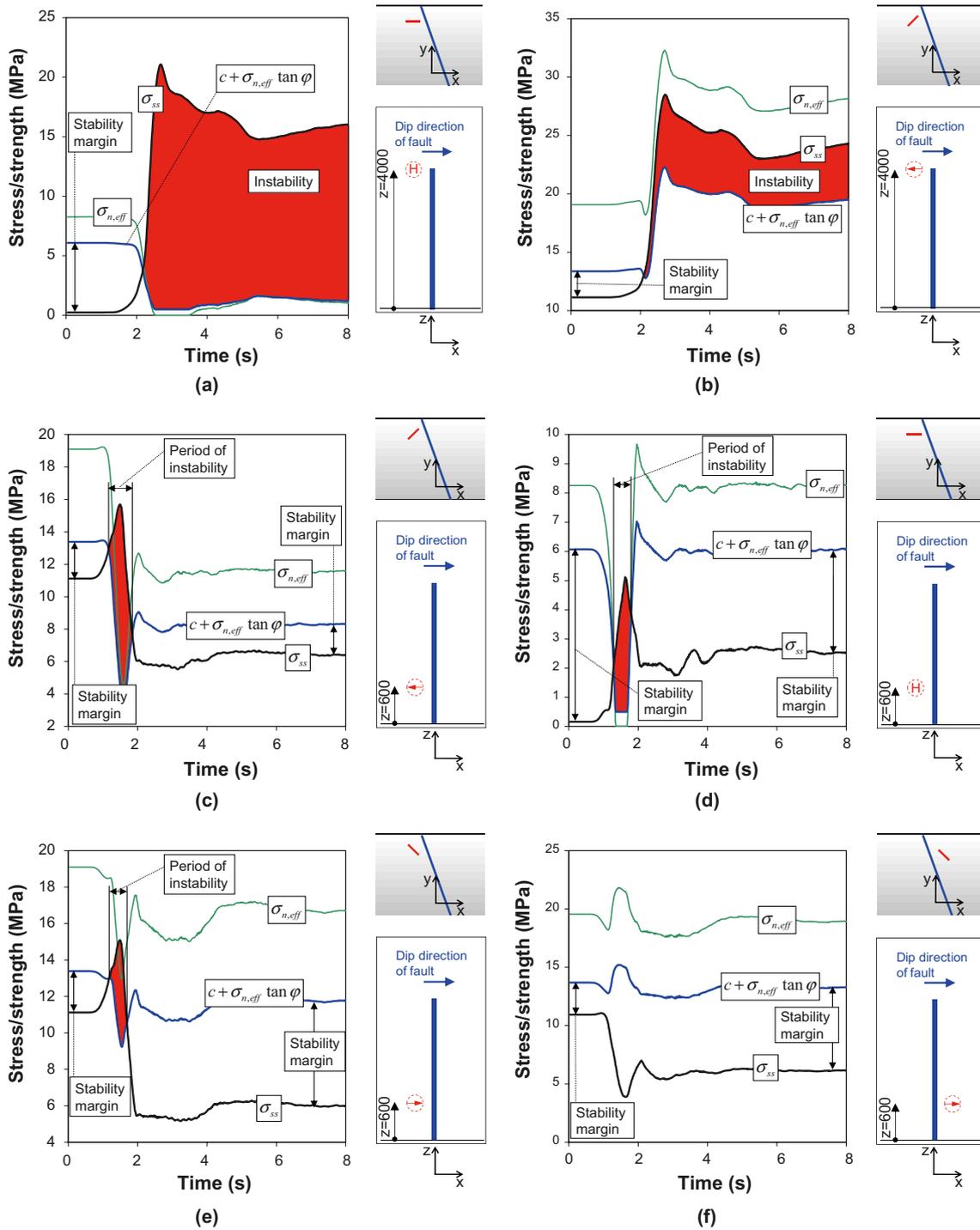
Figure 5-13. *Stress histories and corresponding shear strength of six hypothetical fractures at different points 200 m from the primary fault in the M6_str1_tfBASE_rt05 model. The sketches to the right of each diagram indicate the location and orientation of the plane in which the stresses were recorded. The blue line represents the primary fault. An arrow indicates dip direction for a dipping plane whereas "H" indicates a horizontal plane.*

5.4 Induced target fracture shear displacements

The amount of induced shear displacement in the target fractures is the main result of this study. The first subsection of Section 5.4 describes the temporal development of target fracture shear displacement at different distances from the fault in one M_w 5.5 model and in one M_w 6.2 model. The next subsection after that presents the maximum induced shear displacements at two different distances away from the primary fault in all twenty models, which represent earthquakes with different moment magnitudes, primary fault geometries, fault slip velocities and average stress drops.

The modelling results show that the primary fault slip velocity is an important parameter that controls the magnitudes of the induced fractures displacements. This is discussed in Section 5.4.3

Both the amount of fracture shear displacement and the shear velocity can be of concern to the canister safety assessment. Since the shear stiffness of the bentonite buffer is rate- dependent, the fracture shear velocity influences the forces that the canister may be subjected to. The rate dependence has been verified by lab tests that have been carried out using shear rates in the range of $5 \cdot 10^{-8}$–1 m/s /Börgesson and Hernelind 2006/. The highest shear velocities found in *3DEC* models considered realistic and conservative are of the order of some hundreds of mm per second. The shear velocity results are presented in Section 5.4.5. In addition to the fracture shear velocity, the sense (i.e. normal or reverse sense of shear) of shearing is also important to the response of the buffer-canister system /Börgesson and Hernelind 2006/. The sense of fracture shear displacement found in the models is presented in Section 5.4.6.

Even though the target fracture radius is set at a constant 150 m in all models analysed during this study, it may be of interest to use the results to estimate induced shear displacements and velocities for fractures of a different size. Section 5.4.7 presents results that show how the amount of induced shear displacement and shear velocity is influenced by the fracture size.

When the probability of canister-fracture intersections is calculated and used as input to the safety assessment, a closed-form solution for the distribution of shear displacement over the fracture area is used /Hedin 2005/. The degree of agreement between this closed-form solution and results from the *3DEC* models is presented in Section 5.4.8.

The last subsection, Section 5.4.9, presents results from a sensitivity analysis where the sensitivity to target fracture shear strength parameter values is studied.

5.4.1 Temporal development of shear displacements

Figure 5-14 through Figure 5-16 show temporal development of induced target fracture shear displacements at three horizontal distances from the primary fault in the M5_Str1_tfBASE_rt05 and M6_Str1_tfBASE_rt05 models. The different response of fractures in the footwall and hanging wall are shown. Results from all target fracture are not included in the plots; only results from the fracture that displaced most are shown. In each figure one fracture orientation is considered. The following can be observed:

- Fractures on both sides of the fault show displacements regardless of their orientation and regardless of whether the net stability margin increased or decreased as a result of the stress redistribution. This is in keeping with the stability analysis made in Section 5.3 and confirms that the dynamic effects are important to the amount of target fracture slip.

- The lower left diagram in Figure 5-15 shows results from the M_w 6.2 model. The fracture at 200 m distance has about the same location as the recording point for the stresses shown in Figure 5-13c, e. The initiation of slip for this fracture coincides in time with the loss of stability that can be observed in Figure 5-13c, e.

- The displacements are generally larger, but not significantly larger, in the M_w 6.2 model. At the smallest distance the M_w 5.5 model actually gives a larger displacement for one orientation at the hanging wall side (Figure 5-15, right). This demonstrates that the earthquake magnitude alone is not decisive of the effects, in particular at short distances from the fault. Also, the results at a particular location depend on the static stress redistributions and on the timing and magnitudes of different stress waves as they reach that location.
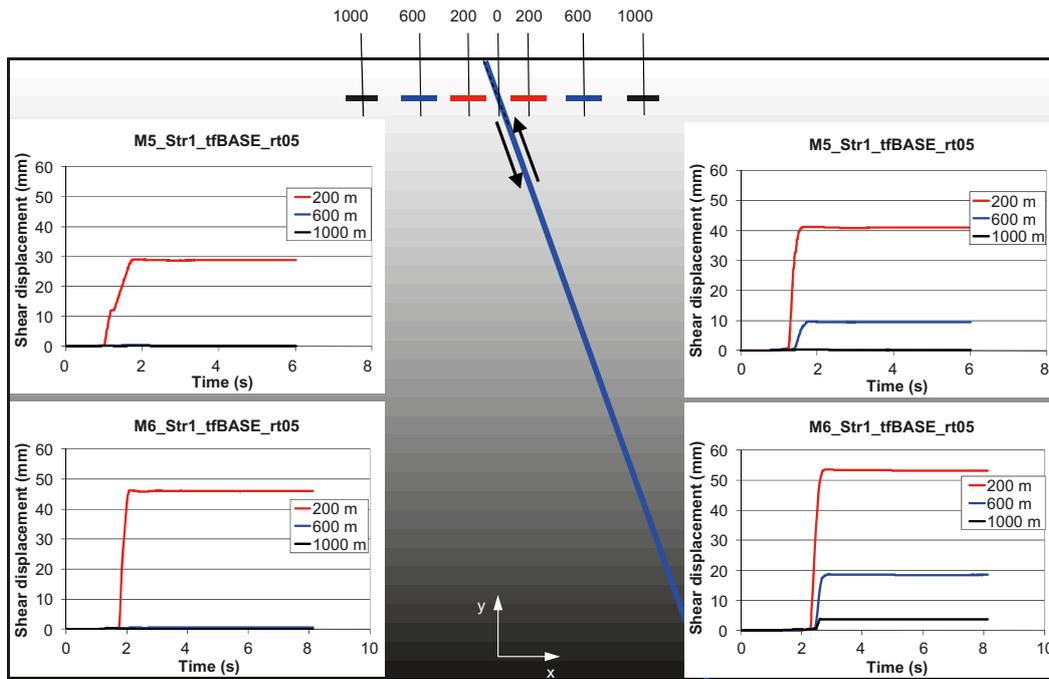
Figure 5-14. *Temporal development of induced target fracture shear displacements at three horizontal distances from the primary fault in the M5_Str1_tfBASE_rt05 and M6_Str1_tfBASE_rt05 models. The plots show displacements on horizontal fractures. Left diagrams: footwall side. Right diagrams: hangingwall side.*
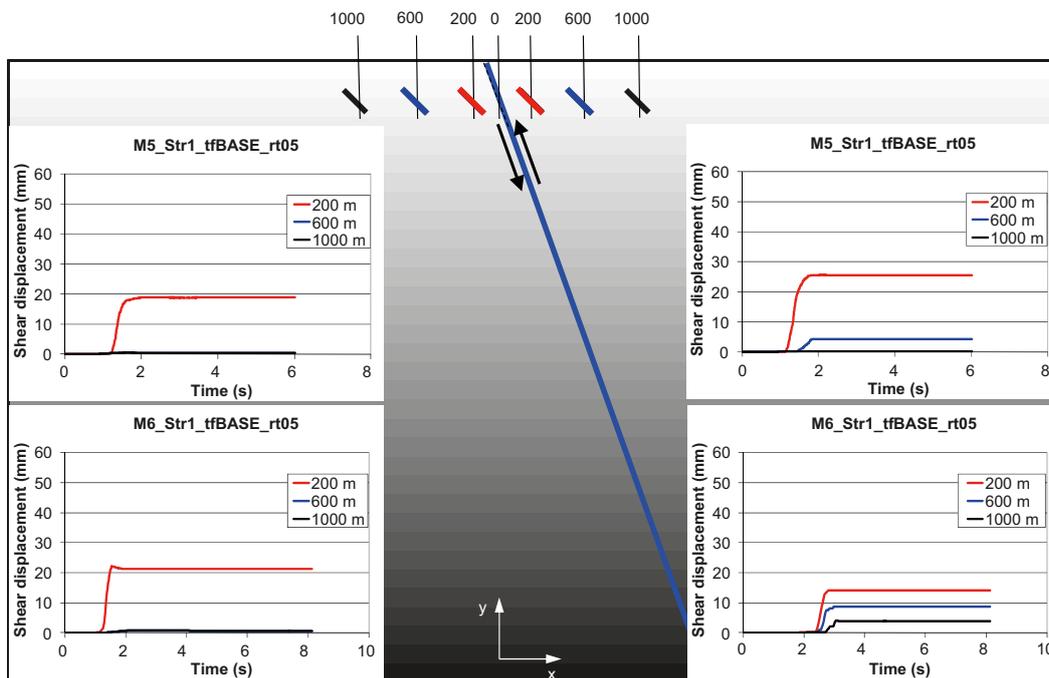
Figure 5-15. *Temporal development of induced target fracture shear displacements at three horizontal distances from the primary fault in the M5_Str1_tfBASE_rt05 and M6_Str1_tfBASE_rt05 models. Dip direction: same as fault dip direction. Left diagrams: footwall side. Right diagrams: hangingwall side.*
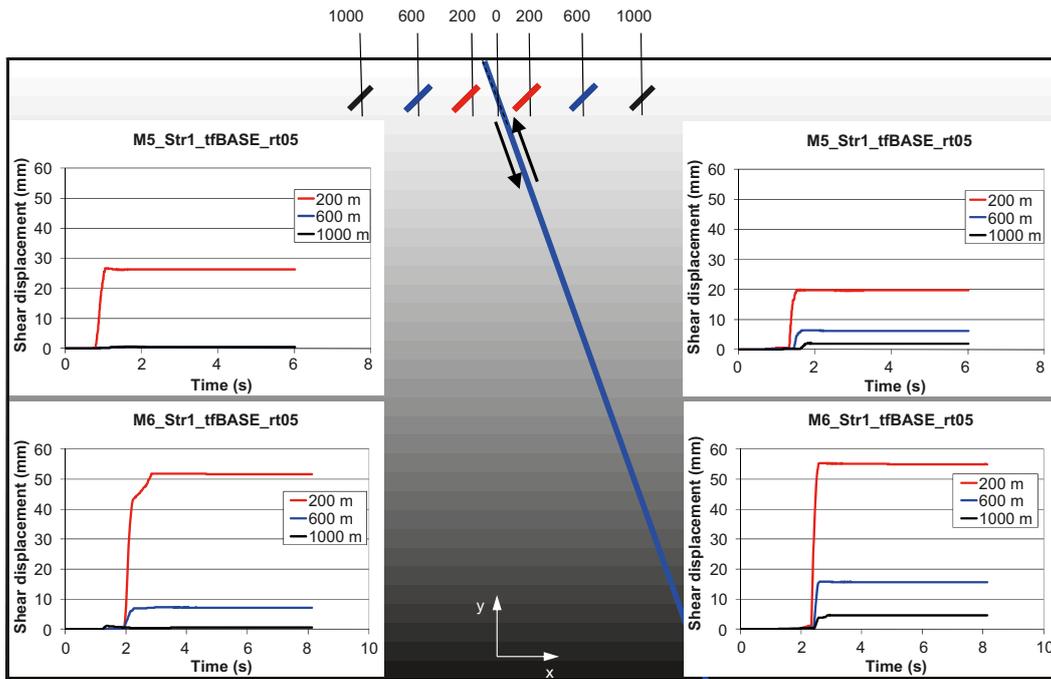
Figure 5-16. *Temporal development of induced target fracture shear displacements at three horizontal distances from the primary fault in the M5_Str1_tfBASE_rt05 and M6_Str1_tfBASE_rt05 models. Dip direction: opposite to fault dip direction. Left diagrams: footwall side. Right diagrams: hangingwall side.*

5.4.2 Target fracture peak shear displacements

This section presents the peak values of target fracture shear displacements from all models. The section is divided into three subsections, each of which present results from the M_w 5.5, M_w 6.2 and M_w 7.5 models, respectively. The results are displayed graphically in Figure 5-17 through Figure 5-20 as cumulative plots of induced target fracture shear displacements. All plots follow the same concept:

- The line colours indicate differences in model assumptions (fault residual strength, fault dip angle, initial stress state and strength reduction time, *rt*) and the presence of excess pore pressure. Note that results from different *3DEC* models with identical model assumptions (albeit with different target fracture configurations) may be represented by one curve.

- The plot symbols indicate target fracture orientations according to the pole plots in the insets (Each plot symbol represents the peak slip of one particular fracture).

- Each plot shows slip distributions for two different fault-target distances.

M_w 5.5 models

Figure 5-17 and Figure 5-18 present results from M_w 5.5 models with fault dip angles 70° and 30°, respectively (The actual magnitude range is M_w 5.3– M_w 5.6). The following parameters are varied: Pore pressure in target fractures (5 and 6 MPa, i.e. zero and 1 MPa above hydrostatic), fault residual shear strength (zero friction and 6° friction), fault dip angle (30° and 70°), target fracture dip (0°, 30° and 45°). The following can be observed:

- Effects of pore pressure assumption: Note that the pore pressure influences the target fracture stability but not the programmed behaviour of the fault (slip velocity, stress drop, moment magnitude etc).
  - In the absence of any excess pore pressure the largest displacement is about 40 mm and is found at 200 m distance in the model with 70° fault dip angle. At 600 m distance the peak displacement in the same model is about 15 mm. At 200 m distance, 90% of the fractures move less than 30 mm. The corresponding number at 600 m distance is 10 mm (Figure 5-17a).
  - Applying the effect of 1 MPa excess pore pressure in the target fractures has a minor influence on the results. The maximum displacement increases from 41 mm to 45 mm, i.e. about 10% (Figure 5-17a).

- Effects of fault residual strength assumption: The fault residual strength may potentially influence the behaviour of the slipping fault (cf. discussion in Section 5.1), with the following consequences for the target fractures:
  - Steeply-dipping fault (dip 70°): The fault residual strength has a large impact on target fracture slip. For example, if the fault is given a residual strength equivalent to a friction angle of 6 degrees, the result is a 75% reduction of the largest fracture displacement (Figure 5-17). This is a consequence of the decrease in fault slip velocity, stress drop and moment magnitude associated with the increase in fault strength. For the strength assumption made here (6 degrees of fault friction), the moment magnitude is reduced from M_w 5.5 to M_w 5.3 (Figure 5-17b). Yet this is a conservatively represented earthquake with a large maximum displacement given the moment magnitude (cf. Figure 6-8, left).
  - Gently-dipping fault (dip 30°): The effects of the fault residual strength is negligible (Figure 5-18). The moment magnitude is M_w 5.6, regardless of fault residual strength assumption (cf. discussion in Section 5.1).

- Effects of fault dip angle: There is a significant influence of the fault dip angle. For the target fracture orientations tested here, the model with 30° fault dip angle gives target fracture slip about half of that found in the model with 70° fault dip (Figure 5-17 and Figure 5-18). One possible explanation is that a gently-dipping fault gives a more effective relaxation of stresses resulting in increased stability for dipping fractures.

- Effects of fracture orientation: There seems to be a tendency that horizontal and gently-dipping fractures move a little bit more than fractures dipping 45° (Figure 5-17a). For very small fractures movements (at larger distances and in model with fault dip 30°) it is not meaningful to distinguish between fractures of different orientations.
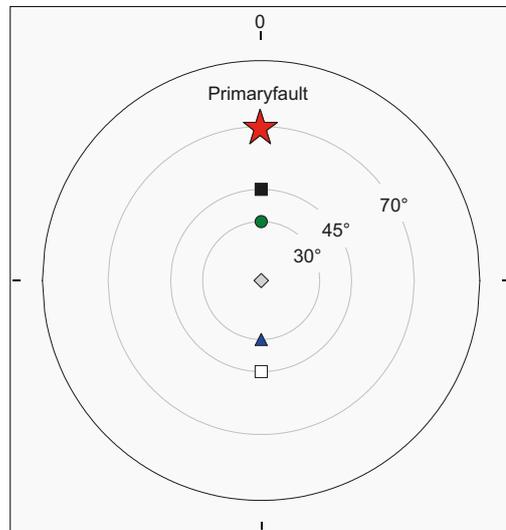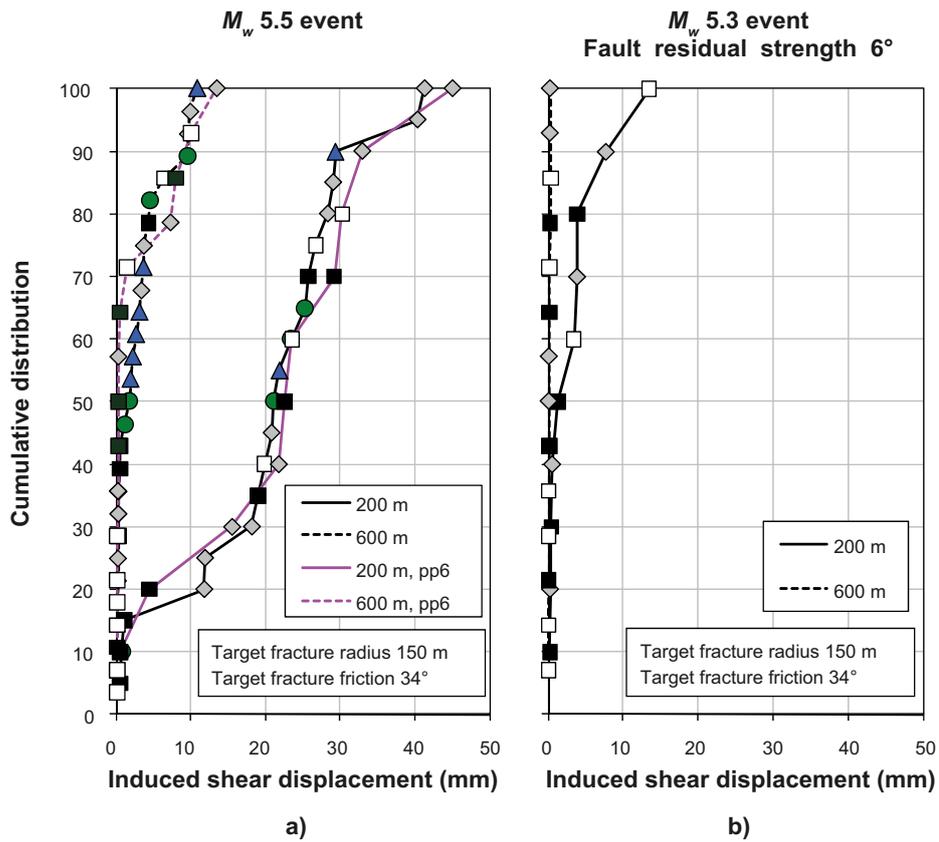
Figure 5-17. *Cumulative distribution of induced target fracture shear displacements at 200 m and 600 m distance from the primary fault in M_w 5.5 models with fault dip angle 70°. The plot symbols denote target fracture orientation according to the pole plot in the inset (Each plot symbol represents the result of one particular fracture). a) Models with zero residual fault shear strength. In one of the models a one MPa pore overpressure is applied (giving a total of 6 MPa). b) Model with residual fault shear friction angle 6°.*
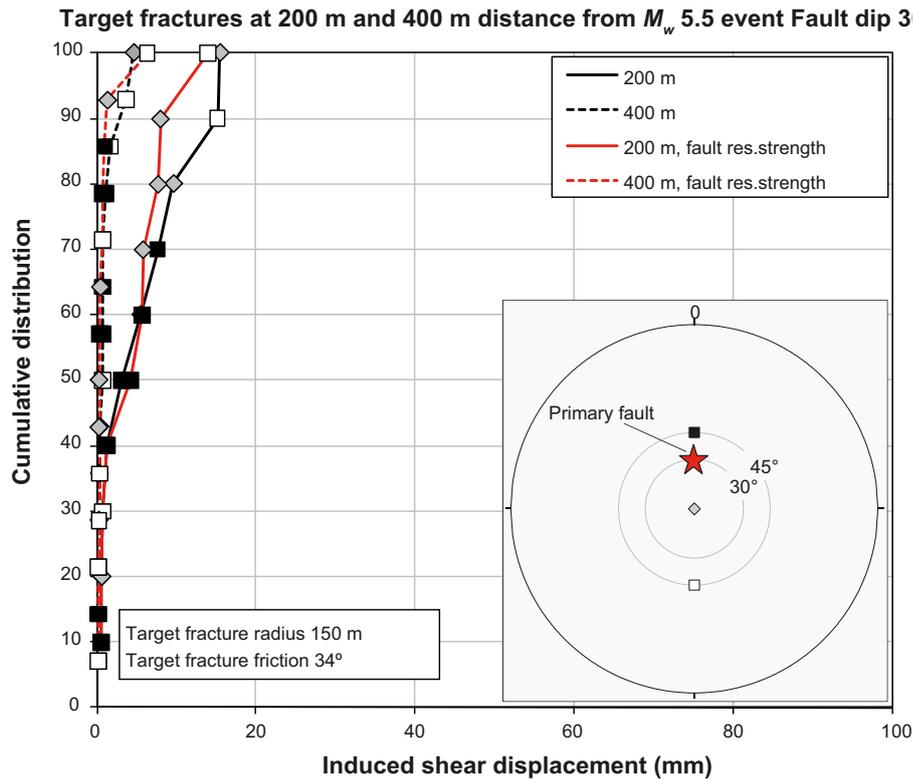
Figure 5-18. *Cumulative distribution of induced target fracture shear displacements at 200 m and 400 m distance from the primary fault in M$_w$ 5.5 models with fault dip angle 30°. There are two sets of curves: one for the model with fault residual strength and one for the model without. The plot symbols denote target fracture orientation according to the pole plot in the inset (Each plot symbol represents the result of one particular fracture).*

M$_w$ 6.2 models

The results from the M_w 6.2 models are shown in Figure 5-19. The following parameters are varied: strength reduction time, *rt* (Values are 0.5 s and 2 s. This parameter contributes to control the fault slip velocity), target fracture orientation (dip 0° and 45°, strike 0°, 45°, 135°, 180°, 225° and 315°). The following can be observed:

- Effects of *rt* assumption: The strength reduction time has a significant and systematic importance. For similarly-oriented fractures the slower ramping scheme (*rt* = 2 s) gives 20–30% smaller fracture slip. This is due to the lower fault slip velocity obtained with the slower ramping scheme. For the fast ramping scheme (*rt* = 0.5 s) the maximum peak slip exceeds the 0.05 m canister damage threshold. However, the fast ramping scheme seems to give unrealistically high fault slip velocities (cf. discussions in Sections 6.1 and 7.1).

- Effects of target fracture orientation: Contrary to the results pictured for the M_w 5.5 models in Figure 5-17 there is no systematic dependence of fracture orientation on fracture slip.
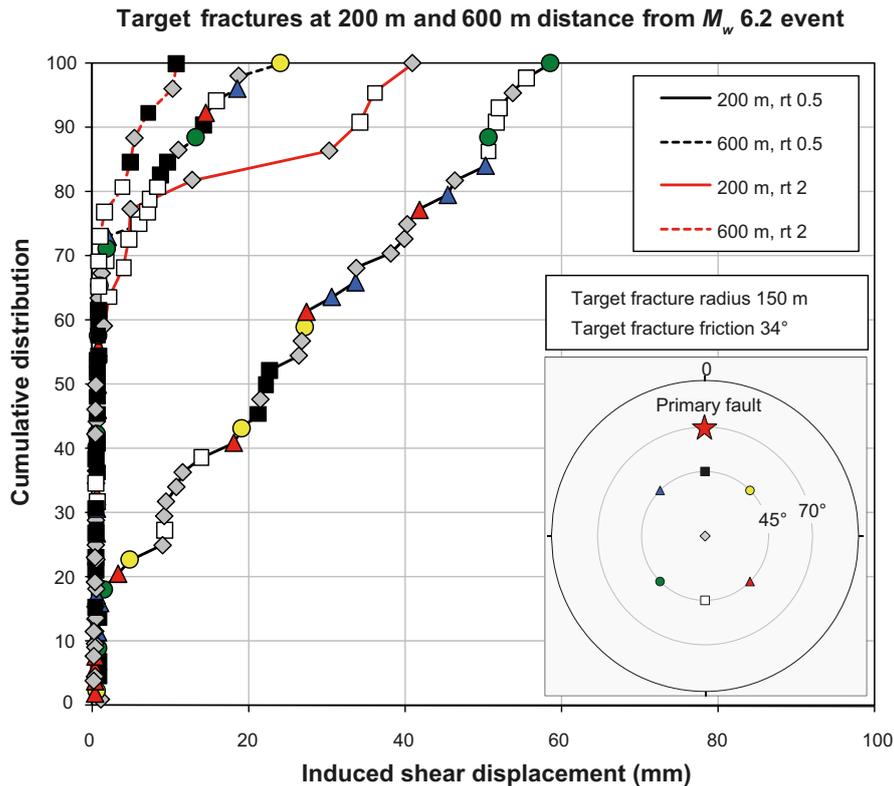
Figure 5-19. *Cumulative distribution of induced target fracture shear displacements at 200 m and 600 m distance from the primary fault in M_w 6.2 models. The different curves correspond to different strength reduction times (schemes for ramping down the fault strength during the rupture). The plot symbols denote target fracture orientation according to the pole plots in the inset (Each plot symbol represents the result of one particular fracture).*

M_w 7.5 models

Figure 5-20 presents results from M_w 7.5 models. The following parameters are varied: Pore pressure in target fractures (5 and 6 MPa, i.e. zero and 1 MPa above hydrostatic), strength reduction time, *rt* (Values are 0.5 s, 1 s and 2 s. This parameter contributes to control the fault slip velocity), target fracture dip (0°, 30°, 45° and 60°), target fracture strike (0°, 45°, 180° and 225°), initial stress field (Stress2, Stress3 and Stress4, cf. Section 4.10.4). For the Stress2 and the Stress3 models the fault width is 16 km whereas it is 21 km for the Stress4 models. The fault width was however modified just to obtain the intended moment magnitude. The following can be observed:

*   Effects of pore pressure assumption: For equally-oriented fractures the excess pore pressure gives limited increase in slip. (Note that the pore pressure influences the target fracture stability but not the programmed behaviour of the fault).

*   Effects of *rt* assumption: The strength reduction time has a significant and systematic importance. For similarly-oriented fractures a slower ramping schemes (*rt* = 1 s instead of 0.5 s) gives 40–50% smaller fracture slip. This is due to the lower fault slip velocity obtained with the slower ramping scheme. For the fast ramping scheme (*rt* = 0.5 s) the maximum peak slip exceeds the 0.05 m canister damage threshold. However, the fast ramping scheme gives unrealistically high fault slip velocities (cf. discussions in Sections 6.1 and 7.1), meaning that these particular results are not relevant for the risk assessment.

*   Effects of target fracture orientation: Steeply-dipping fractures (dip 60°) slip systematically less than fractures with smaller dip angles. In the 0°–45° dip range there are no clear differences. Similarly, there is no clear influence of the fracture strike.

*   Effects of initial stress field: The initial stress field appears to have a significant influence. The stress field at the repository depth influences the target fracture's initial stability as discussed in Section 5.3. The different assumptions regarding the initial stress field at large depths were made only to check whether the details of the conditions at large depths would have any unexpected consequences. The differences seen here are all due to the resulting differences in fault slip velocity, cf. Section 5.4.3.
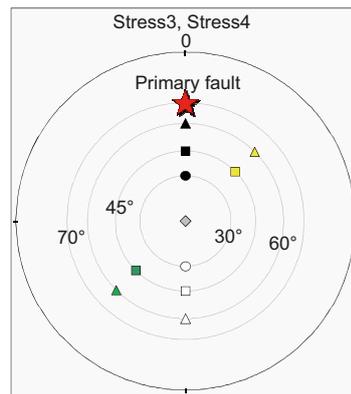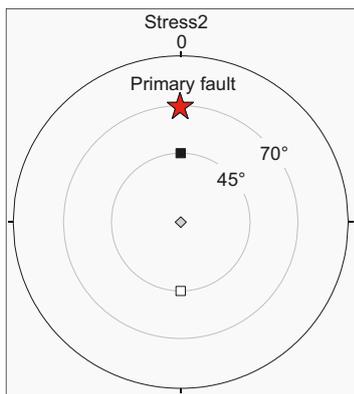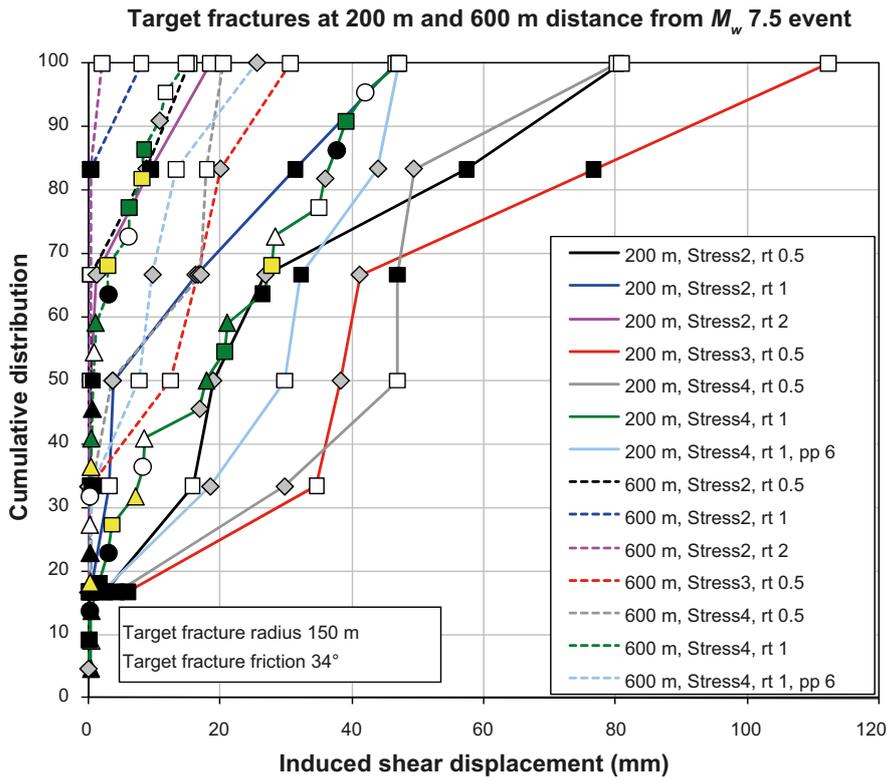
Figure 5-20. *Cumulative distribution of induced target fracture shear displacements at different distances from the primary fault in M_w 7.5 models. The line colours correspond to different modelling assumptions. The plot symbols denote target fracture orientation according to the pole plot (Each plot symbol represents the result of one particular fracture).*

5.4.3 Importance of primary fault slip velocity

According to the results presented in Figure 5-19 and Figure 5-20 there is a strong correlation between the strength reduction time, rt, and the amount of induced target fracture shear displacement. The strength reduction time controls the ramping scheme used to represent the rupture and appears to influence the fault slip velocity. This means that the fault slip velocity is a key output parameter for which it, contrary to the model parameter rt, is possible to compare *3DEC* results with records from real earthquakes.

Figure 5-21 shows the maximum induced shear displacement for target fractures of different orientations versus maximum primary fault slip velocity. Results from M_w 5.5, M_w 6.2 and M_w 7.5 models with different stress drops and fault geometries were used. The left part includes results from all positions around the fault, i.e. also positions close to the fault edge. In the right part, only positions away from the edge are included. The maximum fault slip velocity of the 1999 Chi-Chi earthquake, particularly reputed for its high slip velocities (cf. Chapter 3), is indicated for reference. The following can be observed:

- For the results obtained from models with faults dipping 70°, there is a significant correlation between the primary fault slip velocity and the amount of induced target fracture shear displacement.

- The correlation is more evident if slip on fractures located close to the fault edge is disregarded. For these fractures, the quasi static stress redistribution is, relatively seen, more important than dynamic effects (Figure 5-21b).

- The models with a fault dip angle of 30° give significantly smaller induced fracture displacements than other models with similar fault slip velocities. This large importance of the fault orientation indicates that these results cannot be directly compared with the other results in the diagram, which were obtained from models with steeper faults. The smaller amounts of induced displacements can be explained by the larger amount of stress relaxation caused by a more gently-dipping fault. This is further discussed in Section 6.1.

The correlation shown in Figure 5-21 can be explained by the fact that the amplitudes of the stresses at a particular location in a continuum are correlated to the particle velocities at that location (cf. /Itasca 2003/). Thus, the amplitudes of the stress waves that are radiating out from a rupturing fault are proportional to the continuum velocities generated by the rupture. Stronger stress waves will induce higher velocities around target fractures and will thus have a larger impact.
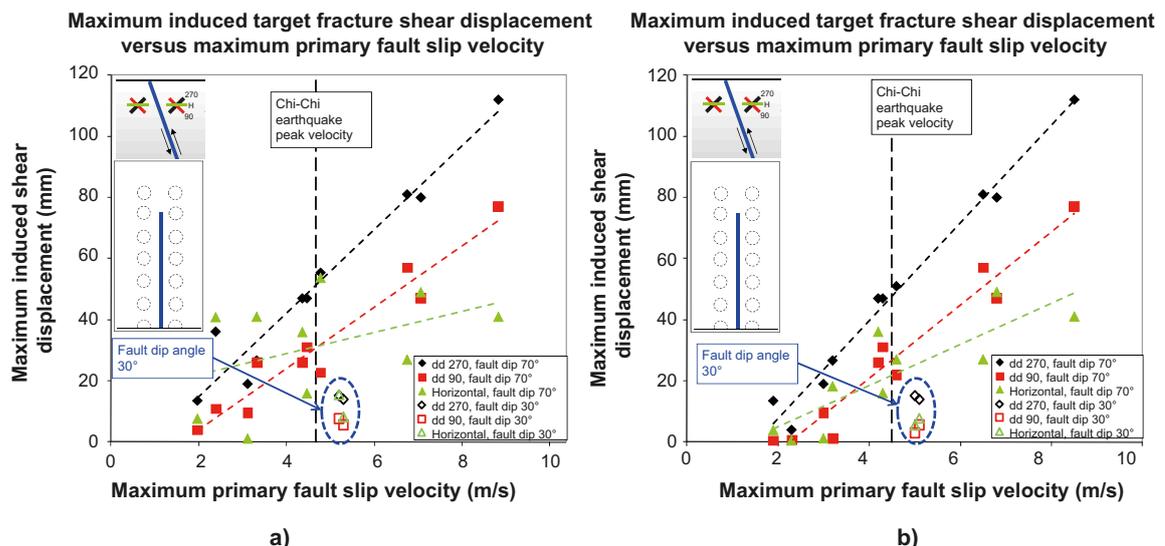
Figure 5-21. Maximum induced target fracture shear displacement versus maximum primary fault slip velocity. a) All target fractures. b) Only fractures away from the fault edge. Results from M_w 5.5, M_w 6.2 and M_w 7.5 models with different stress drops and fault geometries are shown. Note the large importance of the fault dip angle.

5.4.4   Importance of the distance from the source fault

Figure 5-22, Figure 5-23 and Figure 5-24 show plots of the amount of induced target fracture displacement versus distance from the fault in a number of models. Each figure shows results for one target fracture orientation. In the M_w 6.2 and M_w 5.5 models, the results are picked in fractures located far away from the primary fault vertical edge. This means that for these models it is not necessarily the largest displacement that is shown here. The following can be observed:

• In all models, the displacement at 600 m distance is about 50% or less than the displacement found at 200 m distance. At longer distances the displacements are yet smaller.

• For the dipping fractures the induced displacements are in general larger in the footwall. This is particularly true for the fractures with the same dip direction as the primary fault.

• The induced slip is given for the discrete distances where fractures are located in the models (i.e. 200 m, 600 m, 1,000 m, 1,500 m). An estimate of the possible induced slip at other distances than those given in the diagrams could be obtained through linear interpolation. However, given the shape of the distance–slip curves, this will overestimate target fracture slip at intermediate distances.
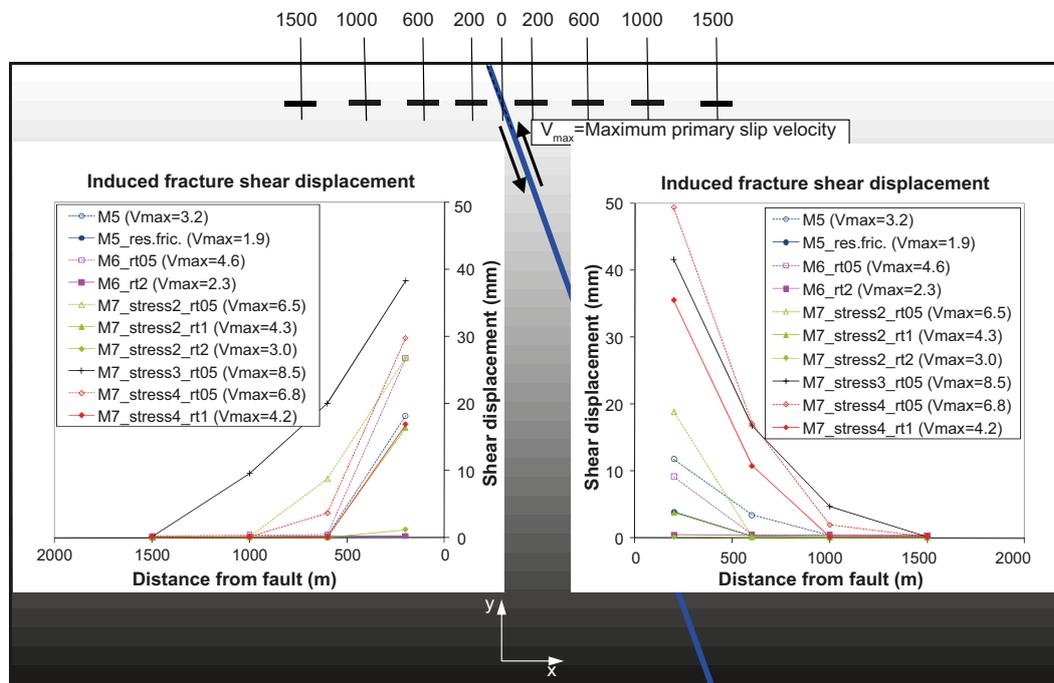

Figure 5-22. *Induced shear displacement in horizontal target fractures versus distance from the primary fault.*
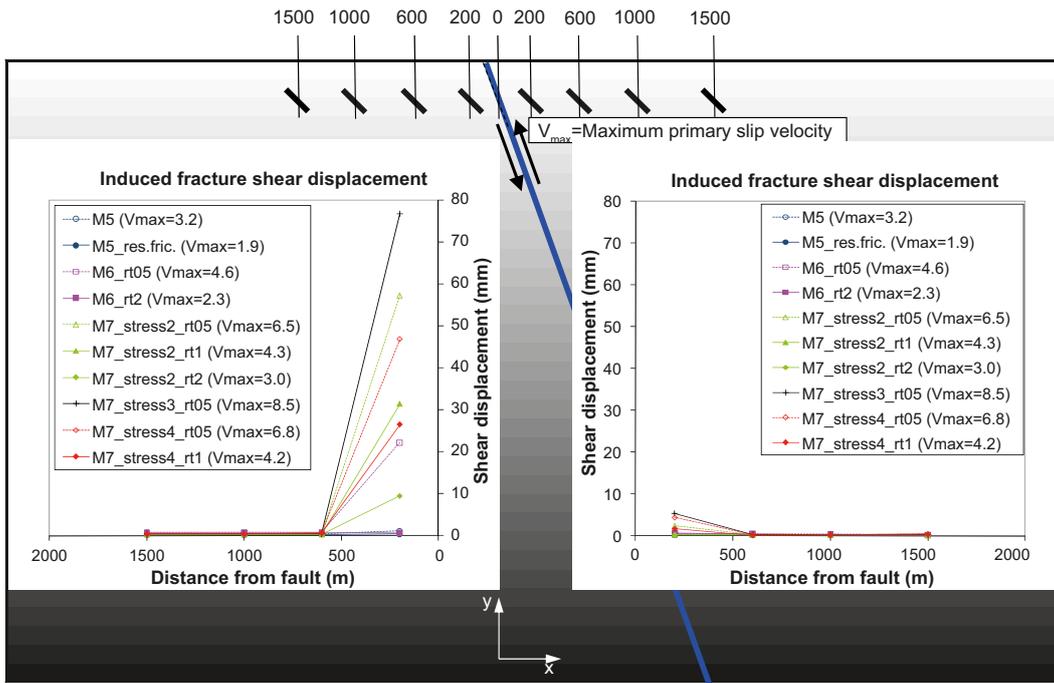
Figure 5-23. *Induced shear displacement in dipping target fractures versus distance from the primary fault.*
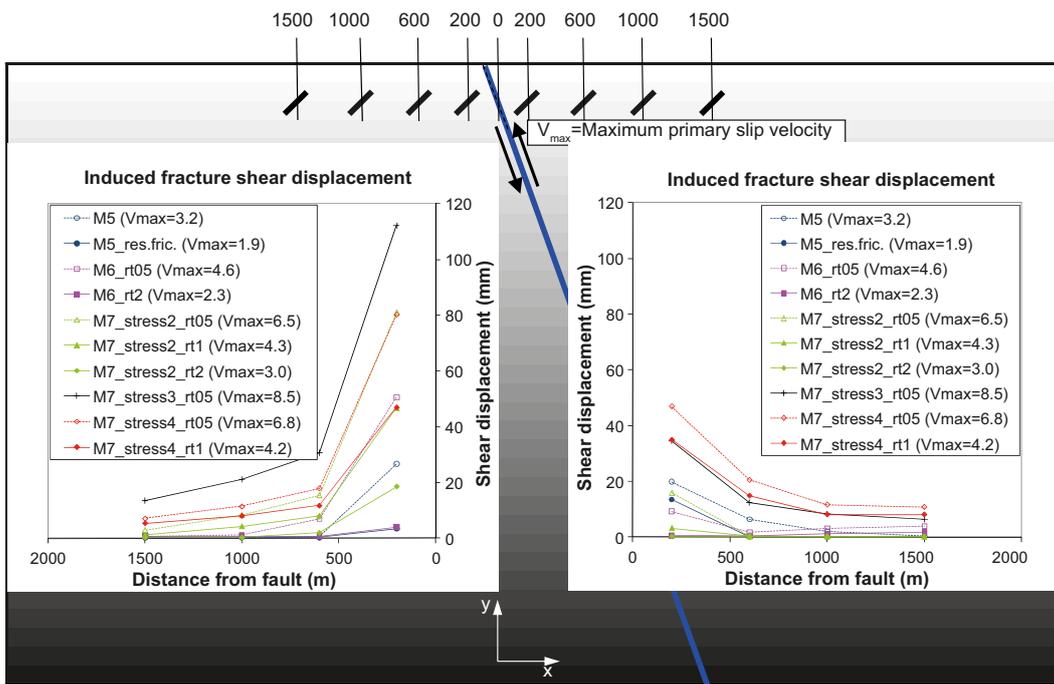

Figure 5-24. *Induced shear displacement in dipping target fractures versus distance from the primary fault.*

5.4.5 Target fracture shear velocities

The canister failure criterion applied by SKB is based on results from simulations where the buffer-canister system is subjected to a shear load /Börgesson and Hernelind 2006/. The rheological properties of the bentonite buffer are dependent on the loading rate. The higher the shear velocity the stiffer the response of the bentonite buffer and the more adverse the associated effects on the canister. Thus, it is of interest to establish upper- bound estimates of the shear velocities the buffer-canister system might be subjected to during an earthquake.

In this section we focus mainly on three models (Table 5-2). The models M6_Str1_tfBASE_rt05 and M7_Str4_tfBASE_rt1 have primary fault slip velocities that are similar to what has been reported for the 1999 Chi-Chi, Taiwan earthquake. The ground stations around this earthquake recorded the largest values of ground velocity ever instrumentally measured /Ma et al. 2003/. Thus, these two models can be regarded to be conservative-realistic. The M7_Str4_tfBASE_rt05 uses the same initial conditions as M7_Str4_tfBASE_rt1 but the rupture process is modified (shorter *rt*) such that a higher maximum primary fault slip velocity is achieved. Thus, in M7_Str4_tfBASE_rt05, the target fractures are subjected to extremely high dynamic loads.

Peak shear velocities

Fracture shear velocities are not a regular output from *3DEC*. The shear velocities were derived from the shear displacement histories by calculation of the time derivative of the displacement (Figure 5-1). The sampling frequency used when the displacements are recorded during the simulations is of the order of 100 recordings per second, which means that the shear velocities were averaged over time intervals of about 0.01 s.

Figure 5-25 and Figure 5-26 are diagrams showing shear velocities plotted versus shear displacement in the M6_Str1_tfBASE_rt05 and M7_Str4_tfBASE_rt1 models, respectively. The curves in the diagrams represent the fractures that moved more than 30 mm.

The maximum shear velocity is in the range 0.4–0.5 m/s (hi #66 in Figure 5-25). This is lower than what was reported by /Fälth and Hökmark 2006/. They recorded a maximum target fracture shear velocity of about 0.86 m/s in a similar model. The difference in results is due to details in the finite difference mesh. The highest velocity has a short duration. The velocity exceeds 0.4 m/s during about 7 mm of the total 50 mm movement. Out of all the other fractures, none has a peak velocity higher than about 0.3 m/s.

Table 5-2. Models for which fracture shear velocities have been specifically evaluated.

Model	Moment magnitude (M_w)	Peak fault slip velocity (m/s)	Maximum induced target fracture displacement (mm)
M6_Str1_tfBASE_rt05	6.2	4.4	55
M7_Str4_tfBASE_rt05	7.5	6.8	80
M7_Str4_tfBASE_rt1	7.5	4.1	47

M6_Stress1_tfBASE_rt05
Fractures moving > 30 mm
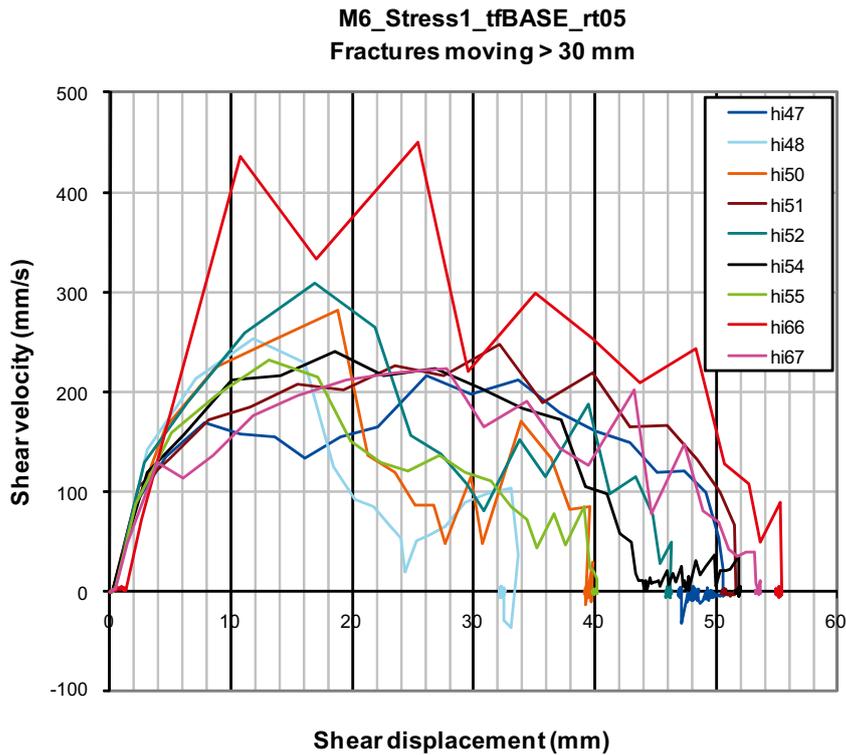
Figure 5-25. *Target fracture shear velocity versus displacement in the fractures with displacements > 30 mm in the M6_Str1_tfBASE_rt05 model. For the fracture with the highest peak velocity (hi66) the velocity is higher than 400 mm/s during about 7 mm of the 50 mm total displacement.*

M7_Stress4_tfBASE_rt1
Fractures moving > 30 mm
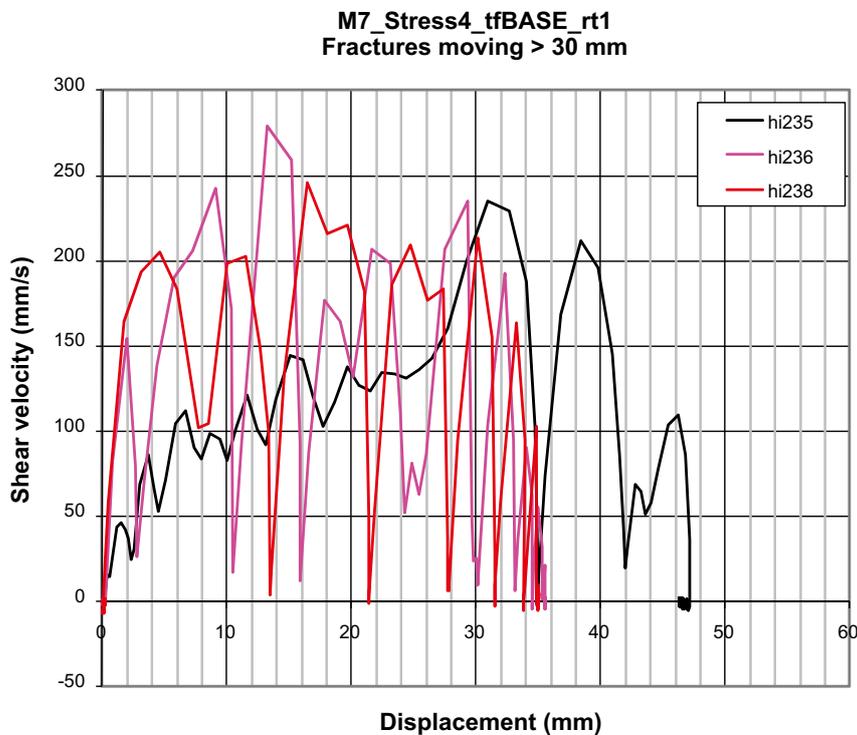
Figure 5-26. *Target fracture shear velocity versus displacement in the fractures with displacements > 30 mm in the M7_Str4_tfBASE_rt1 model.*

Effective shear velocities

In the buffer-canister stress-deformation analyses it was assumed that the shear velocity is constant during the entire shear movement /Börgesson and Hernelind 2006/. According to Figure 5-25 and Figure 5-26 the highest shear velocities found here correspond only to parts of the total shear movement. In order to compare these numerically obtained shear velocities with the constant velocity assumed by /Börgesson and Hernelind 2006/, it appears to be relevant to average the velocity over the total shear displacement by integration of the curves in Figure 5-25 and Figure 5-26. In the following, this is what is meant by "effective shear velocity". Note that the time average would always be lower and is not a relevant measure (since the majority of the slip typically occurs within a short time interval).

Figure 5-27 shows a cumulative distribution of effective target fracture shear velocities in the M6_Str1_tfBASE_rt05 model. Results from fractures at both 200 m and 600 m distance from the primary fault are shown. The highest effective shear velocity is about 270 mm/s and is found at 200 m distance. At this distance, about 90% of the fractures have shear velocities below 180 mm/s. The results also indicate a clear dependency on the distance from the source. At 600 m distance, the maximum velocity is about 100 mm/s.

Figure 5-28 shows a cumulative distribution of effective shear velocities in the two M_w 7.5 models. M7_Str4_tfBASE_rt1 gives a lower value of the maximum effective shear velocity than the M6_Str1_tfBASE_rt05 model (Figure 5-27), which has about the same primary fault slip velocity. This may reflect the differences between the *in situ* stress states which give differences in the initial stability of the target fractures.

M7_Str4_tfBASE_rt05 has a maximum effective fracture shear velocity of about 430 mm/s, significantly higher than M7_Str4_tfBASE_rt1, which has the same initial conditions. The difference depends on the difference in the primary fault slip velocity. The importance of the primary fault slip velocity is discussed further in the next subsection.

The results in Figure 5-27 and Figure 5-28 show that fractures at longer distances from the fault in general have lower shear velocities. It has been concluded in Section 5.4.2 that also the shear displacement is dependent of the fault-fracture distance. This suggests that there is a correlation between a fracture's shear velocity and its shear displacement. In Figure 5-29, the effective target fracture shear velocities are plotted versus the corresponding shear displacements. The results are compiled from the models specifically discussed in this section (cf. Table 5-2). Two of the models are discarded in the final assessment (Section 7.1). These are represented by the unfilled plot symbols. The results are picked at both 200 m and 600 m distance. Even if there are some values that deviate from the trend, the results indicate that effective shear velocity correlates with shear displacement.

Dependency on fault slip velocity

Figure 5-30 is a plot of target fracture effective shear velocity versus maximum primary fault slip velocity. The diagram is based on data from all M_w 5.5, M_w 6.2 and M_w 7.5 models and not just the three models discussed in the previous section. From each model, the largest effective shear velocity is plotted. The diagram illustrates a dependency between the target fracture velocity and the maximum primary fault slip velocity. A higher primary fault slip velocity produces a larger dynamic impact on the surrounding target fractures. This dependence is similar to what has been found for the induced displacements (cf. Figure 5-21). For the models with primary slip velocities equal to or lower than what has been reported for the Chi-Chi earthquake, no model shows effective shear velocities higher than about 270 mm/s. None of the models show effective velocities higher than 450 mm/s.

TR-08-11

Target fractures at 200 m and 600 m distance from M6.2 event
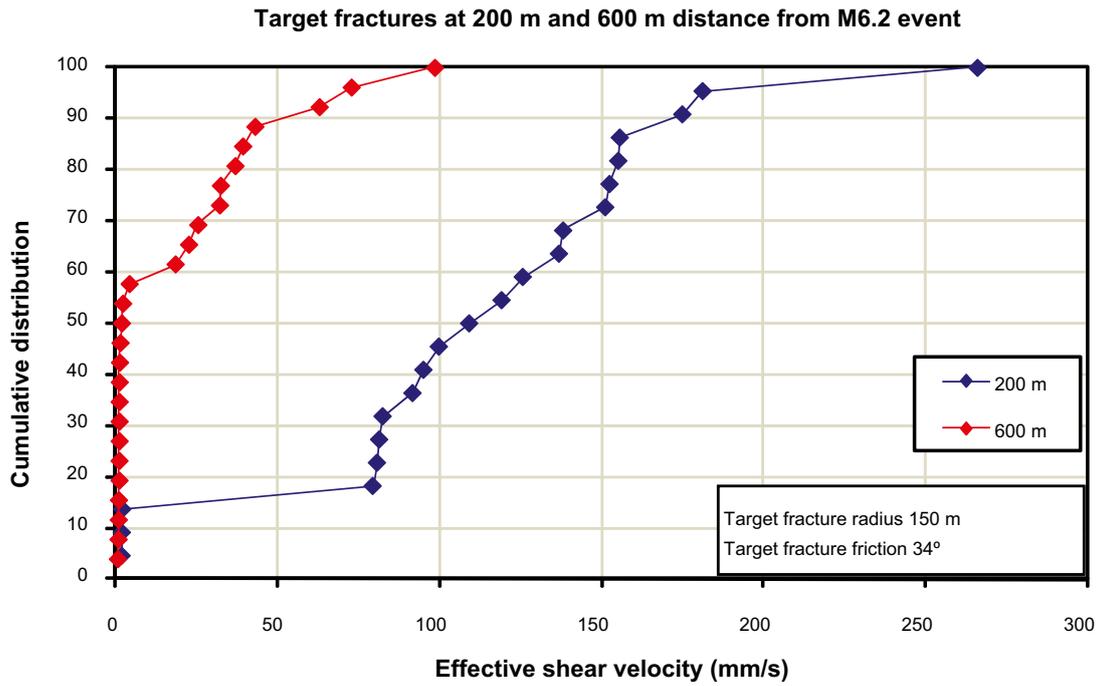
Figure 5-27. *Cumulative distribution of effective shear velocities in the M6_Str1_tfBASE_rt05 model. Results at 200 m and at 600 m distance from the primary fault are shown.*

Target fractures at 200 m and 600 m distance from M7.5 events
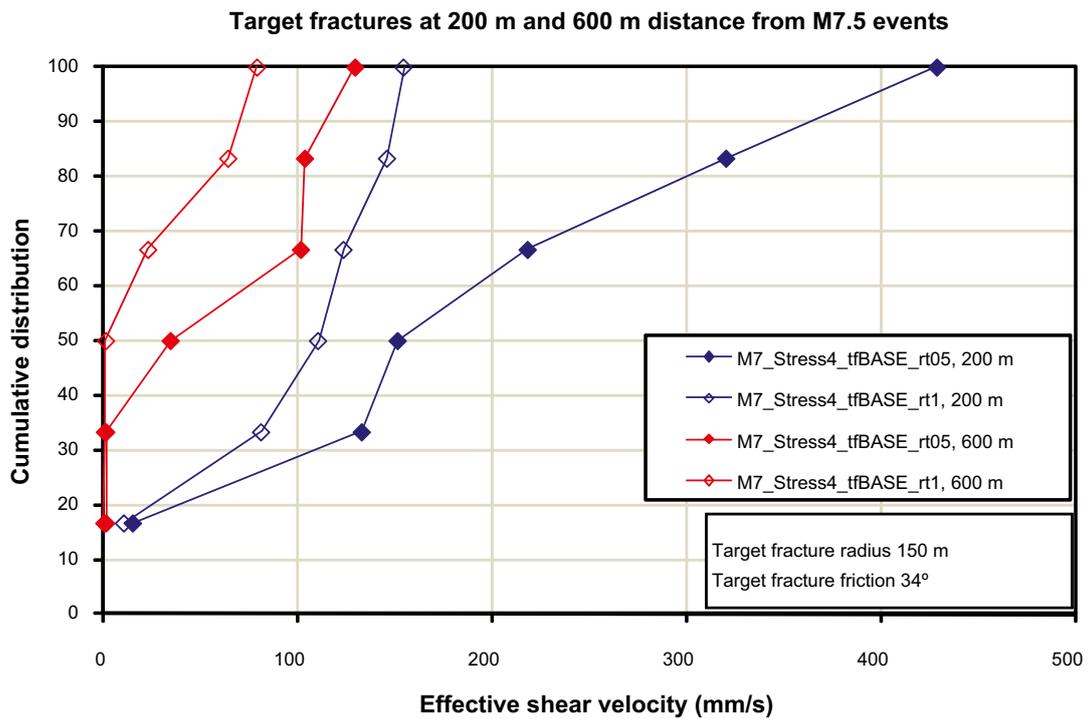
Figure 5-28. *Cumulative distribution of effective shear velocities in the two M$_w$ 7.5 models. Results at 200 m and at 600 m distance from the primary fault are shown.*

Figure 5-29. *Effective target fracture shear velocity plotted versus corresponding maximum fracture shear displacement. Results compiled from the models discussed in this section (cf. Table 5-2). Two of the models are discarded in the final assessment (Section 7.1). These are represented by the unfilled plot symbols. The dashed line is a linear regression line.*

Figure 5-30. *Effective target fracture shear velocity plotted versus maximum primary fault slip velocity. Results compiled from M_w 5.5, M_w 6.2 and M_w 7.5 models. The highest target fracture effective shear velocity in each model is plotted. The dashed line is a linear regression line.*

5.4.6 Sense of shear displacement

Dipping fractures

Buffer-canister stress-deformation analyses /Börgesson and Hernelind 2006/ indicate that the sense of fracture shear displacement is of importance to the scope and extent of canister damage. Figure 5-31 shows reverse (left) and normal (right) sense of shear across a deposition hole. In this study it is assumed that the post-glacial stress conditions at 500 m depth are of reverse type and the stresses in all numerical models are based on this assumption. If this kind of stress condition prevails in the bedrock it is reasonable to assume that the dip-slip component of the induced target fractures shear displacements is of the reverse type rather than of the normal type. This hypothesis is verified by the modelling results as illustrated in Figure 5-32.

Figure 5-32 shows plots that illustrate the shear sense of all dipping fractures in eight of the models (bottom). The models are the same as those used to provide input to the interpretation model developed in Section 7.1. Each vector represents the slip on one fracture and its length represents the amount of displacement. The directions of the vectors indicate the shear modes. A slip vector orientation of 0° and 180° represent pure reverse-slip and pure normal shear displacement, respectively, whereas 90° and 270° represent strike-slip mode. The left plot shows results from fractures slipping less than 15 mm, while the right plot from fractures with more than 15 mm slip. The results are extracted at the end state of the simulations.

All fracture shear displacements that exceed 15 mm are of reverse type (Figure 5-32b). There are however also components of strike-slip, depending on details in the target fracture orientation and location relative to the fault plane and the progress of the fault rupture. The largest deviation from the pure reverse shear mode in these fractures is about 60°. Among the fractures moving less than 15 mm (Figure 5-32a) there are some that exhibit normal-slip (direction between 90° and 270°). However, these movements are very small. The largest movement that takes place with a normal sense of slip is less than 1 mm.

Figure 5-33 and Figure 5-34 are vector plots that illustrate how the fracture shear displacement directions vary depending on the location of the fractures.

Horizontal fractures

Figure 5-35 shows a top-down vertical view of resulting shear displacement vectors in horizontal target fractures in the M6_Str1_tfBASE_rt05 model. The dashed blue line indicates the intersection between the fault plane and the repository horizon. The vectors are coloured according to their magnitudes. The plot illustrates how the shear displacements take place in different directions at different locations. The plot also shows the circular shapes of the target fractures.
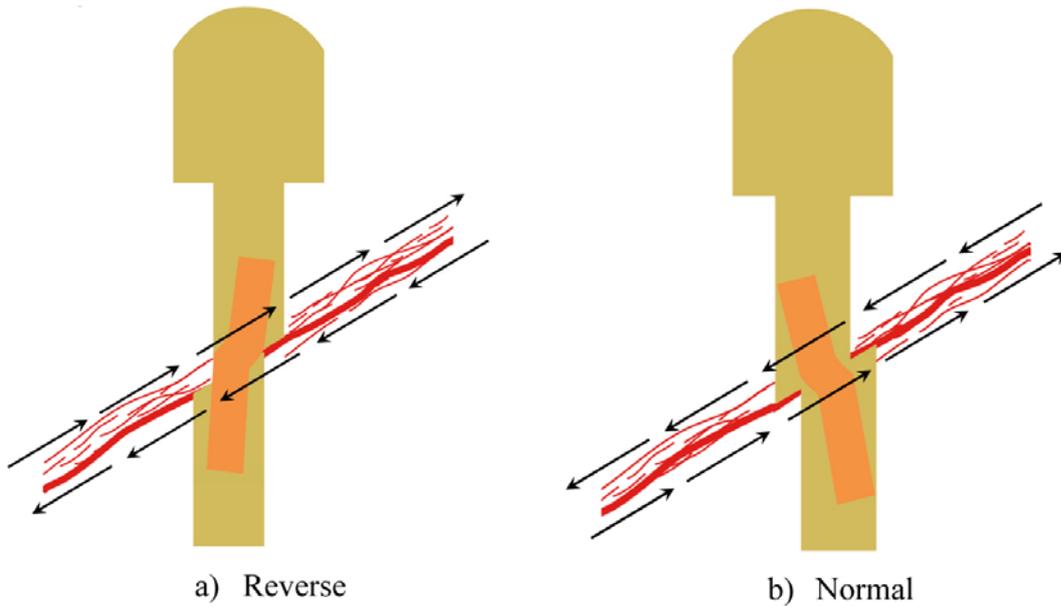
Figure 5-31. *Sense of fracture shear displacement: a) Reverse shearing. All significant target fracture displacements found in the 3DEC models are of this type. b) Normal shearing.*

0 – 15 mm slip

a)

15 – 47 mm slip

b)
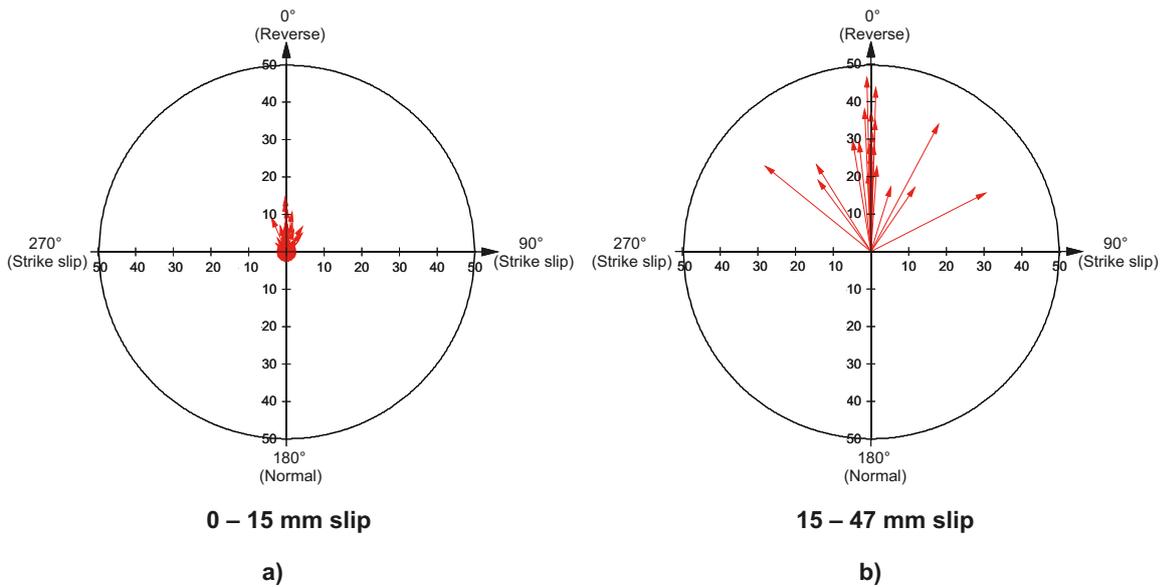
Results obtained from the following models

M5_Str1_tfBASE_rt05_pp6	M7_Str4_tfBASE_rt1	M7_Str4_tfALT1_rt1	M7_Str4_tfALT3_rt1
M6_Str1_tfBASE_rt2	M7_Str4_tfBASE_rt1_pp6	M7_Str4_tfALT2_rt1	M7_Str4_tfALT4_rt1

Figure 5-32. *Top: Vector plots showing the modes of shear displacement on dipping fractures. The lengths of the vectors indicate the amount of displacement whereas the directions indicate the shear modes. The left plot shows results from fractures slipping less than 15 mm and the right plot shows results from fractures slipping more than 15 mm. Bottom: List of models from which the results are obtained.*
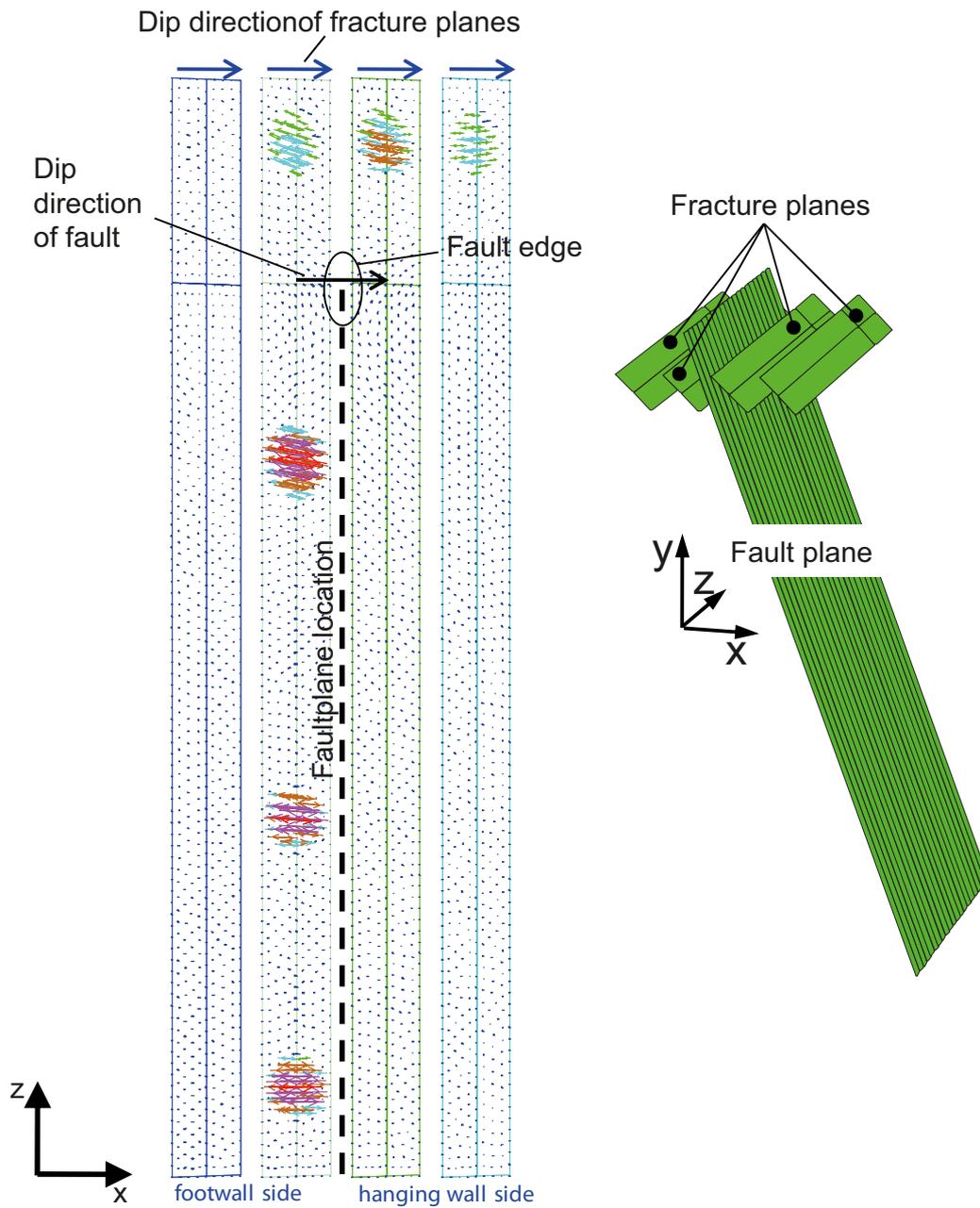
Figure 5-33. *Left: Vector plot showing induced fracture shear displacements in fractures with same dip direction as the fault in the M6_Str1_tfBASE_rt05 model. The fracture planes are viewed from above. The black and blue arrows indicate dip directions of fault and fracture planes, respectively. Right: Locations and orientations of fracture planes.*
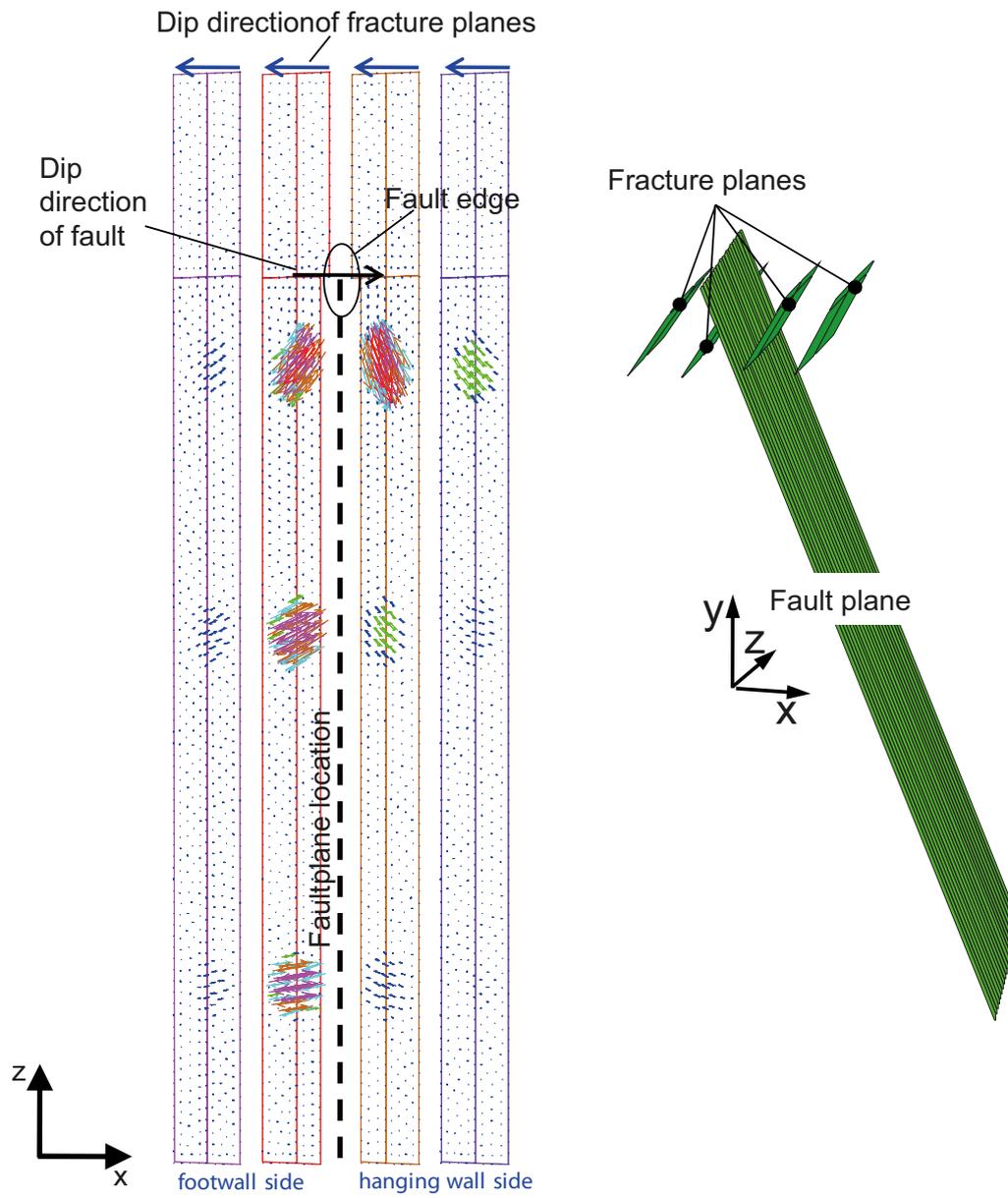
Figure 5-34. *Left: Vector plot showing induced fracture shear displacements in fractures with opposite dip direction to the fault in the M6_Str1_tfBASE_rt05 model. The fracture planes are viewed from above. The black and blue arrows indicate dip directions of fault and fracture planes, respectively. Right: Locations and orientations of fracture planes.*
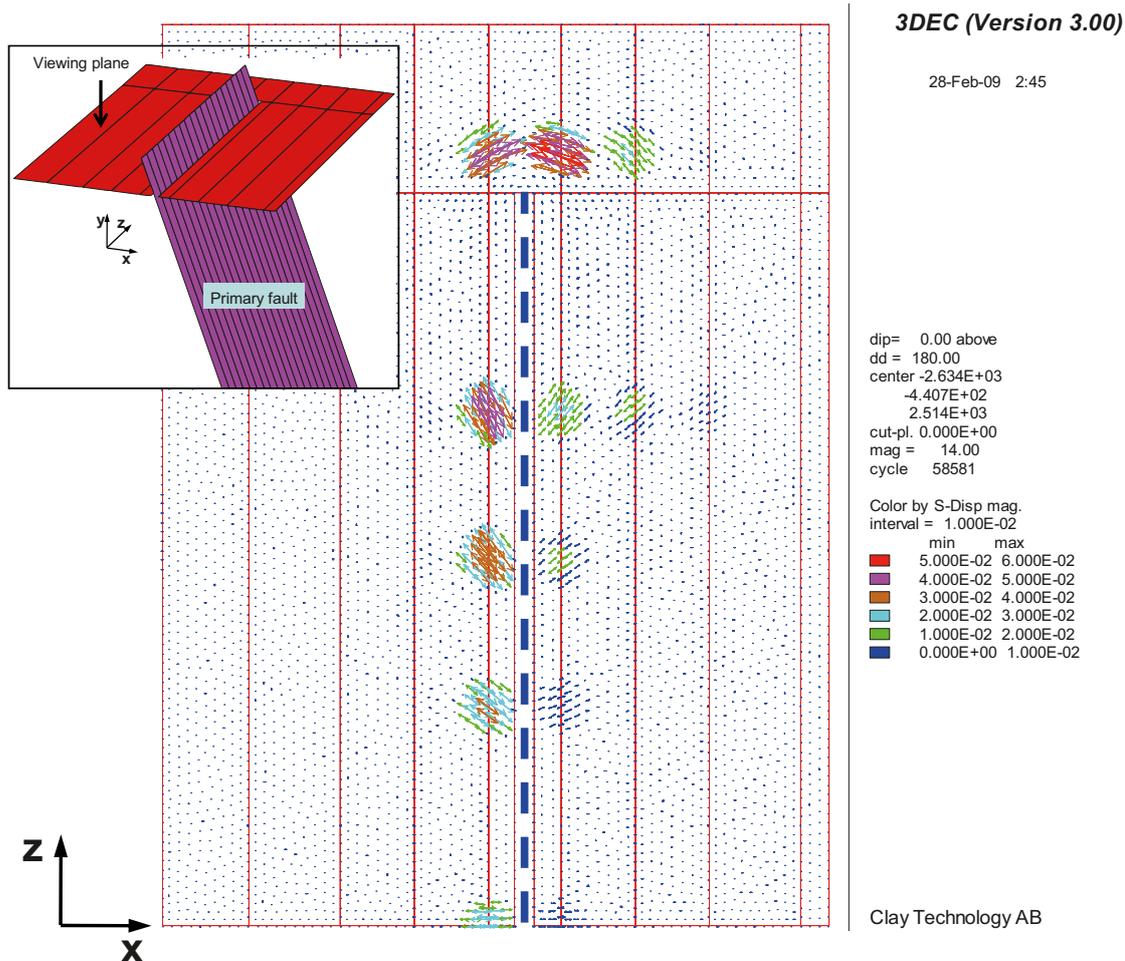
Figure 5-35. View from above of resulting shear displacement vectors in horizontal target fractures in the M6_Str1_tfBASE_rt05 model. The dashed blue line indicates the intersection between the fault plane and the repository horizon. The colour code gives displacements in metres according to the colour legend. Text above the colour legend is 3DEC plot information (relating to orientation and position of viewing plane) and runtime information.

5.4.7 Importance of fracture size

Even though the target fracture radius is 150 m in all models presented above, it may be of interest to make estimates of possible induced shear displacements and shear velocities for fractures of different sizes. For static cases the displacements in a circular fracture with radius, *a*, can be calculated by /Eshelby 1957/:

$$u_r = \frac{24}{7\pi} \frac{\tau_{drop}}{G} \left[a^2 - r^2 \right]^{\frac{1}{2}}$$

Equation (5-2)

Here, u_r is the shear displacement at the radial position *r*, while *G* is the shear modulus of the elastic surrounding rock. The stress drop, τ_{drop}, is the difference between the nominal shear stress acting on the plane of the fracture and the fracture shear strength. In order to examine if this linear correlation can be assumed to hold also for fractures subjected to dynamic loads, four test models with two different target fracture radii and two different target fracture orientations were analysed (Table 5-3.). All four models had an identical finite-difference mesh, which was specifically dense in the target fracture region in order to give a more accurate solution for smaller fracture sizes.

Table 5-3. Test models.

	150 m radius	75 m radius
Horizontal fractures	150_h	75_h
Dipping fractures	150_d	75_d

Figure 5-36 shows time histories of induced fracture shear displacements for fractures with 150 m and 75 radii. The left and right diagrams show results for dipping and horizontal fractures, respectively. The amount of displacement in the 75 m fractures is about half of that in the corresponding 150 m fractures during the entire deformation. The dynamic effects give a displacement peak in the horizontal fractures. Even during this peak the displacements in the 75 m fractures are half that of the corresponding displacements in the 150 m fractures. The displacements develop in the same way but with different magnitudes during the same time periods in the 75 m and the 150 m fractures. These results indicate that displacements and velocities both scale linearly with fracture size under both static and dynamic conditions. This means that the results in this report (induced target fracture shear displacements and shear velocities) can be applied to arbitrary fracture sizes by linear scaling to the fracture radius.

5.4.8 Distribution of shear displacement

For a fracture in a linear elastic medium, the displacement u_r of a fracture of radius a varies from u_{max} at the fracture centre ($r = 0$) to zero at its periphery ($r = a$) according to /Eshelby 1957/.

$$\frac{u_r}{u_{max}} = \sqrt{1 - \left(\frac{r}{a}\right)^2}$$

Equation (5-3)

Figure 5-37 is a plot of normalised slip distribution according to Equation 5-3 along with results from three target fractures in the M6_Str1_tfBASE_rt05 model. The diagram shows that the slip in the numerical model tapers off a little faster than predicted by the analytical model. The numerical results differ from the analytical solution by at most 15%.
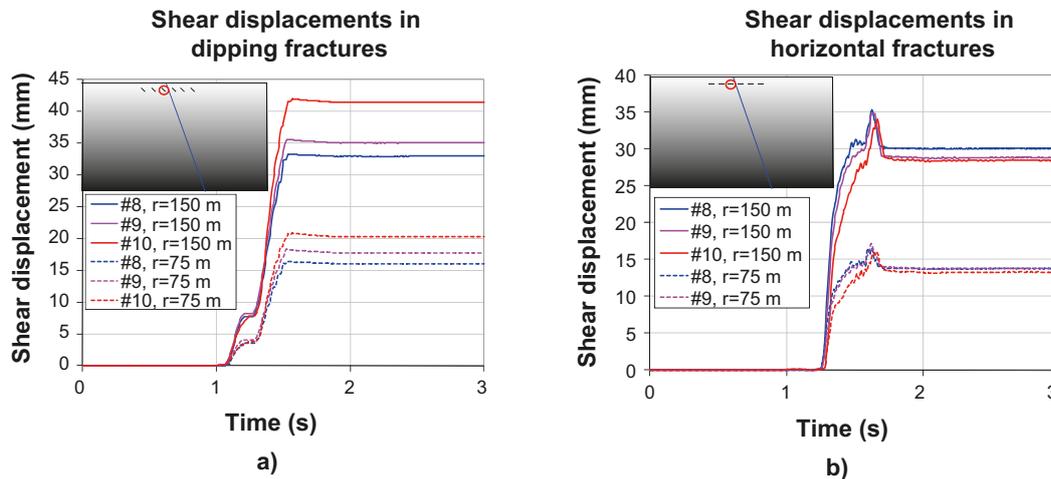
Figure 5-36. *Induced shear displacements in test models. a) Dipping fractures and b) horizontal fractures. The results indicate that both displacements and velocities scale linearly with fracture size.*

Normalised fracture displacement
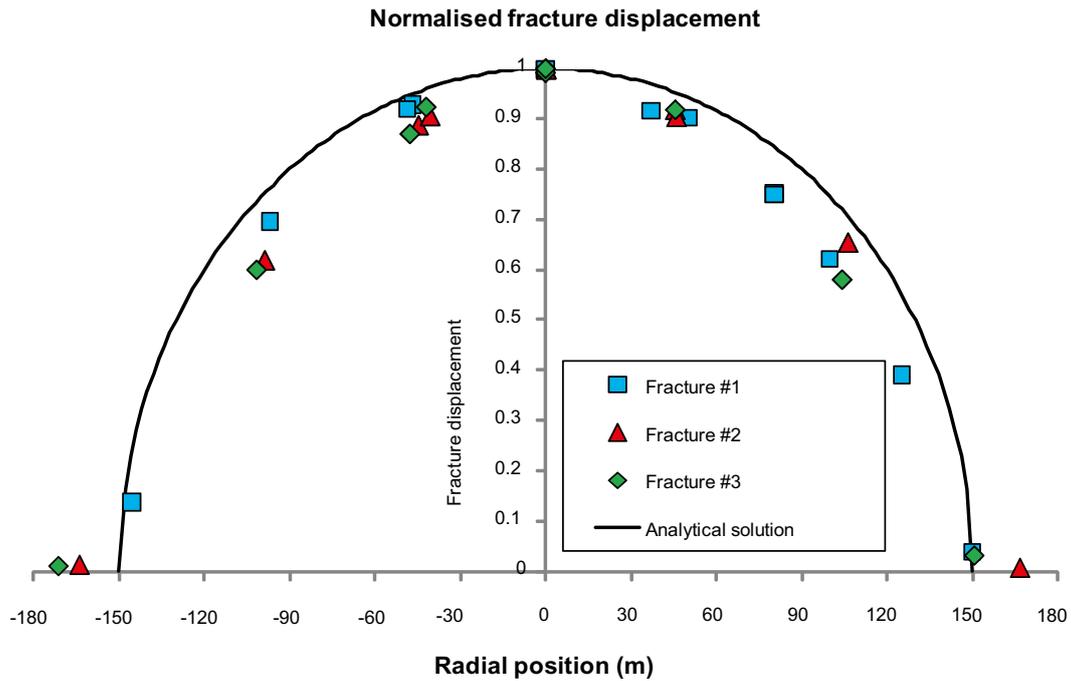
Figure 5-37. Normalised fracture displacement distribution as function of radial position. Analytical results and results from the M6_Str1_tfBASE_rt05 model.

5.4.9 Sensitivity to fracture strength parameter values

A number of M_w 5.5 models are run in order to study their sensitivity to fracture strength parameter values. Different assumptions regarding pore pressure, friction coefficient and dilation angle are tested. The models are summarised in Table 5-4. The basic assumption is to have a friction angle of 34° and apply a hydrostatic pore pressure of 5 MPa (model #1). Model #2 is similar to #1 but with an additional 1 MPa excess pore pressure, i.e. 6 MPa total. Models #3, #4 and #5 all have a dilation angle of 15°, but utilize different friction angles. The value of the dilation angle is obtained from direct shear tests at a normal stress of 0.5 MPa /Glamheden et al. 2007/. The values of friction angle in model #4 and #5 are obtained by assuming that the friction angle may vary within ±2.5° (about one standard deviation) /Glamheden et al. 2007/.

Figure 5-38 shows the cumulative distribution of induced shear displacements in models #1–5. Results from fractures at 200 m and 600 m distance from the primary fault are shown. Each plot symbol represents the result for one particular target fracture. Including dilation gives a reduction of the maximum slip of about 5 mm (10%) (cf. model #2 and #3). Reducing the friction angle from 36.5° to 31.5°gives about a 6 mm (17%) increase in maximum slip (cf. model #4 and #5).

As no fractures in nature are perfectly planar, it is conservative to assume zero dilation, as in model #2. Note that the layout rules developed in Chapter 7 are based on results from this model and on other models using the same fracture strength parameter values.

Table 5-4. Models used in sensitivity analysis.

Model	Pore pressure (MPa)	Friction angle (degrees)	Dilation angle (degrees)	Max induced slip (mm)	Comment
#1	5	34	0	41	M5_Str1_tfBASE_rt05
#2	6	34	0	45	M5_Str1_tfBASE_rt05_pp6*
#3	6	34	15	39	
#4	6	31.5	15	42	
#5	6	36.5	15	36	

*Used in Chapter 7 when layout rules are developed.
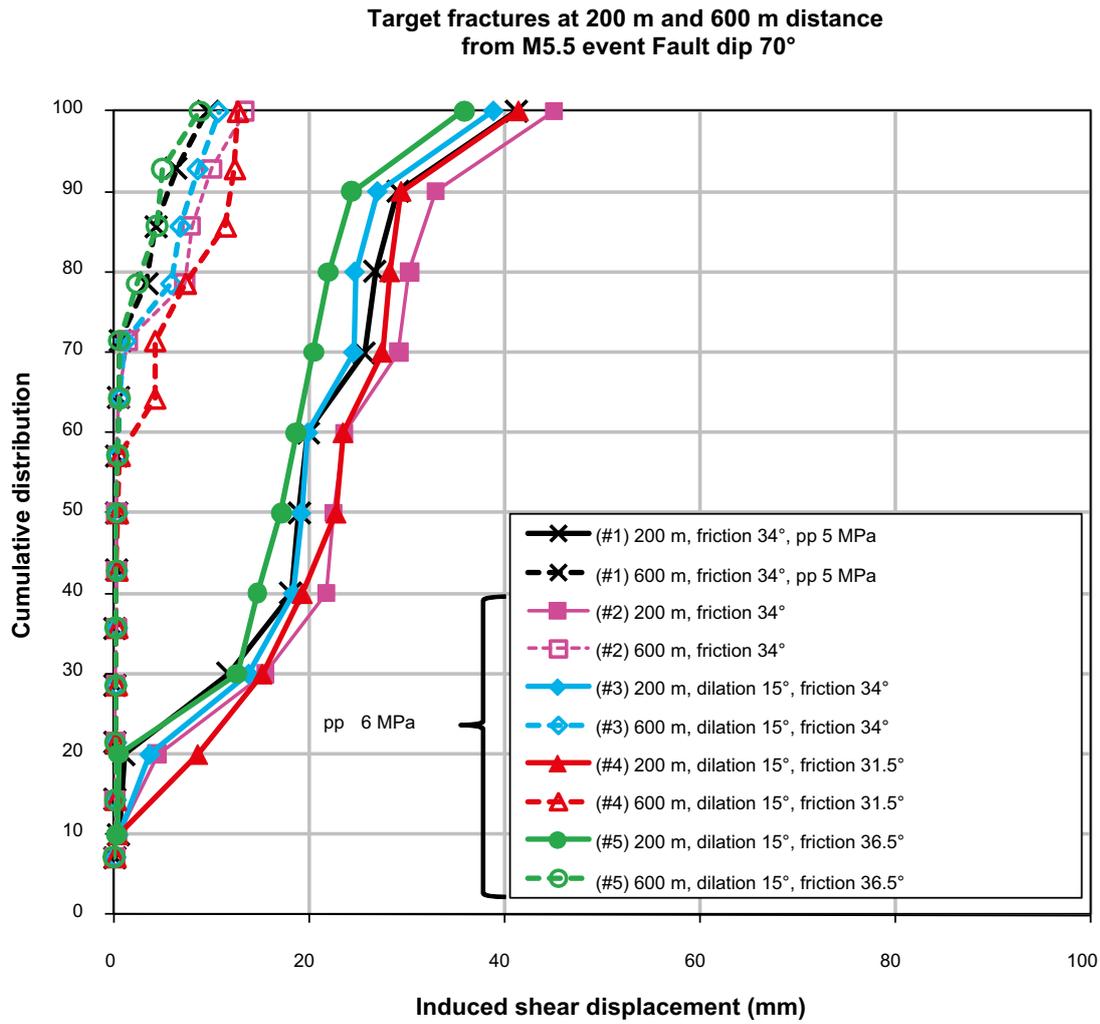
Figure 5-38. *Cumulative distribution of induced target fracture shear displacements at different distances from the primary fault in M_w 5.5 models. The colours denote models with different fracture strength parameter values. Each plot symbol represents the result of one particular fracture.*

6 Relevance and validity of numerical models

The earthquake simulations presented in this report were carried out with idealised models utilizing schematic representations of earthquake mechanisms and of target fractures. Therefore, it is necessary to assess the relevance and validity of the results through a comparison of certain model parameters with data found in the literature. This chapter also presents a comparison between results from one of the present models with results reported by /Munier and Hökmark 2004/.

6.1 Stress drop and primary fault slip velocity

6.1.1 Stress drop

The magnitude of the stress drop is a much debated quantity, as it is difficult to measure. Stress drop estimates for a single rupture event usually agree only within factor of 4 or 5, depending on ambiguities in the underlying physics /Scholz 2002/. The stress drop may also vary significantly between different parts of the same fault (cf. Figure 6-1). /Scholz 2006/ confirms that local asperity stress drops may be one order of magnitude larger than the fault average stress drop, possibly 100 MPa and upwards.

The average stress drop may be approximated through the use of the slip/width ratio /Scholz 2002/:

$$\varDelta\sigma = CG\frac{\bar{u}}{W}; \quad C = \frac{4(\lambda+G)}{\pi(\lambda+2G)} \qquad \text{Equation (6-1)}$$

Here G is the shear modulus, $\bar{u}$ is fault average slip and W is fault width. The expression for C is valid for an infinite length dip-slip rupture (λ is the Lamé constant).
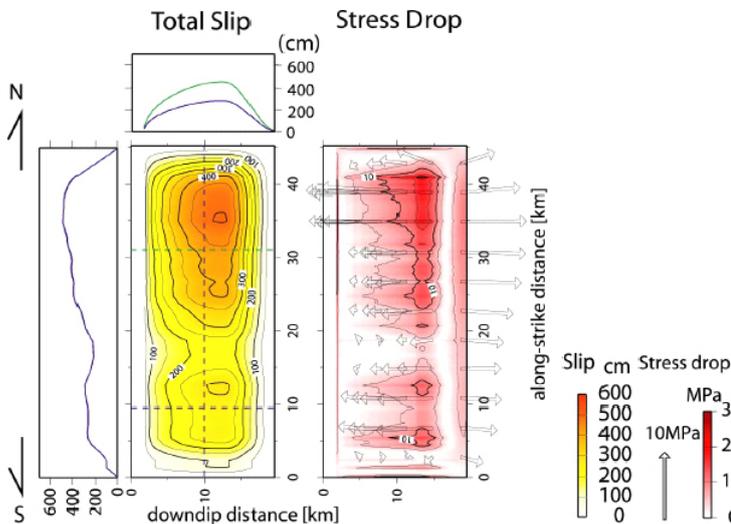
Figure 6-1. Static slip model and static stress drop model for the Uemachi Fault system. This figure illustrates how both the magnitude of slip and the stress drop can vary in a single fault due to in-plane asperities and spatial variability of in situ stresses. From /Sekiguchi et al. 2004/.

Figure 6-2 shows results from the synthetic *3DEC* earthquakes plotted in average stress drop- fault peak slip velocity space. The green, blue and red plot symbols represent M_w 5.5, M_w 6.2 and M_w 7.5 models, respectively. The legend at the bottom of the figure summarises models data (M_w, rt, target fracture (TF) maximum slip and average stress average drop). The average stress drops are calculated in two ways.

1. Approximation: The average stress drop is approximated through the use of Equation 6-1 with the average fault slip, $\bar{u}$, obtained by integration over the rupture area in each model and by putting $\lambda = G = 30$ GPa. These values correspond to the positions of the plot symbols. The corresponding stress drop approximations are made for the Lapland post-glacial Lansjärv and Pärvie earthquakes and the 1999 Chi-Chi earthquakes indicated in the diagram. The fault slip/width ratios for the two post-glacial earthquakes are based on estimates by /Arvidsson 1996, Muir Wood 1993/, while the corresponding ratio for the Chi-Chi earthquake is based on modelling published by /Ma et al. 2001/.

2. Actual stress drop: For the synthetic *3DEC* earthquakes, it is possible to calculate the actual change in shear stress at every point of the fault plane and then integrate over the rupture area to find the average stress drop. In the models where the fault shear strength is zero, this stress drop equals the initial average shear stress along the fault plane (cf. Sections 4.9.4 and 4.10.4).

The dotted arrows indicate the shift of positions in the diagram obtained if the actual stress drop in the models is considered instead of the approximate one. The following can be observed regarding the average stress drop.

• Using Equation 6-1 to determine the approximate average stress drop in the model: The M_w 6.2 and M_w 7.5 models have relatively high stress drops. Four of the models have stress drops that are about 90% larger than those estimated for the Pärvie Fault, while in four other models the stress drop is about 30% larger. The M_w 5.5 models produce 30–75% of the estimated Pärvie stress drop and about the same as the Chi-Chi earthquake.

• Considering actual model stress drops: For most of the models the actual average stress drop is higher than the values obtained from Equation 6-1. For the M_w 5.5 models it is more than 100% higher and for the M_w 6.2 models about 60%. In the four M_w 7.5 models with the highest stress drops it is 20–30% higher whereas it is about 15% lower in two of the M_w 7.5 models. These large differences can be attributed to the fact that the models don't have both uniform stress drop distributions and infinite lengths, which is assumed in the derivation of Equation 6-1.

• The amount of induced target fracture slip may vary considerably between models with approximately the same average stress drop.

These observations are in accordance with the notion discussed above that it is difficult to estimate the stress drop in an unambiguous way. The amount of slip, and thus the average stress drop as estimated by the closed-form solution, is not dependent only on the actual stress drop but also on its distribution along the fault plane and on the fault geometry. Note that the M_w 5.5 and M_w 6.2 models have finite length fault planes whereas it is assumed in Equation 6-1 that the rupture plane has infinite length. Irrespectively of which measure that is used for the average stress drop, it can be concluded that many of the models seem to be conservative in terms of stress drop when compared to the post-glacial faults. However, the results indicate that the average stress drop is not the parameter that primarily determines what effect the earthquake has on surrounding target fractures in terms of induced slip. As can be observed in Figure 6-2 and has been shown earlier in this report (see Section 5.4.3), there is a significant correlation between the induced target fracture slip and the fault slip velocity. Thus, this parameter is a much better indicator of the conservativeness of a model. This is discussed in next subsection.
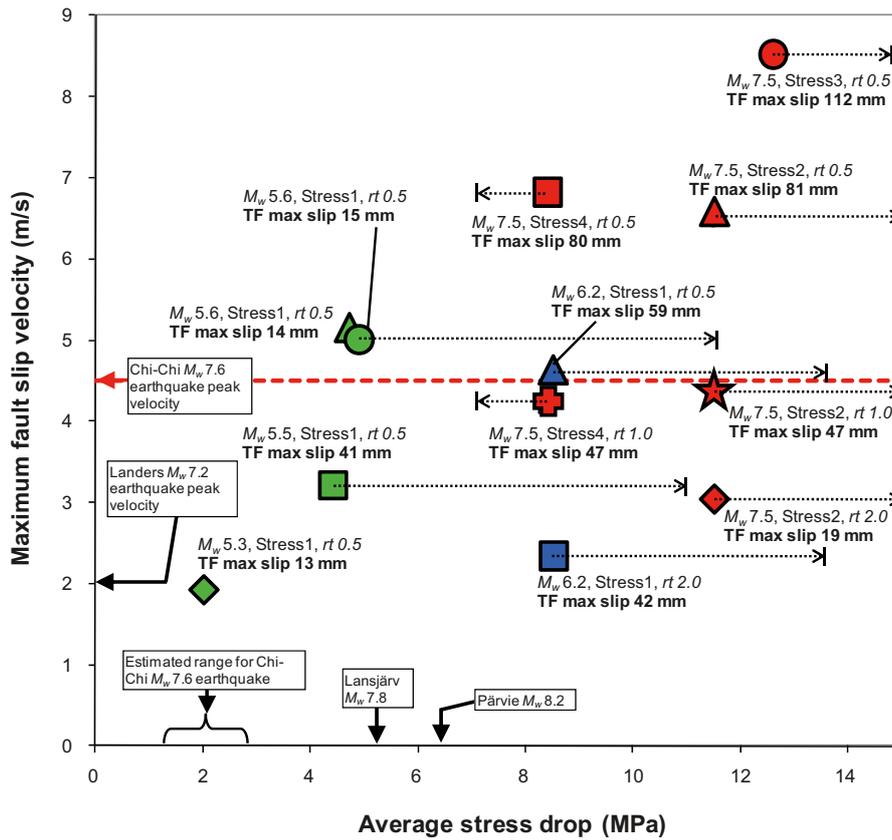
	M_w	rt (s)	TF max slip (mm)	Stress drop estimated through Equation 6-1 (MPa)	*3DEC* model actual stress drop (MPa)	Comment
■ (green)	5.5	0.5	41	4.4	11.3	
◆ (green)	5.3	0.5	13	2.0		Fault residual strength
● (green)	5.6	0.5	15	4.9	11.6	Fault dip 30°
▲ (green)	5.6	0.5	14	4.7		Fault dip 30°, fault residual strength
▲ (blue)	6.2	0.5	59	8.5	13.7	
■ (blue)	6.2	2.0	42	8.5	13.7	
▲ (red)	7.5	0.5	81	11.5	15.0	
★ (red)	7.5	1.0	47	11.5	15.0	
◆ (red)	7.5	2.0	19	11.5	15.0	
● (red)	7.5	0.5	112	12.6	14.8	
■ (red)	7.5	0.5	80	8.4	7.1	
✚ (red)	7.5	1.0	47	8.4	7.1	

Figure 6-2. *Average stress drop and primary fault slip velocity diagram. 3DEC synthetic earthquakes are compared with estimates based on literature data. The green, blue and red symbols represent M_w 5.5, M_w 6.2 and M_w 7.5 models, respectively. All average stress drops are approximated using Equation 6-1. The numbers of target fracture (TF) maximum induced slip are results picked at 200 m distance from the fault. The vertical dashed line indicates the estimated average stress drop of the Pärvie post-glacial earthquake. The horizontal dashed line indicates the estimated peak slip velocity of the Chi-Chi earthquake.*

6.1.2   Fault slip velocity

There are no maximum slip velocity records for any of the Lapland post-glacial earthquakes. In Figure 6-2, the *3DEC* maximum slip velocities are instead compared with data reported for the Chi-Chi earthquake /Ma et al. 2001, Ma et al. 2003/, and with the slip velocity of the 1992 magnitude 7.2 Landers, California, earthquake. The Landers maximum slip velocity estimate is based on ground velocities reported by /Wald and Heaton 1994/. Several of the *3DEC* models have fault peak slip velocities that are about the same as that of the Chi-Chi earthquake. Some have even higher velocities. The most extreme model has a slip velocity almost twice as high as that of the Chi-Chi earthquake. The figure illustrates again the importance of the fault slip velocity (cf. Figure 5-21 in Section 5.4.3). The modelling results indicate that neither the earthquake magnitude nor the average stress drop are important for the induced target fracture slip (given the same fault dip angle, see Section 6.2). According to the modelling results, the induced fracture displacement seems to be more related to the fault slip velocity. This is logical since the maximum slip velocities in the models are always recorded close to the ground surface and thus close to the target fracture region. Since the fault-target distances considered here are small, the impact on the target fractures is mainly determined by the fault behaviour at shallow depths. Even if, in the real case, there may be high stress drops locally at larger depths (caused for instance by strong asperities) resulting in high slip velocities at these locations, this has very little importance for the target fractures at shallow depths.

Figure 6-3 shows the peak slip velocity distribution along the Chelungpu Fault during the Chi-Chi earthquake, as estimated by /Ma et al. 2003/. The triangles at the top show the locations of measurement stations, while the numbers are peak slip velocities that were measured directly from the seismograms at these stations. The maximum slip velocity close to the ground surface during the Chi-Chi earthquake was about 4.5 m/s. Roughly the same primary peak slip velocity was recorded close to the ground surface in some of the *3DEC* models. This is shown in Figure 6-2 and by the diagram in Figure 6-4 which shows the temporal development of primary fault slip velocity close to the ground surface and at hypocentre depth in one M_w 6.2 model and in one M_w 7.5 model. The fault peak slip velocity at the ground surface exceeds 4 m/s in both models. It can also be seen in the diagram that the maximum slip velocities at hypocentre depth are in the order of 0.5 and 1.5 m/s, respectively. Except for the high velocity region in the Chelungpu Fault, these simulated maximum slip velocities are about the same as those estimated for deeper segments of the Chelungpu Fault during the Chi-Chi earthquake (Figure 6-3).
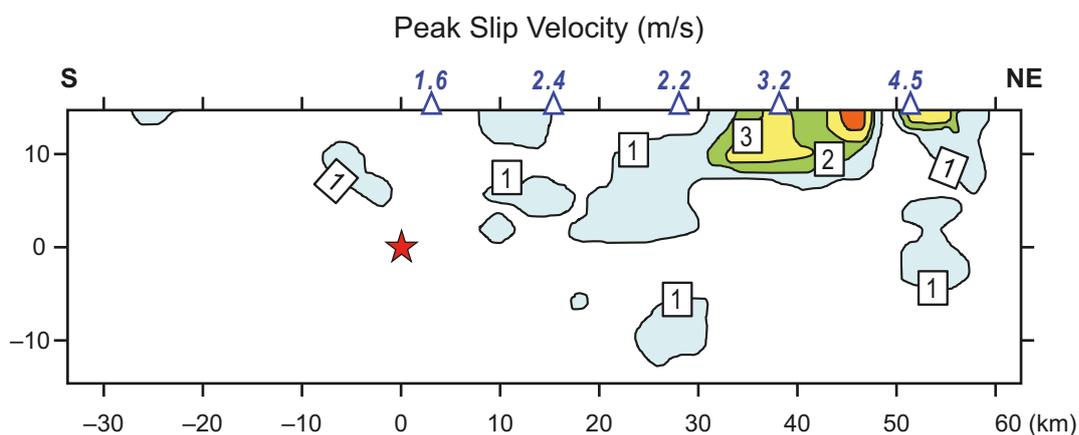
Figure 6-3. *Estimated peak slip velocity distribution in the Chelungpu Fault during the 1999 Chi-Chi earthquake. The triangles indicate measurement stations. The peak slip velocities measured directly from the seismograms at the five stations are given by the numbers next to the station locations. Redrawn from /Ma et al. 2003/.*

TR-08-11
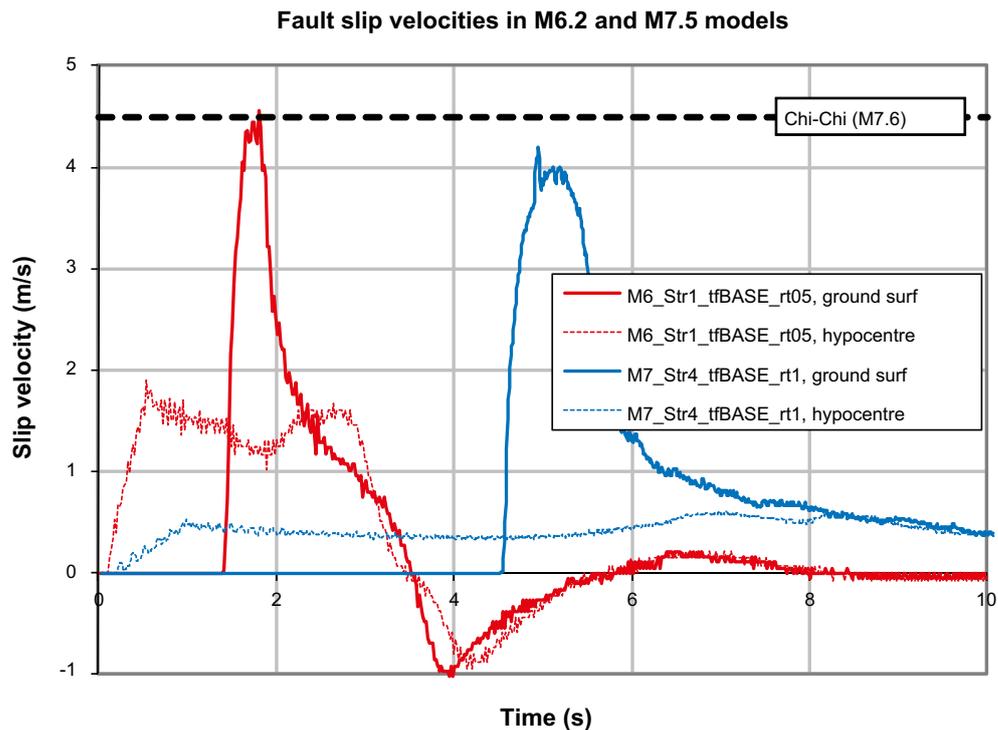
Figure 6-4. *Temporal developments of primary fault slip velocities in the M6_Str1_tfBASE_rt05 and M7_Str4_tfBASE_rt1 models.*

The highest slip velocities during the Chi-Chi earthquake were observed only along one part of the fault (Figure 6-3) whereas the schematic representation of the rupture in the *3DEC* models gives high primary slip velocities along a considerable portion of the fault plane. This is illustrated by Figure 6-5, which shows primary fault slip velocity vector plots after 1.7 s and 2 s in the M6_Str1_tfBASE_rt05 model. The plots show that the slip velocity at the ground surface exceeds 3 m/s along at least 75% of the fault length. Thus, the impact on the near-field of the M_w 6 earthquake simulated by the *3DEC* model can be considered to be at least as powerful as that of the M_w 7.6 Chi-Chi earthquake.

6.2 Fault dip angle

As indicated in Figure 6-2, the M_w 5.5 models with fault dip angles of 30° (instead of 70°) have primary fault slip velocities higher than that of the Chi-Chi earthquake. These models also have a larger average fault slip/fault width ratio than the other M_w 5.5 models (indicated as a higher average stress drop in the figure). In spite of this, they produce significantly smaller induced target fracture displacements than other models with similar primary slip velocities (also clearly shown by Figure 5-21 in Section 5.4.3). The reason for this seems to be that the mechanism of stress release may differ as a function of fault dip. Figure 6-6 shows Mohr's circles diagrams that illustrate the stress states before and after the earthquake in two M_w 5.5 models with fault dip angles of 30° and 70°. The left and right diagrams show results from the footwall and the hanging wall sides, respectively. The gently-dipping fault geometry (dip angle of 30°) results in a more efficient stress relaxation than the steeper one. A more extensive stress relaxation gives lower residual shear stresses (smaller Mohr circles) and a corresponding increase in fracture stability.

The more extensive stress relaxation obtained with smaller primary fault dip angles can also be observed in Figure 6-7, which shows principal stress vector plots in vertical sections before and after the earthquake in M_w 5.5 models with dip angles of 30° and 70°. The vectors are coloured according to the magnitude of the major principal stress. The initial stresses are equal in the models before rupture initiation. After the earthquake the major principal stress is about 10 MPa lower at repository level in the model with the gently-dipping fault. Note that compressive stresses are negative in *3DEC*.
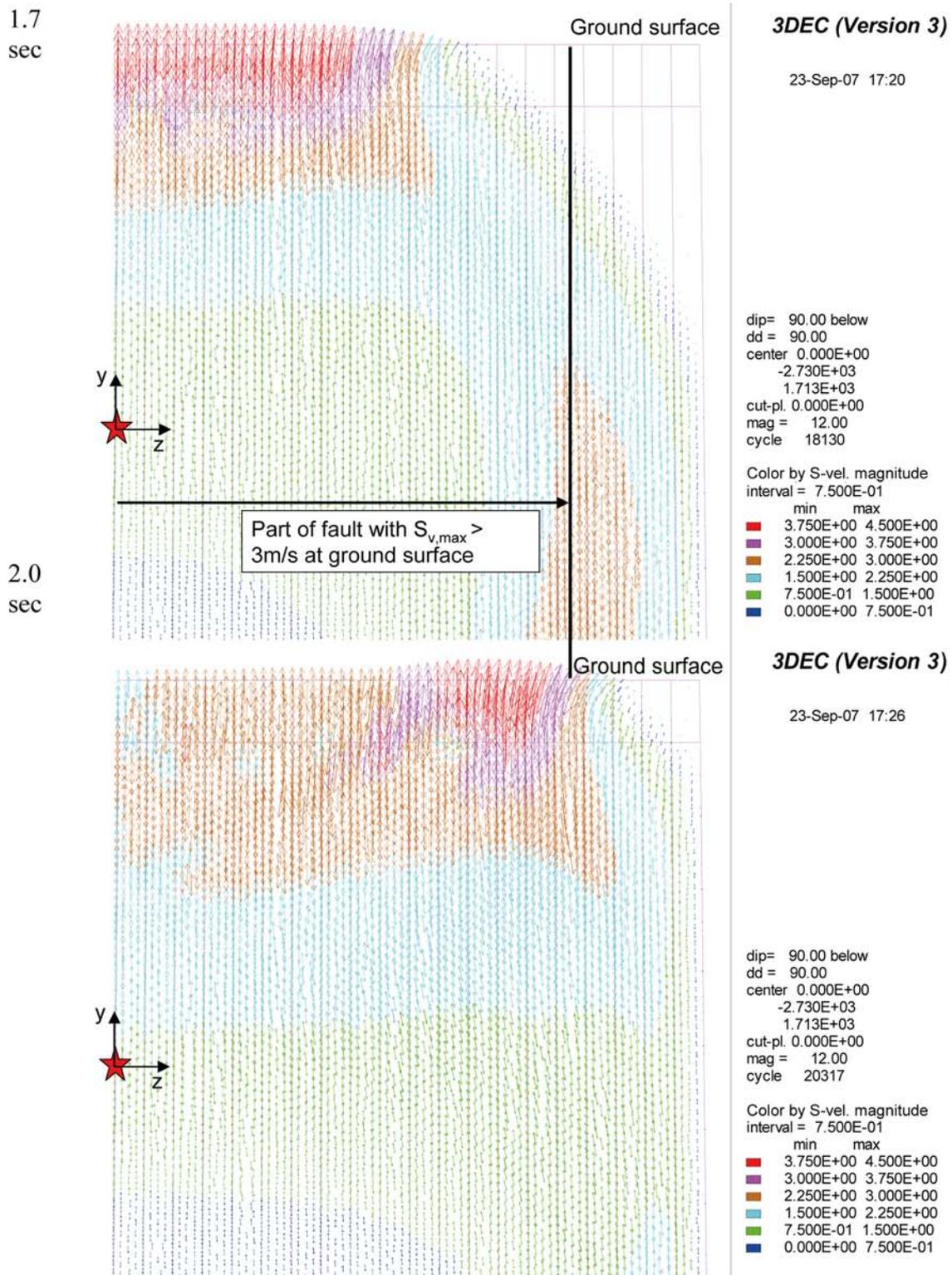
Figure 6-5. *Upper: Primary fault slip velocity vectors after 1.7 s. Lower: Primary fault slip velocity vectors after 2.0 s. Results from the M6_Str1_tfBASE_rt05 model with strength reduction time 0.5 s. The hypocentre is indicated with a red star. Note: The lower part of the fault plane is hidden in the plots.*
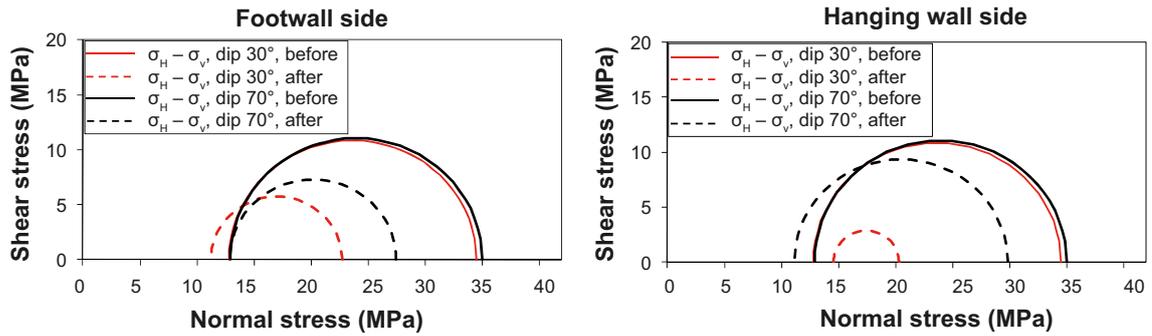
Figure 6-6. *Mohr's circle diagrams illustrating stress states before and after earthquake in M_w 5.5 models with fault dip angles 30° and 70°.*
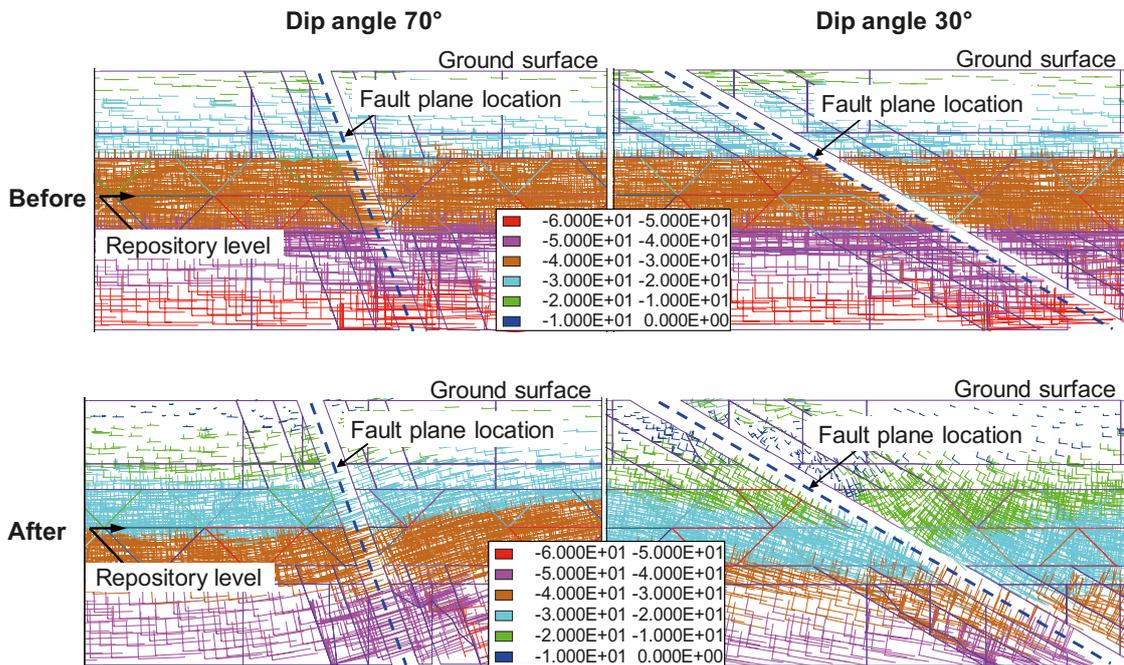
Figure 6-7. *3DEC principal stress vector plots in vertical sections in M5.5 models with fault dip angle 70° (left) and with fault dip angle 30° (right). The vectors are coloured according to the magnitude of the major principal stress. Top: Before earthquake. Bottom: After earthquake. Note that compressive stresses are negative in 3DEC.*

6.3 Fault displacement and rupture area

The left diagram in Figure 6-8 shows a regression analysis of the correlation between fault maximum displacement and moment magnitude for earthquakes contained in the database compiled by /Wells and Coppersmith 1994/. The right diagram shows the correlation between rupture area and moment magnitude. The regressions are based on data from a large number of events. Data points corresponding to the *3DEC* models are appended to the diagrams. The following observations can be made from these regressions:

- The maximum fault displacements in the M_w 5.5 and M_w 6.2 models fall almost within the range of observed real-life data, but are generally on the conservative side; i.e. the modelled displacements are large compared to most of the observation data. For the M_w 5.5 models with a fault dip angle of 70° there is a significant influence of the fault residual strength on the amount of slip. For the M_w 5.5 case with fault dip 30° the residual strength makes no significant difference (the red and pink markers coincide in the plot). The amount of slip in the M_w 7.5 models coincides well with the regression line.

- The rupture areas in the models fall within the range of the observed data. However, the model areas are smaller than the areas of the corresponding real events. Even if the areas would be increased by a factor 3–4 they would still be within the data range. This also means that the average fault displacements could be reduced correspondingly without changing the moment magnitudes of the simulated earthquakes. Note that all M_w 5.5 models have the same rupture area.

The observations indicate that the models have relatively large fault displacements that are concentrated along faults with relatively small rupture areas. Thus, it can be concluded that, as far as the fault displacement and rupture area is concerned, the models seem to be realistic, albeit conservative.
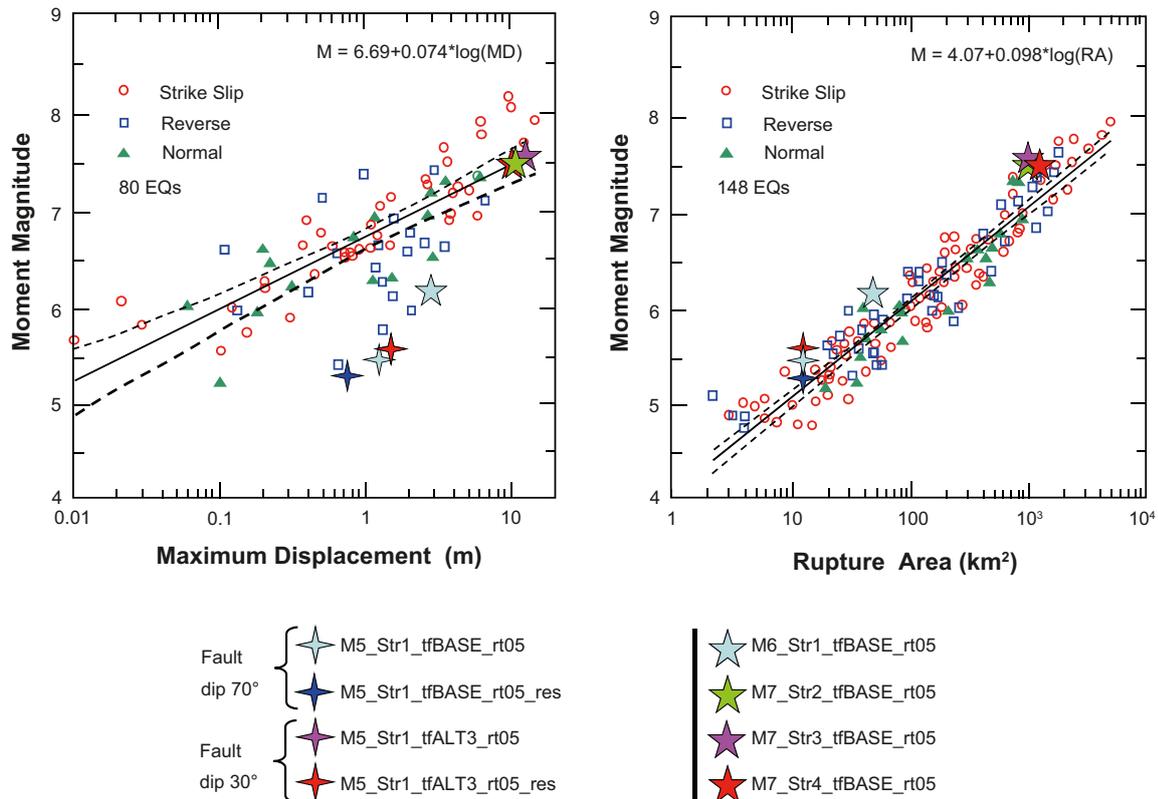
Figure 6-8. *Left: Database regressions of the correlation between earthquake magnitude and maximum displacement. Right: Database regressions of the correlation between earthquake magnitude and rupture area. Redrawn from /Wells and Coppersmith 1994/. Data from the 3DEC models are indicated in the diagrams according to the legend at the bottom.*

6.4   Ground velocities

Figure 6-9 and Figure 6-10 show time histories of velocities in the x-and y-directions at the ground surface in the M6_str1_tfBASE_rt05 and M7_str4_tfBASE_rt1 models, respectively. It is interesting to compare these modelling results with the velocities measured during the 1999 Chi-Chi earthquake. Figure 6-11 shows horizontal (E-W) and vertical velocity components recorded at six stations during that earthquake. When the modelling results are compared with the real earthquake data, the following results are observed:

- The peak velocities are of the order of 100 cm/s 1 km from the fault surface break in both *3DEC* models. In the northern high-velocity region of the Chelungpu Fault, the TCU068 and TCU052 stations recorded very high velocities with peaks in the range of 200–300 cm/s. This is considerably higher than the peak velocities recorded in the *3DEC* models. However, if the modelling results are compared with the velocities at the other stations, there is a better agreement. These stations had maximum velocities similar to those of the models.

- The shapes of the curves recorded in the models are similar to the recordings at station TCU068 and TCU052. The curves are dominated by low frequency waves with durations in the range of 3–10 sec. The absence of high frequencies in the northern part of the rupturing fault has been explained by /Ma et al. 2003/ to be caused by slip-induced high pore pressures inside the fault, which resulted in lubrication of the slipping surfaces. This kind of relatively smooth slip behaviour is, with some exception, also found in the *3DEC* models. This may be a result of the idealised representation of the earthquake, i.e. the rupture was propagated along a perfectly planar surface by use of an algorithm that controlled the fault strength reduction. In addition, the residual fault strength was set to zero. The recordings at the other stations along the Chelungpu Fault were more dominated by high frequencies.

We only have velocity recordings from one historical event (Chi-Chi) to use as a reference. However, comparison of the model results with that earthquake indicates that the temporal development of velocities in the models is similar to what occurs in real events. Qualitatively, the models behave similarly to the northern high velocity region during the Chi-Chi earthquake, whereas the model behaviours are quantitatively in better agreement with other regions around the Chelungpu Fault.
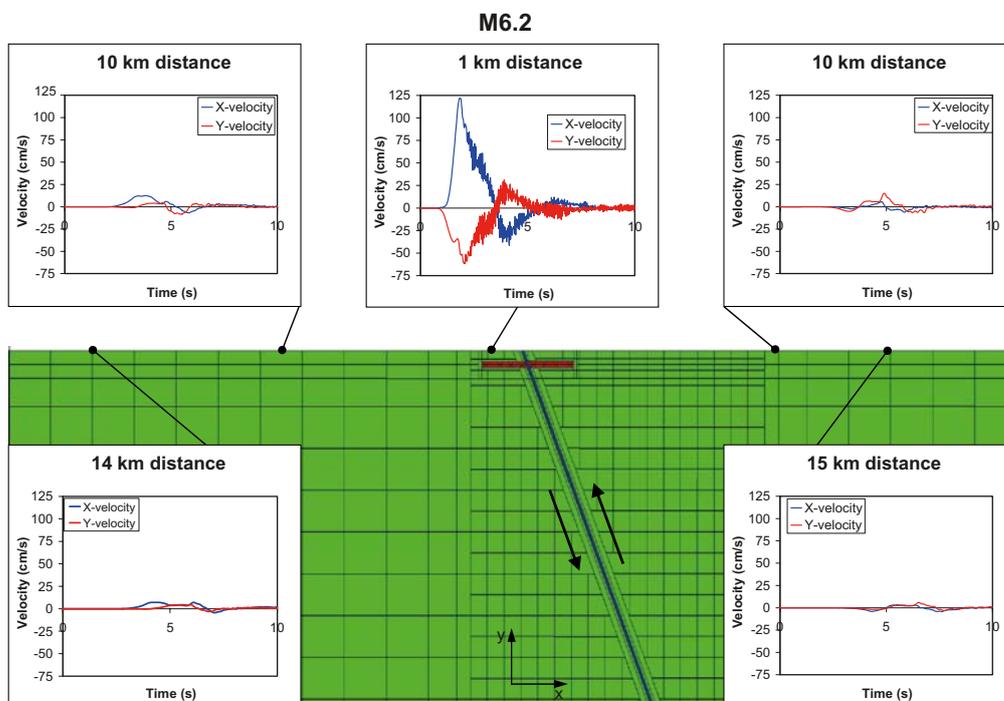
Figure 6-9. *Velocities at the ground surface in M6_str1_tfBASE_rt05. The distances that are given are with respect to the surface break of the fault.*
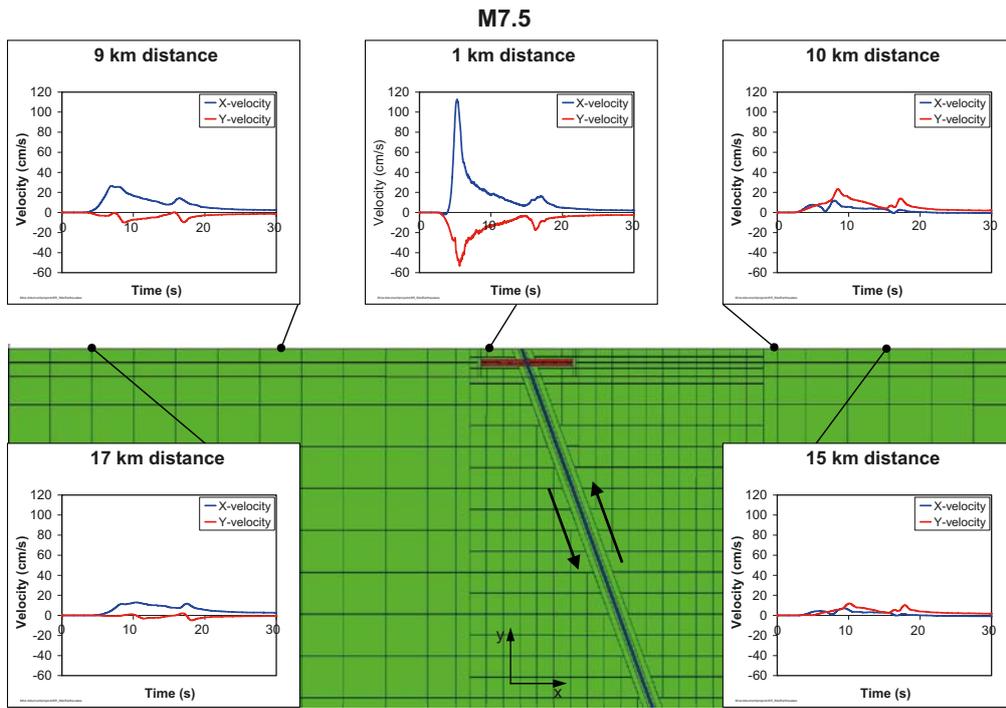
Figure 6-10. *Velocities at the ground surface in M7_str4_tfBASE_rt1. The distances that are given are with respect to the surface break of the fault. The wave passing after 17–18 s is due to reflections at the truncation boundary. This does not have any importance for the results.*
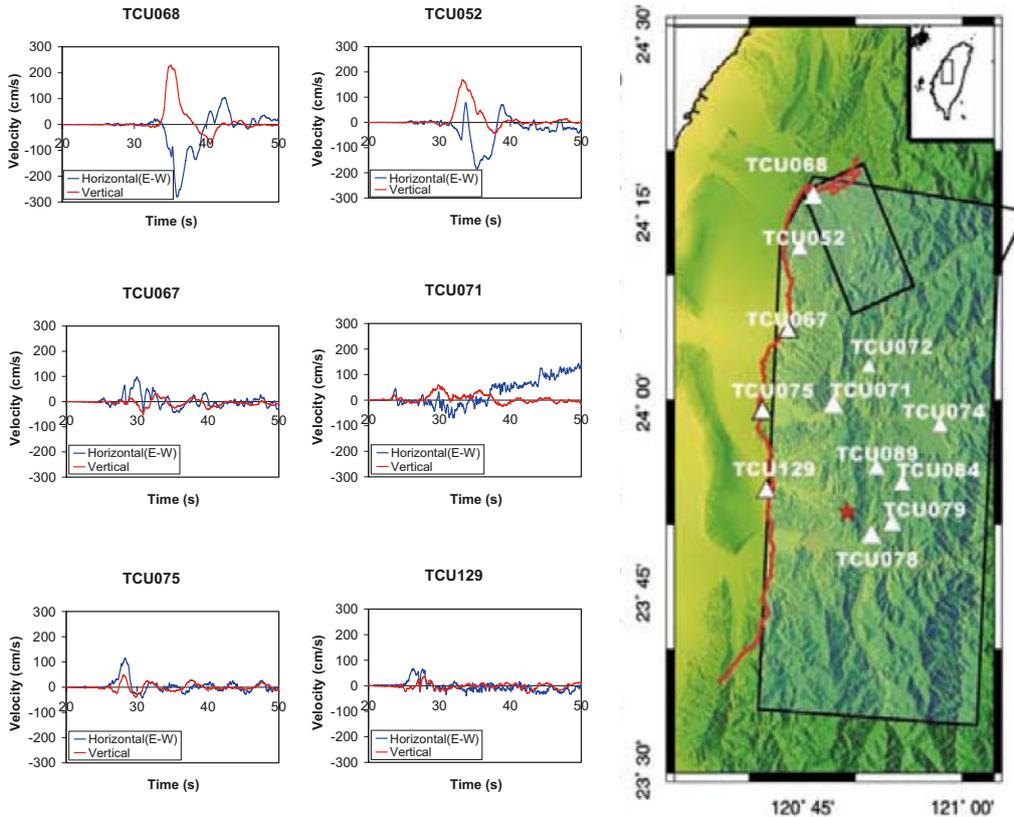
Figure 6-11. *The diagrams show the east-west and vertical components of ground velocities measured during the 1999 Chi-Chi earthquake. The velocities were derived based on acceleration data downloaded from the web site of the Central Weather Bureau of Taiwan /CWB 2009/. The map indicating the locations of the stations around the Chelungpu Fault is from /Ma et al. 2003/. The solid red line indicates the surface breaks of the Chelungpu Fault and the asterisk indicates the epicentre of the Chi-Chi earthquake.*

6.5   Seismic attenuation

The attenuation of ground accelerations (PGA), ground velocities (PGV) and ground displacements (PGD) in the models are compared with empirical relationships found in the scientific literature. Figure 6-12 shows the horizontal components of PGA, PGV and PGD in the M5_Str1_tfBASE_rt05 model (fault dip of 70° with no residual friction), M6_Str1_tfBASE_rt05 model and the M7_Str4_tfBASE_rt1 model plotted together with empirical relations developed by /Campbell 1989, Skarlatoudis et al. 2003, 2004, 2007, Boatwright et al. 2003/, scaled to the actual earthquake magnitude. Since the relation by /Campbell 1989/ is based primarily on data from small to moderate size earthquakes ($2.5 \leq M_L \geq 5.0$) it is only compared with the M_w 5.5 model data. The following can be observed:

* The model values follow two trends – one with higher values and one with lower. These correspond to recordings on the footwall and the hanging wall sides of the fault, respectively. The difference in the response between the hanging wall side and the footwall side is marked by a significant jump in the values at the location of the fault surface break. All recording points at smaller distances from the epicentre than the fault surface break are located at the same side (hanging wall) of the fault (Figure 6-13).

* Compared to /Skarlatoudis et al. 2003, 2004/ there is some overestimation of the attenuation of PGA in the model results. However, at distances less than about 2 km in the M_w 5.5 and M_w 6.2 models, within the region of interest here, the agreement is reasonable. At 2 km, the values may differ within half on an order of magnitude. In general, the best fit is achieved by the M_w 6.2 model. The fit for the M_w 7.5 model is less good.

* The best agreement between models and empirical relations is achieved for the PGV. The fit is reasonable good both at shorter and longer distances, in particular for the M_w 5.5 and M_w 6.2 models.

* The PGD values are in general much higher than those predicted by the empirical relationships. At a 2 km distance from the primary fault the values differ by about one order of magnitude or more.

The reasonably good agreement between model data and the empirical relationships regarding accelerations and velocities indicates that the models may produce velocities and accelerations of about the same magnitudes that are produced by real events.

The reason for the large difference in the displacement results is probably due to the fault geometry; all *3DEC* faults breach the ground surface. Additionally, they have zero residual strength, which allows for large continued displacements after the rupture has been completed (cf. Figure 5-5).

The calculated velocities are in good agreement with results from numerical 2D analyses of dip-slip events of approximately M_w 7 performed by /Oglesby et al. 1998/ who obtained a ground velocity of about 2 m/s at the fault surface trace and about 0.5 m/s at 5 km distance from the fault surface trace.

6.6   Pore pressure

During a glacial cycle, increased pore pressures will develop in the rock and soil below the ice sheet. The residual excess pore pressure at the repository level after ice retreat can vary depending on the duration of the ice cover and on the bedrock hydraulic properties (cf. Section 1.1.1). The residual pressure might be of the order of 1 MPa /Chan et al. 2005, Hökmark et al. 2010/.

Earthquakes can produce sudden pore pressure changes due to large fault displacements. For instance, the pore pressure in the high velocity region of the rupturing fault during the 1999 Chi-Chi earthquake has been estimated to be as high as 20 MPa /Ma et al. 2003/. However, local pore pressure transients inside the fault induced by large displacements are judged here to be of little importance for target fractures located in the competent rock hundreds of metres from the fault.

More moderate fracture pore pressure changes may arise in the surrounding rock as a result of the stress waves accompanying the fault slip. Fracture pore pressures will increase in response to increasing normal compression and decrease when the compression is reduced /Björnsson et al. 2001/, i.e. the varying pore pressure will tend to balance the effects of fracture normal load variations on the fracture effective stress and, consequently, on the fracture shear strength. In the *3DEC* target fractures, pore pressures are fixed and cannot vary which could mean that the temporary loss of strength found to be responsible for some of the slip in the models may have been slightly exaggerated. Considering that the influence of the fixed 1 MPa excess pore pressure set in two models in accordance with the estimates by /Chan et al. 2005, Hökmark et al. 2010/ was found to be modest, the implications of this cannot be significant. Ignoring pore pressure variations is, however, conservative.

	PGA	PGV	PGD
M5.5			
M6.2			
M7.5			
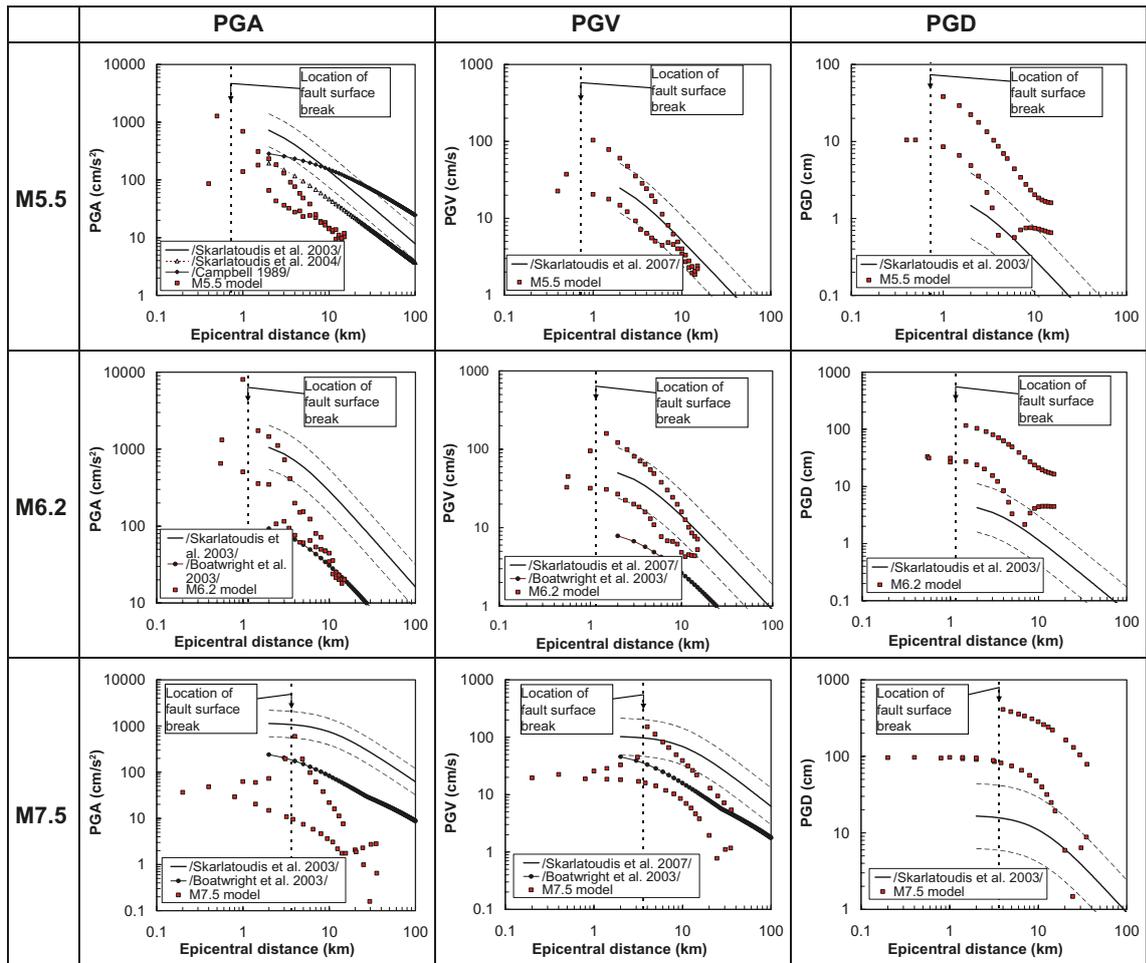
Figure 6-12. *Comparison of PGA, PGV and PGD in (upper) M_w 5.5 models, (middle) M_w 6.2 models and (bottom) M_w 7.5 models with empirical attenuation relations from /Campbell 1989, Skarlatoudis et al. 2003, 2004, 2007, Boatwright et al. 2003/ scaled to the actual earthquake magnitude. The ±1σ-curves are from /Skarlatoudis et al. 2003, 2007/. The location of the fault surface break is also indicated.*
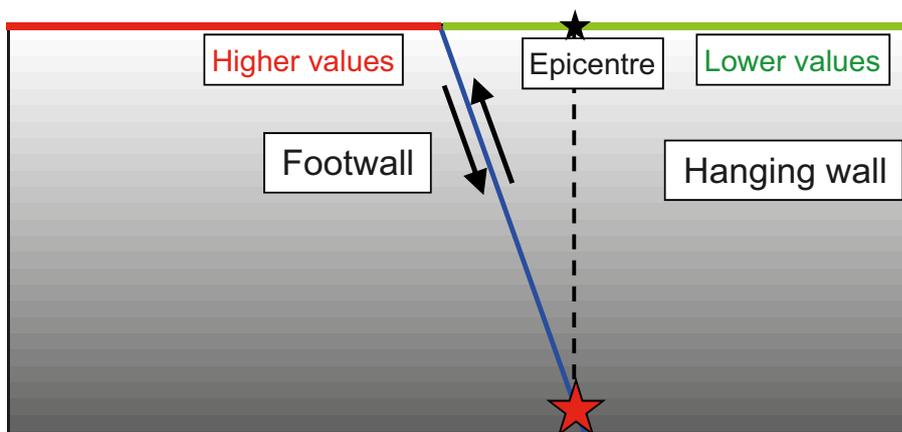
Figure 6-13. *The models give in general higher values of PGA, PGV and PGD on the footwall side.*

6.7   Target fracture shear strength

The target fracture shear strength parameter values are in accordance with site investigation data /Glamheden et al. 2007/. These data were obtained from tests with typical test sample sizes, i.e. in the order of 0.1 m, whereas the target fractures in the models here have radii of 150 m. The strength properties are homogenously distributed over the entire fracture areas. All target fractures are assumed to be perfectly planar and continuous without kinks or large-scale rough irregularities. These assumptions imply that the effective fracture size (length in slip direction) may be overestimated here. From the modelling point of view, as far as the average fracture slip is concerned, this is equivalent to underestimating the fracture shear strength. The importance of fracture irregularities is indicated by the sensitivity study made in Section 5.4.9. The application of a 15° dilation angle resulted in a 10% reduction of the maximum induced fracture slip.

6.8   Fracture propagation

In the models described in this report, the host rock is assumed to behave in a linear elastic fashion, i.e. no effects of crack propagation at the tips of slipping target fractures are considered. This means that no energy is expended on crack propagation at the expense of slip. /La Pointe et al. 2000/ made an attempt to quantify such effects and found that crack propagation would reduce the slip considerably. However, in that study the fracture propagation criterion was schematic and generic, meaning that the effects were much exaggerated. In this study, with modest slip and, consequently, low stress concentrations around the fracture tips, the potential slip overestimates caused by not accounting for crack propagation are probably small. However, neglecting crack propagation is conservative.

6.9   Fracture population

Estimating the amount of energy that is released during an earthquake and could be expended on target fracture slip is complicated. We concluded that if estimates of possible fracture slip based on available strain energy were to be attempted, the energy would have to be distributed over a certain fracture area. The fracture area per unit of modelled rock mass volume is small compared with what is found in real rock masses. In the models, the specific fracture area is of the order of 0.006 m^2/m^3 in the target fracture region, whereas it is estimated to be in the order of 5 m^2/m^3 at the Forsmark site[3]. Therefore, it can be concluded that the amount of released energy per unit target fracture area in the models is high, which is conservative.

There may be a concern that most of the strain energy available is spent on slip in the target fractures at the smallest distances at the expense of underestimated slip in more distant fractures. However, /Fälth and Hökmark 2006/, who analysed models similar to those used here (*3DEC* models with numerous target fractures at different distances), cf. Section 2.2.2), compared the temporal development of slip in a target fracture at about 3 km distance from the fault with the development of slip in a similar fracture at the same distance in a earlier *FLAC3D* analysis (cf. Section 2.2.1). The *FLAC3D* model included only this single fracture and thus there were no other fractures at smaller distances that could spend strain energy on slip. The comparison showed a very good agreement between the results, both qualitatively and quantitatively. This indicates that the influence of the target fractures at smaller distances on the slip in more distant fractures is negligible in the models.

6.10   Fault edge effects

In all models analysed in this study the continuum was assumed to behave in a linear elastic fashion. Elastic models can be used to predict stresses and deformations far from fault edges. Close to fault edges, however, the linear elastic assumption will be less valid since it does not allow for inelastic deformations and thus introduces stress singularities at such locations. Real faults always exhibit inelastic deformations around their tips /Scholz 2002/. This suggests that the stress redistributions and the corresponding target fracture instability indicated by the diagram in Figure 5-12, induced around the vertical fault edges in the M_w 5.5 and M_w 6.2 models, are over- predicted rather than under-predicted. Hence, the fracture displacements found close to the fault edges seem to be over-estimated rather than under-estimated.

---

[3] Modelldatabasen, 2007a. Model: PFM DFN 2.2.xls. Version 0.6. Approved 2007-11-29. Modified 2009-05-18. Modeller: A. Fox. Simon ID: GEO_WTAGLLAA. https://service.projectplace.com/pp/pp.cgi/r232241793.

6.11 Code precision and meshing

3DEC models can be analysed using either the single or double precision version of the code /Itasca 2003/. The models analysed by /Fälth and Hökmark 2006/ were run using the double precision version of *3DEC*. The double precision version requires three times the amount of computer memory required by the single precision version. The intention of this study was to analyse yet larger models than those analysed by /Fälth and Hökmark 2006/. Due to memory allocation limitations in *3DEC*, it was necessary to use the single precision version in the present work.

In the models, the continuum was discretised using finite-different zones. In general, a finer discretisation produces more accurate results. Figure 6-14 shows two models with different discretisations. The upper picture shows the zone outlines of a coarser meshed model. This discretisation corresponds to what was used in the *3DEC* models analysed by /Fälth and Hökmark 2006/. The lower picture shows a model where the volume with high density zoning has been extended and the number of zones has been increased significantly. The discretisation shown by the lower picture was used in the M_w 6.2 models in the present study.

In order to examine the possible differences in results due to code precision and discretisation, results from two single precision models with different meshes were compared with corresponding double precision results from /Fälth and Hökmark 2006/. The results are shown in Figure 6-15 as cumulative frequencies of induced target fracture displacements. It can be concluded that the results from the models are similar. However, the displacements in the more densely meshed model are in general smaller than in the two less less-refined models. It seems, at least for these three models, that the increase in mesh density is more important to model results than the code precision.

Coarse model:
~1,000,000 zones
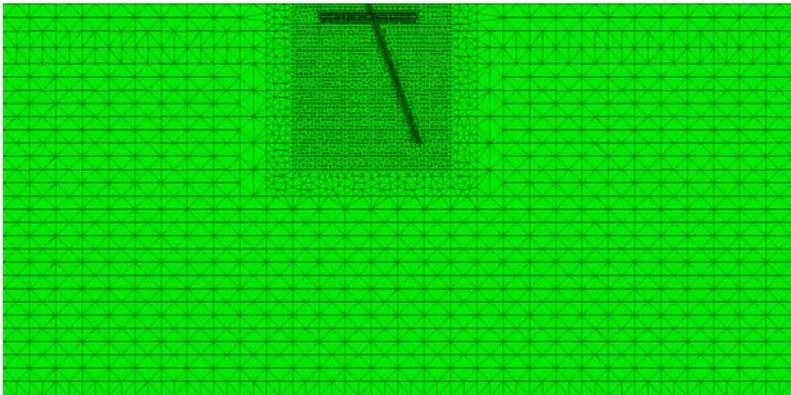
Fine model:
~2,800,000 zones
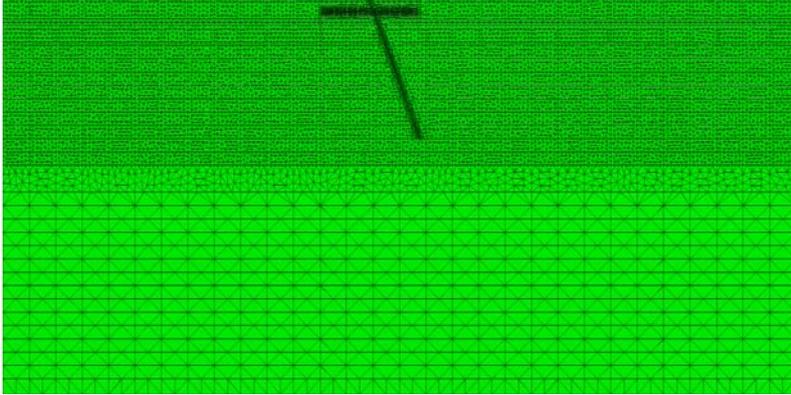
Figure 6-14. *Different discretisations of the continuum in M_w 6.2 models.*

Target fractures at 200 m and 600 m distance from M6.2 event
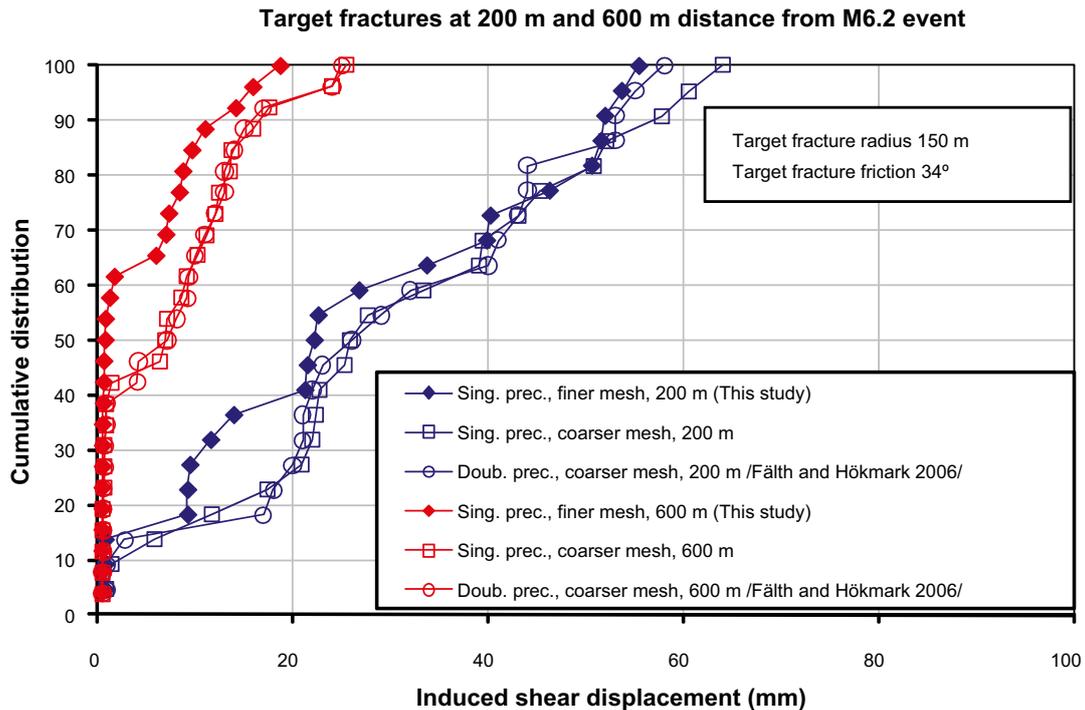
Figure 6-15. *Cumulative distribution of induced target fracture shear displacements. The results from three models are shown: (1) Double precision model, coarser discretisation /Fälth and Hökmark 2006/, (2) Single precision model, coarser discretisation, (3) Single precision model, finer discretisation (this study).*

6.12 Comparison between *3DEC* and *WAVE* results

In a study conducted in conjunction with earlier SKB safety assessment work, dynamic earthquake models were analysed and reported in /Munier and Hökmark 2004/. One of the models in that study was analysed by Applied Seismology Consultants Ltd (UK) with the program *WAVE* /Hildyard et al. 1995/ (cf. Section 2.2.1). The effects of a magnitude 6 earthquake were simulated by the prescription of shear displacements along a fault plane. The displacement pattern was designed to simulate the effect of the propagation of a rupture along the plane. The net average stress drop in the *WAVE* model was 15 MPa, which is similar to what was used in the M_w 6.2 *3DEC* models in the present study. The mechanical properties for the continuum used in the *WAVE* model were also similar to what was used in the *3DEC* models.

Even though previous sections have presented comparisons between *3DEC* model results and literature data from real events, it is interesting to compare the results from the *3DEC* model used here with the *WAVE* results. Velocity records from the *WAVE* model were compared with velocity records from the *3DEC* M_w 6.2 model. The conceptual geometries of the models and the locations of the recording points are shown in Figure 6-16. Due to the non-vertical primary fault in the *3DEC* model the resulting velocity histories are not equal at both sides of the fault. Therefore, two recording points were used in that model.

When the results from the models are compared one should consider the following differences between the models.

- The fault plane ends 1 km below the ground surface in the *WAVE* model whereas it breaches the ground surface in the *3DEC* model.

- The fault plane is vertically-oriented in the *WAVE* model. In the *3DEC* model the fault plane is dipping 70°.
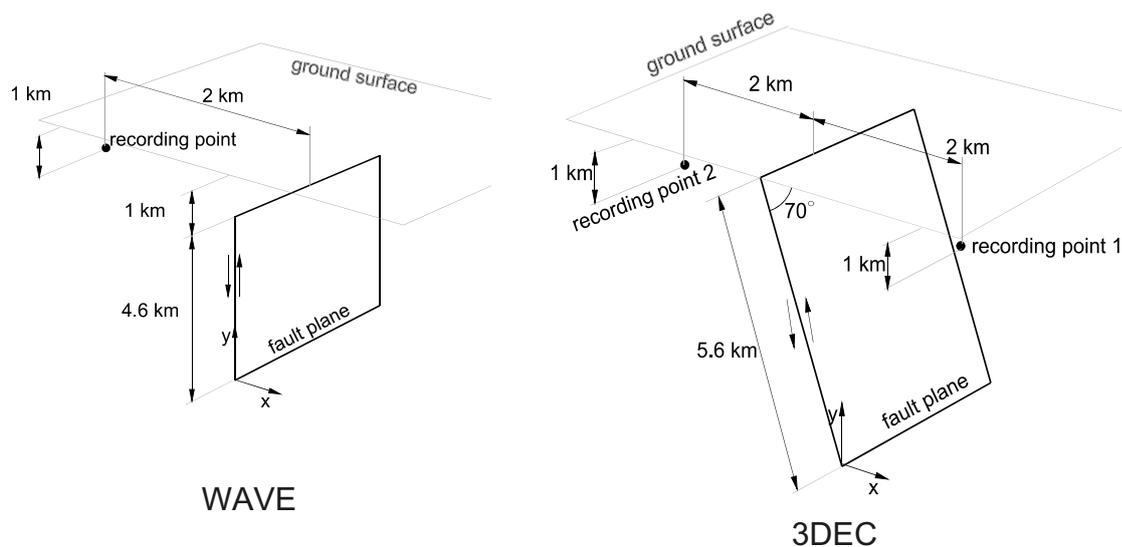
Figure 6-16. *Conceptual geometries of the models and location of recording points. Left: WAVE model. Right: 3DEC model.*

In Figure 6-17 and in Figure 6-18, the *3DEC* velocity records at recording points 1 and 2, respectively are compared with the velocity records from the *WAVE* model. The recording points were located 2 km from the fault's upper edge at a depth of 1 km. The following observations were noted:

• The seismic response occurs at about the same time in both models.

• The time period of the oscillation is about the same in the models. The slightly longer periods and higher amplitudes in the *3DEC* model may be due to the lower stiffness of that mechanical system, which has a ground surface breaching fault geometry.

• The *3DEC* velocities at point 2 have the same directions as the *WAVE* velocities (Figure 6-18). This is logical since the location of the recording point in the *WAVE* model corresponds to the footwall side in the *3DEC* model (in terms of the direction of the fault movement).

6.13 Summary of confidence and relevance considerations

6.13.1 General

The modelling technique applied here in the numerical simulations is the same as that used for establishing the background material for the SR-Can seismic risk assessment /Fälth and Hökmark 2006/. That study included models simulating M_w 6.2 earthquakes only, whereas the model catalogue is expanded significantly in the present study. In total 20 models are analysed, with a magnitude range of M_w 5.5–7.5. The models simulate earthquakes of different moment magnitude, primary fault geometry, average stress drop and fault slip velocity. The present study can be regarded both as a continuation and expansion of the work by /Fälth and Hökmark 2006/.

Expanding the numerical background material as described above was the primary objective of the present study, while strengthening the general confidence in the modelling technique was an important secondary objective. This secondary objective was accomplished, as summarized here below, by checking that the rock mass response to the synthetic *3DEC* earthquakes is consistent with recordings from real earthquakes. The tertiary objective of the modelling work was to establish whether or not the numerical approach and the numerically obtained results were relevant and sufficiently conservative for the layout and risk assessment purposes. The outcome of the evaluation of the modelling with this objective in mind is summarized here below. The fourth main objective, to provide recommendation of the handling of the results in layout and risk assessment work, is addressed in Chapter 7.

Seismic velocities for magnitude 6 earthquake at 2 km distance
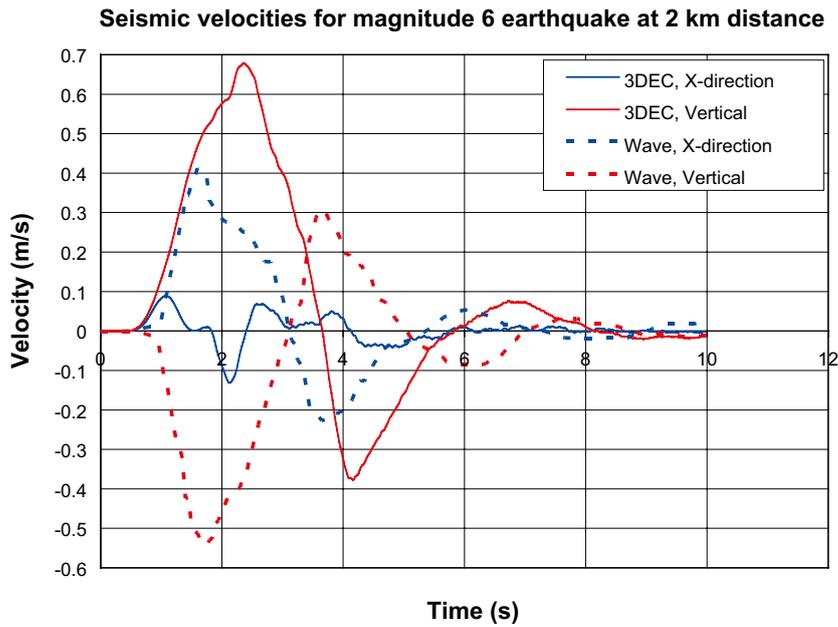
Figure 6-17. *Comparison between velocity records from the 3DEC model and WAVE model. The 3DEC results were taken from the hanging wall side (recording point 1).*

Seismic velocities for magnitude 6 earthquake at 2 km distance
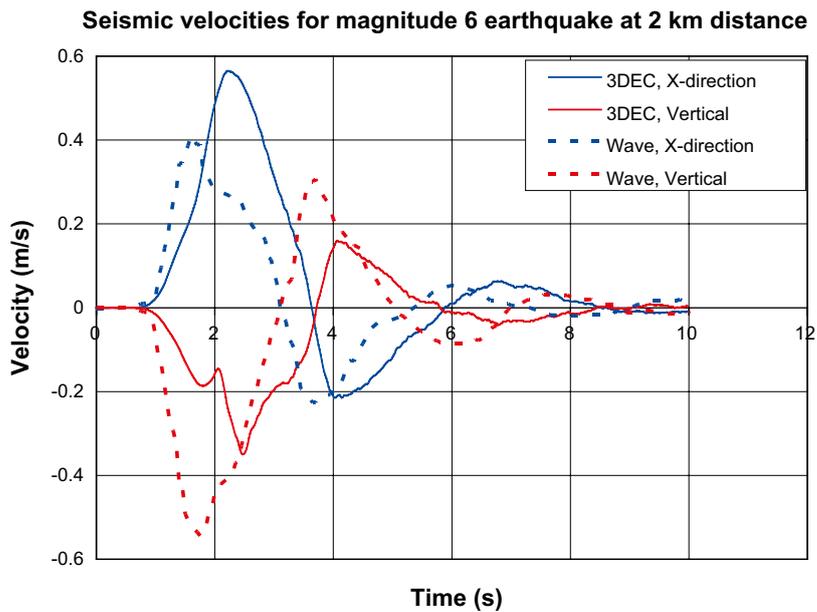
Figure 6-18. *Comparison between velocity records from the 3DEC model and WAVE model. The 3DEC results were taken from the footwall side (recording point 2).*

6.13.2 Confidence in the modelling technique

Source mechanism

It is assumed that the accelerations, velocities and displacements produced by a model can be used as indicators of how well the model is able to simulate the effects of a real earthquake. Ground velocity recordings in one M_w 6.2 model and in one M_w 7.5 model are compared with ground velocities recorded around the Chelungpu Fault during the 1999 Chi-Chi earthquake. The peak velocities are of the order of about 100 cm/s 1 km from the fault surface break in both *3DEC* models. In the northern high velocity region of the Chelungpu Fault very high velocities, with peaks in the range of 200–300 cm/s, were recorded. However, at several other stations around the Chelungpu Fault the velocities were similar to those in the models. It was also observed that the shapes of the velocity curves from the models are similar to those recorded during the earthquake.

The attenuation of peak ground accelerations (PGA), peak ground velocities (PGV) and permanent ground displacements (PGD) in some models are compared with empirical relations based on earthquake data. The comparisons indicate that the models give PGA values close to the epicentre that are in agreement with the empirical relations, but that there is some over-estimation of the PGA attenuation. Regarding the PGV values, there is good agreement between models and the literature data, both at shorter and longer distances. The PGD values are in general strongly exaggerated by the models. The good agreement at short distances for PGA and PGV values indicates that the region close to the primary fault, where the target fractures are located, is subjected to dynamic forces similar to those produced by a real seismic event.

Velocity records from a M_w 6.2 *3DEC* model are compared with corresponding results from a M_w 6 model analysed with the dynamic code *WAVE* /Munier and Hökmark 2004/. Despite the fact that there are differences between the fault geometries, the results are similar. The seismic waves have the same propagation speed and the velocity curves agree both qualitatively and quantitatively. The amplitudes of the velocity curves are larger in the *3DEC* model but this can be accounted for by the difference in fault geometry.

The *3DEC* models analysed by /Fälth and Hökmark 2006/ were run assuming double precision. Due to memory allocation limitations in the code this is not possible when analysing larger models; consequently, all models developed during the current project were run in single precision. A comparison between single and double precision indicates that the maximum difference in results is about 10%.

Target fractures

The correlation between the amount of induced target fracture shear displacement and the fracture diameter was examined. The results show that, under dynamic conditions, both the shear displacement and the shear velocity on a fracture scale linearly with the fracture diameter. This is in agreement with closed-form solutions /Eshelby 1957/ used for the calculation of fracture shear displacements under static conditions. The results indicate that the target fracture displacement results obtained from the models (with target fracture radii 150 m) can be applied to other fracture sizes by linear scaling.

The distribution of shear displacement in the target fractures is checked against a closed-form solution. The comparison shows that the *3DEC* model results and the analytical results agree within less than 15%.

6.13.3 Relevance and conservativeness

Source mechanism

Model results are compared with earthquake data compiled by /Wells and Coppersmith 1994/. The comparison shows that the maximum fault displacements in the models are large given the rupture areas. This means that the simulated earthquakes are of the largest possible magnitudes consistent with their fault sizes.

The large fault displacements relative to the fault dimensions are also reflected by a comparison of the average stress drop in the models with literature data. The average stress drops (based on fault displacement/fault width ratios) of the models are compared with corresponding stress drop estimates for the post-glacial faults (Pärvie and Lansjärv) in northern Fennoscandia and the 1999 Chi-Chi earthquake. The comparison indicates that all M_w 6.2 and M_w 7.5 models have average stress drops that are well

above the estimated value for the Pärvie Fault and that the average stress drops in the M_w 5.5 models are on par with the Pärvie stress drop and well above that of the 1999 Chi-Chi earthquake. Hence, in this respect the models can be regarded to be realistic and conservative.

There is a significant correlation between the fault slip velocity and the amount of induced fracture displacement in the models. This indicates that the fault slip velocity is a good indicator of how large impact an earthquake can have on the surrounding bedrock. The peak fault slip velocities in the models are compared with the peak fault slip velocity recorded during the high velocity Chi-Chi earthquake. Several of the models have fault peak slip velocities that are about the same as those associated with the Chi-Chi earthquake, while some models have velocities that are 40–90% higher. Further, the highest slip velocities during the Chi-Chi earthquake were found along only a limited part of the fault, whereas the models show high velocities along major parts of their surface breaks. This means that the synthetic earthquakes do not only have large maximum slip velocities, but also that a disproportionally large fraction of the target fractures are subjected to high dynamic effects.

The modelling results indicate that an earthquake along a steeply-dipping fault results in larger secondary shear displacements than an earthquake along a gently-dipping fault. This difference can be explained by the fact that a gently-dipping fault gives a more effective relaxation of stresses, which results in greater fracture stability. The layout rules set up in the following chapter are based on results from models with steeply-dipping faults. Applying these rules to gently-dipping faults should therefore be conservative.

In all of the models implemented during this study, the bedrock is represented by a linear elastic continuum. As such, many (smaller) deformation zones and fractures that are present in the real rock mass have not been explicitly modelled. Since inelastic movements in such structures will cause seismic waves to attenuate, the elastic continuum representation tends to over-predict the magnitude of induced fracture displacements. This is particularly true close to the edges of the faults. According to /Scholz 2002/ the linear elastic assumption is a good approximation far from fault edges but close to the edges, where real faults always show plastic deformations, it results in singularities and over-estimated stress concentrations. In conclusion, it seems reasonable to assume that, as far as the rock mass representation is concerned, the induced fracture shear displacements may be viewed as over-estimates of the potential seismic response, and are therefore conservative.

Target fractures

The target fractures are assumed to respond to loads according to an idealised elasto-plastic material model with linear joint stiffness, zero tensile strength and shear failure according to a Coulomb criterion. The shear strength parameter values are in accordance with data obtained from the site investigations at the Forsmark site /Glamheden et al. 2007/. There are some idealisations in the models that imply that the shear displacement results may be on the conservative side:

- All target fractures are, despite their sizes (150 m radius), assumed to be perfectly planar and continuous without kinks or large-scale irregularities. These assumptions imply that the effective fracture size is overestimated.
- Due to the linear elastic assumption, no energy is expended on fracture propagation and fracturing at the fracture tips. This may mean that the amount of energy available for shear slip is overestimated.
- The specific fracture area per unit rock mass volume in the models is about three orders of magnitude less than at the candidate sites, which means that the released strain energy per unit fracture area in the models is high.

There is no account of any fracture dilation in the models. A sensitivity study (Section 5.4.9) indicates that including a 15° dilation angle (in agreement with Forsmark site data) results in a reduction of the induced fracture slip of about 10%. Omitting this effect in the models is conservative.

The basic assumption regarding the pore water pressure is that all target fractures have a 5 MPa pore pressure, i.e. the undisturbed hydrostatic pressure at 500 m depth. Studies indicate however that the pore pressure at this depth may increase at most by about 1 MPa during a glacial period /Chan et al. 2005, Hökmark et al. 2010/. The effect of a 1 MPa excess pore pressure is included in two models. The pore pressure increase has limited importance. In one of these models (M_w 5.5) the maximum induced shear displacement at 200 m distance increases by about 10% whereas it stays unaffected in the other model (M_w 7.5). These two models are chosen to be included in the background material for the safety assessment.

6.13.4 Remarks

The synthetic *3DEC* earthquakes give realistic values and distance dependence of parameters used in seismic hazard assessments and earthquake engineering (PGA, PGV). For the PGV results there is also a very good agreement with results obtained from independent simulations made with a different code /Oglesby et al. 1998/. They also give near surface fault slip velocities in agreement with (or larger than) velocity ranges reported in the literature for large and damaging earthquakes (Chi-Chi, Landers, cf. Figure 6-2). Also the ground velocity wave forms agree with those of real earthquakes. Stress drops agree with estimates made for the post-glacial faults in northern Fennoscandia (Pärvie, Lansjärv, cf. Figure 6-2). This indicates that the modelling approach is valid as far as the overall dynamic and quasi-static behaviour is concerned. In real faults the rupture initiation and propagation are influenced by fault irregularities, whereas the rupture propagates smoothly along a perfectly planar fault with uniform properties in the *3DEC* models. This does not appear to influence parameters of potential importance to response of nearby shallow rock volumes, which indicates that the approach is adequate for its purpose, i.e. to assess the stress impact on repository host rock fractures.

As for the response of the target fractures (slip and slip velocities), there is no obvious way of conducting a reality check. For the purpose of this study it may be sufficient to establish that, given the seismic stress impact, the conservative representation of the target fractures (perfectly planar, uniform properties, elastic embedment) gives slip magnitudes that are likely to be overestimates.

In order to be applicable in the layout- and risk assessment work, the modelling results have to be compiled and organized such that unambiguous and robust layout rules can be set up. This topic is addressed in Chapter 7.

7 Recommendations for use of results in layout- and risk assessment work

7.1 Interpretation model

The target fracture slip results presented in previous chapters were generated in models which cover wide ranges of assumptions regarding the initial stress state and details of the seismic source mechanism. All model results taken together give a good and reasonably systematic picture of the factors that control induced slip on target fractures. However, all models are not relevant for the purpose of establishing realistic upper-bound estimates of the induced slip caused by reverse, post-glacial faulting in Swedish bedrock. For some of the models, the maximum fault slip velocity exceeds that of the Chi-Chi earthquake by many tens of percent (cf. Figure 6-2), which is quite unrealistic. Note that the fault slip velocity appears to be the single parameter that impacts most on the induced slip (cf. Figure 5-21). Table 7-1 lists the M_w 5.5, M_w 6.2 and M_w 7.5 models that are judged to be the most relevant, i.e. sufficiently conservative but not over-conservative.

For practical use the results shown in Table 7-1 must be translated into a safe and robust interpretation model:

- The M_w 6.2 results are not as conservative as the others. There is no excess pore pressure in this particular model and the fault slip velocity is (relatively seen) not as high as for the other two. This suggests that the M_w 6.2 results should be up-scaled. To simplify future modelling and analysis, it is suggested that only two classes of faults be considered:
  - Small faults with surface trace lengths between 3 km and 5 km. The M_w 5.5 results are taken to be valid for potential earthquakes occurring on this category of faults.
  - Large faults with surface trace lengths larger than 5 km. The M_w 7.5 results are taken to be valid for these faults.

Table 7-1. Selected numerical modelling results.

Source-target distance	Target dip range	Moment magnitude (M_w) and selected model characteristics		
		5.5	**6.2**	**7.5**
		Fault slip velocity 70% of Chi-Chi M5_Str1_tfBASE_rt05_pp6	Fault slip velocity 51% of Chi-Chi M6_Str1_tfBASE_rt2	Fault slip velocity 93% of Chi-Chi M7_Str4_tfBASE_rt1, M7_Str4_tfBASE_rt1_pp6, M7_Str4_tfALT1_rt1, M7_Str4_tfALT2_rt1, M7_Str4_tfALT3_rt1, M7_Str4_tfALT4_rt1
200	0–55	One (out of 10) slipped 45 mm	One (out of 22) slipped 41 mm	One (out of 28) slipped 47 mm
	55–90	No results	No results	One (out of 8) slipped 28 mm
600	0–55	One (out of 14) slipped 13 mm	One (out of 26) slipped 11 mm	One (out of 28) slipped 26 mm
	55–90	No results	No results	One (out of 8) slipped 1 mm
1,000	0–55	< 1 mm	< 1 mm	One (out of 28) slipped 12 mm
	55–90	No results	No results	All (8) slipped < 1 mm
1,500	0–55	< 1 mm	< 1 mm	One out of (12) slipped 8 mm
	55–90	No results	No results	All (8) slipped < 1 mm

The surface trace length ranges are based on the regressions shown in Figure 1-6. A M_w 5.5 earthquake would have a rupture area a little larger than 20 km^2 and, assuming the width-length ratio to be about 1, a surface rupture length of 4–5 km. Assuming that the surface trace length is an upper bound estimate of the potential rupture length, the length ranges suggested here for the two categories of earthquakes appear to be plausible.

- Steeply-dipping target fractures slip systematically less than horizontal fractures and gently-dipping fractures. Here, steeply-dipping fractures are assumed to slip 25% less. This is conservative; the results in Table 7-1 indicate that they slip at least 40% less.

- There are results for 200 m and 600 m fault-target distances. Results for intermediate distances (e.g. 400 m) can be estimated using linear interpolation. This is conservative: The distance – slip curves (Figure 5-22, Figure 5-23, Figure 5-24) show that this will mean a small overestimate at the intermediate distances.

- The slip distributions (cf. Figure 5-17 through Figure 5-20) are approximated by linear relations (cf. Figure 7-1).

- An extra margin is added to the max slip results. The max slip for M_w 5.5 models is set at 50 mm for the 200 m distance and at 60 mm for the M_w 7.5 model. The reason for adding a smaller margin to the M_w 5.5 result is that the M_w 5.5 model must count as particularly conservative: A fault slip velocity almost on par with that of the M_w 7.6 Chi-Chi earthquake is very high for a M_w 5.5 event. (Note that peak ground velocities vary with magnitude, cf. Figure 6-12). For the other distances (400 m and 600 m) proportional margins are added.

The upper part of Figure 7-1 shows the actual results while the lower part shows the idealised target fracture slip distributions. The idealised linear distributions are used throughout the analyses presented in this chapter.
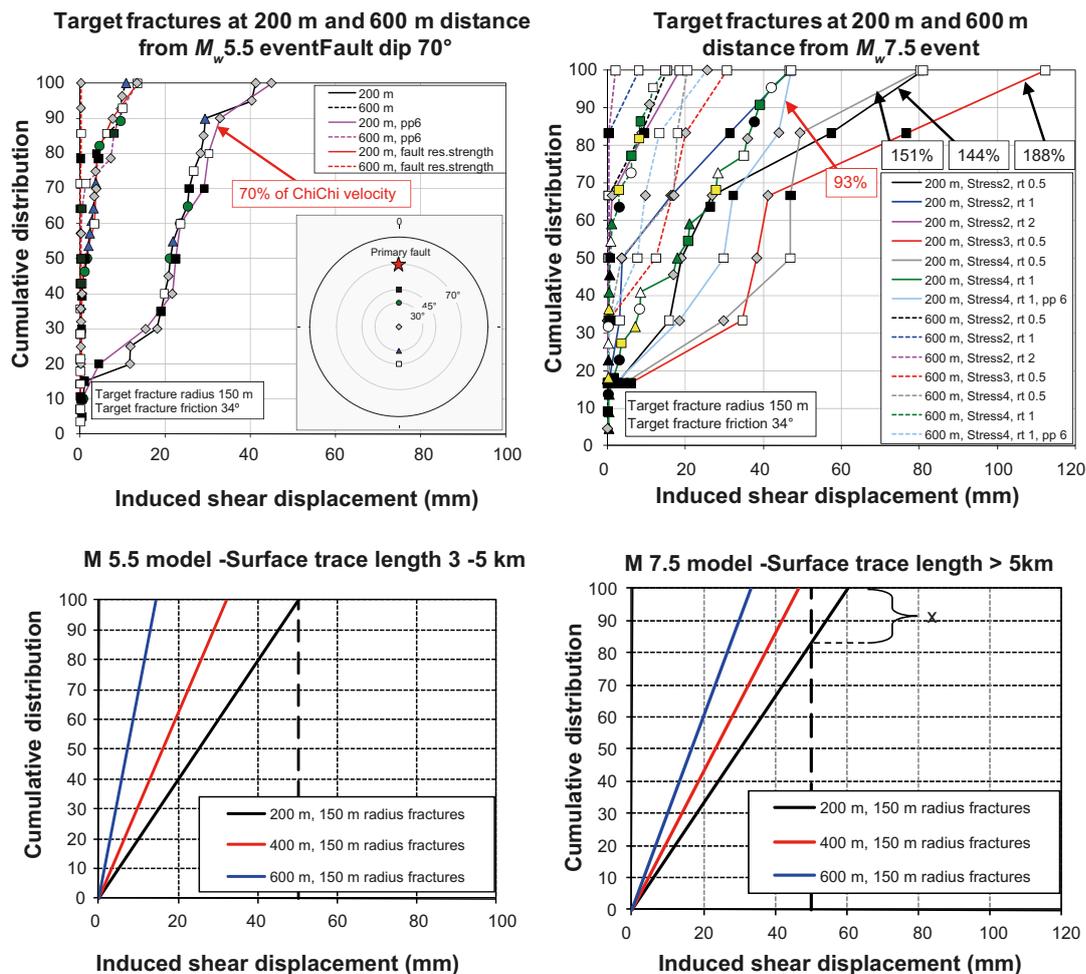
Figure 7-1. *Upper: Modelling results for M_w 5.5 and M_w 7.5 earthquakes. Red arrows denote the results selected for the continued processing. Lower: schematic representation with linear slip distributions. "x" (lower, right) denotes the percentage of 150 m radius fractures that would slip more than the 50 mm canister damage threshold.*

The target fracture shear velocity has importance for the loads that the canister potentially will be subjected to as a fracture intersecting a deposition hole slips /Börgesson and Hernelind 2006/. In Section 5.4.5 the shear velocities found in some models are presented and discussed, and the concept of effective shear velocity is presented. For buffer-canister analyses as those in /Börgesson and Hernelind 2006/, the effective velocity is here considered a relevant measure of slip velocity. For the models listed in Table 7-1, no fracture peak shear velocity is higher than 300 mm/s and the highest effective velocity is less than 200 mm/s.

7.2 Critical fracture radius and fraction of damaging slip

Given the linear slip distributions, the percentage x of fractures of radius r that slip more than a given threshold can be calculated as:

$$x = 100 \cdot \frac{a \cdot r - threshold}{a \cdot r}$$
<div style="text-align: right">Equation (7-1)</div>

Here, a is the slip/radius ratio for the maximum slip at a given distance (e.g. 200 m, 400 m or 600 m) for a given event category (e.g. occurring on small 3–5 km faults or on faults larger than 5 km), and a given target dip range (e.g. 0–55 or 55–90). The expression is based on the notion that fracture slip scales linearly with fracture size. Setting x to zero and solving for r gives the critical radius, i.e. the radius of a fracture that may slip by the threshold but not more.

The schematic slip distributions shown in Figure 7-1 (left; small zones) give

- a = 50 mm/150 m = 0.33 mm/m for the 200 m distance,
- a = 32.2 mm/150 m = 0.22 mm/m for the 400 m distance,
- a = 14.4mm/150 m = 0.096 mm/m for the 600 m distance.

The schematic slip distributions shown in Figure 7-1 (right; large zones) give

- a = 60 mm/150 m = 0.40 mm/m for the 200 m distance,
- a = 46.6 mm/150 m = 0.31 mm/m for the 400 m distance,
- a = 33.2mm/150 m = 0.22 mm/m for the 600 m distance.

Corresponding values for steeply-dipping target fractures are set at 75% of the values above.

7.2.1 50 mm threshold

Figure 7-2 (left) shows examples of application of Equation 7-1 for horizontal and gently-dipping fractures. Figure 7-2 (right) shows examples for steeply-dipping fractures. The intersection with the x-axis shows the critical radius for different distance ranges. The 200 m results are taken to apply for the 200–400 m distance range, the 400 m results for the 400–600 m range and the 600 m results for distances larger than 600 m. This assumption overestimates the percentages of fractures slipping more than the threshold; the effective percentage for each of the range intervals would be the interval average. The results are summarized in Table 7-2 and schematically illustrated in Figure 7-3. The red and blue boxes show the critical radii that apply in different distance ranges around two intersecting zones.

The radii given for the 100 m–200 m distance range are not directly calculated, but are based on a linear dependence on size and the assumption that fractures at 100 m will not slip more than twice as much as those at 200 m (Figure 5-22, Figure 5-23 and Figure 5-24).

Canister positions intersected by fractures with radii larger than the critical radius given for that position should be avoided. If features of this size are not detected, the fracture slip will damage canisters in deposition holes intersected by the central parts of the fracture with a probability x given by Equation 7-1. The shaded areas in Figure 7-3 show regions that should not see any canister damage provided that fractures with radii > 225 m can be safely detected.
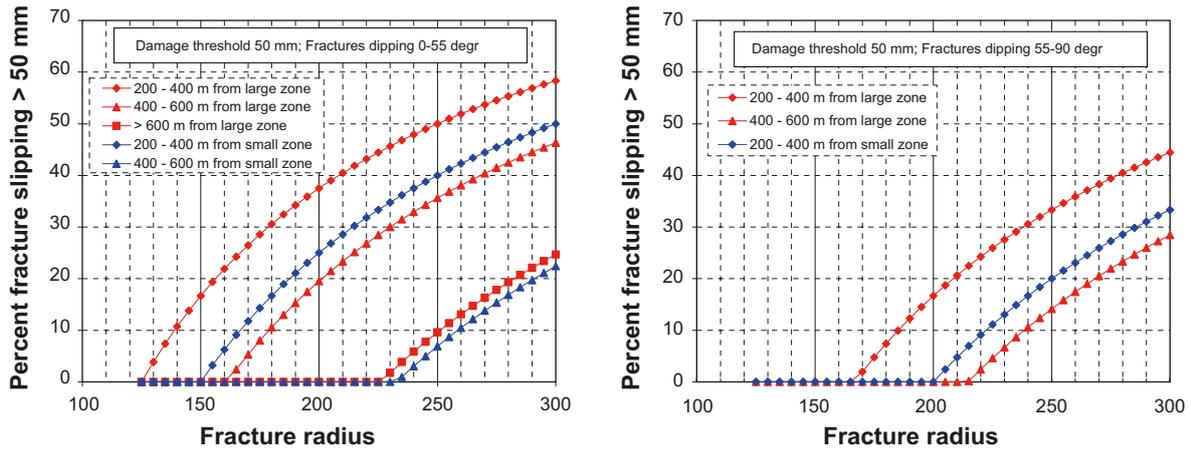
Figure 7-2. *Percentage of horizontal and gently-dipping (left) and steeply-dipping (right) fractures that will slip more than 50 mm as function of fracture radius. Red: fracture outside large zones. Blue: fractures outside small zones.*

Table 7-2. Critical radii.

Surface trace length > 5 km

Distance range (m)	Critical radius (m)	
	Target dip range 0°–55°	Target dip range 55°–90°
0–100	No deposition of canisters in this zone	No deposition of canisters in this zone
100–200	62.5	85
200–400	125	170
400–600	160	215
> 600	225	> 300

Surface trace length 3–5 km

Distance range (m)	Critical radius (m)	
	Target dip range 0°–55°	Target dip range 55°–90°
0–100	No deposition of canisters in this zone	No deposition of canisters in this zone
100–200	75	100
200–400	150	200
400–600	235	> 300
> 600	> 300	>> 300
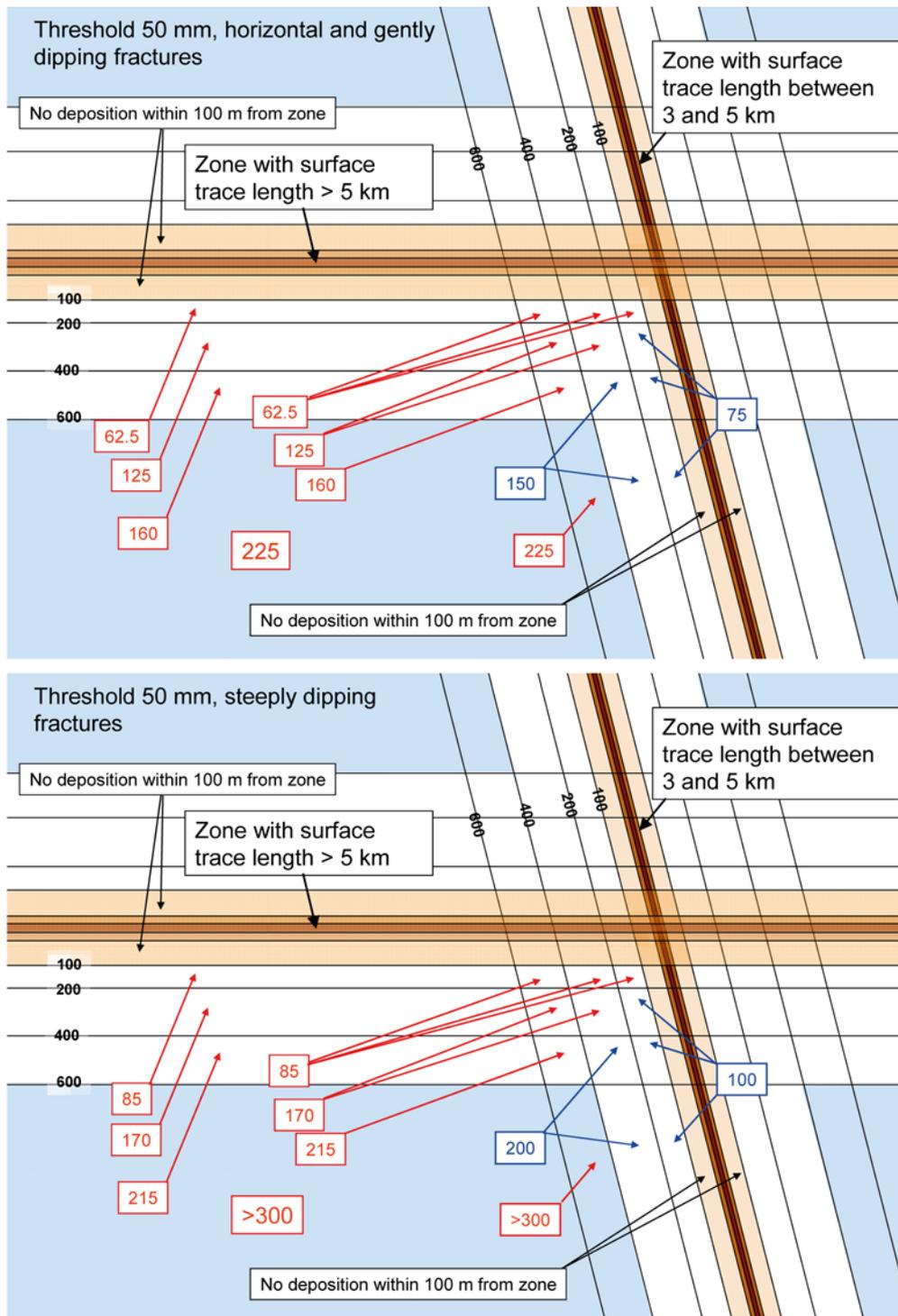
Figure 7-3. *Schematics of avoidance rules for reference value of damage threshold (50 mm). Numbers in boxes denote the critical fracture radii at different distances from large zones (red) and small zones (blue). Upper: horizontal and gently-dipping target fractures (Dip between 0° and 55°). Lower: steeply-dipping fractures (Dip between 55° and 90°). The shaded areas denote regions with no canister damage on condition that all fractures with radii > 225 m are safely detected.*

7.2.2 Sensitivity to damage threshold definition

The results in Subsection 7.2.1 relate to the present day reference value of the canister damage threshold (50 mm). Corresponding results for other possible damage definitions can easily be generated using the schematic interpretation model and Equation 7-1. Figure 7-4 shows the results for hypothetical thresholds 70 mm and 80 mm. For the 70 mm threshold the results are illustrated in Figure 7-5. The example shows the importance of the damage threshold; for the 70 mm threshold all canisters at distances larger than 400 from any zone should count as safe provided that all fractures with radii > 225 m can be detected. This is true irrespective of the fracture orientation. For steeply-dipping fractures the safe regions would be even larger and include all positions outside 200 m of any deformation zone.
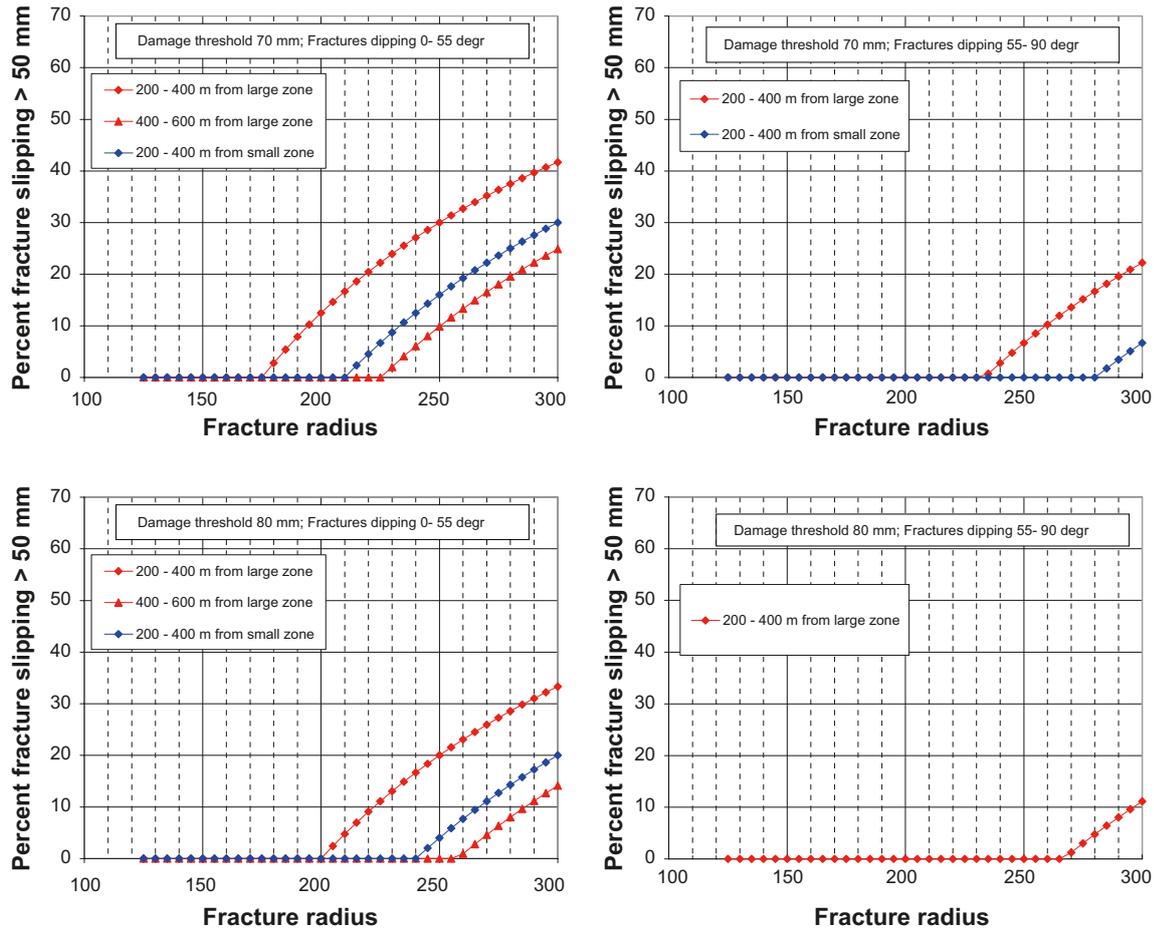

Figure 7-4. *Percentage of horizontal and gently-dipping (left) and steeply-dipping (right) fractures that will slip more than 70 mm (upper) and 80 mm (lower) as function of fracture radius. Red: fracture outside large zones. Blue: fractures outside small zones.*
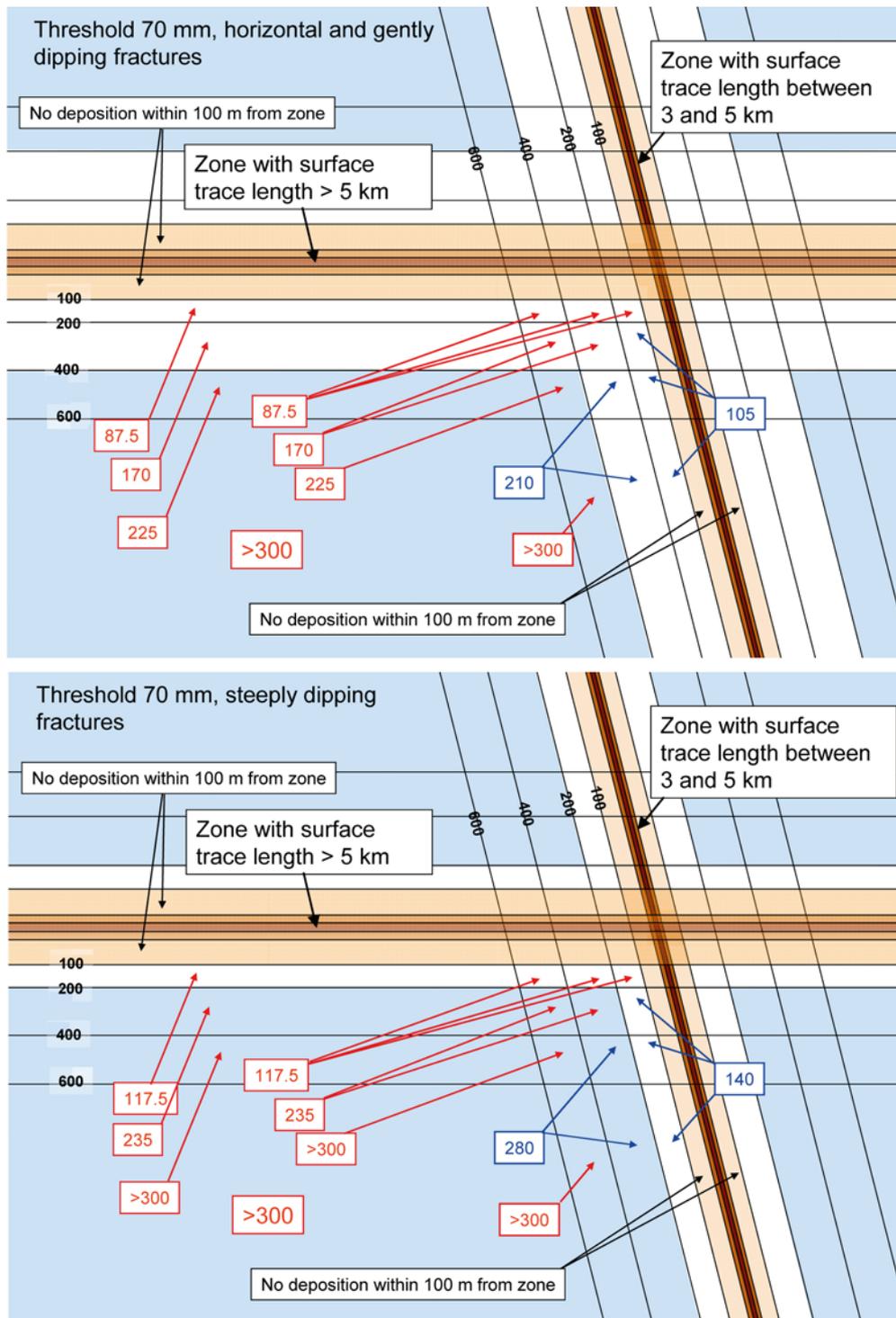
Figure 7-5. *Schematics of avoidance rules for hypothetical value of damage threshold (70 mm). Numbers in boxes denote the critical fracture radii at different distances from large zones (red) and small zones (blue). Upper: horizontal and gently-dipping target fractures (Dip between 0° and 55°). Lower: steeply-dipping fractures (Dip between 55° and 90°). The shaded areas denote regions with no canister damage on condition that all fractures with radii > 225 m are safely detected.*

7.3 Site application

7.3.1 General

The consequences of the schematic respect distance layouts (cf. Figure 7-3) suggested in the previous sections imply that all deformation zones with surface trace length > 3 km count as potentially seismogenic and able to produce the largest possible earthquake consistent with the size of the deformation zone. This is obviously an exaggerated view of the seismic risk; many deformation zones will have orientations that result in no or little instability during the glacial cycle. It is also conservative to assume that the full length of any given fault will rupture in a single seismic event. In this section the stability of the deformation zones at the Forsmark site is assessed, and recommendations are provided as to which of the Forsmark deformation zones should count as stable and which should require respect distances.

The fault stability estimate is based on a Mohr-Coulomb failure criterion. The stress field used in the calculation is a sum of the *in situ* stress field and the glacially-induced stresses as calculated by /Lund et al. 2009/. It turns out that fault stability is mainly dependent on the *in situ* stress field, since the glacially-induced stresses are low compared to tectonic stresses. This is particularly true at larger depths. Since there are uncertainties about the *in situ* stresses at depth, different stress-state assumptions are considered. The following two subsections discuss the assumed *in situ* stress fields and the glacially-induced stress additions, respectively. After that, the evaluated zone stabilities are presented.

7.3.2 In situ stress

In order to assess the stability of faults at seismogenic depths, some assumptions have to be made regarding the stress regime and stress magnitudes at these depths. The Forsmark site report /Glamheden et al. 2007/ does not describe the stress field at depths much below the repository horizon. In general, stress data from large depths are limited. Data from the World Stress Map Project /Heidbach et al. 2008/ indicate that the direction of the maximum horizontal stress in southern Sweden is in agreement with ridge push from the Mid-Atlantic. This is likely to be the case at all upper- to mid-crustal depths. Data from stress measurements in the deep Siljan borehole, for instance, indicate that that the maximum horizontal stress direction is in agreement with ridge-push down to about 6 km depth. Additionally the stress field at depth around that deep borehole appears to be of strike-slip type with magnitudes consistent with the notion of the crust being in frictional equilibrium (see e.g. /Stephansson et al. 1989, Lund and Zoback 1999/). In order to study how the stability depends on the *in situ* stresses, three *in situ* stress assumptions are considered:

1. Reverse stress regime at all depths (Figure 7-6a).

2. Mixed stress regime. (Reverse stress regime down to 2.4 km depth and strike-slip regime at larger depths) (Figure 7-6b).

3. Site stress regime. The stress model according to the site report /Glamheden et al. 2007/ is assumed to hold at all depths. (Figure 7-6c, Table 7-3).

For stress models #1 and #2, the stresses at all depths are assumed to be consistent with the crust being in an equilibrium state determined by the frictional strength of suitably-oriented faults and by the hydrostatic pore pressure. The assumption of frictional equilibrium is also used by /Lund et al. 2009/ when constructing synthetic *in situ* stress fields and is in agreement with stress observations made in deep boreholes in a variety of tectonic regimes /Scholz 2002/. In this study, the stresses are determined using a Mohr-Coulomb failure criterion (see /Jaeger and Cook 1979/) according to

$$\frac{\sigma_1 - P}{\sigma_3 - P} = (\sqrt{\mu^2 + 1} + \mu)^2 \qquad\qquad \text{Equation (7-2)}$$

Here σ_1 is the major principal stress, σ_3 the minor principal stress, P is the pore pressure and μ is the coefficient of friction. Equation 7-2 involves only the major and minor principal stress components. The intermediate principal stress component, σ_2, is constrained by (after /Gephart and Forsyth 1984/):

$$R = \frac{\sigma_1 - \sigma_2}{\sigma_1 - \sigma_3} \qquad\qquad \text{Equation (7-3)}$$

Reverse stress field (#1)

Using Equations 7-2 and 7-3, a reverse stress field can be constructed according to

$$\sigma_1 = A(\sigma_3 - P) + P = \sigma_H$$
$$\sigma_2 = \sigma_1(1-R) + R\sigma_3 = \sigma_h \qquad\qquad\qquad\text{Equation (7-4)}$$
$$\sigma_3 = \sigma_v$$

with $A = (\sqrt{(\mu^2 + 1)} + \mu)^2$.

At 500 m depth in Forsmark there are reverse stress conditions with the major and minor horizontal stresses equal to 41 MPa and 23 MPa, respectively. The vertical stress is approximately 13 MPa, and corresponds roughly to the load of the overlying bedrock. The major horizontal stress trends 145° /Glamheden et al. 2007/. These stress magnitudes are used in order to determine the friction coefficient, μ, and the stress ratio R according to Equation 7-4, which gives $\mu = 0.78$ and R = 0.65. These parameter values are then used in Equation 7-4 to define the reverse stress field (#1) field shown in Figure 7-6a.

Mixed stress field (#2)

The mixed stress regime is constructed as follows:

- Above 1 km depth, the *in situ* stress field is identical to the reverse field (#1), i.e. $\mu = 0.78$ and $R = 0.65$.

- Between 1 km and 2.4 km depth the stress field is still of reverse type, with the vertical stress and the major horizontal stress identical to those of stress field #1, i.e. $\mu = 0.78$. The depth gradient of the minor horizontal stress is changed at 1 km depth such that the vertical and the minor horizontal stresses are equal in magnitude at a depth of 2.4 km.

- Below a depth of 2.4 km the stress field is of strike-slip type. The depth gradient of the major horizontal stress is changed at 2.4 km depth such that $\mu = 0.78$.

This means that the mixed field is of reverse type from the ground surface down to 2.4 km depth and strike slip below (Figure 7-6b), and that the friction coefficient controlling the equilibrium is 0.78 at all depths. According to /Stephansson et al. 1989/ there is a clear strike-slip regime below about 0.5 km in the Siljan borehole. At Forsmark, however, there is a reverse regime down to about 1 km depth /Glamheden et al. 2007/. Thus, if there is a shift from reverse regime to strike-slip regime at Forsmark, it may take place at some few kilometres depth. Keeping this in mind, the depths for the two breakpoints are arbitrarily selected to be 1 km and 2.4 km, respectively.

- Below 1 km depth the minor horizontal stress is defined as $\sigma_h = 32.9 - 13.3y$, which gives that $\sigma_h = \sigma_v$ at 2.4 km depth.

- Below 2.4 km depth the major horizontal stress, σ_H, is defined such that a strike-slip stress regime in frictional equilibrium is obtained, i.e. $\sigma_H = A(\sigma_h - P) + P$. This relationship is derived from Equations 7-2 and 7-3, assuming that $\sigma_H = \sigma_1$ and $\sigma_h = \sigma_3$ in a strike-slip regime.

Site model stress field (#3)

The site stress model (Figure 7-6c) is defined in Table 7-3. According to the site report /Glamheden et al. 2007/, this stress model is valid at depths of 400–600 m, but is here extrapolated to the ground surface as well as to large depths.

Table 7-3. *In situ* stress model according to the site report /Glamheden et al. 2007/. According to the report the model is valid at 400–600 m depth but is here used for all depths (cf. Figure 7-6c). Note that *y* is here assumed to be negative below ground surface.

	Stress as function of depth, y (in km)
Major horizontal stress, σ_H	29.5–23y MPa
Minor horizontal stress, σ_h	9.2–28y MPa
Vertical stress, σ_v	–26.5y MPa

Stress field – comparison

At all depths in the three different *in situ* stress models, the trend of the major principal stress, σ_H, is assumed to be 145°. The vertical stress, σ_v, always corresponds to the rock overburden and is always assumed to be a principal stress.

At large depths the reverse stress model (#1) (Figure 7-6a) differs significantly from the site stress model (#3) (Figure 7-6c). As far as the difference between the major and minor principal stresses is concerned, the results of the reverse stress model (#1) is in keeping with the rheological profile given by /Milnes et al. 1998/, which implies depth-independent stress ratios. The site stress model (#3) gives much lower values of the difference between the major and minor principal stresses (Figure 7-7). The σ_1–σ_3 differences in stress models #1 and #2 are in keeping with values presented by /Wu 2009/.

For stress model #3, with the site report stress model extrapolated to large depths, the ratio between the mean horizontal stress and the vertical stress will approach unity at large depths, whereas it is constant (about 2.4) in the reverse model (#1), cf. Figure 7-8, left. The stress ratio of model #3 is in qualitative agreement with the picture given by /Brown and Hoek 1978/, cf. Figure 7-8, right. In terms of stress ratio, the mixed stress model (#2) is in agreement with model #1 at shallow depths (constant ratio down to 1 km) but then the ratio tends to approach unity at larger depths in a similarly manner to model #3. The stress ratio is however larger in model #2 than in model #3 down to about 5 km depth (Figure 7-8, left).
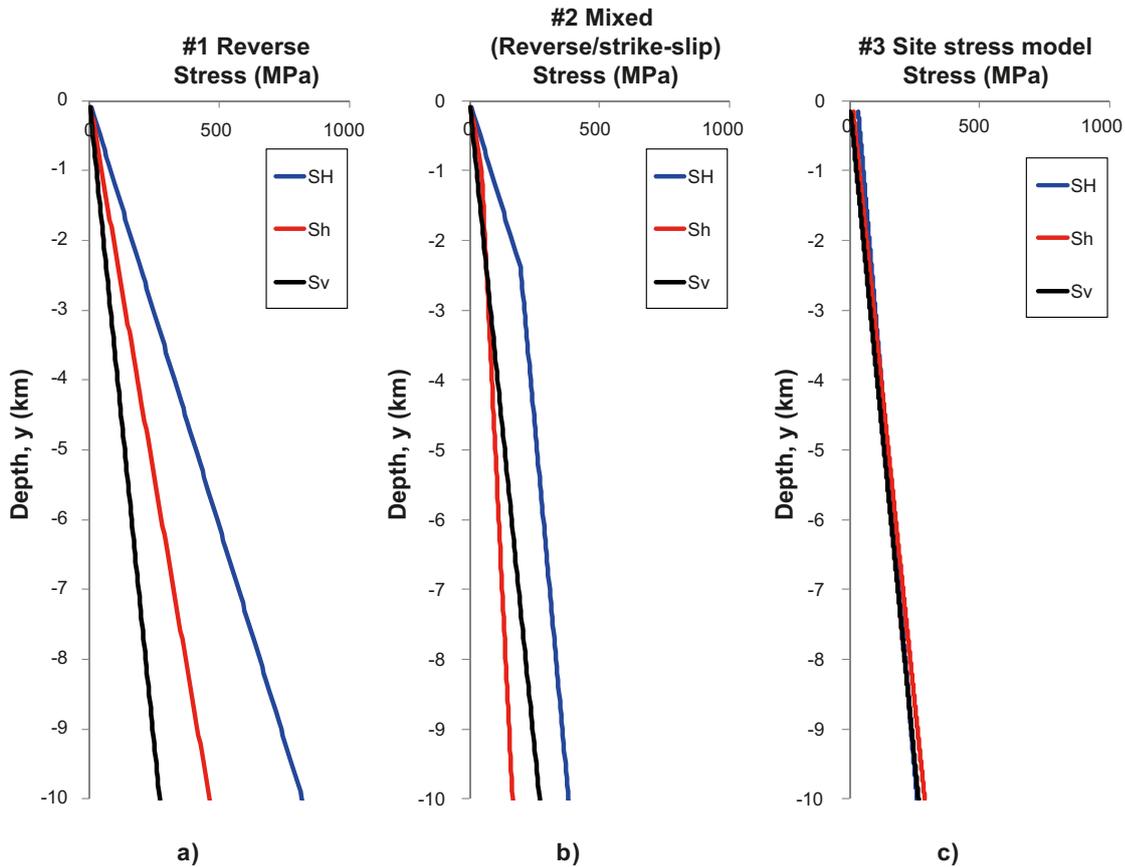
Figure 7-6. *In situ stresses assumed in this chapter. At 500 m depth they agree with the stress model suggested in the site report /Glamheden et al. 2007/. a): #1 Reverse stress regime. b): #2 Mixed stress regime, i.e. reverse regime at 0–2,400 m depth and strike-slip regime at larger depths. c): #3 Site stress model extrapolated to large depths.*
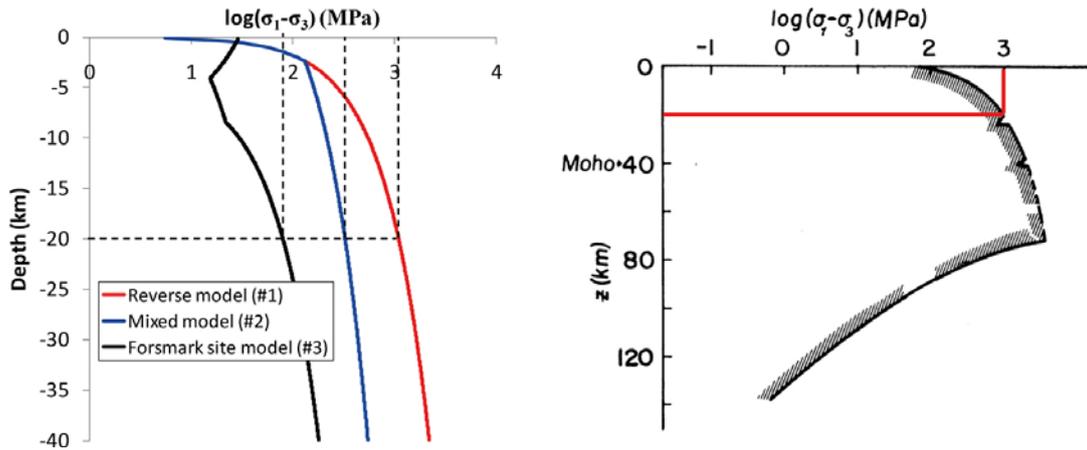
Figure 7-7. *Left. Maximum principal stress difference as function of depth for the reverse and mixed stress models. Right: Maximum principal stress difference redrawn from /Milnes et al. 1998/*
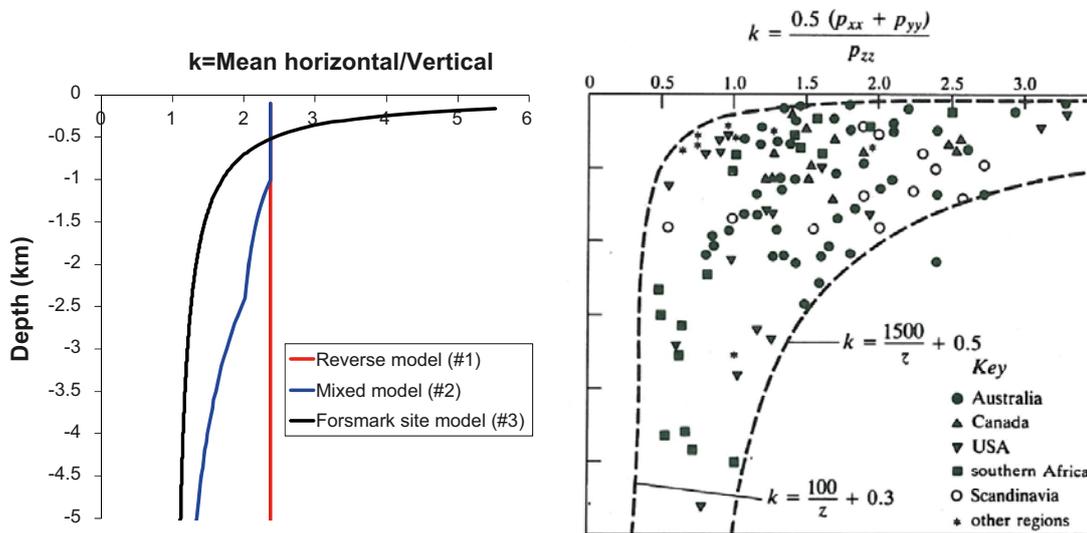
Figure 7-8. *Ratio between mean horizontal stress and vertical stress. Left: The stress models considered here. Right: Measured data, worldwide (After /Brown and Hoek 1978/; note that max depth is 3 km).*

Without more stress data it is difficult to make a qualified assessment of the relevance of different rheological models and their implications on the *in situ* stresses at large depths for the Forsmark site. The model pictured in Figure 7-7 (right) is consistent with the notion of a strong upper mantle and the lack of a weak zone in the lower parts of cold cratonic crusts /Milnes et al. 1998/. The model pictured in Figure 7-8 (right) is consistent with the principle of time-dependent elimination of shear stresses in rock masses /Brady and Brown 1993/. It should be noted that the mixed stress model (#2) is in agreement with 1) the principle of frictional equilibrium, 2) the notion that the horizontal/vertical stress ratio approaches unity at large depths and 3) observations of focal mechanisms in Fennoscandia suggesting strike-slip conditions at seismogenic depths /Bödvarsson et al. 2006/.

7.3.3 Evolution of the glacial load

To assess the stability of the many differently-oriented deformation zones during the glacial cycle, glacially-induced stresses are added to the *in situ* stress field.

/Lund et al. 2009/ calculated the glacially-induced stresses at Forsmark during the most recent glaciation cycle using the SKB reference ice model and state-of-the-art mechanical descriptions of the crust and the mantle. In the following stability estimates, these time-dependent glacial stresses are added to the *in situ* stresses as described above. It should be noted that the study by /Lund et al. 2009/ only includes the effects of the ice load and does not account for the effects of potential tectonic strain accumulation under the stabilising ice-sheet.

The temporal development of the glacially-induced stresses at 500 m depth in Forsmark site as calculated by /Lund et al. 2009/ are shown in Figure 7-9, upper left. The time scale indicates time before present day (BP) in thousands of years. The black solid lines along the horizontal axis indicate periods with ice cover. The diagram shows how the glacial load tends to increase the horizontal stresses at all times except during a period before the arrival of the ice.
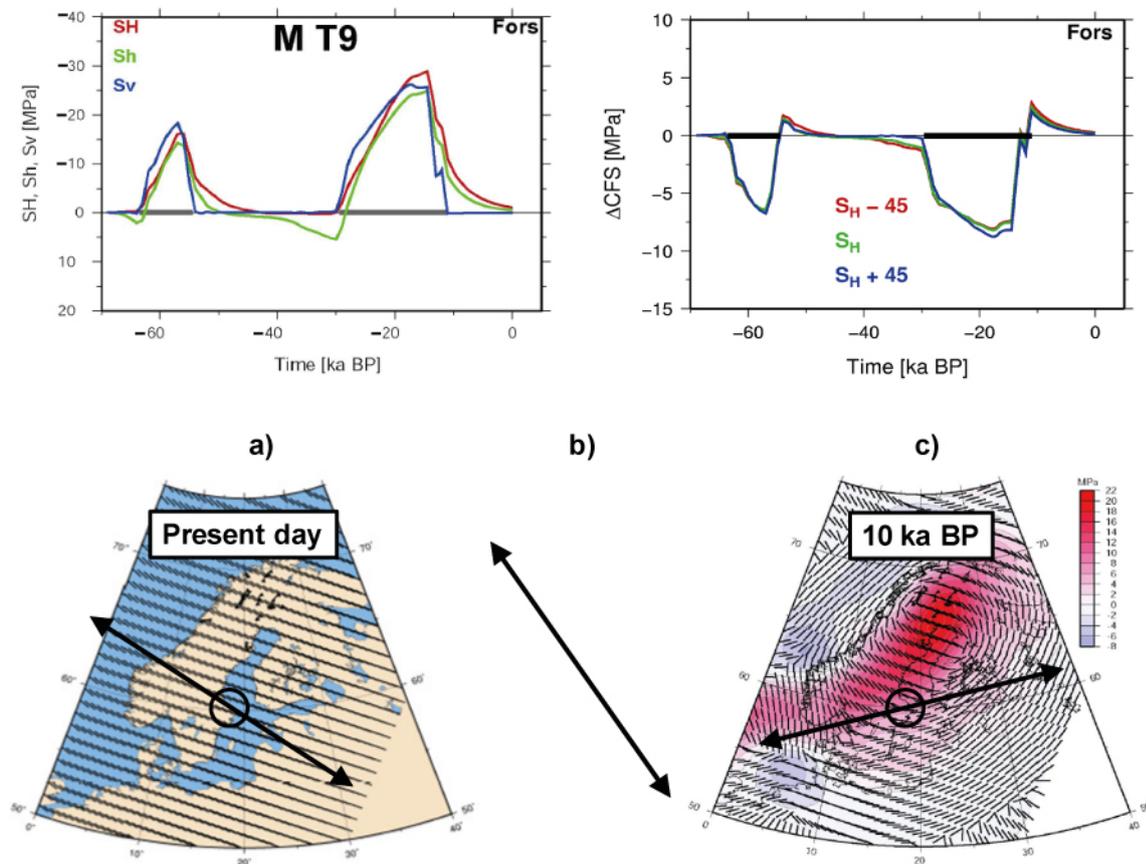
Figure 7-9. Upper left: Glacially-induced stress additions (negative values mean compression) at 500 m depth as function of time BP. Upper right: Associated instability quantity ΔCFS as function of time BP (positive values mean instability). Redrawn from /Lund et al. 2009/. Lower (a): Present-day orientation of σ_H according to model proposed by /Lund et al. 2009/. Lower (b): Present day orientation of σ_H according to site report /Glamheden et al. 2007/. Lower (c): Orientation of major glacially-induced stress at 2.5 km depth in Forsmark at the approximate time of maximum instability during the last glaciation /Lund et al. 2009/.

Based on the calculated stress additions, /Lund et al. 2009/ evaluated the stability in the crust. The temporal development of stability at 9.5 km depth in Forsmark is shown in Figure 7-9, upper right (positive values mean instability). The stability estimate is based on the assumption that there is a reverse *in situ* stress regime at all depths. The major horizontal stress addition at times of instability, i.e. when the stabilizing ice cover has disappeared (about 10 ka BP) is shown in Figure 7-9, lower right.

When the stability of deformation zones are evaluated (see Section 7.3.4), the glacially-induced stresses are added to the *in situ* stresses. Two of the *in situ* stress models (Figure 7-6a, b) considered here are based on the assumption that the stresses in the earth crust are governed by the strengths of the most suitably-oriented planes of weakness. This means that, before the glacial stresses are added, the crust is at the stability limit at all depths and that the stability limit is exceeded due to the glacial stresses additions. However, it can be noted that the glacial stress additions are moderate in magnitude compared to the *in situ* stresses and that they show only small variations with depth as shown in Figure 7-10. The small variation with depth also means that their relative importance is smaller at larger depths. The dashed red line shows the effect of adding 5 MPa to the largest glacial stress component in order to account for uncertainties in the glacially-induced stresses and for the possibility of tectonic strain accumulation below the stabilizing ice (cf. Section 1.1.1).
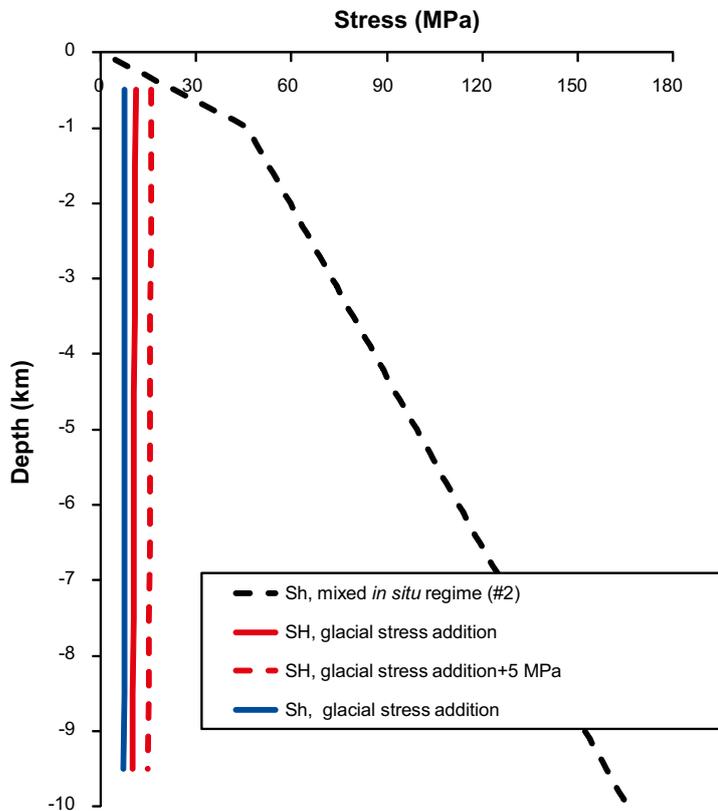
Figure 7-10. Comparison between the minor horizontal stress component in the mixed in situ stress model and the glacial stress addition components at 11 ka BP /Lund et al. 2009/. The diagram shows that the glacial stress additions are relatively low compared to the in situ stresses and that they are relatively insensitive to the depth. This means that their relative importance decreases with depth.

7.3.4 Fault stability

The stability of faults is evaluated using the stability quantity *CFS* (Coulomb Failure Stress) which is defined as

$$CFS = \tau - \mu(\sigma_n - P_f) - c$$ Equation (7-5)

Here τ and σ_n are the shear and normal stresses, respectively, acting on a given plane, P_f is the pore pressure, μ is the coefficient of friction and c is the cohesion. The cohesion is set at zero. Positive values of *CFS* mean instability. The coefficient of friction is set at 0.78, which is the value required to keep the rock mass just at frictional equilibrium, given the reverse and mixed *in situ* stress fields described above (Figure 7-6a, b). Values of τ and σ_n obtained from the total stress tensor, i.e. the glacially-induced stresses from /Lund et al. 2009/ added to the *in situ* stresses (Figure 7-6). The glacially-induced stresses are picked at the time when the ice edge passes the Forsmark site, 11 ka BP (cf. Figure 7-9, upper left). This is the time for which /Lund et al. 2009/ estimated the largest instability (Figure 7-9, upper right).

The poles of the Forsmark deformation zones[4] /Stephens et al. 2008/ are here presented in lower hemisphere equal angle pole plots along with contours of the instability quantity *CFS* at the time of maximum induced instability (11 ka BP). The poles are colour coded to indicate safe or unsafe zone orientations. The stabilities are evaluated taking into account that strike and dip of the zones may vary within ±10° (cf. /Stephens et al. 2007/) and that the trend of the *in situ* stresses may vary within ±15° as indicated in Figure 7-12, lower right (cf. /Glamheden et al. 2007/). There is also an additional safety margin of 10 MPa in order to account for other data uncertainties (see legends in Figure 7-11 and Figure 7-12).

For the reverse (#1) and the mixed (#2) *in situ* stress models the stability is evaluated at three depths (500 m, 3,500 m and 5,500 m). For the site stress model (#3), one depth is considered (3,500 m). In all three stress models, two assumptions regarding pore pressure and the stress additions are considered:

1. Basic assumption: The glacial stress additions as calculated by /Lund et al. 2009/ are applied and hydrostatic pore pressure conditions are assumed.
2. Worst case assumption: The largest horizontal glacial stress addition component is arbitrarily increased by 5 MPa and the smaller one is increased proportionally. This is done in order to account for uncertainties in the stress addition results and for the possibility of tectonic strain accumulation under the stabilizing ice cover, which is not included in the results from /Lund et al. 2009/. The possibility of having residual excess pore pressures left as the ice disappears is accounted for (cf. Section 1.1.1). The excess pore pressures are set according to: 1 MPa at 500 m depth, 7 MPa at 3,500 m and 10 MPa at 5,500 m.

The pole plots based on the reverse *in situ* stress model (#1) (Figure 7-6a) are shown in Figure 7-11. The following can be observed:

* The contours confirm that the maximum instability will be found for deformation zones dipping along the major stress, i.e. with dip direction around 145°.
* Only gently-dipping zones are characterised as unsafe (i.e. potentially unstable). Steeply-dipping zones have considerable stability margins. This is particularly true at larger depths where the glacial stress additions have less relative importance (cf. Section 7.3.3). The smaller relative importance at larger depths is manifested by smaller ranges of instability.
* The worst case assumption (right column) gives higher maximum *CFS* values in the unstable regions. However, the ranges of instability are only slightly increased.

The pole plots assuming the (#2) mixed *in situ* stress model (Figure 7-6b) are shown in Figure 7-12. The following can be observed:

* At 500 m depth the *in situ* stress state and the stability picture are identical to those of the stress #1 model by definition (cf. Figure 7-11).
* At 3,500 m and 5,500 m depth, the stability picture differs from that of the 500 m depth due to the shift of stress regime. For the worst case assumptions (right column) at 3,500 m depth, the ranges of unsafe zones include both gently-dipping and steeply-dipping zones. However, steeply-dipping zones that may become unstable and start to move at 3,500 m depth are stable at shallower depths.

---

[4] Modelldatabasen, 2007b. Model: DZ_PFM_REG_v22.rvs. Version 0.3. Approved 2007-08-31. Modified 2007-11-29. Modeller: A. Simeonov. Simon ID: GEO_IZTKKYIL. https://service.projectplace.com/pp/pp.cgi/r180716254.

The pole plots assuming the (#3) site specific *in situ* stress model (Figure 7-6c) are shown in Figure 7-13. Here, the stability is shown for 3,500 m depth only; the stability pictures at 500 m depth obtained with this stress model are identical to that of the other two models (Figure 7-11 and Figure 7-12). The stability margins obtained at 3,500 m depth with this *in situ* stress assumption are considerable. At larger depths, the stability margins are yet larger. The reason for the high stability is that the *in situ* stress ratios tend to approach unity at larger depths with low stress anisotropy as consequence.
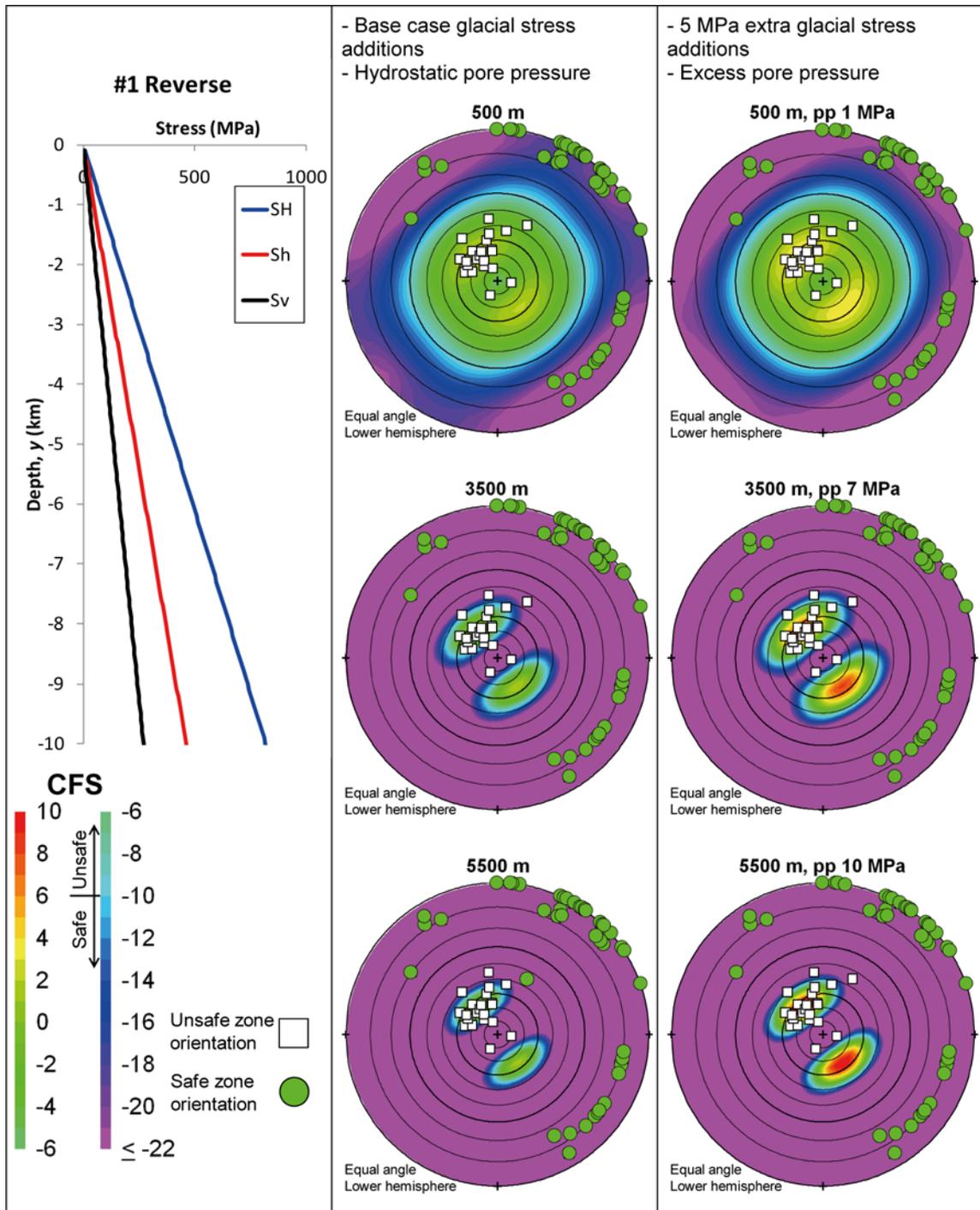
Figure 7-11. *Contours of CFS values at three depths plotted along with the poles of Forsmark deformations zones. The colours of the plot symbols indicate zone orientations considered safe or unsafe according to the legend. Positive CFS values indicate instability. Circles denote 10° dip intervals. Upper left: The assumed in situ stress field. Middle: Hydrostatic pore pressure and stress additions only. Right: Excess pore pressure and 5 MPa extra glacial stress addition.*
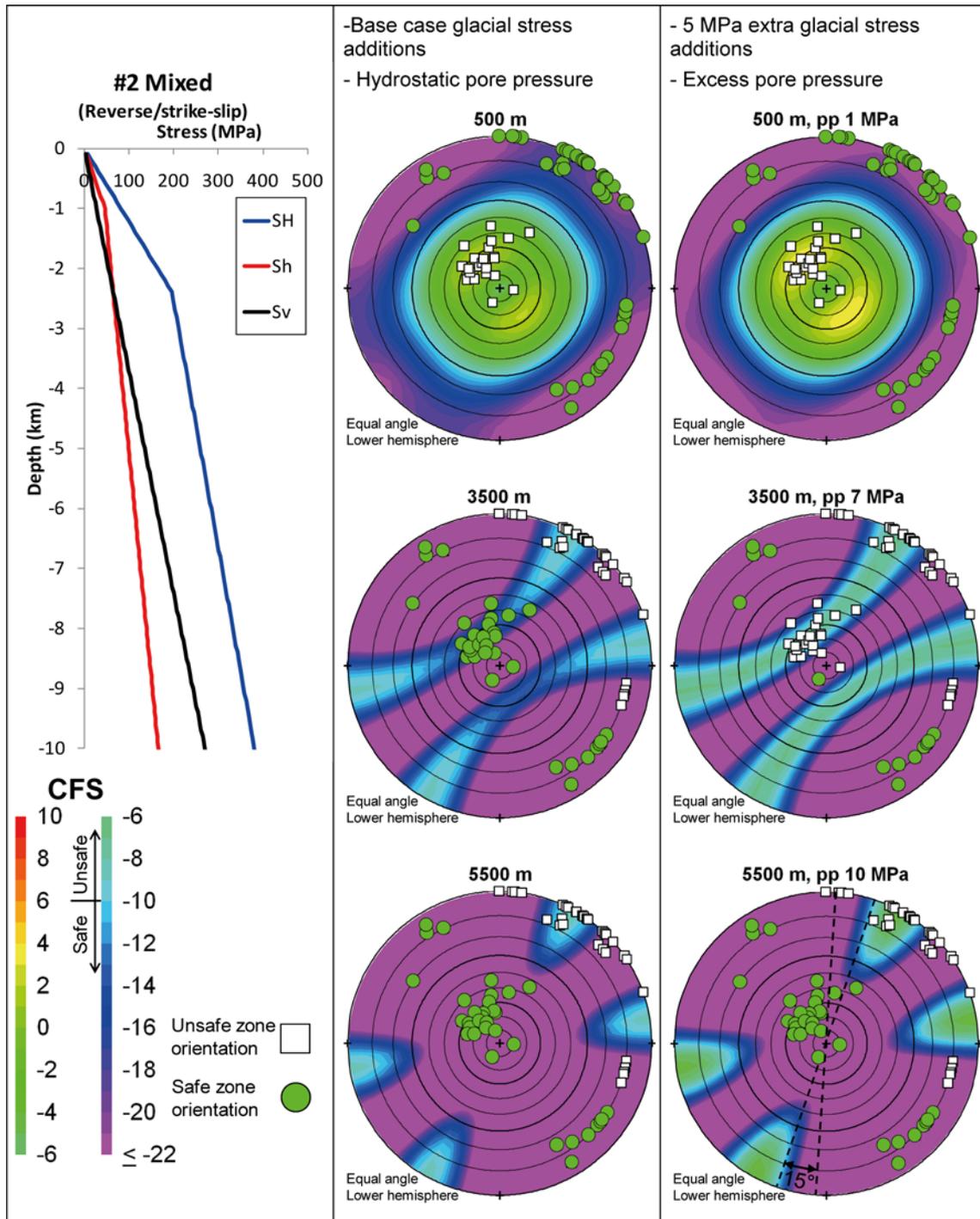
Figure 7-12. *Contours of CFS values at three depths plotted along with the poles of Forsmark deformations zones. The colours of the plot symbols indicate zone orientations considered safe or unsafe according to the legend. Positive CFS values indicate instability. Circles denote 10° dip intervals. Upper left: The assumed in situ stress field. Middle: Hydrostatic pore pressure and stress additions only. Right: Excess pore pressure and 5 MPa extra glacial stress addition.*
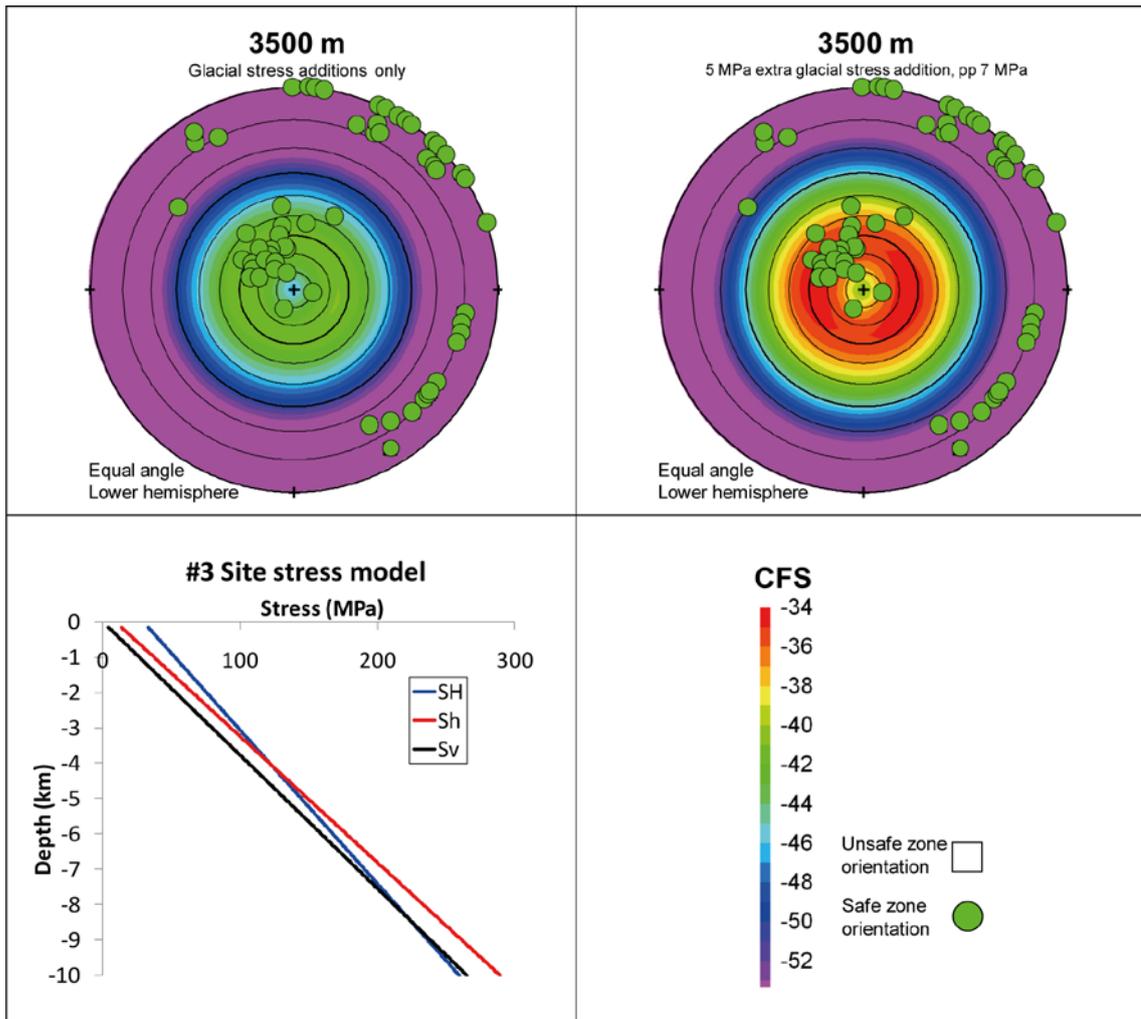
Figure 7-13. *Contours of CFS values at 3,500 m depth plotted along with the poles of Forsmark deformations zones. The colours of the plot symbols indicate zone orientations considered safe or unsafe according to the legend. Positive CFS values indicate instability. Circles denote 10° dip intervals. Upper left: Hydrostatic pore pressure and stress additions only. Upper right: Excess pore pressure and 5 MPa extra glacial stress addition. Lower left: The assumed in situ stress field.*

7.3.5 Recommendations

For layout concerns the question is whether or not the results presented in Figure 7-11 through Figure 7-13 can be used to identify deformation zones at Forsmark that need not count as potential earthquake faults. The site specific stress model (#3) gives considerable stability margins at seismogenic depths compared to the #1 and #2 stress models, provided that the same failure model applies (Mohr-Coulomb with friction coefficient $\mu = 0.78$). Models #1 and #2 are both in agreement with the notion of uniform frictional equilibrium at all depths, and are conservatively selected as points of departure for the discussion on site application below.

Figure 7-14 shows a map of deformation zones at repository depth, –470 m. Zones with trace lengths > 3 km are shown. Zones within 600 m distance from any canister are coded with respect to their stability at 3.5 km depth according the worst case version of the reverse (#1) stress results shown in Figure 7-11, i.e. with account of additional pore overpressures, potential tectonic strain effects and uncertainties in the glacial stress addition results. Also uncertainties in orientation of zones and stresses are included. A corresponding map based on the mixed (#2) stress regime (Figure 7-12) is shown in Figure 7-15.

From Figure 7-14 it appears that only one zone (ZFMA2) would count as a potential earthquake fault if the *in situ* stress state could be trusted to be of reverse type from ground surface to large depths. For the mixed stress state (#2) there are five potentially unstable zones (ZFMA2, ZFMNW0017, ZFMWNW0123, ZFMWNW0809A, ZFMWNW1200).

There is no clear-cut answer to the question "which of the *in situ* stress models considered here that is the most relevant at seismogenic depths?". Table 7-4 summarizes comparisons with various relevance criteria.

Based on Table 7-4 and the fact that the mixed state (#2) appears to be more conservative (at least as far as the number of potential earthquake zones are concerned) the recommendation is to count the five zones marked in Figure 7-15 as potential earthquake zones.

Table 7-5 presents the five zones that are characterised as unstable. The values within parenthesis are the *CFS* values including the 10 MPa safety margin (cf. Section 7.3.4). It can be noted that none of the zones is characterised as unstable from ground surface to large depths. Additionally, the instability quantity *CFS* is consistently lower for the five unstable zones in the mixed *in situ* state than it is for the single unstable zone in the reverse state. This suggests that the effects on target fractures should be smaller than those produced by the synthetic earthquakes with maximum instability from the bottom edge of the fault to the ground surface analysed in previous chapters. Therefore it may be worthwhile analysing the effects of earthquakes initiated in a less schematic stress environment (such as the mixed one) and to arrive at possibly less conservative critical radii estimates.

Note that the zones ZFMNW0017 and ZFMNW1200 have negative nominal *CFS* values but are still characterised as unstable. This is because of the margins applied to account for uncertainties in the *in situ* stress trend (cf. Figure 7-12, lower right) and for uncertainties in zone orientations.

The zones that are characterised as stable in Figure 7-14 and Figure 7-15 are presented in Table 7-6. Note the considerable stability margins, which are particularly large at greater depths.

Table 7-4. Comparison with relevance criteria.

Criterion	#1 (reverse)	#2 (mixed)
In agreement with site data at repository depth	Yes	Yes
Uniform frictional equilibrium (same coefficient of friction) at all depths (qualitatively in agreement with model suggested by /Milnes et al. 1998/, cf. Figure 7-7)	Yes	Yes
Horizontal/vertical stress ratio approaches unity at large depths (qualitatively in agreement with model suggested by /Brown and Hoek 1978/, cf. Figure 7-8)	No	Yes
Strike-slip conditions at large depths (as suggested by focal mechanism observations, /Bödvarsson et al. 2006/)	No	Yes

Table 7-5. Unstable zones. Values within parenthesis are the *CFS* values (MPa) including the 10 MPa safety margin (cf. Section 7.3.4).

Depth (m)	#1 (reverse)	#2 (mixed)			
500	ZFMA2 (13.2)	ZFMA2 (13.2)			
3,500	ZFMA2 (15.3)	ZFMA2 (1.9)	ZFMNW0017 (−11.6)	ZFMWNW0123 (3.2)	ZFMWNW0809A (2.9) ZFMWNW1200 (−16.5)
5,500	ZFMA2 (16.1)		ZFMNW0017 (−11.3)	ZFMWNW0123 (5.1)	ZFMWNW0809A (5.4) ZFMWNW1200 (−16.9)

Table 7-6. Stable zones. Values within parenthesis are the *CFS* values (MPa) including the 10 MPa safety margin (cf. Section 7.3.4).

Depth (m)	#1 (reverse)					
500	ZFMNW0017 (–12.6)	ZFMWNW0123 (–9.9)	ZFMWNW0809A (–11.3)	ZFMNW1200 (–12.7)	ZFMENE0060A (–21.9)	ZFMENE0062A (–22)
3,500	ZFMNW0017 (–76.8)	ZFMWNW0123 (–62.4)	ZFMWNW0809A (–65.9)	ZFMNW1200 (–81.0)	ZFMENE0060A (–169)	ZFMENE0062A (–170)
5,500	ZFMNW0017 (–120)	ZFMWNW0123 (–97.7)	ZFMWNW0809A (–103)	ZFMNW1200 (–126)	ZFMENE0060A (–267)	ZFMENE0062A (–268)
	#2 (mixed)					
500	ZFMENE0060A (–21.9)	ZFMENE0062A (–22)				
3,500	ZFMENE0060A (–123)	ZFMENE0062A (–125)				
5,500	ZFMENE0060A (–132)	ZFMENE0062A (–123)				
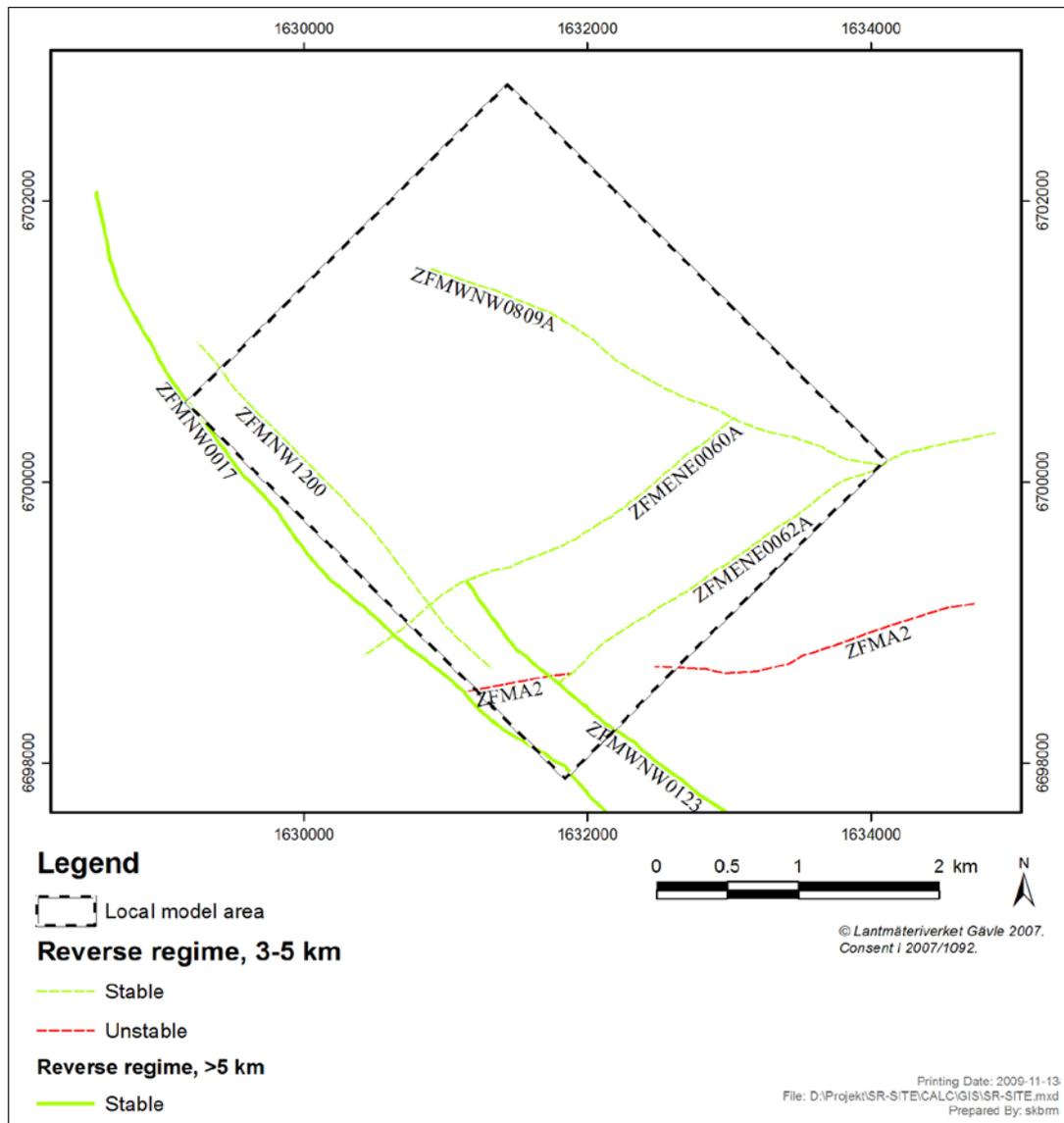
Figure 7-14. *Map of deformation zones[5] at repository depth, –470 m /Stephens et al. 2008/. Zones with trace lengths > 3 km are shown. Zones within 600 m distance from any canister are coded with respect to their stability at 3.5 km depth according the (#1) reverse stress regime assumptions applied in Figure 7-11. Stable zones are green and unstable are red.*

---

[5] Modelldatabasen, 2007b. Model: DZ_PFM_REG_v22.rvs. Version 0.3. Approved 2007-08-31. Modified 2007-11-29. Modeller: A. Simeonov. Simon ID: GEO_IZTKKYIL. https://service.projectplace.com/pp/pp.cgi/r180716254.
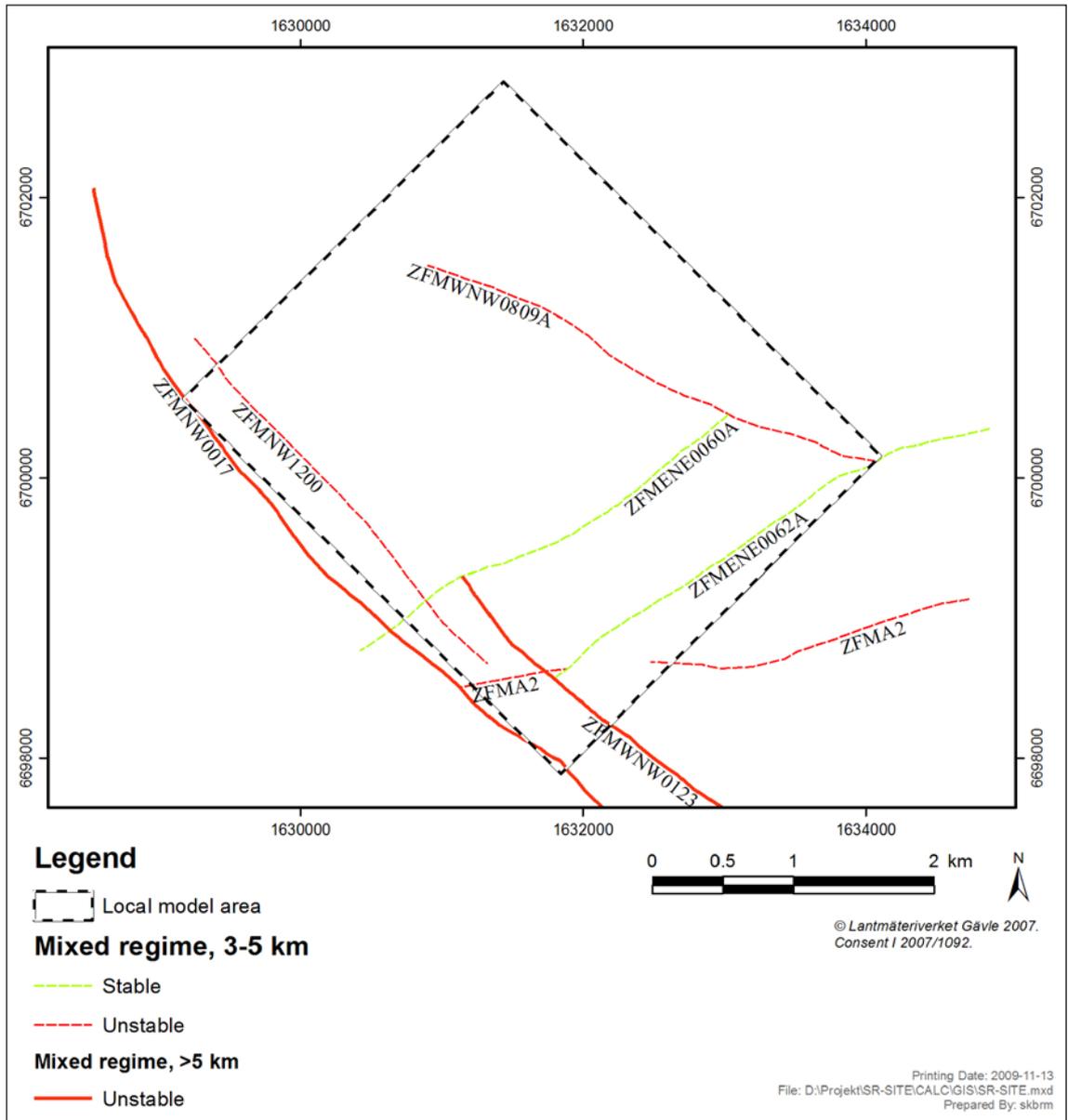
Figure 7-15. Map of deformation zones at repository depth[6], –470 m /Stephens et al. 2008/. Zones with trace lengths > 3 km are shown. Zones within 600 m distance from any canister are coded with respect to their stability at 3.5 km depth according the (#2) mixed stress regime assumptions applied in Figure 7-12. Stable zones are green and unstable are red.

---

[6] Modelldatabasen, 2007b. Model: DZ_PFM_REG_v22.rvs. Version 0.3. Approved 2007-08-31. Modified 2007-11-29. Modeller: A. Simeonov. Simon ID: GEO_IZTKKYIL. https://service.projectplace.com/pp/pp.cgi/r180716254.

8   Conclusions and discussion

8.1   General

The earthquake risk relevant to the safety of a KBS3-type spent-fuel repository in Sweden is that of direct canister damage due to fracture shear displacements across deposition holes. Vibrations of the buffer-canister system will not damage the canister.

Theoretically, three shear processes could damage canisters (cf. Figure 1-5):

1. The deposition hole is intersected by a seismogenic fault. Considering the regressions presented in Chapter 1 it will always be possible to detect and avoid fractures and fracture zones large enough to produce a displacement larger than the 50 mm threshold.

2. The deposition hole is intersected by a fracture that is directly connected to a seismogenic fault. A respect distance of 100 m (counted from the damage zone, cf. Figure 1-8) is judged to be sufficient to eliminate the risk. Deformation zones with trace lengths less than 3 km are not judged capable of producing displacement in excess of the 50 mm threshold on connected fractures, and therefore do not require any respect distance. For such small zones, it is sufficient to avoid the core of the zone itself and its surrounding damage zone.

3. The deposition hole is intersected by a fracture at some distance from the seismogenic fault. The concern is that the fracture slips as a result of dynamic effects and stress redistribution from an earthquake on the distal fault. To handle this risk it is necessary to explore how target slip correlates with potentially relevant earthquake parameters (magnitude, stress drop, slip velocity, etc.) and factors that control the displacement of the reactivated target fracture (fault-target distance, orientation and size of the target fracture, etc).

The main body of this report concerns dynamic modelling results relevant to the third process described above. Present-day seismicity in the Swedish bedrock does not seem to pose any safety problems, as current frequencies of earthquakes of moment magnitude 4 and larger are extremely low with typical focal depths of many kilometres (i.e. well below the repository horizon). The type of earthquakes that could potentially impact on the safety of the repository would occur in connection with the retreat of future ice covers in a way similar to that of the large northern Lapland post-glacial earthquakes, which occurred approximately 10,000 years ago. Therefore the dynamic modelling is focused on this type of events. The following issues are discussed below:

1. Earthquake representation,

2. response of the target fractures,

3. use of the results in layout and risk assessment work.

8.2   Earthquake representation

In this study, earthquakes are simulated by use of generic numerical models in the distinct-element code *3DEC*. The modelling approach is as follows:

• It is assumed that earthquakes relevant to the safety of the repository, i.e. post-glacial events, take place along pre-existing faults. The faults are represented by perfectly planar features inside a large rock mass represented by a linear elastic, isotropic, homogenous and continuous medium.

• Earthquakes of three categories (moment magnitudes) are simulated: M_w = 5.5, 6.2 and 7.5. For each of these, the dimensions of the rupture (down-dip width and along-strike length) are set at values small enough that the rupture area will be close to the minimum values reported by /Wells and Coppersmith 1994/ for crustal earthquakes. Minimizing the rupture areas means that the seismic moment per unit area will be maximized, given the fixed total moment associated with the moment magnitude considered.

- Reverse regime *in situ* stresses are applied. The stresses have no couplings to any specific site or any specific earthquake, past or recent. The vertical stress corresponds to the rock overburden in all models while the horizontal stresses are calibrated to give the intended seismic moment, given the prescribed rupture area and the properties of the surrounding rock mass.

- The earthquake is generated in a schematic way. The rupture, initiated at a prescribed hypocentre, is simulated by a programmed reduction of the fault shear strength, resulting in fault slip and accompanying strain energy release. A typical value of the rupture propagation velocity (70% of the shear wave velocity) is used and the fault strength properties are assumed to be uniform over the fault plane.

The majority of the *3DEC* models analysed in this study have fault geometries that are in accordance with common descriptions of post-glacial faults, which tend to be steeply-dipping reverse faults. The results of the modelling work include the following observations:

- The *3DEC* models produce peak ground accelerations and velocities that are in accordance with those from records of real earthquakes. This indicates that both the *3DEC* models and the experimental technique (mesh, boundary conditions, rupture initiation and propagation) are adequate for their intended purpose of analyzing effects at small fault distances.

- All earthquakes are, given the intended moment magnitudes, conservatively represented in the *3DEC* models. They have larger, or much larger, maximum displacement and less, or much less, rupture area than typical crustal earthquakes of corresponding moment magnitude, cf. Figure 6-8. This gives large seismic moments per unit rupture area and high values of the average stress drop.

- The slip velocities of the *3DEC* seismogenic faults turned out to be high or very high. This is a consequence of the scheme used to ramp down the shear strength along the fault during the rupture event, and is exaggerated by both the low residual strength assumed for the faults and of the large magnitudes of the stress drop. For the cases selected to be the basis for layout consideration and risk assessment (cf. Chapter 7), the maximum fault slip velocity is on par with the maximum slip velocity recorded for the 1999 Chi-Chi (Taiwan) M_w 7.6 earthquake. This event is specifically reputed for its high slip velocity /Ma et al. 2003/. While the highest slip velocities of the Chi-Chi earthquake were localized in a relatively short segment of the fault, the synthetic *3DEC* earthquakes have large peak velocities along substantial fractions of the surface rupture length. Considering that the fault slip velocity turns out here to be strongly correlated with large secondary displacements, this suggests that the calculated stress impact on target fractures indicated by the *3DEC* models are on the conservative side.

- The assumption of steeply-dipping faults as a base case is conservative. The models indicate that induced target fracture slip depends strongly on the fault dip angle. The M_w 5.5 model with a gently-dipping fault (30°) gives a maximum induced slip that is about 60% less than that of the corresponding model with a steeply-dipping fault (70°). This large difference holds in spite of the fact that the gently-dipping fault has a maximum slip velocity that is about 60% higher than the steeply-dipping one. The difference in the amount of induced fracture slip can be attributed to the more extensive stress relaxation caused by slip along gently-dipping faults. The layout rules set up in Chapter 7 are based on results produced by models with steeply-dipping faults.

According to the modelling results, the idealised and schematically-represented earthquakes produce static and dynamic effects that are both realistic (PGA and PGV values are in reasonable agreement with literature data, in particular for the short distances considered here) and conservative (values of stress drop and slip velocity are high compared to literature data). Therefore, the models can be regarded as adequate for their intended purpose, which is to simulate the possible static and dynamic effects of seismic events on nearby rock fractures, i.e. target fractures, and to provide estimates of the amount of induced fracture displacement. The response of the target fractures is discussed in the following section.

8.3 Response of target fractures

There does not appear to be any records of seismically-induced secondary movements in crystalline rocks at repository depths. Therefore, the relevance of the modelled response of target fractures cannot be checked by comparison to real cases (as opposed to the relevance of modelled primary slip on seismogenic "primary" faults for which some comparisons can be made between synthetic *3DEC* earthquakes and real seismic events). Data from records of aftershocks would not be generally applicable, even if aftershock regression relations similar to the main-shock relations pictured in Figure 1-6 were available:

- For dipping fractures, the induced slip (as calculated in the *3DEC* models) is typically a result of a temporary loss of strength caused by the seismic waves, whereas aftershocks are a process of relaxing stress concentrations produced by the main shock. For dipping fractures, the main shock does not produce any stress concentration; it rather relaxes the existing fracture shear stress and increases the stability margin. This means that induced slip is possible only during a short (approximately 0.5 second) period of time when the seismic waves reach the fracture a few seconds after rupture initiation.

- For horizontal fractures (and possibly for dipping fracture located around the edges of the primary fault), the induced slip may have more of an aftershock nature; the stress redistribution following the primary slip will destabilize some fractures and possibly cause them to slip. Because of the material model assumed for the target fractures and (possibly, depending on the sense of shear) the action of the dynamic shear stress, the slip occurs without delay in the *3DEC* models. Given a different material model, part of the slip could be delayed by minutes, days or weeks as observed for aftershocks.

Following the comments made in the points above, it is not meaningful to attempt comparing induced target fracture slip calculated in the *3DEC* models with general size-slip relations such as those shown in Figure 1-6. This means that the magnitude of the calculated displacements cannot be checked for realism. Given the stress impact of the slipping primary fault, the representation of the target fractures ensures, however, that the calculated displacements are overestimates rather than underestimates:

- All modelled target fractures are perfectly planar. This is clearly a conservative assumption; irrespective of the surface roughness observed in the laboratory, fractures may be undulated or stepped on the large scale /ISRM 1978/. Additionally, fractures that actually are planar would be the least likely ones to elude detection.

- All modelled target fractures have uniform properties over their entire surface area. This, too, is a conservative assumption; for fractures of the sizes considered here, there is a strong probability that the roughness locally is significantly higher than that observed in the laboratory, such that the two fracture surfaces are locally locked due to the effects of in-plane asperities.

- All modelled target fractures are embedded in linearly elastic rock. This means that no energy is expended on crack propagation or other inelastic deformations and, consequently, that the calculated slip magnitudes are overestimates (cf. /La Pointe et al. 2000/).

There is no safe way of quantifying the consequences of fractures being stepped, rather than planar, or having strong local in-plane asperities. Both would mean that the effective fracture size would be reduced or that part of the energy would have to be expended on fracturing rather than on friction work and, consequently, give smaller induced slip. Undulation can be taken into account in *3DEC* by specifying a relevant dilation component to the fracture shear strength. In the main set of models described in this report, no dilation is assumed. The sensitivity analysis, presented in Section 5.4.9, indicates that applying a dilation angle, typical to those obtained from lab-scale shear box tests on Forsmark samples reported by /Glamheden et al. 2007/, gives a 10–15% reduction of the maximum induced fracture displacement. Accounting for large-scale undulation effects would require the dilation angle to be increased, giving further reduced slip magnitudes.

The value of the friction angle used here is not necessarily conservative. In the sensitivity analysis it is, however, found that a variation of the friction angle corresponding to one standard deviation /Glamheden et al. 2007/ gives a variation of the maximum displacement of not more than about 10%.

Given the bounding assumptions of planar fracture geometry, uniform properties and elastic continuum, a number of observations can be made regarding the response of the target fractures:

- There is a strong correlation between the amount of induced target fracture slip and the distance from the seismogenic fault. For the M_w 7.5 models judged to be realistic/conservative, the maximum induced slip at 600 m distance is 55% of that at 200 m distance and 26% at 1,000 m. In the M_w 5.5 and M_w 6.2 models, the induced slip tapers off even faster with increasing distance.

- The slip decreases with distance in approximately the same way regardless of the slip mechanism, i.e. whether fractures slip because of a temporary loss of strength (which typically is the case for dipping fractures) or because of stress redistribution (which typically is the case for horizontal fractures).

- At the smallest fault-target distances, earthquake magnitude is not very important. The slip produced at 200 m from a M_w 7.5 earthquake is only about 20% larger than the slip produced by a M_w 5.5 earthquake. At larger distances, the magnitude becomes, relatively seen, more important; at 600 m distance the slip produced by a M_w 7.5 earthquake is about 100% larger than that produced by a M_w 5.5 earthquake (Figure 7-1). This is logical; disturbances generated by remote parts of a large fault are, compared to the disturbances generated by nearby parts, less important at small fault-target distances.

- The target fracture slip is not determined only by the distance to the fault. For a given event and a given distance, the calculated slip ranges from close to zero to the maximum slip observed for that event at that distance. The linear distributions suggested in Figure 7-1 are based on cumulative plots of results obtained for differently-oriented fractures at different locations relative to the epicentre and are judged to be reasonable approximations of the actual probability distributions (although the target fracture orientations may not be representative of a relevant distribution of fracture orientations at the given site).

- Steeply-dipping target fractures slip systematically less than horizontal and gently-dipping fractures. This is a logical consequence of the reverse stress regime assumed at 500 m depth with a considerable stability margin for steeply-dipping fractures.

- Target fracture slip scales with the size of the fracture. This should be expected for a fracture in an elastic medium subjected to quasi-static load changes, but appears to hold true also for the type of dynamic impact generated here by slipping earthquake faults.

- The slip is at maximum at the centre of the fracture and tapers off according to expressions valid for fractures in elastic media subjected to quasi-static load changes, cf. Figure 5-37. For the assessment of the risk of canister damage this is essential.

- The peak target fracture slip velocity found for fractures in the *3DEC* models, which are considered relevant for use in the interpretation model in Section 7.1, is less than 0.3 m/s. For the stress-deformation analyses of the buffer-canister system in /Börgesson and Hernelind 2006/, the effective velocity, i.e. the velocity evolution averaged over the total displacement, is the relevant measure of slip velocity. The effective velocities are a bit lower than the peak velocities, but higher than the average velocity over time. The effective velocities are less than 0.2 m/s for all fractures in the models used in Section 7.1.

- Similar to what was found for the displacements, the slip velocities scale with target fracture size and decrease with increasing fault-target distances. The highest slip velocities are found at the smallest distance (200 m).

- For dipping fractures all significant target fracture displacements are found to be mainly of reverse type, although sometimes with elements of strike-slip. No target fractures slip in excess of a few mm in the normal mode. This is a consequence of the post-glacial stress field with high horizontal stresses and low vertical stress. The style of slip is potentially important to the risk of canister damage, since reverse type slip produces a horizontal compression of the buffer-canister system, whereas normal slip would produce a horizontal extension with, possibly, different consequences.

8.4   Use of the results in layout and risk assessment work

8.4.1   Layout sketches

The numerical modelling results selected for layout and risk assessment (Section 7.2) are judged to be conservative because of the high earthquake slip velocities and the high magnitudes allowed for faults with short surface trace lengths. Additionally, there is a general conservativeness (described in the previous section) in the representation of target fractures. For the critical radii (Table 7-2.) and the schematic layout sketches (Figure 7-3) there are several over-estimates of target fracture slip due to conservatism in the modelling process:

- The 400 m slip results are slightly overestimated because of the linear interpolation between values calculated for the 200 m and 600 m distances.

- The slip values given for the different distance ranges are based on the value calculated for the smallest distance. The range average would be smaller.

- Steeply-dipping fractures are assumed to slip 25% less than corresponding gently-dipping fractures. At the average they slip even less.

The schematic layout sketches are based on the assumption that all deformation zones are capable of producing the largest and most damaging earthquake consistent with their (surface trace) length. In reality, this cannot be the case; even during periods of maximum general instability some deformation zones (those approximately aligned with the principal stress directions of the post-glacial stress field) will be almost perfectly stable. The problem is to establish the stress field with reasonable certainty and, based on that, assess the fault stability at the site and identify potential seismogenic faults.

8.4.2   Fault stability

The stability of deformation zones during the glacial cycle was assessed using a Coulomb failure criterion (Section 7.3). In order to calculate shear and normal stresses in differently-oriented planes, glacially-induced stresses obtained from ice-crust/mantle analyses were added to the *in situ* stresses. Three different models for the *in situ* stress field at larger depths were tried. However, there are large uncertainties in the instability calculations even with the condition that future glacial cycles will be identical to the latest one:

- There is no clear-cut answer to the question of the *in situ* stress at sub-repository depths. However, the *in situ* stresses assumed in the stability calculations would tend to overestimate rather than underestimate the instability compared to *in situ* stress models based on the principle of regression to a lithostatic state at depth by viscoplastic flow.

- The pore pressure evolution and the strength model that would be relevant for deformation zones at the time following the retreat of the ice are uncertain.

- There are large uncertainties also in the glacially-induced stresses. For instance, there are uncertainties in the ice model used by /Lund et al. 2009/; if there were longer periods of unbroken ice cover, the crustal flexural stresses would be larger. In addition, the glacial stress model does not account for the possible contribution of tectonic strain that could be accumulated under the stabilising ice cover /Lund et al. 2009/. These uncertainties were here accounted for by an addition of 5 MPa to the glacially-induced stresses.

While there are large uncertainties in the numbers given for the instability contours, the indicated orientations of stable deformation zones can probably be trusted. The projected major glacially-induced stress direction is approximately aligned with the present-day major stress direction (and with the major stress component of the tectonic strain contribution). The uncertainties related to the glacial stress addition are largely in the magnitudes rather than in the orientations. Therefore, the deformation zones found in the high-stability regions of the contoured pole plots (Figure 7-11, Figure 7-12) should be considered stable. The consequences for the Forsmark site would be as indicated in the maps in Figure 7-14 and Figure 7-15.

8.5 Final remarks

Summarizing the results and the discussion, the following recommendations for the Forsmark site are suggested:

8.5.1 Layout

For deformation zones indicated as potentially unstable in Figure 7-15, respect distances should be applied in principle as shown in the schematic layout sketches in Figure 7-3:

- No deposition within a 100 m band outside the damage zone of the deformation zones.

- Outside the 100 m band, fractures larger than the critical radii as defined in Table 7-2 need to be avoided.

According to the simulation results, gently-dipping zones (with dip angles of 30° or less) do not produce secondary displacements large enough to require any consideration of critical radii. This applies to the gently-dipping zone ZFMA2. The 100 m respect band, however, is still needed to eliminate the risk of intersecting directly connected fractures.

The 100 m band is not based on results from any calculations, but is rather a general safety measure. If the critical radii results (cf. Table 7-2) are interpolated between 100 m and 0 m distance, the critical radius at 30 m distance would be around 20 m. This means that it would be possible to make use of canister positions located between 30–100 m from the potential fault plane. However, at these small distances, the details in the description of the deformation zone may become important. For future layout versions it may be worthwhile to explore this possibility.

For the steeply-dipping zones ZFMENE0060A and ZFMENE0062A, which are indicated as stable in Figure 7-15, there is no need for any respect distances or any consideration of critical radii. These two zones have very considerable stability margins (Table 7-6) and are oriented such that these margins remain large even when accounting for possible variations in zone orientation and stress trend. Table 8-1 summarizes the deposition/respect distance rules that should be utilized by repository design in future layout revisions.

Table 8-1. Recommended deposition rules for zones with trace lengths > 3 km.

Deformation zone	0–100 m	100 m and further
ZFMENE0060A	Free	Free
ZFMENE0062A	Free	Free
ZFMA2	No deposition*	Free (Note: fractures intersecting the fault should be avoided)
ZFMNW0017	No deposition*	Consider critical radii (Table 7-2)
ZFMWNW0123	No deposition*	Consider critical radii (Table 7-2)
ZFMWNW0809A	No deposition*	Consider critical radii (Table 7-2)
ZFMNW1200	No deposition*	Consider critical radii (Table 7-2)

* See discussion on the 100 m band in the text.

8.5.2 Risk assessment

This report does not attempt to estimate the probability that a M_w 5, M_w 6 or M_w 7 earthquake will occur at Forsmark (or Laxemar) within the safety assessment timeframe, nor the probability that, if one occurs, it will be at a shallow-enough depth to impact the safety of the repository. The simulation results show that fault-target distances larger than about 1 km produce insignificant secondary displacements. This means that M_w 5, and possibly M_w 6, earthquakes that originate at a depth of 10 to 15 km are not likely to impact the repository. To assess the risk of canister damage, the point of departure should be the probability of M_w 5, M_w 6 and M_w 7 earthquakes occurring on mapped deformation zones that have the potential of breaching the ground surface and cannot be characterised as stable in a post-glacial stress environment.

Given the relevant occurrence probabilities, rough and conservative upper-bound estimates of the probability of induced target fracture shear displacements exceeding the threshold at different locations within the layout can be obtained using the results presented in this report. It is, however, very difficult to speculate on the degree of conservativeness in the upper-bound estimates. There is, for instance, no way of assessing the probability that earthquakes of given magnitudes will be of the kind assumed here (high-velocity, high-stress drop events) or that mapped deformation zones will produce earthquakes that are systematically of the largest potential magnitude. Reducing the fault slip velocity by 50%, (which still would give considerable slip velocities, cf. Figure 6-2) would effectively reduce all target fracture displacements by about 50%. More realistic assumptions regarding the velocity distribution (maximum velocities only along small portions of the fault surface rather than along a large fraction of the central fault area) would change the target slip distributions and greatly reduce the probability of exceeding the 50 mm threshold for fractures of all sizes at all distances.

For recurrence (i.e. multiple-slip events on a target fracture), to increase the probability of exceeding the threshold more than marginally, the earthquakes cannot be further apart than approximately 1 km (cf. Appendix C). The probability of one high-stress drop, high-velocity earthquake of M_w 5 or larger within or just outside the target volume is in itself very low. The probability for a second event of that magnitude within a distance of 1 km would be extremely low even if it would occur independently of the first one. In reality the first earthquake will relax existing tectonic stresses by releasing stored tectonic strain energy accumulated over long periods of time, resulting in a stabilizing effect on the rock surrounding the seismogenic fault for a period of time. For M_w 5 earthquakes, the stabilizing effects were found to stretch distances of several kilometres, in keeping with observations of interfault distances. The time scale for the stabilizing effects to disappear depends on the tectonic strain rate. A tectonic strain rate of 10^{-11} per year (as suggested by /Muir Wood 1995/), would produce an increase of less than 1 MPa during a 1 million year period, which should be compared with the stress release effects found here (on the order of 5 MPa at 1 km distance). The significant stress relaxation effects of potentially damaging earthquakes found in this report suggest that, regardless of the delicate and complicated details of how and at what rate, the stabilizing effects disappear, the probability of a nearby second earthquake within the time frame of the safety assessment is judged to be reduced sufficiently that the recurrence aspect should not need any further consideration. In addition, it is likely that a different and larger threshold should apply for the total effects of multiple slip episodes distributed over long periods of time (cf. Appendix C).

9 References

SKB's (Svensk Kärnbränslehantering AB) publications can be found at www.skb.se/publications.

Andrews D J, 2006. Deterministic Modelling of Physically-Limited Ground Motion, in Report of the Workshop on Extreme Ground Motions at Yucca Mountain, August 23–25, 2004. Open-File Report 2006-1277. Reston, Virginia, U.S. Geological Survey.

Arvidsson R, 1996. Fennoscandian earthquakes: whole crustal rupturing related to postglacial rebound. In: Science, vol 274(1): pp 744–746.

Arvidsson R, Wahlström R, Kulhánek O, 1992. Deep-crustal earthquakes in the southern Baltic Shield. Geophysical Journal International 108(3): pp 767–777.

Aydan Ö, Ohta Y, Genis M, Tokashiki N, Ohkubo K, 2010. Response and Stability of Underground Structures in Rock Mass during Earthquakes. Rock Mechanics and Rock Engineering.

Björnsson G, Flovenz Ó G, Saemundsson K, Einarsson E H, 2001. Pressure changes in Iceland geothermal reservoirs associated with two large earthquakes in June 2000. Twenty-Sixth Workshop on Geothermal Reservoir Engineering, Stanford University, Stanford, California.

Boatwright J, Bundock H, Luetgert J, Seekins L, Gee L, Lombard P, 2003. The Dependence of PGA and PGV on Distance and Magnitude Inferred from Northern California ShakeMap Data. Bull. Seism. Soc. Am. 93(5): pp 2043–2055.

Brady B H, Brown E T, 1993. Rock Mechanics for underground mining, Chapman & Hall. London, UK.

Brown E T, Hoek E, 1978. Trends in relationships between measured in situ stresses and depth. Int J. Rock Mech. Min. Sci. & Geomech. Abstr 15: pp 211–215.

Bäckblom G, Munier R, 2002. Effects of earthquakes on the deep repository for spent fuel in Sweden based on case studies and preliminary model results. SKB TR-02-24, Svensk Kärnbränslehantering AB.

Bödvarsson, R., 2002-2010. Swedish National Seismic Network (SNSN). Series of quarterly reports on recorded earthquakes. TD-02-16, P-02-04, P-03-02, P-03-37, P-03-79, P-04-24, P-04-73, P-04-197, P-04-248, P-05-32, P-05-71, P-05-200, P-05-243, P-06-11, P-06-78, P-06-158, P-06-235, P-07-16, P-07-82, P-07-163, P-07-201, P-08-01, P-08-51, P-08-60, P-08-75, P-09-03, P-09-22, P-09-44, P-10-04, Svensk Kärnbränslehantering AB

Börgesson L, Hernelind J, 2006. Earthquake induced rock shear through a deposition hole. Influence of shear plane inclination and location as well as buffer properties on the damage caused to the canister. SKB TR-06-43, Svensk Kärnbränslehantering AB.

Bödvarsson R, Lund B, Roberts R, Slunga R, 2006. Earthquake activity in Sweden. Study in connection with a proposed nuclear waste repository in Forsmark or Oskarshamn. SKB R-06-67, Svensk Kärnbränslehantering AB.

Campbell K W, 1989. The dependence of peak horizontal acceleration on magnitude, distance and site effects for small magnitude earthquakes in California and Eastern North America. Bull. Seism. Soc. Am. 79(5): pp 1311–1346.

Chan T, Christiansson R, Boulton G S, Eriksson L O, Hartikainen J, Jensen M R, Mas Ivars D, Stanchell F W, Wistrand P, Wallroth T, 2005. DECOVALEX III/BENCHPAR projects. The thermal-hydro-mechanical responses to a glacial cycle and their potential implications for deep geological disposal of nuclear fuel waste in a fractured crystalline rock mass. Report of BMT3/WP4. SKI Report 2005:28, SKI – Statens kärnkraftinspektion (Swedish Nuclear Power Inspectorate) Stockholm Sweden.

CWB, 2009. The home page of the Central Weather Bureau of Taiwan, www.cwb.gov.tw, Accessed 2009-02-26.

Eshelby J, 1957. The Determination of the Elastic Field of an Ellipsoidal Inclusion, and Related Problems. Proceedings of the Royal Society of London. Series A, Mathematical and Physical Sciences 241(1226): pp 376–396

Falcão S M J, Bento R, 2004. Seismic assessment to oil and gas lifelines. Paper no. 3150. 13th World conference on earthquake engineering. Vancouver, Canadian Society for Earthquake Engineering c/o Dept. of Civil Engineering, University of Ottawa, Canada.

Fälth B, Hökmark H, 2006. Seismically induced slip on rock fractures. Results from dynamic discrete fracture modeling. SKB R-06-48, Svensk Kärnbränslehantering AB.

Gephart J W, Forsyth D W, 1984. An improved method for determining the regional stress tensor using earthquake focal mechanism data: Application to the San Fernando earthquake sequence. J. Geophys. Res. 89: pp 9305–9320.

Glamheden R, Fredriksson A, Röshoff K, Karlsson J, Hakami H, Christiansson R, 2007. Rock Mechanics Forsmark. Site descriptive modelling Forsmark stage 2.2. SKB R-07-31, Svensk Kärnbränslehantering AB.

Glamheden R, Fälth B, Jacobsson L, Harrström J, Berglund J, Bergkvist L, 2010. Counterforce Applied to Prevent Spalling. SKB TR-10-37, Svensk Kärnbränslehantering AB.

Hakami E, Fredriksson A, Berg Bygg Konsult A B, Wrafter J, 2008. Rock mechanics Laxemar. Site descriptive modelling SDM-Site Laxemar. SKB R-08-57, Svensk Kärnbränslehantering AB.

Hanks T, Kanamori H, 1979. A Moment Magnitude Scale. J. Geophys. Res. 84(B5): pp 2348–2350.

Hedin A, 2005. An analytic method for estimating the probability of canister/fracture intersections in a KBS-3 repository. SKB R-05-29, Svensk Kärnbränslehantering AB.

Heidbach O, Tingay M, Barth A, Reinecker J, Kurfeß D, Müller B, 2008. The World Stress Map – Release 2008, www.world-stress-map.org.

Hildyard M W, Daehnke A, Cundall P A, 1995. WAVE: A computer program for investigating elastodynamic issues in mining. 35th U.S. Symposium on Rock Mechanics. Nevada, Balkema, Rotterdam**:** 519–524.

Hökmark H, Lönnqvist M, Fälth B, 2010. THM-issues in repository rock. Thermal, mechanical, thermo-mechanical and hydromechanical evolution of the rock at the Forsmark and Laxemar sites. SKB TR-10-23, Svensk Kärnbränslehantering AB.

ISRM, 1978. ISRM Commission on Standardization of Laboratory and Field Tests. Suggested methods for the quantative description of discontinuities in rock masses. In: Int. J. Rock Mech. Min. Sci. & Geomech. Abstr. Vol. 15(1978): pp 319–368.

Itasca, 2003. *3DEC* – 3-Dimensional Distinct Element Code, User's Guide, Version: 3. Itasca Consulting Group Inc. Minneapolis, USA.

Jacobsson L, Flansbjer M, 2005. Borehole KFM06A. Normal loading and shear tests on joints. Forsmark site investigation. SKB P-05-122, Svensk Kärnbränslehantering AB.

Jacobsson L, Flansbjer M, 2006. Borehole KFM09A Normal loading and shear tests on joints. Forsmark site investigation. SKB P-06-29, Svensk Kärnbränslehantering AB.

Jaeger J C, Cook N G W, 1979. Fundamentals of rock mechanics. Third ed, Science Paperbacks/ Chapman and Hall London UK.

Jing L, Stephansson O, 2007. Fundamentals of Discrete Element Methods for Rock Engineering: Theory and Applications, Elsevier. Amsterdam, The Netherlands. ISBN: 978-0-444-82937-5.

Johnston A C, 1989. The effect of large ice sheets on earthquake genesis, in Earthquakes at North-Atlantic passive margins; neotectonics and postglacial rebound, Gregersen S, Basham P W, Eds. Dordrecht-Boston, D. Reidel Publishing Company. 581–599.

Kanamori H, 1977. The Energy Release in Great Earthquakes. J. Geophys. Res. 82(20): pp 2981–2987.

La Pointe P, Wallmann P, Thomas A, Follin S, 1997. A methodology to estimate earthquake effects on fractures intersecting canister holes. SKB TR 97-07, Svensk Kärnbränslehantering AB.

La Pointe P R, Cladouhos T T, Outters N, Follin S, 2000. Evaluation of the conservativeness of the methodology for estimating earthquake-induced movements of fractures intersecting canisters. SKB TR-00-08, Svensk Kärnbränslehantering AB.

Lagerbäck R, 1979. Neotectonic structures in northern Sweden. In: Geologiska Föreningens i Stockholm Förhandlingar, Vol 100(1978): pp 263–269.

Lagerbäck R, 1988. Postglacial faulting and paleoseismicity in the Landsjärv area, northern Sweden. SKB TR 88-25, Svensk Kärnbränslehantering AB.

Lagerbäck R, Sundh M, 2008. Early Holocene faulting and paleoseismicity in northern Sweden. Research Paper C 836. SGU – Sveriges Geologiska Undersökning.

Larsson S Å, Tullborg E-L, 1993. Tectonic regimes in the Baltic Shield during the last 1200 Ma – A review. SKB TR 94-05, Svensk Kärnbränslehantering AB.

Leijon B, 1993. Mechanical properties of fracture zones. SKB TR 93-19, Svensk Kärnbränslehantering AB.

Lund B, 2006. Stress variations during a glacial cycle at 500 m depth in Forsmark and Oskarshamn: Earth model effects. SKB R-06-95, Svensk Kärnbränslehantering AB.

Lund B, Zoback M D, 1999. Orientation and magnitude of in situ stress to 6.5 km depth in the Baltic Shield. In: International Journal of Rock Mechanics and Mining Sciences, vol 36: pp 169–190.

Lund B, Schmidt P, Hieronymus C, 2009. Stress evolution and fault stability during the Weichselian glacial cycle. SKB TR-09-15, Svensk Kärnbränslehantering AB.

Lönnqvist M, Kristensson O, Fälth B, 2010. Assessment of a KBS-3 nuclear waste repository as a plane of weakness. SKB R-10-36, Svensk Kärnbränslehantering AB.

Ma K-F, Mori J, J L S, Yu S B, 2001. Spatial and Temporal Distribution of Slip for the 1999 Chi-Chi, Taiwan, Earthquake. Bull. Seism. Soc. Am. 91(5): pp 1069–1087.

Ma K-F, Brodsky E E, Mori J, Ji C, Song T-R A, Kanamori H, 2003. Evidence for fault lubrication during the 1999 Chi-Chi, Taiwan, eathquake (Mw7.6). In: Geophysical Research Letters, vol 30(5).

Milnes A G, Gee D G, Lund C-E, 1998. Crustal structure and regional tectonics of SE Sweden and the Baltic Sea. SKB TR-98-21, Svensk Kärnbränslehantering AB (SKB) Stockholm Sweden.

Muir Wood R, 1989. Extraordinary deglaciation reverse faulting in northern Fennoscandia, in Earthquakes at North-Atlantic passive margins; neotectonics and postglacial rebound, Gregersen S, Basham P W, Eds. Dordrecht-Boston, D. Reidel Publishing Company. 141–173

Muir Wood R, 1993. A review of the seismotectonics of Sweden. SKB TR 93-13, Svensk Kärnbränslehantering AB (SKB) Stockholm Sweden.

Muir Wood R, 1995. Reconstructing the tectonic history of Fennoscandia from its margins: The past 100 million years. SKB TR 95-36, Svensk Kärnbränslehantering AB.

Muir Wood R, King G C P, 1993. Hydrological Signatures of Earthquake Strain. Journal of Geophysical Research 98(B12): pp 22,035–22,068.

Munier R, 2006. Using observations in deposition tunnels to avoid intersections with critical fractures in deposition holes. SKB R-06-54, Svensk Kärnbränslehantering AB.

Munier R, 2010. Full perimeter intersection criteria. Definitions and implementations in SR-Site. SKB Rapport TR-10-21, Svensk Kärnbränslehantering AB.

Munier R, Fenton C, 2004. Review of postglacial faulting. Current understanding and directions for future studies, in Respect distances – Rationale and means of computation, SKB R-04-17, Svensk Kärnbränslehantering AB.

Munier R, Hökmark H, 2004. Respect distances. Rationale and means of computation. SKB R-04-17, Svensk Kärnbränslehantering AB.

O'Rourke T D, Wang Y, Shi P, 2004. Advances in lifeline earthquake engineering. Paper no. 5003. 13th World conference on earthquake engineering. Vancouver, Canadian Society for Earthquake Engineering c/o Dept. of Civil Engineering, University of Ottawa, Canada.

Oglesby D D, Archuleta R J, Nielsen S B, 1998. Earthquakes on Dipping Faults: The Effects of Broken Symmetry. Science 280(1055).

Olesen O, 1988. The Stuoragurra Fault, evidence of neotectonics in the Precambrian of Finnmark, northern Norway. Norsk Geologisk Tidsskrift 68: pp 107–118.

Richter C, 1935. An Instrumental Magnitude Scale. Bull. Seism. Soc. Am. 25: pp 1–32.

Scholz C H, 2002. The Mechanics of Earthquakes and Faulting, 2nd edition, Cambridge University Press.

Scholz C H, 2006. Strength of faults and maximum stress drops in earthquakes, in Report of the Workshop on Extreme Ground Motions at Yucca Mountain, August 23–25, 2004. Open-File Report 2006-1277. Reston, Virginia, U.S. Geological Survey.

Sekiguchi H, Horikawa H, Kase Y, Ishiyama T, Satake K, Sugiyama Y, Mizuno K, Pitarka A, 2004. Ground motion prediction in Osaka Basin, central Japan, based on geological, geophysical and paleo-seismological data and numerical simulations of earthquake rupture and ground motion. Paper no. 1768. 13th World conference on earthquake engineering, Vancouver, August 2004, Canadian Society for Earthquake Engineering c/o Dept. of Civil Engineering, University of Ottawa, Canada.

Skarlatoudis A A, Papazachos C B, Margaris B N, Theodulidis N, Papaioannou C, Kalogeras I, Scordilis E M, Karakostas V, 2003. Empirical peak ground motion predictive relations for shallow earthquakes in Greece. Bull. Seism. Soc. Am. 93(6): pp 2591–2603.

Skarlatoudis A A, Theodulidis N, Papaioannou C, Roumelioti Z, 2004. The dependence of peak horizontal acceleration on magnitude and distance for small magnitude earthquakes in Greece. 13th World conference on earthquake engineering, Vancouver, August 2004, Canadian Society for Earthquake Engineering c/o Dept. of Civil Engineering, University of Ottawa, Canada.

Skarlatoudis A A, Papazachos C B, Margaris B N, Theodulidis N, Papaioannou C, Kalogeras I, Scordilis E M, Karakostas V, 2007. Erratum to Empirical peak ground motion predictive relations for shallow earthquakes in Greece. Bull. Seism. Soc. Am. 97(6): pp 2219–2221.

SKB, 1999. SR 97 – Deep repository for spent nuclear fuel. SR 97 – Post-closure safety. Main report – Vol. I, Vol. II and Summary. SKB TR-99-06, Svensk Kärnbränslehantering AB.

SKB, 2003. Planning report for the safety assessment SR-Can. SKB TR-03-08, Svensk Kärnbränslehantering AB.

SKB, 2005a. Preliminary site description. Simpevarp subarea – version 1.2. SKB R-05-08, Svensk Kärnbränslehantering AB.

SKB, 2005b. Preliminary site description. Forsmark area – version 1.2. SKB R-05-18, Svensk Kärnbränslehantering AB.

SKB, 2006a. Long-term safety for KBS-3 repositories at Forsmark and Laxemar – a first evaluation. Main report of the SR-Can project. SKB TR-06-09, Svensk Kärnbränslehantering AB.

SKB, 2006b. Climate and climate-related issues for the safety assessment SR-Can. SKB TR-06-23, Svensk Kärnbränslehantering AB.

SKB, 2006c. Preliminary site description. Laxemar subarea – version 1.2. SKB R-06-10, Svensk Kärnbränslehantering AB.

SKB, 2009a. Design premises for a KBS-3V repository based on results from the safety assessment SR-Can and some subsequent analyses. SKB TR-09-22, Svensk Kärnbränslehantering AB.

SKB, 2009b. Underground design Forsmark Layout D2. SKB R-08-116, Svensk Kärnbränslehantering AB.

SKB, 2010a. Buffer, backfill and closure process report for the safety assessment SR-Site. SKB TR-10-47, Svensk Kärnbränslehantering AB.

SKB, 2010b. Geosphere process report for the safety assessment SR-Site. SKB TR-10-48, Svensk Kärnbränslehantering AB.

SKB, 2010c. Forsmark Site Engineering Report. Guidelines for Underground Design Step D2. SKB R-08-83, Svensk Kärnbränslehantering AB.

Slunga R S, 1991. The Baltic Shield earthquakes. In: Tectonophysics, vol **189**: pp 323–331.

Stanfors R, Ericsson L O, 1993. Post-glacial faulting in the Lansjärv area, Northern Sweden. Comments from the expert group on a field visit at the Molberget post-glacial fault area, 1991. SKB TR 93-11, Svensk Kärnbränslehantering AB.

Stein S, Wysession M, 2003. An introduction to Seismology, Earthquakes, and Earth structure, Blackwell Publishing, Malden, USA.

Stephansson O, Savilahti T, Bjarnason B, 1989. Rock mechanics of the deep borehole at Gravberg, Sweden. A.A. Balkema, Rotterdam, Netherlands (NLD). ISBN: 9061919746.

Stephens M B, Fox A, La Pointe P, Simeonov A, Isaksson H, Hermanson J, Öhman J, 2007. Geology Forsmark. Site descriptive modelling Forsmark stage 2.2. SKB R-07-45, Svensk Kärnbränslehantering AB.

Stephens M B, Simeonov A, Isaksson H, 2008. Bedrock geology Forsmark. Modelling stage 2.3. Implications for and verification of the deterministic geological models based on complementary data. SKB R-08-64, Svensk Kärnbränslehantering AB.

Thomas A L, 1993. Poly3D: A three dimensional polygonal element displacement discontinuity boundary element computer program with applications to fractures, faults and cavities in the earths crust, Version 1.0, Stanford University.

USGS, 2008. Geological Survey WebSite: http://neic.usgs.gov/neis/last_event/world_sweden.html

Wald D J, Heaton T H, 1994. Spatial and temporal distribution of slip for the 1992 Landers, California, earthquake. In: Bulletin of the Seismological Society of America, vol 691(1994).

Wells D L, Coppersmith K J, 1994. New empirical relationships among magnitude, rupture length, rupture width, rupture area and surface displacement. Bull. Seism. Soc. Am. 84(4): pp 974–1002.

Wu P, 2009. State-of-the-Science Review of the Stress Field during a Glacial Cycle and Glacially Induced Faulting. NWMO TR-2009-09, Nuclear Waste Management Organization.

Yoshizaki K, Sakanoue T, 2004. Analytical study on soil-pipeline interaction due to large ground deformations. Paper no. 1402. 13th World conference on earthquake engineering, Vancouver, August 2004, Canadian Society for Earthquake Engineering c/o Dept. of Civil Engineering, University of Ottawa, Canada.

Zoback M D, Townend J, 2001. Implications of hydrostatic pore pressures and high crustal strength for the deformation of intraplate lithosphere. Tectonophysics 336(1–4): pp 19–30.

Static large-scale model

A static large-scale model is set up in order to make an estimate of what stress levels are needed to produce the displacements that have been reported for the post-glacial faults in Lapland by /Muir Wood 1993, Arvidsson 1996/. These authors have estimated the average fault slip, $\bar{u}$, of the Pärvie Fault to be 8–10 m and its width, W, to be 40–45 km. This gives an average slip/fault width ratio in the range of $1.8\cdot10^{-4}$–$2.5\cdot10^{-4}$.

The geometry of the model is shown in Figure A-1. The model dimensions are 60 km in the x- and y-directions and 120 km in the z-direction. A fault plane dipping 70 degrees with respect to the horizontal plane is defined. The plane is 40 km deep and 80 km along strike. The vertical boundary that cuts off the fault is a symmetry plane. Thus, the actual simulated fault length is 2 x 80 km = 160 km. All boundaries except for the top boundary have rollers, i.e. they are locked for displacements in their normal directions. The top boundary that represents the ground surface is free. The rock is assumed to be a linear elastic material with a Young's modulus $E = 75$ GPa and Poisson's ratio $\upsilon = 0.25$.

The initial stress magnitudes are calibrated to give the intended slip/width ratio given that the residual fault shear strength is set to zero. The stresses vary with depth, y, according to the equations in Table A-1. The stresses are plotted in Figure A-2.

Table A-1. Initial stresses.

σ_H	σ_h	σ_v
$\begin{cases} 35.00\text{–}0.0220y \ (-3{,}000 \leq y \leq 0) \\ 21.72\text{–}0.0264y \ (-20{,}000 \leq y \leq -3000) \end{cases}$	$17.18\text{–}0.0156y$	$-0.0265y$
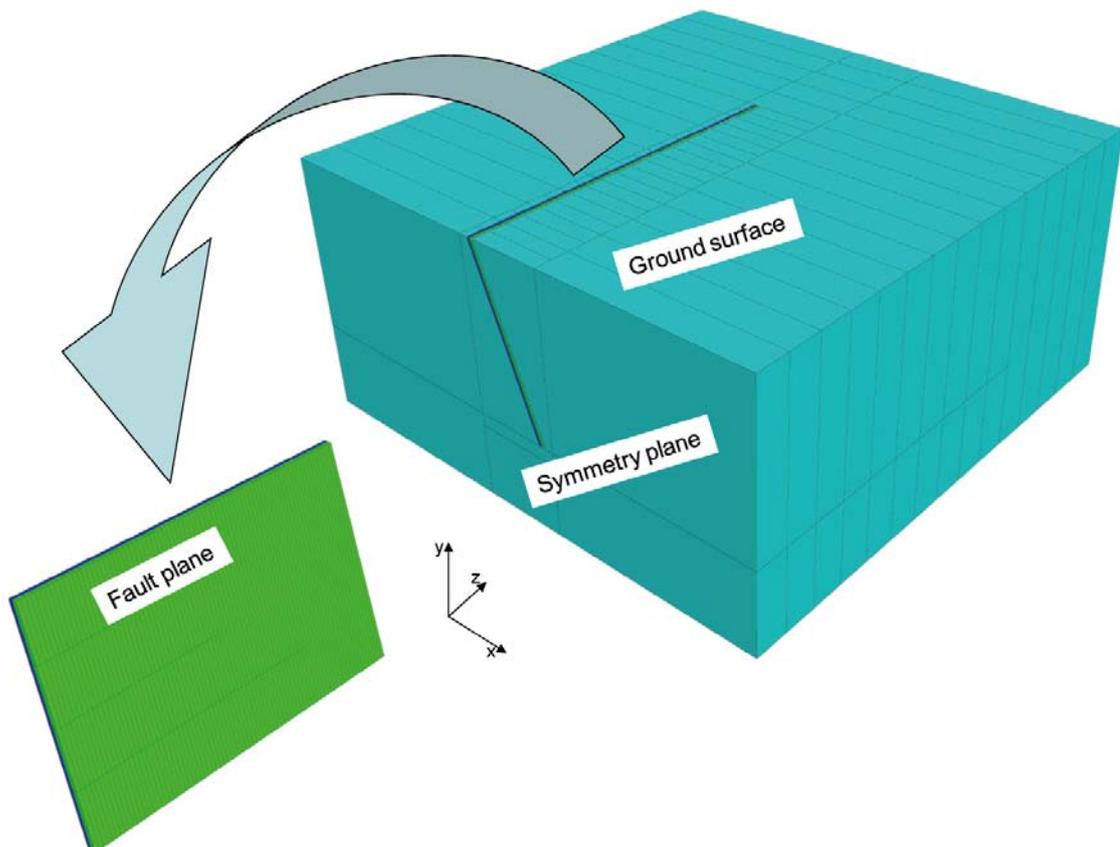
Figure A-1. *Geometric outlines of the model. The model includes half of the fault length.*

Initial stresses

Stress (MPa)
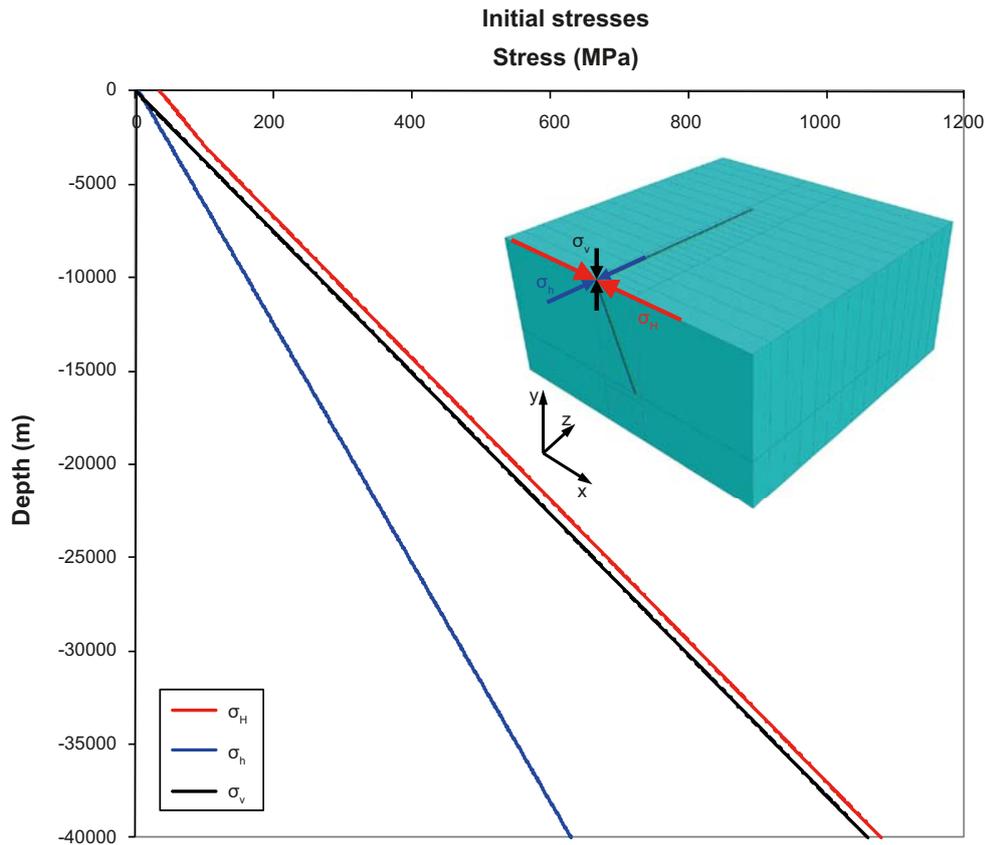
***Figure A-2.*** *Initial stress variations with depth.*

Initially, the fault plane is given a high cohesion in order to prevent slip. Then, four simulation steps are carried out, where each step represents one particular fault geometry. The different geometries are created by assigning zero strength to different portions of the fault plane (Figure A-3). Hence, the resulting fault displacements for earthquakes of four different sizes can be simulated. The fault length/width ratio is about 4:1 in all steps. The dimensions of the active part of the fault plane in each step are presented in Table A-2 along with the corresponding average displacements and moment magnitudes. Due to the symmetry assumption, only half of the simulated fault length is included in the model. The following can be observed:

• The average slip/fault width ratio is in the range $2.23 \cdot 10^{-4}$–$2.55 \cdot 10^{-4}$ which is in line with the estimates made by /Muir Wood 1993/ and /Arvidsson 1996/.

• The fault width and moment magnitude in the last step is in agreement with the estimates made for the Pärvie Fault /Muir Wood 1993/ and /Arvidsson 1996/.

Vector plots of fault shear displacements in the different simulation steps are shown in Figure A-4 through Figure A-7.

Table A-2. Fault geometry and simulation results.

Step	Width, W (km)	Length (km)	Average fault displacement, $\bar{u}$ (m)	$\bar{u}/W$	Seismic moment (Nm)	Moment magnitude, M_w
1	10.6	40	2.7	$2.55 \cdot 10^{-4}$	$3.2 \cdot 10^{19}$	6.9
2	21.3	80	5.3	$2.49 \cdot 10^{-4}$	$2.6 \cdot 10^{20}$	7.5
3	31.9	120	7.7	$2.41 \cdot 10^{-4}$	$8.7 \cdot 10^{20}$	7.9
4	42.6	160	9.5	$2.23 \cdot 10^{-4}$	$1.9 \cdot 10^{21}$	8.1
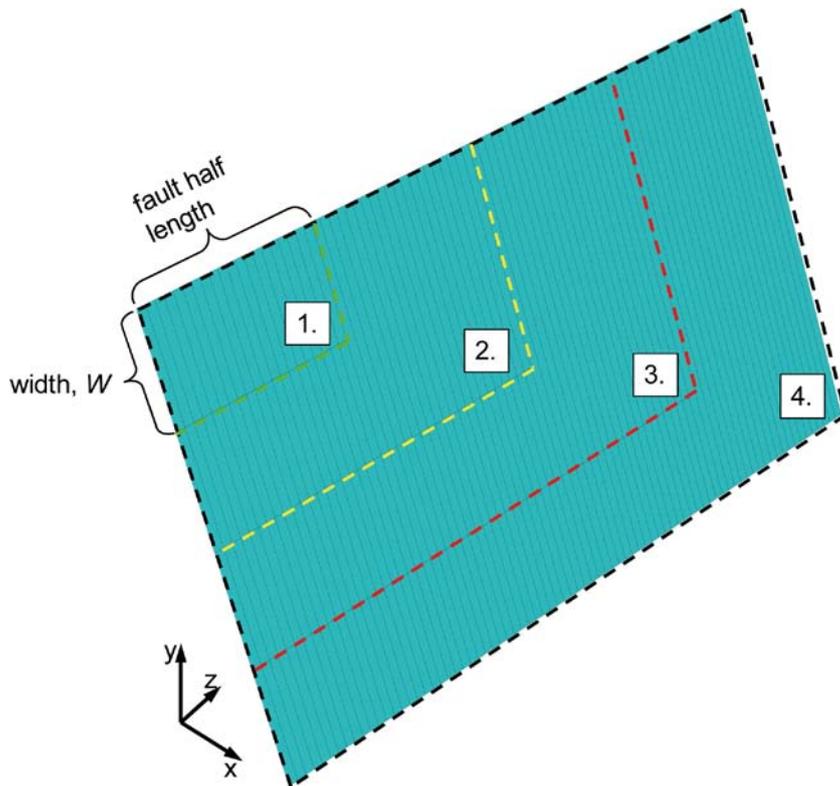
Figure A-3. *The fault areas used during the different calculation steps (cf. Table A-2). The simulated fault length/fault width ratio is about 4:1 in all steps. Note that, due to the symmetry assumption, the simulated fault length is twice the length included in the model.*
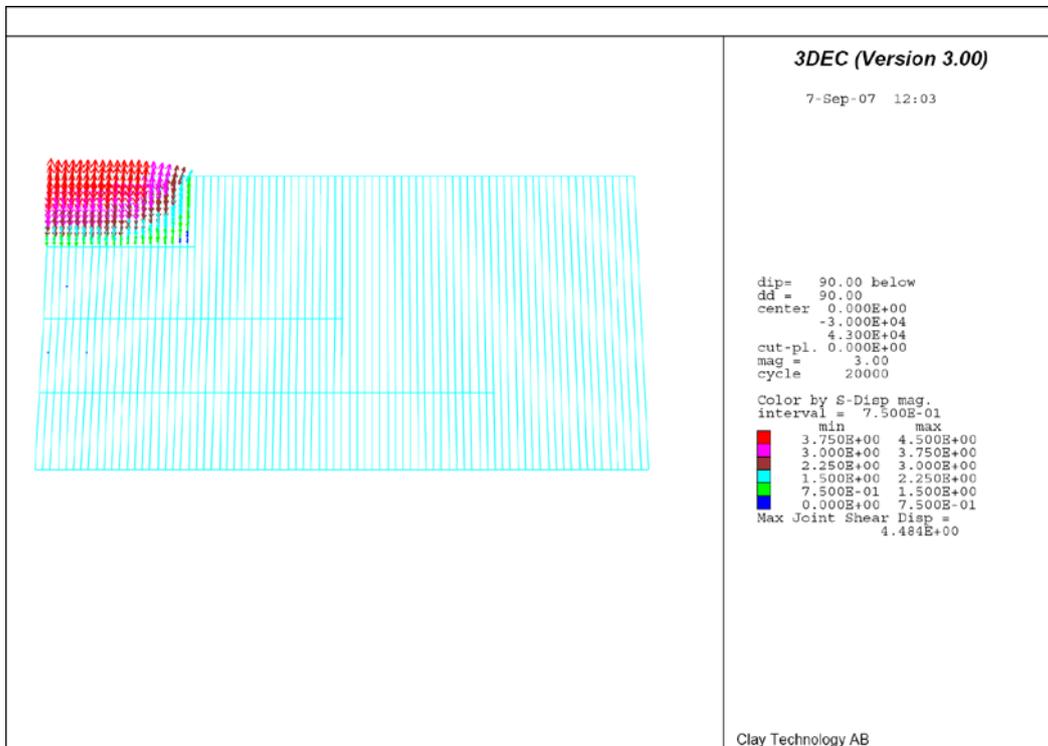
***Figure A-4.*** *Vector plot of fault shear displacements in Step 1.*
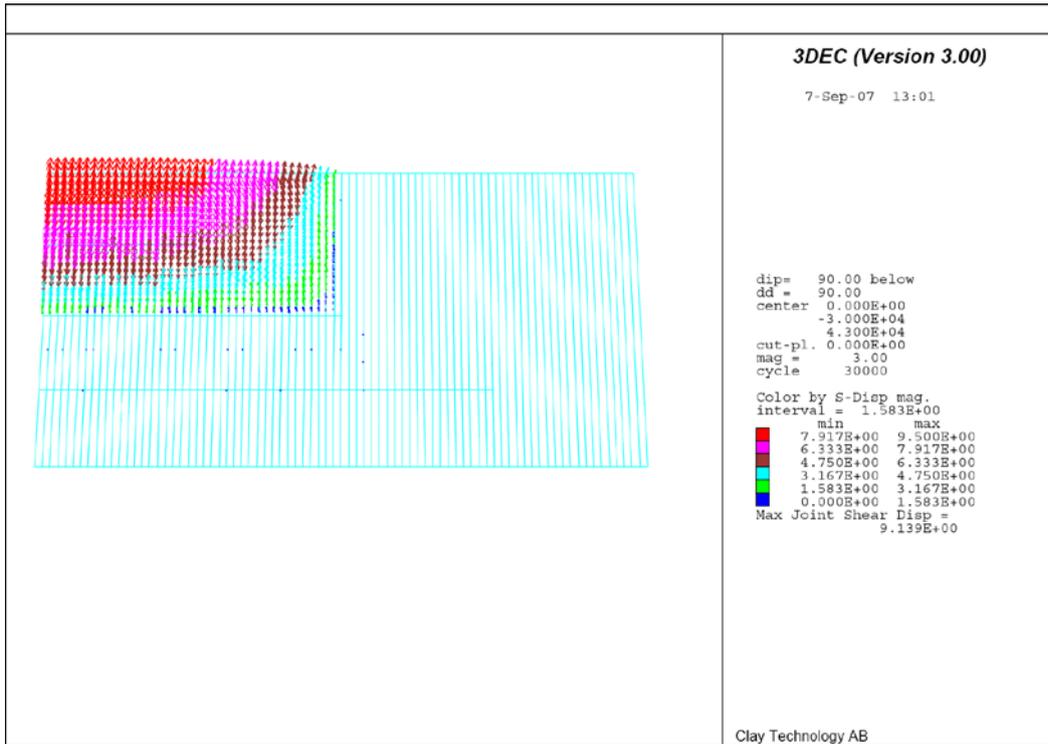
**Figure A-5.** *Vector plot of fault shear displacements in Step 2.*
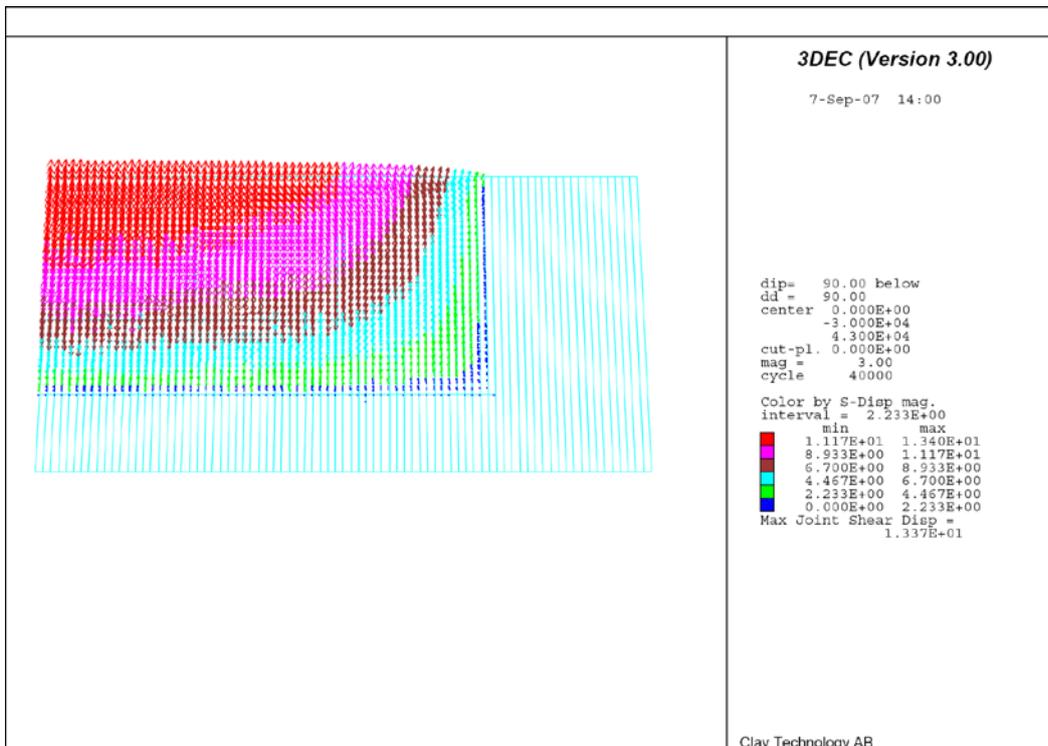
Figure A-6. *Vector plot of fault shear displacements in Step 3.*
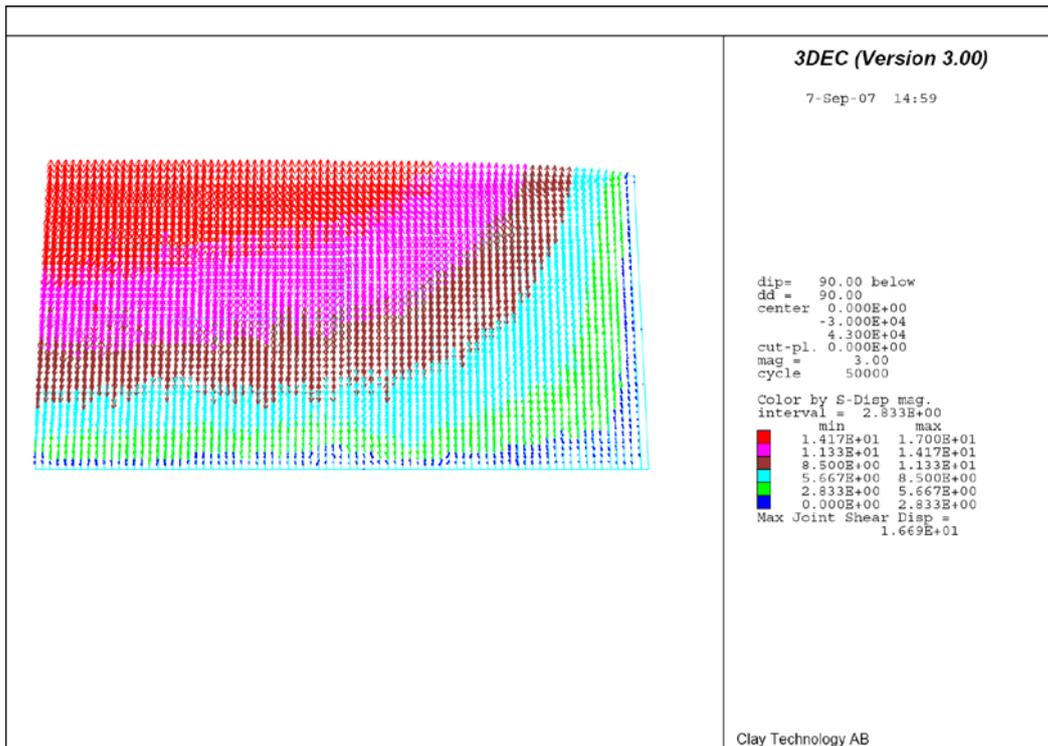
Figure A-7. *Vector plot of fault shear displacements in Step 4.*

Target fractures

The first subsection of this appendix describes how the circular target fractures are created in the *3DEC* cut planes inside the target fracture region. The fracture locations and orientations for the different target fracture configurations are presented in the second (M_w 5.5 and M_w 6.2 models) and third subsections (M_w 7.5 models).

Creation of target fractures

A number of *3DEC* cut planes are created inside the target fracture region at different distances from the primary fault and with different orientations (Figure B-1). The cut planes act as boundaries between blocks (cf. Section 4.3); slip can potentially take place along a cut plane depending on the local stress conditions and on the mechanical properties assigned to the sub-contacts in the plane. The circular target fractures are defined by assigning fracture properties to sub-contacts located in circular areas in the cut planes. In order to prevent slip along the remaining parts of the cut planes, fictitious properties with high strength are assigned to these parts, i.e. to simulate intact rock.

The target fractures are formed using an algorithm developed in the *3DEC* built-in programming language *FISH*. The algorithm is illustrated in Figure B-1. A target fracture is the circular area defined by the intersection between:

1. An imaginary sphere with its centre located in the centre of the target fracture and with its radius equal to that of the fracture.

2. A *3DEC* cut plane with intended dip and dip direction angles intersecting the centre point of the sphere.

In each *3DEC* cut plane a number of target fractures may be defined. By having cut planes with different orientations located at different distances from the fault, each model may contain numerous target fractures at different locations and with different orientations (Figure B-2). All target fractures in this study are circular with a radius of 150 m and are located with their centres at a depth of 500 m.
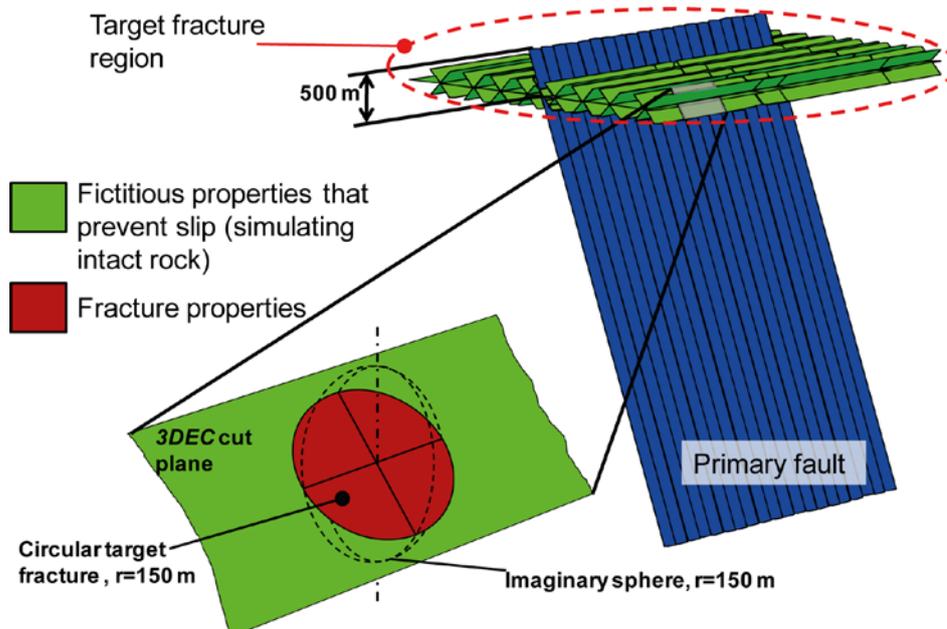
Figure B-1. *The principle used for defining a circular fracture in a 3DEC cut plane. The circular fracture is defined as the intersection between an imaginary sphere and the cut plane. Fracture properties are assigned to the sub-contacts inside the circular area. In order to prevent slip in the remaining parts of the plane (i.e. simulate intact rock) fictitious properties with high strength are assigned to these parts.*

One cut plane may be used to create several target fractures at different locations.
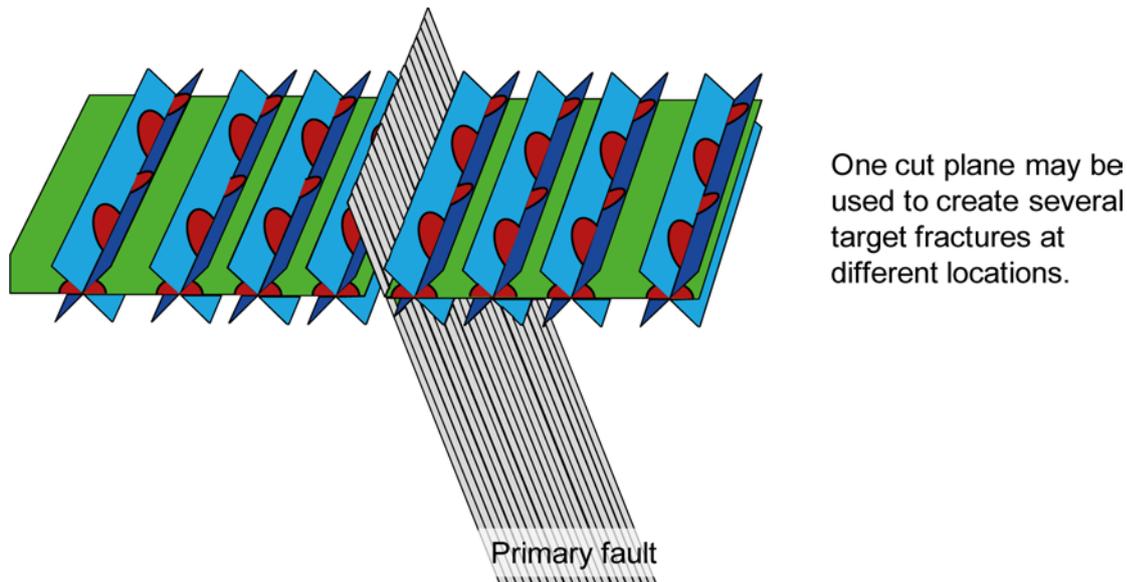
Figure B-2. *Sketch that illustrates how target fractures with different orientations are created at different locations. Several cut planes may intersect one particular location, but only one of them is used to define a target fracture at that location. In the figure three sets of cut planes are shown: 1. Horizontal plane covering the entire fracture region (green). 2. Planes with same dip direction as the primary fault (light blue). 3. Planes with opposite dip direction to the primary fault (dark blue).*

Target fracture configurations used in M_w 5.5 models and M_w 6.2 models

Figure B-3 (right) and Figure B-4 (right) are sketches of the base case configurations used in the M_w 5.5 and M_w 6.2 models, respectively. The sketches are top-down vertical views of the target fracture region. The intersection between the fault plane and the repository horizon at 500 m depth is indicated by the solid blue line. The numbers in the figures indicate the horizontal distances from the fault plane, i.e. the Cartesian distances are smaller. Two target fracture dip directions are used: one in the same direction as the fault and one in a direction opposite to that of the fault. The dip directions of the fractures are indicated by arrows inside the circles. All non-horizontal fractures have a dip angle of 45°. The left insets show the *3DEC* cut planes used to create the fracture configuration.

The right picture in Figure B-5 is a sketch of the principle of fracture configuration ALT1. This configuration is used to examine the effect of having target fractures with strikes that are not parallel to the strike of the primary fault. Four different fracture dip directions are used, as indicated by the arrows inside the circles. All non-horizontal fractures have a dip angle of 45° and strike directions that differ by 45° from that of the primary fault plane. The left inset shows the *3DEC* cut planes used to create the fracture configuration. The vertical planes inside the target fracture region are only construction planes used to define the geometry.

The right picture in Figure B-6 is a sketch of the principle of fracture configuration ALT2. This configuration is used in the M_w 5.5 model with a 30° fault dip angle. The dip directions of the non-horizontal fractures are indicated by arrows. All non-horizontal have dip angle of 45°. The left inset shows the *3DEC* cut planes used to create this fracture configuration.

The right picture in Figure B-7 is a sketch of the principle of fracture configuration ALT3. This configuration is similar to the M_w 5.5 BASE CASE configuration shown in Figure B-3, but with all target fracture dip angles set to 30°. The dip directions of the dipping fractures are indicated by arrows. The numbers in the figure indicate the horizontal distances from the fault plane, i.e. the Cartesian distances are smaller. The left inset shows the *3DEC* cut planes used to create this fracture configuration.
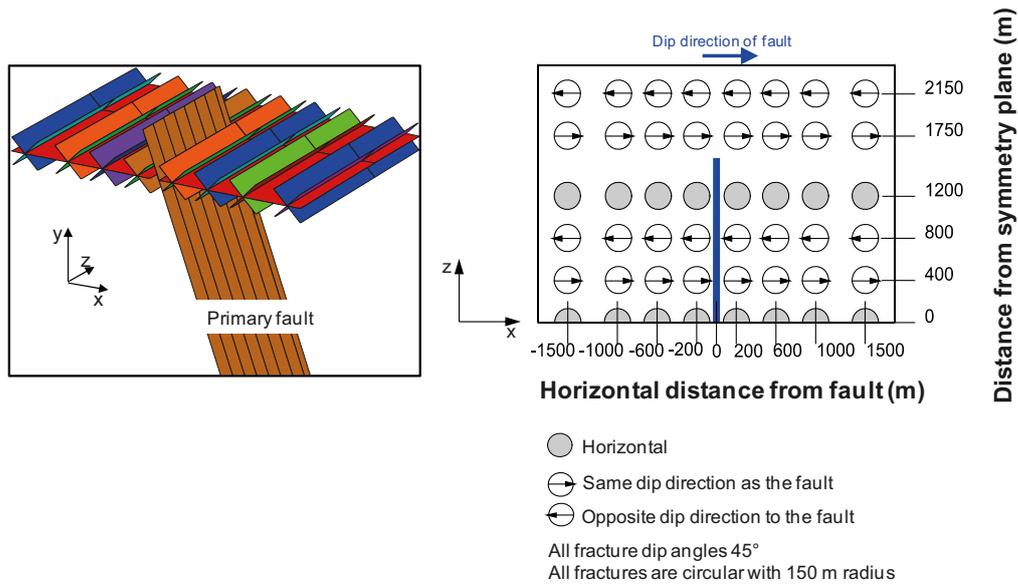
Figure B-3. *The right picture is a sketch of the principle showing the target fracture locations and orientations in the BASE CASE fracture configuration in the M_w 5.5 models. The sketch is a top-down vertical view from above of the target fracture region. The solid blue line indicates the intersection between the fault plane and the repository horizon at 500 m depth. The arrows indicate the dip directions of the dipping fractures which all have dip angle 45°. The left inset shows the 3DEC cut planes used to create this fracture configuration.*
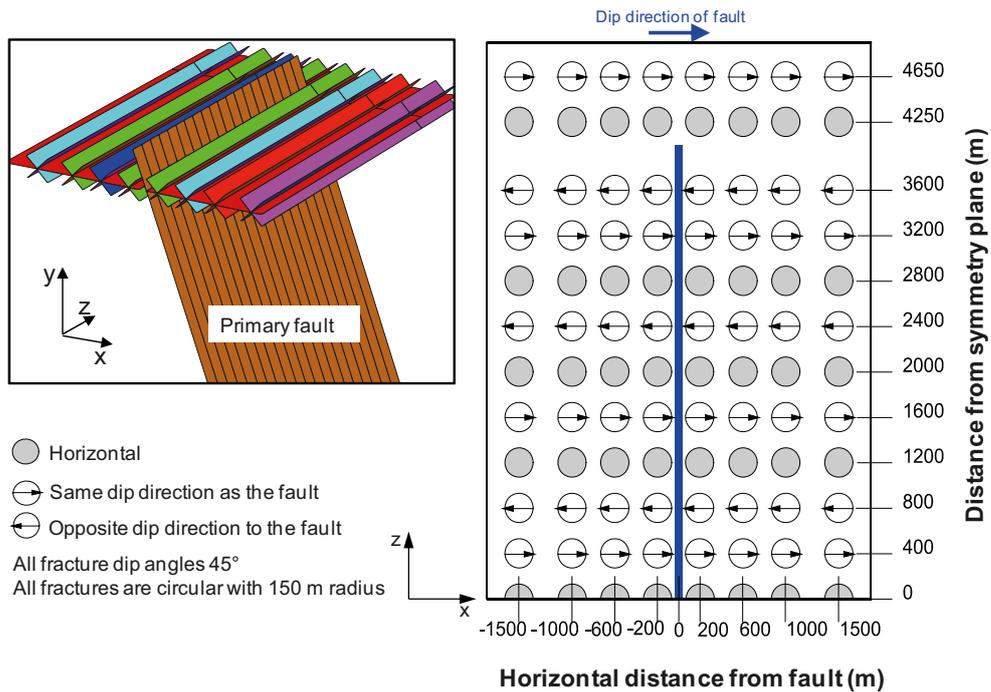
Figure B-4. *The right picture is a sketch of the principle showing the target fracture locations and orientations in the BASE CASE fracture configuration in the M_w 6.2 models. The sketch is a top-down vertical view from above of the target fracture region. The solid blue line indicates the intersection between the fault plane and the repository horizon at 500 m depth. The arrows indicate the dip directions of the dipping fractures which all have dip angle 45°. The left inset shows the 3DEC cut planes used to create this fracture configuration.*
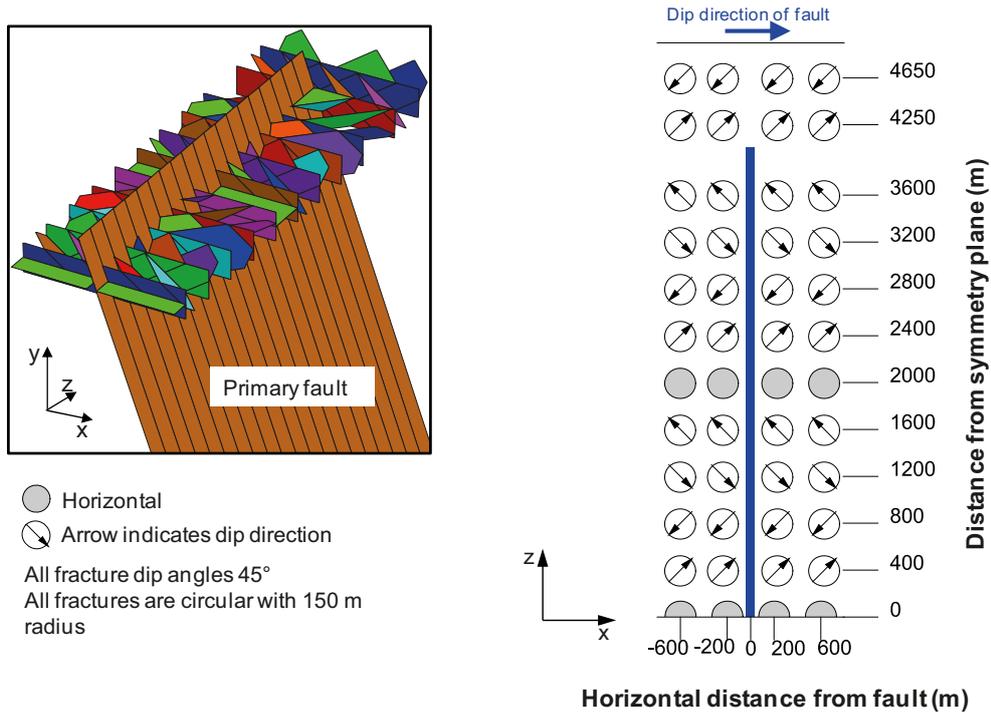
Figure B-5. *The right picture is a sketch of the principle showing target fracture locations and orientations in the ALT1 configuration used in the M$_w$ 6.2 models. The sketch is a top-down vertical view from above of the target fracture region. The solid blue line indicates the intersection between the fault plane and the repository region. The arrows indicate the dip directions of the dipping fractures which all have dip angle 45°. The left inset shows the 3DEC cut planes used to create this fracture configuration. The vertical planes inside the target fracture region are only construction planes used to define the geometry.*
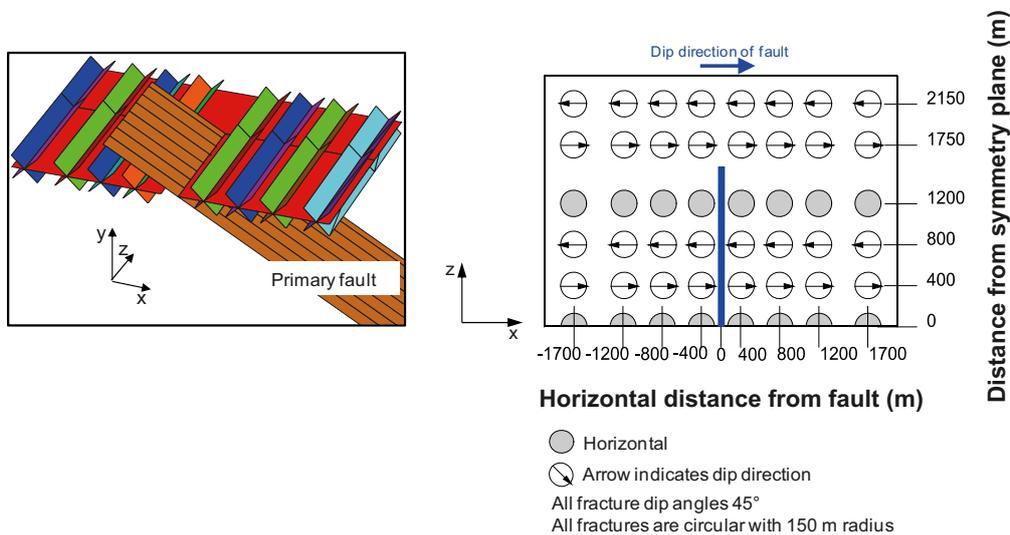
Figure B-6. *The right picture is a sketch of the principle showing target fracture locations and orientations in the ALT2 configuration used in the M$_w$ 5.5 models with primary fault dip angle of 30°. The sketch is a top-down vertical view from above of the target fracture region. The solid blue line indicates the intersection between the fault plane and the repository horizon. The arrows indicate the dip directions of the dipping fractures which all have a dip angle of 45°. The left inset shows the 3DEC cut planes used to create this fracture configuration.*

Horizontal distance from fault (m)

Distance from symmetry plane (m)

Dip direction of fault

⬤ Horizontal
◕ Arrow indicates dip direction
All fracture dip angles 30°
All fractures are circular with 150 m radius
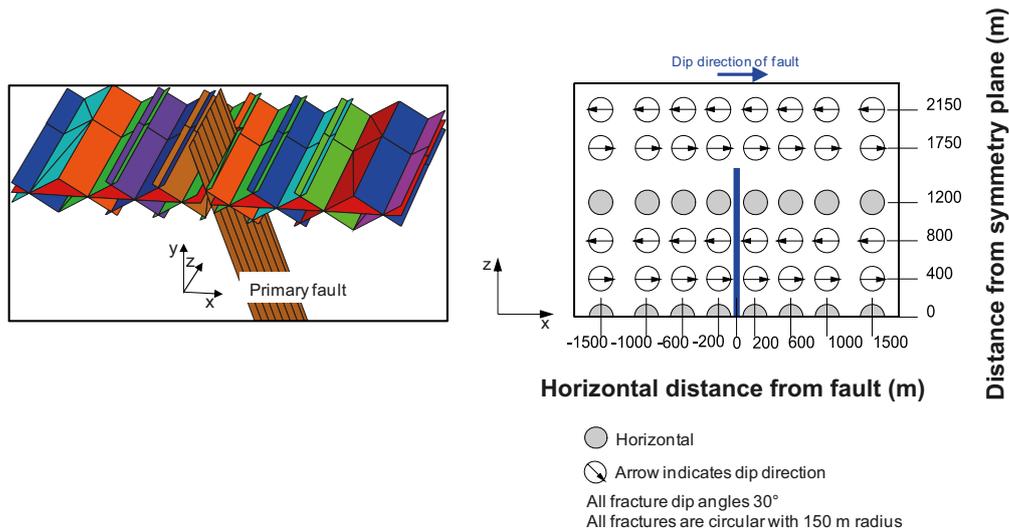
Figure B-7. *The right picture is a sketch of the principle showing target fracture locations and orientations in the ALT3 configuration used in one of the M_w 5.5 models. The sketch is a top-down vertical view from above of the target fracture region. The solid blue line indicates the intersection between the fault plane and the repository horizon. This configuration is similar to the M_w 5.5 BASE CASE configuration shown in Figure B-3, but with all target fracture dip angles set to 30°. The arrows indicate the dip directions of the dipping fractures. The left inset shows the 3DEC cut planes used to create this fracture configuration.*

Target fracture configurations used in M_w 7.5 models

The right picture in Figure B-8 is a sketch of the principle of the BASE CASE, ALT1 and ALT2 target fracture configurations. The sketch is a top-down vertical view from above of the target fracture region. The solid blue line indicates the intersection between the fault plane and the repository horizon. Each of these configurations includes 24 fractures located at different distances from the fault and the symmetry plane. Two different target fracture dip directions are used: one is the same direction as the source fault and one is opposite that of the fault. The dip directions are indicated by arrows in the figure. The configurations are similar, but have different fracture dip angles as indicated by the figure legend. The numbers in the figure indicate the horizontal distances from the fault and from the symmetry plane. The left inset shows the *3DEC* cut planes used to create these fracture configurations.

Figure B-9 shows a sketch of the principle of the ALT3 and ALT4 target fracture configurations. The concept of the plots is the same as in Figure B-8. All dipping fractures have strike directions that differ 45° from that of the primary fault plane.
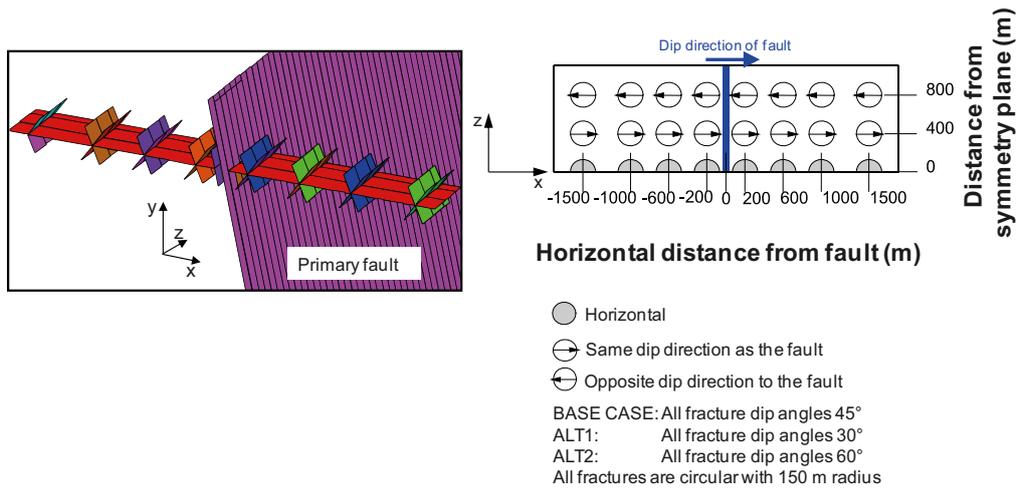
Figure B-8. *The right picture is a sketch of the principle showing target fracture locations and orientations in the BASE CASE, ALT1 and ALT2 fracture configurations. The sketch is a view from above of the target fracture region. The solid blue line indicates the intersection between the fault plane and the repository horizon. These configurations are similar, but have different fracture dip angles as indicated by the legend. The arrows indicate the dip directions of the dipping fractures. The left inset shows the 3DEC cut planes used to create these fracture configurations.*
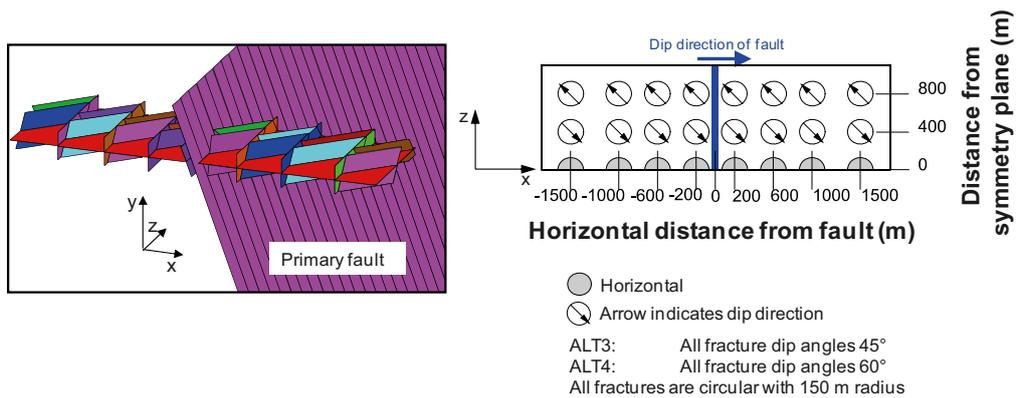
Figure B-9. *The right picture is a sketch of the principle showing the target fracture locations and orientations of the target fractures in the ALT3 and ALT4 fracture configurations. The sketch is a view from above of the target fracture region. The solid blue line indicates the intersection between the fault plane and the repository horizon. These configurations are similar, but have different fracture dip angles as indicated by the legend. The arrows indicate the dip directions of the dipping fractures. The left inset shows the 3DEC cut planes used to create these fracture configurations.*

Recurrence

There is the theoretical possibility that an individual fracture could be subjected to the effects of multiple earthquakes, with each generating an episode of induced slip such that the accumulated slip eventually could exceed the canister deformation threshold, even if the individual displacements are well below the threshold. The sequence of earthquakes could occur on the same fault or on different faults. Theoretically, the earthquakes could occur during the same period of instability or during different periods of instability. As indicated in Figure 7-9, there could be more than one period of instability during a single glacial cycle. For the glacial stress model suggested by /Lund et al. 2009/ there are some 40,000 years between the instability periods.

Multiple earthquakes on one individual fault

Same period of instability

According to empirical correlations among earthquake parameters established by /Wells and Coppersmith 1994/, the earthquakes modelled here have the largest magnitudes consistent with the size of the deformation zones on which they originate (cf. Figure 6-8, right) and the largest displacements consistent with those magnitudes (cf. Figure 6-8, left). For a given stress drop and a given rupture area, the strain energy release scales with the average fault displacement /Scholz 2002/. The seismic (radiated) energy scales with the stress drop and the average fault displacement. This means that the earthquakes modelled here release as much energy as reasonably possible, and that multiple earthquakes, if they occur within the same period of unstable stress conditions, cannot be as large as the modelled earthquakes. Two consecutive and identical M_w 6 earthquakes as the one pictured in Figure 5-2 and Figure 5-4, for instance, would give a total maximum slip of between 5 and 6 m. This is on par with typical maximum displacements of M_w 7 earthquakes (cf. Figure 6-8) releasing more than 10 times the energy of the two M_w 6 earthquakes. The strain energy available for release by fault slip could certainly be partitioned and released in a sequence of earthquakes with small slip and low stress drops distributed over a period of high instability, but the effects of the multiple small events on target fractures would not be larger than for the high stress drop single events modelled here. Therefore, the possibility of repeated slip on a target fracture because of multiple earthquakes on one nearby fault within a limited period of time, e.g. the period of instability following the disappearance of a future ice-cover, does not require any other handling than that described in the previous sections.

Different periods of instability

The question is whether one individual fault can slip a significant amount a second time within the safety assessment time frame, i.e. if the tectonic strain rate is sufficiently high to restore the stress field such that no or only little stabilizing effects of the strain energy release associated with the first earthquake remain. For earthquakes with a stress drop large enough to potentially generate secondary slip, the stress relaxation effects are quite large, as shown for the M_w 5.5 *3DEC* earthquake pictured in Figure C-1. Close to the source fault the major principal compressive stress is systematically reduced by at least 10 MPa, and sometimes more. At a horizontal distance of about 1 km the reduction is about 5 MPa and at 1.5 km about 3 MPa.
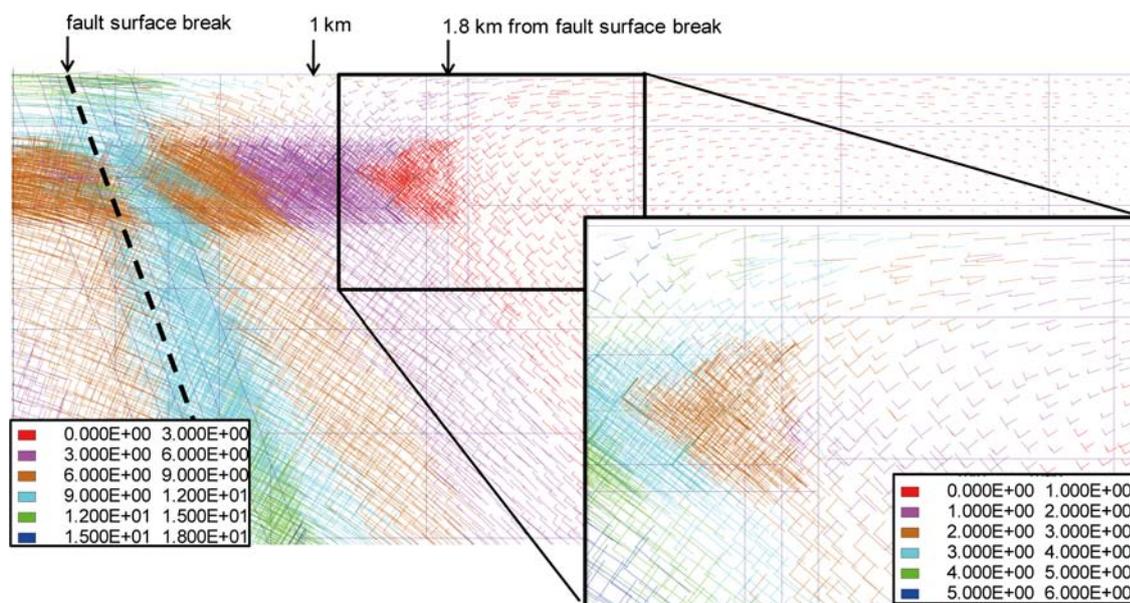
Figure C-1. *Change in stress tensor as a result of M_w 5.5 fault slip. Positive numbers indicate a compressive stress reduction (MPa). The inset shows the change at 1–2 km distance with a higher colour code resolution.*

If the local and considerable stress disturbance caused by the irreversible fault slip is not restored by tectonic compression, it is not likely that the same fault will slip again, at least by amounts that could potentially induce significant secondary target fracture displacements. Even if the tectonic compression would be fast enough to restore some of the stresses, the fault would be more stable than similar faults that did not slip in the past. This is in keeping with the notion that post-glacial earthquakes are triggered rather than powered by glacial disturbances (crustal flexure and pore overpressures), i.e. post-glacial earthquakes release strain energy accumulated over long periods of time. The probability that a given fault generates the largest possible earthquake consistent with the size of the fault is by itself low. The probability that it happens a second time when the fault is (relatively) more stable is much lower. Should a second large slip event take place, there are the following issues to consider:

- The relevance of the damage threshold: It is possible that the period of stability will be sufficient for the bentonite buffer to re-homogenize such that the buffer-canister system is effectively undisturbed at the time of the second earthquake. It is beyond the scope of this report to speculate on whether this means that a different and larger threshold should be established for the total effects of repeated earthquakes on the same fault.

- The probability that both slip vectors of the induced fracture slip are parallel: In order for them to be exactly parallel, the orientation of the stress tensor and the style of the rupture must be very similar for the two earthquakes. If they are not parallel, the total net slip will be less than the sum of the two individual slip movements. Additionally, if the difference in slip vector orientation is not too small, the two movements will not necessarily initiate potentially damaging strain in the same parts of the copper/steel canister. This would mean that the net effect of the two slip movements, both smaller than the damage threshold, would be equivalent to the effect of two non-damaging movements across two different deposition holes.

Earthquakes on different faults

Same period of instability

Using the idealised slip distributions shown in Figure 7-1 (lower) it is possible to obtain upper-bound estimates of the probability that two consecutive slip events on a 150 m radius fracture positioned reasonably close to two earthquake faults will add up to the 50 mm threshold, cf. examples in Figure C-2. Here it is assumed that all combinations of slip 1 (induced by the first earthquake) and slip 2 (induced by the second earthquake) are equally probable. Two cases are shown:

* The slip vectors are parallel.

* The second slip vector is aligned 45° off the orientation of the first one, meaning that the rectangular areas are correspondingly modified.

Note that both earthquakes must be assumed to be high stress drop, high velocity events. (Aftershocks are usually one unit of magnitude smaller than the main shock, cf. /Scholz 2002/). The probabilities are based on distributions valid for target fractures with dip angles smaller than 55°. For steeply dipping fractures different probability distributions with 25% smaller displacements apply (cf. Section 7.1), meaning that the rectangular regions would be correspondingly smaller and the probabilities of exceeding the threshold lower.

Table C-1 shows results, obtained as illustrated in Figure C-2, for different combinations of fault size and fault-target distances. The two slip vectors are assumed to be parallel, which is conservative; some vector additions will reduce the total slip rather than increase it. The table shows that the two zones cannot be further apart than about 1 km in order for the probability of exceeding the 50 mm threshold by more than a few millimetres as a result of the second slip to be non-zero. /Munier and Fenton 2004/ report that there appears to be a self-similar relationship between size of post-glacial faults (length) and interfault spacing, with hundreds of kilometres between large faults and about 10 km between faults of the smallest length considered here (surface trace lengths of 3 to 5 km). This means that typical interfault spacings found in the landscape exceed the maximum spacing between faults that theoretically (i.e. according to Table C-1) may mean a risk (i.e. about 1 km) with very good margins. Yet the probabilities given in Table C-1 are based on very conservative assumptions, including:

* Both earthquakes have the largest slip consistent with the fault size and slip velocities on par with the high velocity Chi-Chi earthquake.

* The two slip vectors are parallel.

* The magnitude of the second slip is independent of the first one. Part of the target fracture slip found in the *3DEC* models appeared to be due to the *in situ* shear load, at least for fractures with non-zero dip. When the second seismic event occurs the shear load will be reduced on fractures that slipped as a result of the first one, meaning that the slip distributions will be different from those shown in Figure 7-1, i.e. the maximum slip will be smaller.

There is no symmetry among the off-diagonal elements in last part of the table. This is because the probability is different depending on whether the small or the large zone is closer.

Different periods of instability

Table C-1 applies irrespective of the time elapsed between the two earthquakes, i.e. they cannot be further apart than about 1 km for the second slip to impact more than marginally on the probability of exceeding the 50 mm threshold. For earthquakes occurring during different periods of instability separated by tens of thousands of years, there are no interfault distance observations. Provided that the tectonic strain rate is not very high, the time aspect is, however, not important: the stress relaxation effects (cf. Figure C-1) reach sufficiently far that faults a couple of kilometres away from the first earthquake can be assumed to be stable (i.e. in agreement with the interfault spacing observed in the North-Fennoscandinavian landscape).
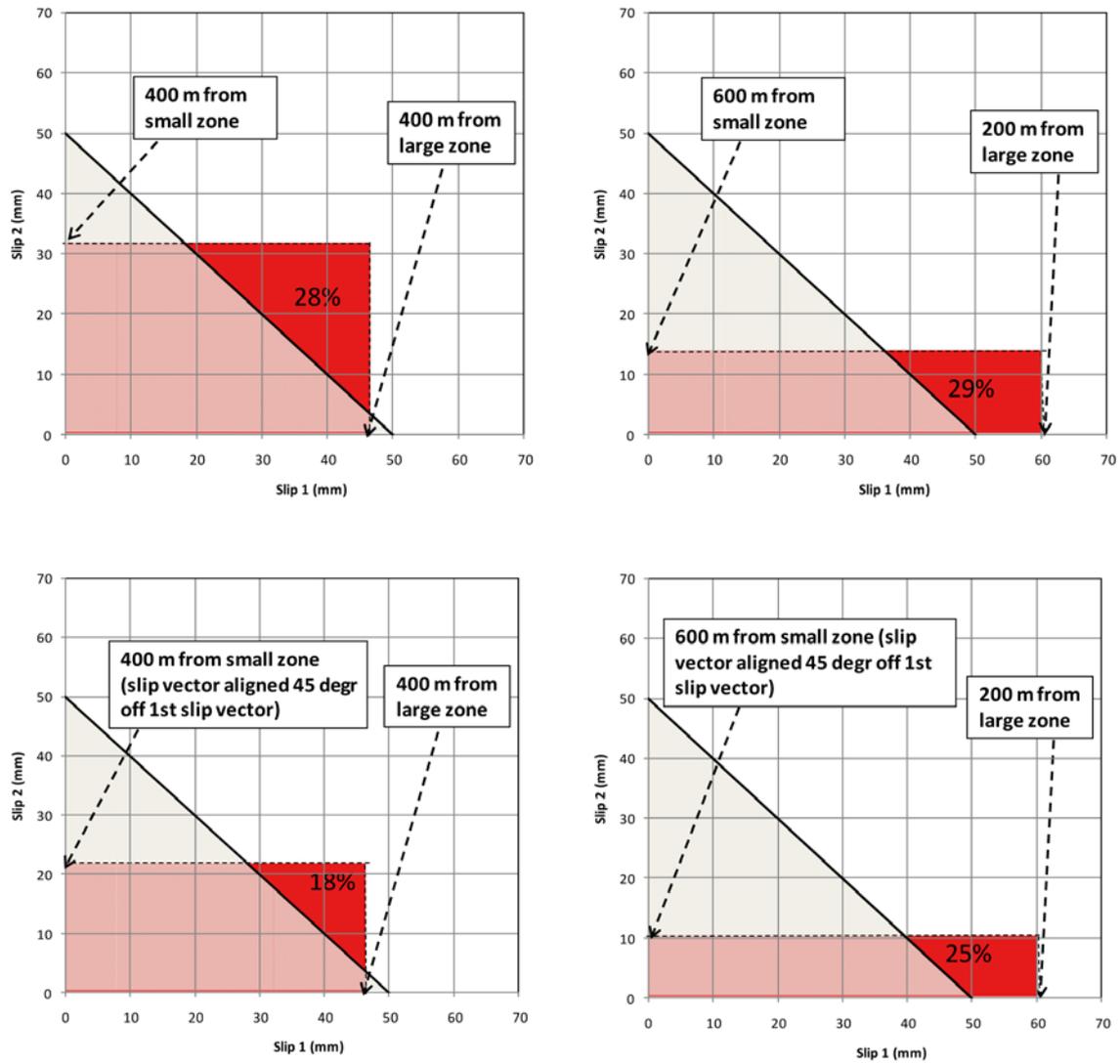
Figure C-2. *Examples showing fraction of slip combinations that give net total slip in excess of the 50 mm threshold for 150 m radius target fractures. The rectangles represent all possible combinations of slip 1 and slip 2. Given the linear slip distributions suggested in Figure 7-1 (main text) and assuming that all combinations are equally probable, the area fractions of the notated upper right corners correspond to the probability that the total slip will exceed 50 mm. Upper: Slip vectors are parallel. Lower: Second vector is offset by 45° compared to the first vector.*

Table C-1. Probability (%) that two consecutive target fracture slip events on a 150 m radius fracture caused by two independent nearby earthquakes will add up to 50 mm. Numbers within parenthesis are corresponding single slip probabilities.

	Target fracture at different distances from two deformation zones with trace lengths < 5 km		
Distance (m)	200	400	600
200	50 (0)	32 (0)	14 (0)
400	32 (0)	10 (0)	0 (0)
600	14 (0)	0	0
	Target fracture at different distances from two deformation zones with trace lengths > 5 km		
Distance (m)	200	400	600
200	68 (17)	55 (17)	44 (17)
400	55 (17)	43 (0)	29 (0)
600	44 (17)	29 (0)	12 (0)
	Target fracture at different distances from one deformation zone with trace length < 5 km and one with trace length > 5 km		
Distance (m)	200 from large zone	400 from large zone	600 from large zone
200 from small zone	58 (17)	47 (0)	33 (0)
400 from small zone	43(17)	28 (0)	11 (0)
600 from small zone	29 (17)	9 (0)	0

Multiple earthquakes – summary

Based on the discussion above, it is concluded that multiple earthquakes will not increase the probability that a given rock fracture will slip in excess of the 0.05 m canister damage threshold, compared to the probability that it will in response to one individual earthquake. The main reason is that there is a limited amount of strain energy that can be released through earthquakes; the earthquakes modelled here release as much energy as theoretically possible. Partitioning that energy release between smaller earthquakes will not increase the maximum induced target fracture slip. On the contrary:

- Fractures that slipped in response to the first earthquake will be, relatively seen, more stable when the next earthquake occurs.
- It is unlikely that the same individual fracture will be subject to the largest possible slip twice (or more), unless the earthquakes are identical with the same hypocentre location.
- It is unlikely that the two slip vectors are exactly parallel.

Tectonic compression is too slow to compensate for the loss of stored strain energy on the time scale of one glacial cycle, cf. Section 1.1.1. This means that the conclusion is valid also if the multiple earthquakes are distributed over at least one glacial cycle. Additionally, for accumulated target fracture slip resulting from multiple slip episodes distributed over a long period of time, one might reconsider the validity of the canister damage threshold.

Recurrence and damage threshold

It is assumed throughout this report that the 0.05 m damage threshold applies for seismically induced target fracture displacements, regardless of displacements that may have taken place in the past, for instance because of thermo-mechanical loads during the temperate phase. During the temperate phase, suitably-oriented 300 m diameter fractures may slip by, at most, about 5 mm, cf. /Hökmark et al. 2010/. The style of that modest slip, i.e. whether it takes place time-continuously as the thermo-mechanical load varies or in discrete steps, is not important. Periods of post-glacial instability will not occur until many thousands of years later. During that long period of time, the water-saturated buffer is likely to re-homogenize such that the buffer-canister system can be assumed to have returned to its initial undisturbed state. This means that there is no need for extra margins to account for previous deforma-tions. For target fracture displacements induced seismically during different periods of instability the same applies: the risk of canister damage is likely to be determined by the magnitude of the individual slip movements, rather than by the total accumulated slip. It is, however, beyond the scope of this study to speculate on how much the 0.05 m single event damage criterion should be modified to apply for accumulated total deformations.

Deformation zone stability at Laxemar

The stability of deformation zones at the Laxemar site are estimated in a similar way as for the zones at the Forsmark site (cf. Section 7.3). The fault stability estimate is based on a Mohr-Coulomb failure criterion. The stress field used in the calculation is the sum of an *in situ* stress field and the glacially-induced stresses as calculated by /Lund et al. 2009/.

The stability of deformation zones at the Laxemar site is evaluated at the time of maximum instability estimated by /Lund et al. 2009/ to occur during ice front arrival, i.e. during a forebulge type stress regime. However, fault instability and faulting in connection with ice front arrival is not in accordance with the observations of post-glacial faulting in northern Fennoscandia (cf. Chapter 3); the analyses are nevertheless presented herein for completeness.

The *in situ* stress field used in the stability calculations presented here, is constructed in a similar way as stress field #1 in Section 7.3, i.e. the stress field is assumed to be in frictional equilibrium at all depths and the stress model parameters are determined from the site model stresses at 500 m depth. At 500 m depth in Laxemar there are strike-slip stress conditions with the major and minor horizontal stresses equal to 22.5 MPa and 12 MPa, respectively. The vertical stress is approximately 13 MPa, and corresponds roughly to the load of the overlying bedrock. The major horizontal stress trends 135° /Hakami et al. 2008/. These stress magnitudes are used in order to determine the friction coefficient, μ, and the stress ratio, R, according to Equation 7-4, which gives $\mu = 0.47$ and $R = 1.17$. These parameter values are used in Equation 7-4 to define the strike-slip stress field shown in Figure D-1.

The temporal developments of the glacially-induced stresses at 500 m depth at the Laxemar site as calculated by /Lund et al. 2009/ are shown in Figure D-2, left. Based on the calculated stress additions, /Lund et al. 2009/ evaluated the stability in the crust. The temporal development of stability at 9.5 km depth in Laxemar is shown in Figure D-2, right (positive values mean instability). As shown on Figure D-2 /from Lund et al. 2009/ , the largest instability at Laxemar was obtained at the times of the ice front arrival about 60 ka BP and 28 ka BP.

Laxemar (strike-slip)
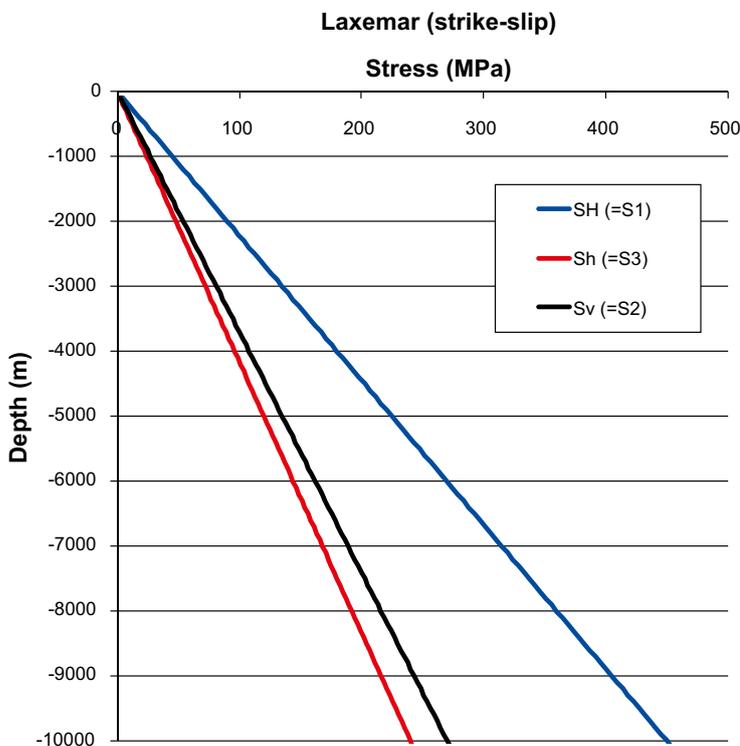
Stress (MPa)

Figure D-1. The strike-slip in situ stress field assumed in this section. At 500 m depth the stresses agree with the stress model suggested in the site report /Hakami et al. 2008/.
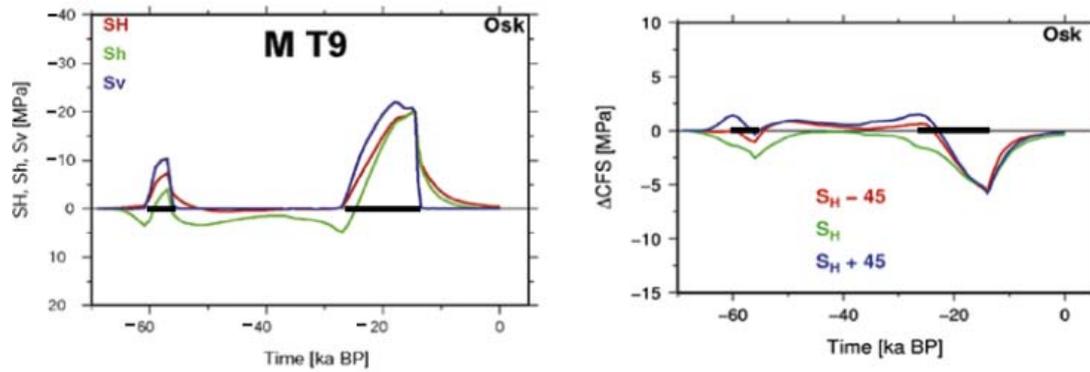
Figure D-2. Left: Glacially-induced stress additions at 500 m depth as function of time BP. Right: Associated instability quantity ΔCSF at 9.5 km depth as function of time BP (positive values mean instability). The solid black lines at zero indicate the temporal duration of the ice sheet. From /Lund et al. 2009/.

The stability of faults is evaluated using the stability quantity *CFS* (Coulomb Failure Stress) which is defined in Equation 7-5. The coefficient of friction is set at 0.47, which is the value required to keep the rock mass just at frictional equilibrium, given the strike-slip *in situ* stress field described above (Figure D-1). The glacially-induced stresses are picked at the time of the second ice front arrival about 28 ka BP (cf. Figure D-2).

Figure D-3 shows the poles of the Laxemar deformation zones[7] in lower hemisphere equal angle pole plots along with contours of the instability quantity *CFS* at the time of maximum induced instability (28 ka BP). The poles are colour coded to indicate safe or unsafe zone orientations. The stabilities are evaluated taking into account that strike and dip of the zones may vary within ±10° (cf. Section 7.3) and that the trend of the *in situ* stresses may vary within ±15° as indicated in the right pole plot (cf. /Hakami et al. 2008/). There is also an additional safety margin of 10 MPa in order to account for other data uncertainties (see legend).

The stability is evaluated at two depths (500 m and 3,500 m). The largest horizontal glacial stress addition component is arbitrarily increased by 5 MPa and the smaller one is increased proportionally. This is done in order to account for uncertainties in the stress addition results and for the possibility of tectonic strain accumulation under the stabilizing ice cover, which is not included in the results from /Lund et al. 2009/. Since no excess pore pressures are anticipated at the initiation of a glacial cycle, this is not accounted for in the calculations. The following can be observed in Figure D-3:

- The stability is larger at larger depths. At 500 m depth, no zone orientations count as stable according to the safety margin criteria applied here. Still, all CFS values are below zero. At 3,500 m depth, however, there are a number of steeply-dipping zones that count as stable.

- The relative importance of the glacially-induced stresses is larger at shallow depths where the *in situ* stresses are lower (cf. Figure 7-10). At 3,500 m depth the *in situ* stresses dominates and hence control in which directions the largest stability is found (at about 135° and 315° in accordance with the major horizontal stress trend 135°). At 500 m depth, however, the largest stability is found in the 155° and 335° directions since the glacially-induced stresses cause a shift in stress directions.

Figure D-4 shows a map of Laxemar deformation zones. Only zones with trace lengths > 3 km are shown. Zones within 600 m distance from any canister are coded with respect to their stability at 3,500 m depth according the results shown in Figure D-3, right. Three out of the ten zones shown in the map are considered stable.

---

[7] Modelldatabasen, 2008. Model: DZ_LX_REG_v23.rvs. Version 0.1. Approved 2008-05-27. Modified 2008-05-27. Modeller: P. Curtis. Simon ID: GEO_UNYMTLYA. https://service.projectplace.com/pp/pp.cgi/r272436908.
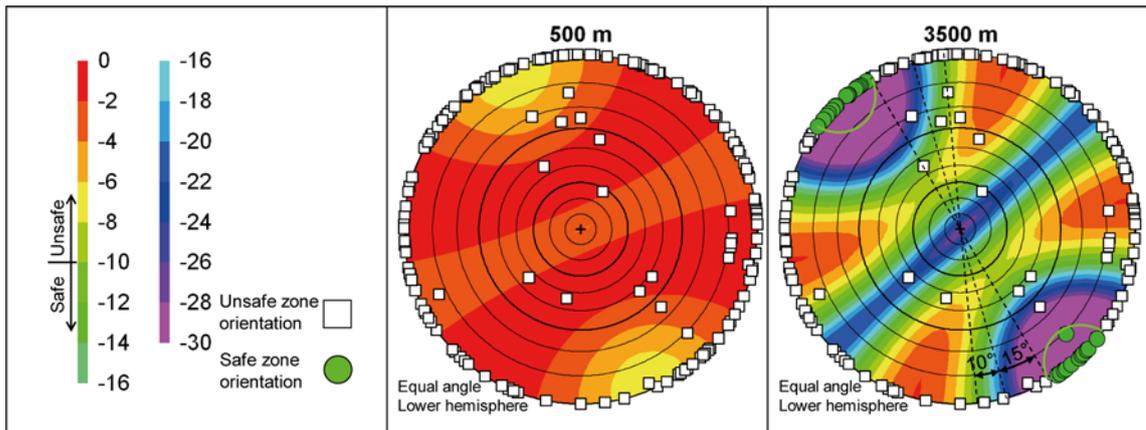
Figure D-3. *Contours of CFS values at 500m and 3,500 m depths plotted along with the poles of Laxemar deformations zones. The colours of the plot symbols indicate zone orientations considered stable or unstable according to the legend. Positive CFS values indicate instability. Circles denote 10° dip intervals.*
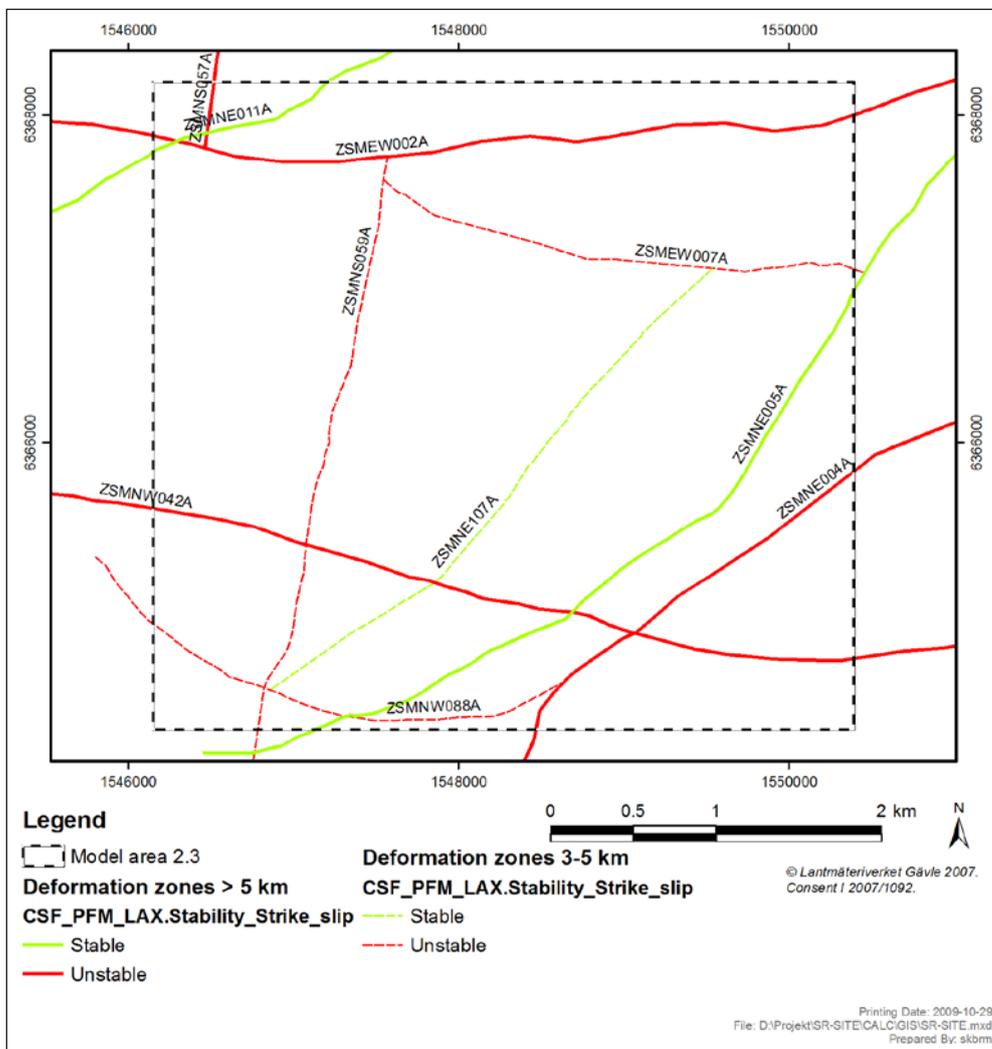
Figure D-4. *Map of Laxemar deformation zones[7]. Zones with trace lengths > 3 km are shown. Zones within 600 m distance from any canister are coded with respect to their stability at 3,500 m depth according the strike-slip stress regime assumption applied in Figure D-3, right. Stable zones are green and unstable are red.*